2005

THE DYNAMICS OF A TIDAL INTRUSION FRONT IN A NATURAL ESTUARY: EFFECTS ON MULTIBEAM SONAR ACCURACY

HOLMAN COLLINGWOOD THAIN, RICHARD

THE DYNAMICS OF A TIDAL INTRUSION FRONT IN A NATURAL ESTUARY: EFFECTS ON MULTIBEAM SONAR ACCURACY

R.H.C. THAIN

Ph.D. 2005

THE DYNAMICS OF A TIDAL INTRUSION FRONT IN A NATURAL ESTUARY: EFFECTS ON MULTIBEAM SONAR ACCURACY

By

RICHARD HOLMAN COLLINGWOOD THAIN

A thesis submitted to the University of Plymouth in
partial fulfilment for the degree of

DOCTOR OF PHILOSOPHY

School of Earth, Ocean and Environmental Sciences
Faculty of Science

In collaboration with
Britannia Royal Naval College

July 2005

Richard Holman Collingwood Thain

The Dynamics of a Tidal Intrusion Front in a Natural Estuary: Effects on Multibeam Sonar Accuracy

Abstract

This research has utilised high-resolution measurements of density and velocity to investigate the formation of a transient tidal intrusion front in a narrow, macrotidal estuary, and model the impact of such a frontal system on the accuracy of multibeam sonar surveys.

The front was found to form during spring tides, when the barotropic inflow was sufficient to arrest the buoyant outflow from the estuary. This has been shown to be driven by changes in channel width and depth, creating a hydraulic control point. These changes in topography are demonstrated to interact with the flow in a similar manner to theoretical two-layer flow over the lee side of a sill. Enhanced shear at the density interface, provided by increasing barotropic and baroclinic flows during the flooding tide, eventually led to the decay of the frontal system. There was no surface manifestation of this front during neap tides. Further measurements have confirmed that the relatively weak barotropic flow at this time was not sufficient to overcome the stratification in a two layer regime. Frontal dynamics have been shown to conform to theoretical predictions, and an evaluation of the key frontal discriminators has confirmed the validity of their use in such an environment.

The development of a multibeam sonar refraction model has facilitated an assessment of the accuracy of hydrographic surveys conducted in the presence of a tidal intrusion fronts. Major reductions in swath width have been shown to be required when traversing a tidal intrusion front, with a flat sonar transducer array providing the most effective survey results. Under-sampling the sound velocity field in the vicinity of a tidal intrusion front leads to major depth errors using all multibeam sonar transducer configurations; hence, accepted methods of sound velocity sampling in estuarine environments should be updated with immediate effect. Recommendations have been made that sampling in such an environment is undertaken at least hourly, at intervals of less than 50 m in order to maximise hydrographic survey efficiency.

List of Tables xvi

List of Figures

List of Tables

List of Plates

Notation list

A	Cross-sectional area
a	Constant depth error
b	Estuary breadth
$\overline{b}$	Factor of depth dependent error
b_p	Width at plunge point
b_e	Channel exit
b_o	Sill crest
c	Velocity of a wave/speed of sound in seawater
c_i	Velocity of a wave in layer i
$c_{i(pred)}$	Sound velocity in layer i, as derived from a predicted, or archived profile
$c_{i(obs)}$	Sound velocity in layer i, as derived from an observed, or new profile
c_z	Sound velocity gradient
D	Depth of water, distance
f	Frequency
Fi	Interfacial Froude number
F_i^2	Densimetric Froude number for layer i
F_Δ^2	Shear Froude number
F_o^2	Inflow Froude number
g	Gravitational acceleration
g'	Reduced gravitational acceleration
G^2	Composite Froude number
h	Height

h_i Height of layer i

h_p Depth at plunge point

h' Dimensionless depth

$\overline{h}$ Mean water depth

h_i Depth of layer i (height above bed)

h_0 Depth at sill crest

K Response time

K_z Eddy diffusivity

K_o Eddy diffusivity in a homogeneous water column

L Transducer element spacing, beam separation

N Brunt Väisälä (buoyancy) frequency

N^2_{max} Interface depth (point of maximum buoyancy frequency)

N_z Eddy viscosity

N_o Eddy viscosity in a homogeneous water column

Δp Acoustic pings per ensemble, acoustic ping rate

q_i Flow rate in layer i

q_r Ratio of flow rates in each layer

q_i' Dimensionless flow rate in layer i

Q Net volume flow rate at the constriction

R Radius

Ri Richardson number

Ri_L Layer Richardson number

S Arc length

ΔS	Difference in arc length
$\bar{s}$	Turbulent salinity component
s'	Average salinity component
T	Temperature
ΔT	Temperature resolution
t	Time
Δt	Time delay
U	Vessel speed
$\overline{U}$	Depth mean velocity
U_o	Barotropic forcing
U_l	Limiting condition (when buoyant outflow is blocked)
u	Flow velocity
u_i	Flow velocity for layer i
u'	Horizontal turbulent velocity
V	Mean flow velocity
v	Velocity
w'	Vertical turbulent velocity
x	Horizontal distance
Δx	Horizontal displacement/horizontal error
y	Horizontal (longitudinal) distance
y'_{1o}	Dimensionless upper layer depth
y'_{2o}	Dimensionless lower layer depth
z	Depth or vertical distance
Δz	Depth or vertical error

$Z_{i(pred)}$ Depth of layer i, as derived from a predicted, or archived profile

$Z_{i(obs)}$ Depth of layer i, as derived from an observed, or new profile

β Beam angle from transducer face

β_a Modified beam launch angle

γ Density anomaly

θ Grazing angle/angle of incidence

λ Wavelength

ρ Density

$\Delta\rho$ Density difference between layers

ρ_i Density anomaly of layer i

σ Random error of horizontal velocity

τ Averaging time

χ Stratification parameter ($h/\overline{U^3}$)

Note that in order to conform with the modern convention, salinity is expressed without units throughout this thesis.

Acknowledgements

At the University of Plymouth, Dr Mark Davidson has been a continual source of inspiration to me throughout my studies. Extremely generous with his time and advice, he has remained notably patient with the part-time nature of this work. Maintaining my enthusiasm with his encouragement and vision, the completion of this thesis owes much to his support. Peter Ganderton made efforts well above and beyond the call of duty in setting up the ADCP, and ensuring that it worked properly after the troublesome initial trials. Thanks are also due to Professor Keith Dyer for taking the time to listen to my early ideas, and in reading an early draft of my publication.

My colleagues at Britannia Royal Naval College have been incredibly helpful and patient, and particular mention must go to Dr Duncan Priestley. His help, encouragement and realistic advice as a third supervisor has been much appreciated. His encouragement and presence at conferences in Italy and, in particular, Poland have also provided unique insights and experiences. Dr Paul Rampling has been most understanding in providing me with time to complete the thesis, and proved to be a most able and patient survey vessel skipper. Dr Alistair Cree has assisted me with many of the mathematical concepts, and in particular, I must thank him for his continual exhortations to 'go and write some thesis'. Professor Mike Chamberlain supplied some much needed assistance with the calculus and remained patient in the face of my continuing struggles. Dr Travis Mason provided me with much encouragement and inspiration throughout this process, and unsplit numerous infinitives in the early days. I can still see her furrowed brow when ploughing though early chapter drafts, a sure sign of an impending grilling. Peter Heal has been most helpful in obtaining charts for me, and engaging with the Hydrographic Office to obtain the necessary copyright permissions. Dr Peter Street

encouraged me to commence this research in the first instance, and has assisted greatly since, in talking through sonar propagation problems and checking my calculations. Dr Richard Porter provided useful advice in the design of the fieldwork, and Mike Floyd in Media Resources has done a superb job with the picket boat drawings, and has provided me with much help over the past few years with the manipulation of all my images. Gary and Martin in reprographics have managed to mask their horror impressively when I've walked in with endless piles of copying, and the library staff, in particular Robert Wardle, have been a great help in the procurement of my literature.

The considerable amount of time taken by Neil Millington in creating the AutoCAD chart of the Dart estuary is gratefully acknowledged, and Mark Crookes was also most generous in providing me with the 'lisp' routine to import the GPS data directly into AutoCAD. My friends and family have been very understanding of my recent hermit-like tendencies, and Dr I Jones has proved to be of great assistance in solving many problems during our afternoon walks.

Most importantly of all, the completion of this thesis owes much to Alex's support and understanding over the last four and a half years

Author's declaration

At no time during the registration for the degree of Doctor of Philosophy has the author been registered for any other University award without prior agreement of the Graduate Committee.

This study was financed by Britannia Royal Naval College.

Word count of main body of thesis: **63 936**

Signed.....

Date.....03 AUGUST 2005.....

Publications and presentations

The following articles have been published, and presentations delivered during the course of this research:

Priestley, A. D. & Thain, R. H. (2005). The physical oceanography of the lower Dart estuary: Temporal trends and frontal dynamics. *ECSA Symposium, Estuaries of South West England, Plymouth, UK.* 6-8 April 2005.

Thain, R. H., Priestley, A. D. & Davidson, M. A. (2004). The formation of a tidal intrusion front at the mouth of a macrotidal, partially mixed estuary: a field study of the Dart estuary, UK. *Estuarine, Coastal and Shelf Science,* **61**, *161-172.*

Priestley, A. D. & Thain, R. H. (2003). Water column variability at an estuarine mouth: implications for multibeam sonar surveys. *Third international conference on high resolution surveys in shallow water, Sydney, Australia,* 17-21 November 2003.

Thain, R. H. & Priestley, A. D. (2002). The importance of tidal intrusion fronts for sonar operations. *Proceedings of the XIIIth International Scientific Conference, Naval University of Gdynia, Poland.*

Thain, R. H. & Priestley, A. D. (2002). Sound speed variability across an estuarine front. *Proceedings of the Undersea Defence Technology conference, La Spezia, Italy.*

Invited speaker

Devon Living Coasts, Kingsbridge, Devon. November 2004.

Temporal variability in the Dart estuary.

Hydrographic Society, Plymouth, Devon. October 2004.

Modelling multibeam sonar performance in an estuarine environment.

Royal Navy Hydrographic Conference, Plymouth, Devon. October 2004.

Developments in estuarine research: implications for surveyors.

Training courses

During the course of this work, the author has attended the following training courses:

- June 2003 — **31st Coastal Multibeam Sonar Training Course.**
  Ocean Mapping Group/University of New Brunswick, 5 days.
- Sept 2002 — **Underwater Acoustics.**
  Imperial College, London, 3 days.
- Aug 2001 — **Matlab fundamentals and programming techniques.**
  MathWorks, Cambridge, 3 days.

1.0. Introduction

Tidal intrusion fronts are a common feature at, or near estuary mouths throughout the world. When buoyant outflow at an estuary mouth becomes blocked by a strong tidal inflow of dense seawater, the inflowing water plunges below the estuarine water as a negatively buoyant gravity current, often forming a distinctive V-shape of foam and debris at the surface. These fronts are commonly static, with a control point associated with a topographical feature such as a sill or width constriction, or may be formed over a gradually increasing bottom slope. They have been noted to occur frequently in bar-built estuaries, but have also been observed in fjord-like systems and in partially mixed estuaries. Tidal intrusion fronts are often transient, appearing for only a few hours of a tidal cycle. Some studies, however, have found tidal intrusion fronts which have proved to be persistent throughout a tidal cycle, moving up and down the estuary with the flood and ebb respectively.

The presence of a tidal intrusion front may influence horizontal dispersion and residual circulation throughout the estuary, and have impacts on local biological processes and estuarine sediment dynamics. The differing water masses on either side of the front will affect sonar propagation patterns, affecting those engaged in surveying or naval warfare activities in such an environment. The impacts of such a frontal system on sonar accuracy are not understood well at the present time, and are represented poorly in the literature. Present surveying practice generally under-samples water column variability and is based rarely on quantitative analysis.

Whilst direct observations of tidal intrusion fronts have been rare, particularly in terms of the velocity field, theoretical knowledge of the hydraulics of plunging flows in a two layer regime is well developed, particularly incorporating the influence of topographic effects. To date,

however, there have been few investigations which have attempted to combine hydraulics theory and field observations in order to explain the formation of a tidal intrusion front, and none to date conducted in a partially mixed estuary.

A pronounced tidal intrusion front has been observed to appear at the mouth of the macrotidal, partially mixed Dart estuary during spring tides. The front appears around the time of low water, and is demarcated by a V-shaped foam line and colour change. Persisting in the same location for several hours before disappearing abruptly, the front has not been observed to form during periods of neap tides. This study aims to use detailed field measurements taken in the Dart estuary during both spring and neap tides to quantify frontal formation and dynamics using an internal hydraulics approach. Furthermore, by setting this work within the context of previous, largely theoretical studies of frontal systems, the most appropriate dimensionless descriptors may be identified for incorporation in further numerical and practical studies of such environments. Modelling the influence of such a frontal system on multibeam sonar system accuracy will be a valuable addition to the literature, and a practical aid to surveyors working in such environments. This study, therefore, has the following aims and objectives:

Aims:

- To identify and quantify the physical processes responsible for the formation of a transient tidal intrusion front at the mouth of a partially mixed estuary.
- To ascertain the effects of such a frontal system on the accuracy of hydrographic surveys.

Objectives:

- Ascertain the hydraulic controls responsible for the formation and decay of a tidal intrusion front at the mouth of the Dart estuary.
- Ascertain which key dimensionless descriptor characterises the location and behaviour of such a front most accurately.
- Quantify the temporal and spatial variations in sound speed at the mouth of the Dart estuary due to the presence of the frontal system.
- Develop a multibeam sonar refraction model in order to ascertain the effects of such a front on survey accuracy.
- Identify the optimum surveying methodology in a partially mixed estuary in order to minimise sonar errors due to refraction.

This thesis is divided into two main sections, the first dealing with the formation and dynamics of the tidal intrusion front, the second with the influence of the frontal system on multibeam sonar system accuracy. The first section commences with a comprehensive review of the current state of knowledge of estuarine frontal systems. Fulfilment of the aims of this research is dependent on the accuracy of the field data, and therefore, the methodology used to gather these data is described in some detail. The presentation of the field data results is followed by a comprehensive analysis and discussion. This latter section explains frontal formation and dynamics using dimensionless analysis tools, in addition to an analysis of the internal hydraulics and estuarine mixing processes. A comprehensive evaluation of the practical use of the generic dimensionless estuarine analysis parameters is provided at the end of this chapter. The second section of the thesis quantifies surveying accuracy at the mouth the estuary. A simple two-dimensional sonar propagation model has been developed covering the most

popular commercially available multibeam systems. This model has determined multibeam sonar errors during both spring and neap tides, using sound velocity data derived from the field data collected in the Dart estuary. Combination of the findings from both sections of the thesis allows both the times when surveying may be undertaken most accurately to be defined, and the most effective temporal and spatial sound velocity sampling interval to be expressed in a quantitative way for the first time.

This thesis has been written to appeal to the widest possible audience in the oceanographic, hydrographic and naval communities. To facilitate its use by both the general reader and the specialist, a chapter overview and summary has been appended to the *beginning* of each major chapter. In this way, a researcher whose interests lie in the sonar modelling section, for example, can examine the appropriate section in its entirety, whilst gaining an understanding of the remainder of the work by reading the summary sections. The practical use of this thesis should, therefore, be maximised, and the intention is that this work will provide a valuable reference to all those with an interest in estuarine oceanography and hydrography.

2.0. Estuarine frontal systems: A review

2.1. Chapter overview and summary

The interaction of two-layer, stratified flows with topographical changes in an estuary, may result in discontinuities, or fronts in the density field. When buoyant outflow at an estuary mouth becomes blocked by a strong tidal inflow of dense seawater, the inflowing water plunges below the estuarine water as a negatively buoyant gravity current, often forming a distinctive V-shape of foam and debris at the surface. Termed a tidal intrusion front, these systems are a common feature at, or near estuary mouths throughout the world.

Tidal intrusion fronts are commonly static, with a hydraulic control point associated with a topographical feature such as a sill or width constriction, or may be formed over a gradually increasing bottom slope. They are likely to occur frequently in bar-built estuaries, but have also been observed in fjord-like and in partially mixed estuaries. A theoretical, internal hydraulics approach to frontal formation, using a dimensionless Froude number analysis of two-layer flow through a channel constriction may describe frontal formation and behaviour most appropriately.

Tidal intrusion fronts are often transient, only appearing for a few hours of a tidal cycle. Some studies, however, have found tidal intrusion fronts which have proved to be persistent throughout a tidal cycle, moving up and down the estuary with the flood and ebb respectively, although the estuaries in which these persistent, mobile fronts occurred changed little in width or depth to provide a hydraulic control point.

The presence of a tidal intrusion front may influence horizontal dispersion and residual circulation throughout the estuary, have impacts on local biological processes and the differing water masses on either side of the front may affect sonar propagation patterns profoundly.

2.2. Stratified flows

Stratified systems occur frequently in the marine environment. If a fluid of a different density is introduced into a homogeneous system, the system will exist, for a time at least, as two or more horizontal layers. Mixing between the layers tends to be inhibited to some extent by the stabilising influence of the density interface between them. For example, in the situation where a buoyant fluid overlies a more dense one, a parcel of water carried into the upper layer from the lower layer will possess a greater density than that of the surrounding waters. This results in a restoring downwards force, returning the parcel to its original position. In a similar manner, if a parcel of water moves down from the upper layer to the lower layer, the parcel is then more buoyant than the surrounding water and must return towards its original position. This counteraction of vertical displacement by gravity requires the density of the fluid to increase with depth, and clearly depends on the rate of change of density with depth. The motion of such a displaced parcel of water may, therefore, behave as if the gravitational acceleration is much reduced (Kranenburg, 1988, Lewis, 1997). Historically, these vertical processes have been hard to distinguish from the horizontal processes due the extreme anisotropy of the water properties in a stratified system (Geyer & Smith, 1987).

Two distinct layers are usually apparent in a stratified system, with a clear interface existing between them. In a steady and uniform situation, the isopycnals are oriented virtually horizontally, and the density variation is stable. Throughout the majority of the deep ocean,

this density variation is continuous, but can form discontinuous interfaces at the surface. These regions characterise frontal zones. The change in location of the density interface is thus dynamically important, even when the change in density is small (Baines, 1995). Introducing a disturbance to a stably stratified system may result in wave motion at the interface between the layers. Such internal waves are characteristic phenomena in stratified systems, and since the interfacial wave will propagate, the resulting disturbance caused by the wave is non-local (Kranenburg, 1988; Van Leussen & Dronkers, 1988).

The degree of stratification may be enhanced or reduced by corresponding changes in density of the two layers. As the density of seawater may be modified by changes in both temperature and salinity, a buoyant surface layer may be created either by surface heating, or advection of fresher water. In deep waters, a buoyant surface layer is usually created by solar heating. A warm layer of lower density water will form over the cooler, more dense underlying seawater. This surface heating effect is mixed downwards to a depth determined by the extent of local wave action. In coastal waters, a stratified water column may be formed by the interaction between the freshwater outflow from an estuary and the denser coastal waters. The preferential heating of the relatively shallow estuarine areas over the deeper coastal waters can also result in the seaward advection of a thinning plume of warm, low density water over the more dense, cooler coastal waters. Within estuaries, density differences are provided by a combination of the freshwater river discharge, localised heating, and the lower layer salt water influx from the ocean. In these complex systems, variations in temperature tend to be small, and salinity variations large, with temperature thus having a relatively small influence on density and stratification (Dyer, 1997).

A *stratified flow* is said to exist when external forcing causes the movement of a stratified fluid. This forcing may be barotropic, baroclinic, or a combination of the two. The former is derived from surface water slope caused by the periodic rise and fall of the tide. Barotropic forces are constant with depth. Baroclinic forces, however, are derived from the pressure gradients resulting from the horizontal gradients of salinity (and, therefore, density) within an estuary. It should be noted that baroclinic forces are zero at the surface and increase to a maximum at the bed (Dyer, 1997; Lewis, 1997). On the flooding tide, the barotropic and baroclinic pressure gradients in a stratified flow act in the same direction. Because of the increase in the baroclinic pressure gradient with depth, the total landwards pressure gradient, and hence tidal flows will be greatest near the bed. On the ebb tide, the barotropic forcing acts to seaward, whilst the baroclinic force is still directed landward. The opposition of the pressure fields creates a stronger relative outwards force near the surface, and hence currents will tend to be strongest in this area (Dyer, 1997; Jay & Smith, 1990).

2.2.1. Mixing and shear in stratified flows

When dense water interacts with a basin of less dense water, it may mix with the ambient water, or it may retain its character as a separate underflowing dense layer (Largier, 1992). Parameterisation of the extent of temporal and spatial mixing in stratified flows is important. For example, the degree of vertical mixing influences the gravitationally driven estuarine circulation, and fronts may form between stratified and well-mixed areas.

The way in which two discrete water masses combine is controlled by the competing mechanisms of advection and mixing (Nepf & Geyer, 1996). This mixing may be caused by turbulence generated at the surface, at the seabed or at the density interface (Lewis, 1997). As

estuaries are generally shallow, the turbulent mixing produced at any of these boundaries can influence substantially the distribution of mean velocity and density in a large part of the flow (Kranenburg, 1988). Internal shear tends to dominate in salt wedge estuaries with little tidal motion, and bottom shear is dominant in well-mixed estuaries (Dyer & New, 1986). Advection and mixing can work together to create a feedback mechanism to either promote or destroy stratification. For example, as lower salinity water is advected over more dense ocean water, stratification increases (increasing the density gradient), and vertical mixing is inhibited. Conversely, as turbulent mixing increases, stratification is reduced, the diminished stratification thus promoting further mixing (Linden & Simpson, 1988). Studies of this feedback mechanism have identified the fact that large changes in local stratification are possible with only moderate changes in tidal stirring energy (Nunes *et al.*, 1989).

The amount of turbulent mixing will change with variations in coriolis force, wind speed, wave action, tidal range, and river discharge (Van Leussen & Dronkers, 1988). In addition, changes in channel bathymetry and channel width, collectively referred to as topographic variations, have an effect. Alternate periods of stratification and mixing will, therefore, occur as the magnitude of any of these parameters changes. Coriolis force may be neglected when examining flows lasting only a few hours with length scales of less than about 5 km (Baines, 1995), and wind effects, which can be important on occasion, may have a smaller influence than some of the other factors, particularly in relatively narrow, sheltered estuaries. It has been shown that in order to collect estuarine data unaffected by variations in wind speed and direction, and atmospheric pressure, would require a sampling interval in excess of 10 days, providing obvious difficulties for the majority of estuarine researchers (Dyer, 1979). The effect of wave action in sheltered estuaries is generally also neglected in the majority of studies. The interaction of flow with longitudinal variations in topography has been identified

as being particularly important, with effects including changes in location of the density interface, shear and mixing of two stratified layers, creation of surface density discontinuities (fronts) and creation of internal waves (Baines, 1995; Dyer & New, 1986; Postma, 1988). It is apparent, therefore, that it is topographic variations, together with changes in barotropic forcing and river discharge which are likely to provide the first order controls on mixing and stratification within an estuary.

Turbulent mixing caused by shear at the horizontal interface can act to decrease the density difference between the two layers (Lewis, 1997). When the interfacial shear increases to a level sufficient to overcome the static stability of the fluid, small waves (Holmboe waves) or billows (Kelvin-Helmholz instabilities) may form at the boundary between the two layers. The smaller waves may eventually break, injecting an element of more dense water from the lower layer into the upper layer. This process, known as entrainment, draws a less turbulent water mass into a more turbulent layer, and also acts to increase the potential energy of the water column (Dyer, 1997). As shear increases further, billows at the point of maximum density gradient thicken the interface, decreasing the gradients of density and velocity, and leading to a degree of mixing between the two layers (Dyer, 1997; Dyer & New, 1986). This process is known as turbulent diffusion. As this mixing process continues, seawater is mixed upward from the seawater below requiring a greater compensating inflow at depth, thus increasing the gravitationally driven estuarine circulation (Griffin & LeBlond, 1990). Continuation of this process for a sufficient period of time would eventually result in the entire water column becoming homogeneous.

If turbulent mixing across the density interface does not continue for a sufficient time to homogenise the water column, the thickening of the density interface results in a transition

zone forming between the layers, where the gradient of the pycnocline is not as marked. The pycnocline at the interface between the two layers remains the zone of steepest density gradient in the water column, and therefore, it is still convenient to treat such a system as a two layer flow regime. Such two layer models have been applied frequently to describe the flow in estuaries (e.g. Huzzey, 1982; Kuo *et al.*, 1988; Pelegri, 1988; Largier *et al.*, 1992), although studies have been conducted recently in the Columbia River by Cudaback & Jay (2001) in identifying the pycnocline as a discrete, middle layer. This approach, whilst yet to be tested comprehensively against field observations, may improve the accuracy of models of circulation and mixing.

Turbulence generated by the shear of tidal flows interacting with the seabed also causes mixing. Rapid flows over a rough or shallow bed may introduce sufficient turbulence into the system to overcome the stability of the fluid and mix the water column. Shallow estuaries with high tidal ranges thus tend to be well-mixed environments, and deep estuaries with significant freshwater inflow and low tidal ranges, such as fjords, may remain stratified throughout the entire tidal cycle (Lewis, 1997). In some estuaries, both the shear generated at the density interface and the seabed may be important, and it is possible for these two mechanisms to interact to some degree. Interfacial shear may reduce stratification to some extent early in the tidal cycle, and bottom-induced mixing may become more effective during periods of maximum current flow. Importantly, internal shear may, therefore, not occur at the time of maximum flow velocity (Dyer & New, 1986). Lewis (1997) suggests that it is the turbulence generated at the density interface which may be more effective in the breakdown of stratification than that generated at the bottom boundary, although this is dependent on the degree of stratification in evidence at the time. Dyer (1997) suggests that the greater the degree of stratification the greater the effects of shear at the density interface in mixing the

water column. Historically, there have been relatively few reported cases of field confirmations of a particular mechanism of vertical mixing in stratified flows, although Geyer & Smith (1987) have found shear instabilities at a density interface to be the principal mechanism of vertical exchange in a salt wedge estuary. Work in well-mixed estuaries, however, has indicated that turbulence at the bed could be responsible for the majority of vertical mixing (Lewis, 1996).

Absolute quantification of turbulence and mixing processes occurring at any one time is extremely difficult. It is usual to represent them as a diffusive process, where the fluctuating turbulent velocity components in the horizontal and vertical directions (u' and w' respectively) are related to a coefficient of eddy viscosity (N_z) thus:

$$-\rho(\overline{u'w'}) = \rho N_z \partial\bar{u}/\partial z \qquad \text{m}^2\,\text{s}^{-1} \tag{2.01}$$

where ρ is the water density, $\bar{u}$ is the mean tidal flow velocity and z is the depth. Additionally, eddy diffusivity (K_z) may be represented by:

$$-\rho(\overline{w's'}) = \rho K_z \partial\bar{s}/\partial z \qquad \text{m}^2\,\text{s}^{-1} \tag{2.02}$$

where s' and $\bar{s}$ are turbulent and average salinity components respectively. Note that these coefficients are not physical properties of the fluid, and will vary temporally and spatially depending on flow conditions (Dyer, 1988). Under well mixed conditions, a homogeneous water column will render N_z and K_z equal. Under stratified conditions, however, the turbulence has to work against the density gradient, turning kinetic energy into potential

energy and reducing K_z and N_z below their homogeneous value (K_o and N_o respectively). Thus, N_z will be inhibited in the presence of a pycnocline, and will increase relatively when stratification is low (Dyer, 1997). The incorporation of an accurate magnitude of N_z, in particular, is an important component of many numerical models, and plays a key role in determining the strength of the vertical circulation within an estuary (Dyer, 1997; Lewis, 1997).

Estuaries have been traditionally classified according to type relating to their stratification (e.g. Hansen & Rattray, 1966; Jay & Smith, 1988). Well known examples include well-mixed, partially mixed or stratified estuaries. More recent work has indicated that estuaries may switch from one type to another in response to varying conditions. For example, Haas (1977) was one of the first researchers to report a regular oscillation between vertically homogeneous conditions during spring tides and stratified conditions during neap tides. He correctly deduced this to be related to increased turbulent mixing, due to increased flow speeds during the spring tides overcoming the stratification present during the low flow speed, neap tide regime. More recently, Griffin & LeBlond (1990) have also noted a "surprisingly strong" relationship between the spring-neap tidal cycle and a spring-neap modulation in surface salinity. Jay & Smith (1990) have also studied the effects of the spring-neap cycle on estuarine variability, noting large cyclical changes in the density field and salinity intrusion length. In addition, they found that the spring-neap variability was much more pronounced during the low-flow season, rather than the high flow season in the Columbia River estuary. It appears, therefore, that analysis of estuarine circulation based on models of tidally averaged dynamics is an over-simplification (Monismith & Fong, 1996).

Mixing will thus vary significantly both spatially and temporally. Stratification may only occur in deeper areas of the estuary during periods of high river discharge, when tidal currents are weak. The boundaries between such regions of stratified and well mixed water are often marked by a front, characterised by a strong horizontal density gradient (Lewis, 1997). Importantly, the work of Dyer & New (1986) has identified the fact that mixing produced at a particular isolated location in an estuary can be advected along the estuary to some extent, possibly into areas where mixing may not have been as marked. Mixing produced locally in only a few parts of the estuary may, therefore, affect the density structure of the entire estuary, and focussing on such areas of localised mixing may thus provide significant insights into the behaviour of the estuary as a whole.

2.2.2. Circulation and tidal straining

The effects of friction near the estuary bed leads to variations in the velocity profile with depth. On an ebbing tide, the more buoyant estuarine water moves more rapidly over the saline waters below, increasing the stratification. On the flooding tide, salinity in the surface layer decreases rapidly, as saline, coastal water is advected over the lower layer at a faster rate (Figure 2.01). This periodic increase of stratification on the ebb tide and decrease of stratification on the flood tide is known as tidal straining (Nepf & Geyer, 1996; Dyer, 1997). Importantly, it can cause a reduction of stratification even in the absence of turbulent mixing (Lewis, 1997).

The effects of tidal straining can be exacerbated by the spring-neap tidal cycle. Periodic stratification due to tidal straining is generally greatest at neap tides in areas where tidal streams are relatively strong and tidal mixing is a significant factor. When tidal stirring is

reduced, due to the lower flow rates during neap tides, the influence of tidal straining can lead to almost permanent stratification at this stage of the tidal cycle (Simpson *et al.*, 1990). During spring tides, however, higher flow rates and a corresponding increase in tidal stirring may result in almost complete mixing of the water column throughout the tidal cycle.

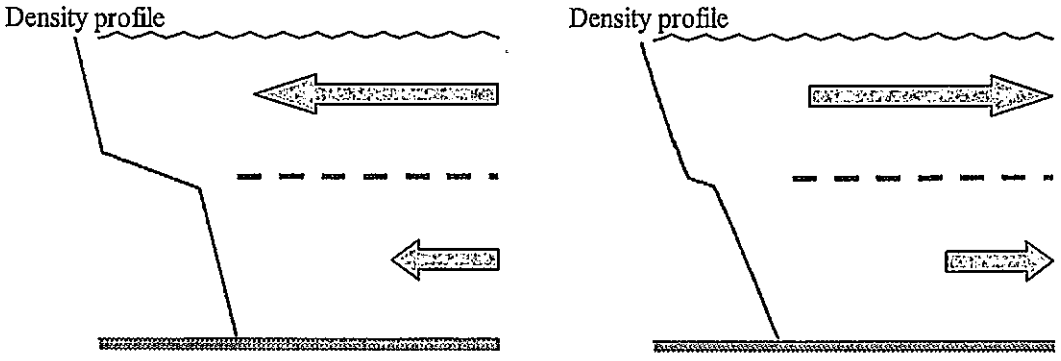

Figure 2.01. Differential advection of surface water (grey arrows) in a stratified flow may exacerbate stratification on the ebb tide (a), and reduce stratification on the flood tide (b). This process is known as tidal straining.

It was assumed at one time that the dependence of the formation of density fronts on stratification resulted in these features forming in estuaries on an ebbing neap tide only (Postma, 1988). At this stage of the tidal cycle, stratification would be most pronounced due to the effects of tidal straining. Further research on the modulations in mixing over variations in topography has found this hypothesis to be incorrect. Topographic changes may cause preferential mixing in shallower areas, and thus well-mixed and stratified areas may co-exist, the regions between them characterised by a front. These spatial variations in mixing may occur on a flooding or an ebbing tide, although the majority of estuarine frontal systems have

been observed to form on a flooding tide (e.g. Simpson & Nunes, 1981; Huzzey, 1982; Pelegri, 1988; Marmorino & Trump, 1996; Largier & Taljaard, 1991).

2.2.3. Interaction of stratified flows with topography

As a stratified flow is accelerated over a topographical change in the seabed, a depression in the pycnocline may form downstream of the feature. The upstream phase velocity of such a wave is of the same magnitude as the flow velocity, and the waves are, therefore, static when the flows are steady. As the flow slackens, the lee wave moves upstream against the decreasing flow as a series of solitary internal waves. Alternatively, if the flows over the obstacle become supercritical (Section 2.3.2), the internal wave will break as an internal hydraulic jump, creating a zone of intense mixing (New *et al.*, 1986; New & Dyer, 1988; Dyer, 1997). Early laboratory studies of this phenomenon provided clear insights into the generation mechanism of such waves (Lee & Beardsley, 1974; Maxworthy, 1979), although it was considered at first that they would form only during an ebbing tide. It is possible under certain flow conditions, however, for internal waves to form on a flooding tide; a possibility entertained by New *et al.* (1986).

The strong density gradient between the two layers in a highly stratified flow results in a zone of high acoustic backscatter. This has facilitated further studies using high frequency echosounders to 'visualise' internal wave formation and propagation. Dyer & New (1986) found internal waves present in a stratified flow on an ebbing tide, at high values of the layer Richardson number, Ri_L (Section 2.3.1.). The waves were not observed to occur at low values of Ri_L. Sturley & Dyer (1992) used a 200 KHz echosounder to visualise the formation of internal waves over an elongated depression in the bed of a partially mixed estuary. These

waves were again noted to form on the ebbing tide, presumably as tidal straining increased stratification during this stage of the tidal cycle, and altered the local stratification considerably. Theoretical investigations have also implied that topography controls horizontal and vertical transport processes, and thereby the stratification and circulation in estuaries, although the majority of these have concentrated on fjords (*e.g.* Stigebrandt, 1988).

2.3. Dimensionless analysis of stratified flows

Stratified flow characteristics may be represented by a variety of dimensionless descriptors, including Richardson numbers and Froude numbers. There are a wide variety of different Richardson and Froude numbers in common use and it is imperative to define clearly the terminology used. For hydraulics applications, mixing conditions are generally related to a Richardson number, and the Froude number is generally used to define critical conditions of the flow (Lewis, 1997).

2.3.1. Richardson numbers

The gradient Richardson number (Ri) is used widely in oceanic and atmospheric fluid dynamics, and has been employed as a fundamental parameter in many instances (Lewis, 1997). Ri is defined here as:

$$Ri = -\frac{g}{\rho}\frac{\partial \rho}{\partial z} \Big/ \left(\frac{\partial u}{\partial z}\right)^2 \qquad (2.03)$$

where ρ is the water density, and u is the velocity at height z above the bed. Theoretically, if $Ri > 0.25$ the flow is laminar and negligible mixing will occur. On the other hand, if $Ri < 0.25$, the flow becomes unstable and mixing will take place (Dyer, 1997). As Ri gradually reduces, a stable parallel shear flow becomes unstable and Kelvin-Helmholz waves form on the interface between the stratified layers, gradually mixing the water column. In the field, this transition from laminar to turbulent flow is far from distinct, and may occur between values of about $Ri = 0.03$ and $Ri = 1$, although on average, the critical value is 0.25 (Dyer & New, 1986). An implicit assumption is made that there is no longitudinal gradient in density, and any indicated shear is solely generating turbulence to break down the stability (Lewis, 1997). In addition, Dyer (1997) warns of the practical difficulty of measuring the gradients precisely. Despite its widespread application to stratified flows, Lewis (1997) advises that Ri has the following limitations:

1. Long period components in the turbulent field which are likely to change values of ρ and u make the selection of an appropriate averaging interval critical.
2. It is possible that turbulent energy may be generated elsewhere and then advected to the point where mixing occurs. For example, wind stress or breaking waves at the surface may cause turbulence in the interior of the fluid
3. Mixing may not take place immediately a critical value of Ri is reached, and it may take time for the density structure to change following the onset of mixing. Allowances may have to be made for such a phase lag.

Due to the limitations of the gradient Richardson number, it is possible to define the layer Richardson number (Ri_L):

$$Ri_L = \frac{(\Delta\rho / \rho)gD}{u^2} \qquad (2.04)$$

Where $\Delta\rho$ is the density difference between two flowing layers, D is the depth of the upper layer, and u is the flow of the upper layer relative to the lower layer. Ri_L is thus a bulk number reflecting the mixing characteristics of the entire flow, rather than the detailed, localised gradient Richardson number. As the layer thickness reduces, the value of Ri_L approaches that of Ri (Dyer, 1997; Lewis, 1997). Dyer (1988) and Dyer & New (1986) define the critical values of Ri_L as follows:

$Ri_L > 20$	A stable interface exists, with some internal wave activity. Bottom-generated turbulence is ineffective in decreasing stratification
$20 > Ri_L > 2$	Mixing dominated by bottom-generated turbulence becomes increasingly active
$Ri_L < 2$	Fully developed mixing occurs

Higher flow speeds during spring tides will lead to more mixing than during the lower flows during neap tides, and as this particular parameter uses the square of the flow speed, it is likely to be particularly sensitive to changes in u. It should be noted that the very nature of Ri_L, that is, a bulk parameterisation of the mixing in the *entire* flow, means that any internal shear which is occurring will also be included within the critical values (Dyer & New, 1986). Care must, therefore, be taken with the application of the parameter, and it cannot be used with any

confidence to compare adequately the relative contributions of shear at the interface and shear at the bed.

2.3.2. Froude numbers

A Froude number is equivalent to the ratio of the velocity of flow in a channel to the velocity of a surface long wave (Lewis, 1997). The speed of such a wave (c) in a channel of uniform depth (h) is given by:

$$c = \sqrt{gh} \tag{2.05}$$

The velocity of a surface long wave in a channel of depth of about 10 m would thus be approximately 10 ms^{-1}. In a stratified flow, however, waves on the interface move at a significantly reduced speed compared with those on the surface, the propagation speed of such an interfacial wave being defined as:

$$c_i = \sqrt{(\Delta\rho / \rho) g h_1} \tag{2.06}$$

In a typical partially mixed estuary, the density difference between the layers may be about 5.0 kg m^{-3}, with a surface layer depth of 2 m. Under such conditions, the speed of long interfacial waves travelling on this interface would be 0.3 ms^{-1} (Lewis, 1997). The interfacial Froude number is the ratio of the flow velocity to the velocity of propagation of a progressive wave along the density interface, and can defined as (Dyer, 1997):

$$Fi = \frac{u}{\sqrt{(\Delta\rho / \rho) g h_1}} \qquad (2.07)$$

where h_1 is the depth of a thin surface layer. Fi may be used to define the conditions under which waves on the density interface are able to move against the flow, carrying energy away from their point of formation. For example, in subcritical conditions ($Fi < 1$) an interfacial wave may be able to move upstream slowly. In a shallow channel, this movement is generally damped by friction, and thus the energy carried upstream by an interfacial wave in subcritical conditions does not have any significant effect on the flow (Lewis, 1997). As u approaches c, the wave energy accumulates, and at critical conditions where $Fi = 1$, the wave breaks with correspondingly energetic mixing. This is known as an *internal* hydraulic jump. When Fi is supercritical ($Fi > 1$) disturbances on the density interface are unable to propagate upstream and the effects of the wave are localised.

It would be unlikely for flow speeds in an estuary to approach or exceed 10 ms^{-1}, and therefore, a hydraulic jump would be unusual in a well-mixed estuary. In a stratified estuary, however, it is possible for the flow velocities to exceed 0.3 ms^{-1}. Flow velocity thus exceeds the speed of propagation of a long internal wave on the density interface, and therefore, such environments are characterised by internal waves and internal hydraulic jumps, with the attendant mixing.

2.4. Estuarine frontal systems

2.4.1. Frontal types

The variations in factors such as stratification, mixing, geomorphology and bathymetry lead to the development of different types of front within estuaries.

Five different types of estuarine front have been identified in the literature:

1 Plume fronts

2 Tidal intrusion fronts

3 Tidal mixing fronts

4 Shear fronts

5 Axial fronts

Several of these common frontal types may be regarded as having the same or similar characteristics. They may, therefore, be grouped into categories, which can be based on either their visual appearance, or more commonly, by the cause of mixing in the frontal zone. Differences appear in the literature in the way that the fronts are grouped together. For example, O'Donnell (1993) and Lewis (1997) compile fronts into three main categories (Table 2.01), with each author using slightly different groupings.

Fronts are categorised most accurately according to the driving mechanism responsible for mixing at the frontal interface. For plume fronts and tidal intrusion fronts, the mixing is generally dominated by the turbulence generated in the interior of the fluid by interfacial shear instability (O'Donnell, 1993). Tidal mixing fronts occur as the result of variations in the

intensity of bottom-generated turbulence, and shear fronts are the result of differences in the rate of horizontal advection in the direction of the local density gradient (O'Donnell, 1993).

O'Donnell (1993)	Lewis (1997)
Plume fronts and Tidal Intrusion fronts	Plume fronts
Tidal mixing fronts	Tidal mixing fronts
Shear fronts	Shear fronts

Table 2.01. Estuarine frontal systems as categorised by different authors

The intensity of any mixing occurring in an estuary is often described using a dimensionless descriptor, such as a Richardson number, or possibly a Froude number to define critical conditions of the flow (Lewis, 1997). These descriptors can provide excellent evidence of frontal occurrence, type and location, especially when a front may not be visible clearly to the naked eye. It should be noted that a front observed in the field may not exhibit the behaviour described exactly, but may exhibit the characteristics of two or more of the categories (O'Donnell, 1993).

2.4.1.1. Plume fronts

In highly stratified estuaries, the buoyant surface layer flows out over the denser seawater, thinning rapidly as it expands to form a surface plume (Figure 2.02). This buoyant outspreading of less dense water over more dense salt water can be likened to a pool of oil

spreading over water, the leading edge of the spreading action being the frontal zone (Garvine, 1977, Dyer, 1997). The colour of the plume water nearly always differs substantially from that of the ambient seawater, and can be seen clearly in photographs. The driving mechanism for the buoyant discharge can be either lowered salinity (from high freshwater runoff), elevated temperature from power station cooling water, or seasonal heating of the water in shallower areas of the upper estuary. A high vertical gradient in density inhibits vertical mixing, and if the buoyant water source was continuous, the plume would spread and expand indefinitely as a steadily thinning sheet over the receiving water. However, entrainment of the denser seawater into the fresh water plume, and friction at the frontal interface eventually leads to the retardation of the buoyant spreading, and the formation of sharp frontal boundaries at the leading edges of the plume (Bowman & Iverson, 1977). Plumes are extremely thin features. For example, the Connecticut River plume has a depth of 1 m over a horizontal distance of 10 km. This represents a width/depth ratio of 10^{-4}, the same as a piece of paper (Garvine, 1977).

The timing of the formation of plumes depends on the stage during the ebb tide when stratification or fresher water reaches the estuary mouth (Dyer, 1997). They generally intensify during the ebb tide, with stronger surface convergences at this time. This tends to accumulate more foam and floating debris at the frontal interface (Bowman, 1988). The extent and timing of plumes can, therefore, be quite variable, and an estuary may exhibit different behaviour at different times of year, since runoff varies on a seasonal and episodic basis.

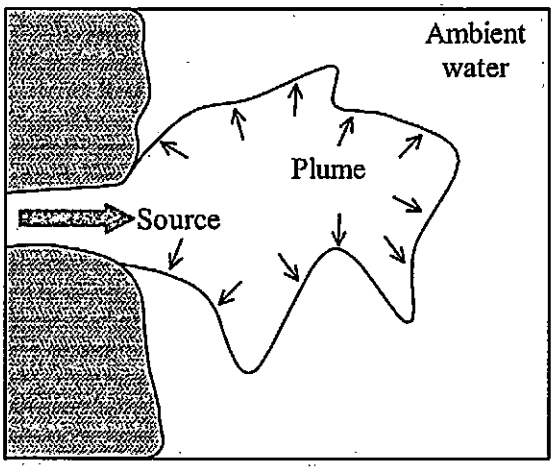

Figure 2.02. Buoyant outspreading of a river plume (from Bowman & Iverson, 1977)

The spatial scale of plumes is also variable, and is dependent on factors such as the intensity of the freshwater runoff into the estuary, the shape of the lower estuary, the strength of tidal mixing, and the prevailing wind patterns near the mouth of the estuary (Bowman, 1988). Thus, plumes can form either within the estuary (particularly if fresh water runoff is high), or outside the mouth, in the coastal ocean. Estuaries in which plumes have been observed include the Amazon, Mississippi, Mersey, Dee, Ribble, Teign, Seiont, and some Norwegian fjords, although many small and seldom surveyed rivers are likely to exhibit this behaviour intermittently (O'Donnell, 1993).

2.4.1.2. Tidal intrusion fronts

A buoyant plume usually flows seaward down the estuary at the internal wave velocity. During the flooding tide, however, the tidal current may exceed the internal wave velocity and the head of the plume is forced back into the estuary. This produces a clearly visible, and very developed V-shaped convergence, pointing upstream (Figure 2.03), with the denser seawater plunging downwards as a negatively buoyant gravity current at the frontal interface

(O'Donnell, 1993). There are usually small eddying motions at the tip of the 'V', and large accumulations of foam and debris occur there (Bowman, 1988). Largier (1992) has divided tidal intrusion fronts into three separate classes, depending principally on the shape of the interface at the surface (Figure 2.04). These frontal sub-categories have been developed from field observations, laboratory experiments and hydraulics theory.

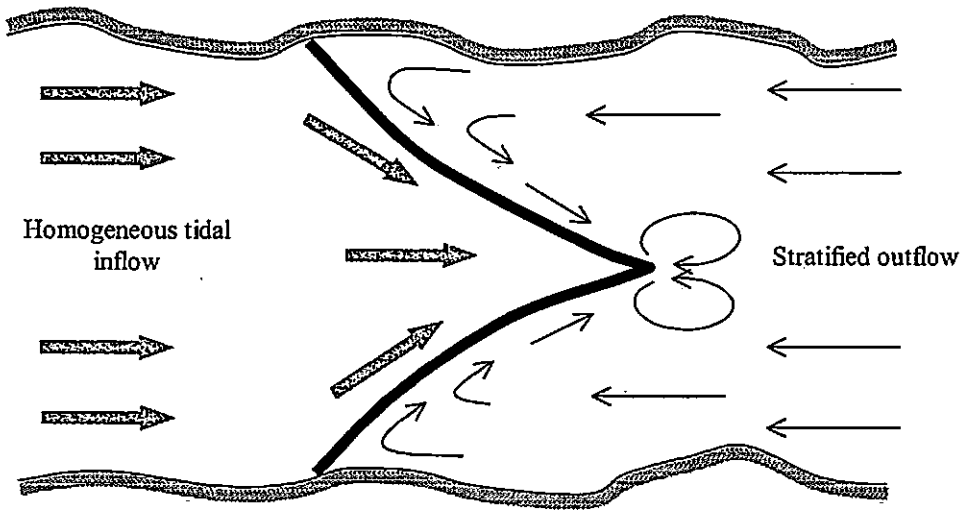

Figure 2.03. Plan view of a tidal intrusion front (heavy line). Adapted from Simpson & Nunes, 1981.

These fronts are generally transient, visible for just a short period at the beginning of the flood tide, before the increasing strength of the tidal stream causes rapid erosion of the two-layer structure (Simpson & James, 1986). This erratic behaviour presents significant obstacles to field study programmes (Brubaker & Simpson, 1999), and observations to date, particularly in the velocity field, have been rare (O'Donnell, 1993). Reports of tidal intrusion fronts to date have thus been relatively sparse, with the River Seiont in Wales being one of the first detailed study areas (Simpson & Nunes, 1981; Simpson & James, 1986). There is increasing evidence

to show that tidal intrusion fronts may be common features in partially mixed estuaries, with reports of frontal formation in the River Conway in the 2 hours immediately after low water (Simpson & Nunes, 1981), in Loch Creran in Scotland, and in the Port Hacking estuary in Australia (Bowman, 1988).

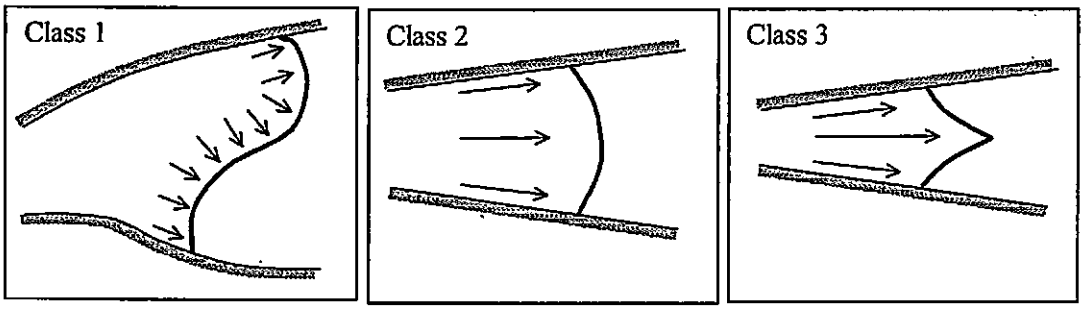

Figure 2.04. Classification of tidal intrusion fronts. (Adapted from Largier, 1992).
Class 1 fronts tend to occur in shallow, unconfined channels. Class 2 fronts have inflows confined to a degree by the bathymetry. Class 3 fronts are characteristic of inflows confined strongly by the bathymetry.

2.4.1.3. Tidal mixing fronts

Tidal mixing fronts can form both in the shelf seas, and within estuaries. In shelf seas, they occur at the boundary between waters which are well mixed by tidal flows, and waters which do not sustain sufficient turbulence to prevent stratification by solar heating (Lewis, 1997). Satellite observations have shown them to be persistent features, with large spatial scales (Simpson & Pingree, 1977; Loder & Greenberg, 1986). In estuaries, the presence of a thermohaline gradient (*i.e.* a horizontal gradient in temperature or salinity) in conjunction with tidal straining can cause a tendency for the system to stratify or destratify (Lewis, 1997). Thus, there will be a continuous change in stratification with tidal range, and over the spring-neap cycle. The net result may be a particular estuary exhibiting temporal and spatial changes

between a partially mixed, and a well mixed water column. At certain states of the tide, and in certain areas of the estuary, vigorous mixing will create an almost homogenous water column. On cessation of this mixing, the more saline waters can form a dense gravity current which pushes under the more buoyant surface waters. Mixing at the head of this current is generally low, and therefore, the density gradient across it is large, the net result being the development of a front. The process whereby a reduction, or cessation in mixing in a horizontal density gradient leads to the formation of a front has been termed 'frontogenesis' (Lewis, 1997).

The varying intensity of tidal stirring and tidal straining in estuaries, and the variations in advection of fresh water by buoyancy driven currents are likely to lead to variations in the intensity of any thermohaline gradient. Therefore, the location of a tidal mixing front (if, indeed, one is present) may be highly variable, and the frontal zone will be highly dynamic. This variability depends on factors such as tidal flow over changing bathymetry, baroclinic instability, internal waves breaking near the shore, seasonal heating, runoff and stage of the tidal cycle (Lewis, 1997). Sharples & Simpson (1993) have studied a tidal mixing front in Liverpool Bay, an area strongly influenced by the input of fresh water from the rivers of north-west England. The area displayed distinct periodic frontogenesis over a spring-neap cycle, caused by variations in tidal mixing and tidal straining.

It should be noted that some authors (e.g. Bowman, 1988) identify a tidal mixing front as a longitudinal feature, occurring in moderately stratified estuaries, and extending for many kilometres parallel to the axis of the channel. Bowman (1988) states that they tend to form in shoaling regions, with faster flowing currents in deeper offshore water advecting (lower salinity) upstream water past slower moving, higher salinity shoal waters. This shear increases the horizontal density gradient across the front, causing an area of convergence. Bowman (1988) also states that the manifestation of this type of front occurs on the ebb tide,

and may weaken or vanish on the flood tide, although he is presumably referring to such a phenomenon in a wide, shallow estuary. The description of such a front, parallel to the axis of the estuary, fits with the description of an axial or shear front by the majority of other authors (Section 2.4.1.4). Bowman's (1988) definition of a tidal mixing front will therefore be assumed to refer to an axial front. For the sake of clarity, this study regards a tidal mixing front as an across-estuary feature, extending to the bed, and occurring between areas of stratified and well-mixed water.

2.4.1.4. Axial fronts and shear fronts

This type of front forms longitudinally, along the axis of the estuary. On the flood tide, the incoming water usually travels fastest on the surface in the middle of the channel. This incoming water has a higher salinity than the water at the sides, and near the bed of the river, and it thus tends to sink towards the bed as it travels upstream. As the more dense water sinks, it draws in water from the banks, and a surface convergence develops, often marked by a distinct longitudinal foam line (Dyer, 1997). On the ebb tide, the opposite occurs, with surface divergence in the middle of the channel (and therefore no visual manifestation).

Dyer (1997) does not term this occurrence a front, but rather 'axial convergence', as do Simpson & James (1986) and Simpson & Turrell (1986). Lewis (1997) and O'Donnell (1993) however, use the term 'shear front'. Such axial convergence has been observed to occur in the River Conway in Wales (Simpson & Turrell, 1986). This appeared during the second half of the flood tide, with a foam convergence line extending for up to 10 km along the axis of the estuary. The front appeared to be strongest on spring tides, with no manifestation visible on the ebb tide. Simpson & Turrell (1986) state that this type of convergence should only happen in regions where there is a significant longitudinal salinity gradient.

2.4.2. Influences and effects of fronts

The presence of a frontal system at the mouth of an estuary may play a key role in determining the characteristics of circulation and mixing within the estuary (Bowman 1977; Simpson *et al.*, 1990; O'Donnell, 1993). The convergent flow characteristic of a front can 'capture' oil slicks and other buoyant pollutants concentrated at the surface, and draw them down into the water column. This may result in the accumulation of a complex mixture of organic and metallic compounds, including hydrocarbons, fatty acids, alcohols and toxic metals (Klemas & Polis, 1977; Simpson & Turrell, 1986). This process is essentially one of 'compartmentalisation', whereby the estuary is divided by fronts which serve to inhibit exchange, and trap effluents and fine sediments (Duck & Wewetzer, 2001).

The transport of water and salt throughout the estuary may be altered by the presence of a front, thus influencing estuarine circulation and impacting on the health of many ecosystems (Cudaback & Jay, 2001). For example, the establishment of a tidal intrusion front at the mouth of an estuary restricts the inflow of seawater, but also sets up a highly stratified basal inflow. This can exacerbate the up-estuary flow, filling up the deeper sections of the estuarine basin with dense seawater. These dense pools may persist for several months, becoming highly anoxic (Largier, 1993). Such a basal inflow has also been found to have positive effects, however, with the enhanced flows in the region of a tidal intrusion front being significant in the transport and retention of oyster larvae in the James River estuary (Kuo *et al.*, 1990).

Frontal convergences have been reported to enhance biological activity, with increased concentrations of phytoplankton often in evidence (Pinckney & Dustan, 1990). Additionally fronts have been noted to support biomass at higher trophic levels, being important feeding

areas for seabirds (Durazo *et al.*, 1998), fish (Brandt, 1993; Ciannelli, 2002) and dolphins (Mendes *et al.*, 2002). As water quality within an estuary may be affected by a frontal system, benthic production may also alter. This fact may be of crucial importance to the quality of the catch from any local fishery (Largier, 1993).

A frontal system is likely to alter sediment transport and deposition within an estuary (McManus, 2000). The supercritical flows in the region of a tidal intrusion front can resuspend loose sediment and deposit it elsewhere in the estuary, the convergent flows potentially accumulating toxic levels of metals in the sediment (Largier, 1993). The presence of a frontal system at an estuarine mouth may also act as a barrier, preventing sediment or pollutant removal from an estuary on the ebbing tide.

The differing water densities on either side of a front are known to affect profoundly sonar propagation patterns (Thain & Priestley, 2002a). In addition, the accumulation of bubbles and suspended matter in the frontal region can act as an acoustic wall, reducing sonar ranges, especially at higher frequencies (Largier, 1993; Madirolas *et al.*, 1997; Thain & Priestley, 2002b; Salvadores & Milou, 2004). This has been shown to degrade high frequency mine warfare sonar performance, and reduce detection ranges by up to 50% (Heathershaw *et al.*, 1996). Coastal warfare tactical and surveillance procedures may, therefore, have to be modified to cope with the acoustic anomalies caused by fronts (EOS, 1978), and estuarine hydrographic surveying practice may also require updating (Priestley & Thain, 2003).

2.5. Prior studies of frontal systems

Fluid mechanics theory has been well developed since the 1950's to explain the behaviour of stratified flows through a channel contraction, and over sills and weirs. Several key studies have examined the processes of frontogenesis (frontal formation) and frontolysis (frontal decay) in tanks in the laboratory. Other work has examined frontal systems at the mouths of fjords. The advent of more accurate oceanographic instrumentation, in particular the ADCP (acoustic doppler current profiler) has enabled many researchers to parameterise frontal behaviour using field data. There have been several recent comprehensive reviews of tidal intrusion fronts, including O'Donnell (1993) and Largier (1992). Some attempts have been made, particularly in the work conducted by Largier (1992), to combine the theories presented by those working in the field of fluid dynamics and the work of estuarine researchers. Few studies, however, have applied the appropriate fluid dynamics theory to field measurements of a tidal intrusion front in order to explain frontal formation and dynamics. Such a validation process is critical in order to develop and use estuarine models with confidence, and to enhance our understanding of estuarine circulation.

2.5.1. An internal hydraulics approach to tidal intrusion fronts

Early work by Stommel & Farmer (1953) was fundamental in identifying the influence of topographic changes at the mouth of an estuary. Their findings indicated that such a narrowing at the entrance, termed a 'transition' by them, could serve to limit the exchange between the reservoirs of water on either side of the transition. They hypothesised that a control section at the mouth of a relatively shallow stratified estuary could provide the primary control over the salinity upstream of the transition. In addition, they postulated that the rate of horizontal exchange of water between the two reservoirs is limited by flow through the

contraction, with a state of 'overmixing' being reached when further mixing in the transition section failed to increase the rate of water exchange or the density of the surface layer. It appears, however, that the applicability of this theory to natural flows is limited, as the authors state that the case is limited to subcritical flow through the transition, with no mixing occurring between the stratified layers. It cannot be applied directly to estuarine flows as variations in barotropic forcing may lead to supercritical flows in certain areas.

Wood (1968) also considered the effects of a horizontal contraction in a channel on unidirectional two-layer flow from one reservoir to another. His investigations identified a control on the flow (a hydraulic control point) exercised at the narrowest point of the contraction, and a further 'virtual control' at some section upstream of the flow. He found that as the velocity of a gravity wave is zero at the control point in an open channel, single layer flow, two wave modes are possible in a two layer flow. Thus the velocity of the first wave mode is zero at the control point and the velocity of the second wave mode is negative. At the virtual control point, the velocity of the second wave mode is zero and the first is positive.

Wood's (1970) later paper investigated the effects of two-layer exchange flows *between* two reservoirs separated by a horizontal contraction. He identified the fact that both a control and a virtual control point could exist in such a flow, in a similar manner to two-layer flow from one reservoir to another. In addition, he parameterised the hydraulics of the flow at the control point in terms of a dimensionless Froude number, but did not continue the analysis through iterations of varying degrees of external forcing.

Yih (1969) briefly mentioned the dynamics of stratified flow in a 'channel expansion', and introduced the concept of the flow dynamics in such a channel with an overlying stagnant

water layer. Importantly, he found that the presence of such a stagnant layer did not alter significantly the dynamics of the flowing layer. Whilst this is a purely theoretical application of fluid mechanics, it also describes the effect of the density difference ($\Delta\rho$) between the two flowing layers on the behaviour of the flow. The speed of propagation upstream of internal waves is a function of the density difference between the layers. If $\Delta\rho$ is large, then the internal waves are unlikely to propagate upstream and his derivations are valid, particularly when flow speeds are relatively low. However, in the situation where barotropic forcing may reduce, or $\Delta\rho$ may increase, internal waves may propagate upstream. In this scenario, the theory is not valid, and thus its use is limited in natural flows.

Mehrotra (1973) examined the action of channel contractions as controls in a relatively unified fashion. He states that if the two-layer flow is critical through the contraction (*i.e.* the speed of the flowing layers is greater than the propagation speed of the interfacial wave) then the contraction will act as a control on the flow. The flows upstream and downstream of the contraction are then subcritical and supercritical respectively, and the interfacial surface is asymmetric around the control. Importantly, he began the process of examining *vertical* channel contractions in the flow. His theoretical investigations lead to the development that the hydraulic control point created by a vertical contraction (a sill) acts only at the shallowest point above the sill when flows are critical. This is contrasted with the two control points which may be created by critical flows through a horizontal contraction. He states that if the flow through a combination of a vertical and horizontal contraction is subcritical throughout, then any control exercised by the two contractions will be coincident.

The seminal work of Armi & Farmer (1986) and Farmer and Armi (1986) in developing these early studies and applying them to natural flows has been an invaluable contribution to those

examining the interaction of stratified flows with topography. Armi & Farmer (1986) examined an exchange flow through a contraction in terms of a composite Froude number (G^2) of two layers, F_1^2 and F_2^2:

$$G^2 = F_1^2 + F_2^2 \tag{2.08}$$

Where F_i^2 is the densimetric Froude number for layer i:

$$F_i^2 = \frac{u_i^2}{g' h_i} \tag{2.09}$$

u_i is the flow speed of layer i, g' the reduced gravity ($g\Delta\rho / \rho_2$), where $\Delta\rho$ is the density difference between the two layers, and h_i is the depth of layer i. The two-layer flow is assumed to be inviscid, with each layer being homogeneous and unsheared. The effect of channel friction is neglected, and is assumed not to affect hydraulic control. Where $G^2 = 1$, this indicates the existence of a hydraulic control point, where the flow undergoes an internal hydraulic transition from sub-critical to critical.

They examined the exchange flow with varying degrees of barotropic forcing, finding that, unlike Stommel & Farmer (1953), the exchange flow at the mouth of an estuary is indeed analogous to a lock exchange flow scenario. Farmer & Armi (1986) studied the combined effects of a sill and contraction (termed a constriction) on two layer, stratified flows. They found that the influence of tidal flow through a contraction is negligible, but is significant over a sill, and through a combination of a sill and a contraction with varying degrees of external forcing.

2.5.1.1. Two-layer flows through a channel constriction

Farmer & Armi (1986) provide a detailed examination of two-layer flow over a sill from a theoretical perspective. A region where two reservoirs of water are separated by a narrow channel of uniform width with a sill located centrally in the channel (Figure 2.05) is analogous to many naturally occurring flows. For example, a fjord entrance, or the mouths of many estuaries are topographically similar to this situation. Farmer & Armi's (1986) work, like that of Wood (1968), indicates that critical conditions occur at the sill crest (b_o) and also at the exit (b_e); the 'exit' term in this case referring to the boundary between the restricted channel section and the open sea. Between these two controls, b_o and b_e, the flow is subcritical. To the right of the sill crest, the lower layer accelerates down the hill as a supercritical flow ($G^2 > 1$). As this supercritical flow decelerates at a location downstream of the sill, it passes from supercritical to subcritical, resulting in a stationary internal hydraulic jump (Lewis, 1997). To the left of the exit (b_e), the surface layer accelerates ($G^2 > 1$) at the entrance to the narrow channel, and also matches the right hand reservoir interface. Baines (1995) examines this process in some detail, identifying a further interesting phenomenon in such flows. He found that the flow on the downstream side of the sill must adjust to a deficit of fluid in the lower layer under certain flow conditions. In this situation, the flow remains supercritical throughout the sill area, and the horizontal interface between the layers descends rapidly on the downstream, or lee side of the sill. He terms this phenomenon a 'supercritical leap', which may also be termed a hydraulic drop.

As long waves cannot propagate beyond the control where $G^2 = 1$, the supercritical flows on either side of the control region serve to isolate the exchange flow processes (Bryden & Kinder, 1991). Such a control section is thus capable of influencing the global movement of fluid between the two reservoirs, irrespective of the detailed processes occurring outside the

control section. The processes occurring at the sill and contraction may, therefore, influence the behaviour of the entire estuary.

Farmer & Armi (1986) express the flow rate ($q_i = y_i u_i b$) of each layer in a non-dimensional form as:

$$q_i' = \frac{q_i}{g'^{1/2}(y_1 + y_2)_o^{3/2}} \tag{2.10}$$

where y_i and u_i are the depth and flow rates for layer i, b is the channel breadth and $(y_1 + y_2)_o$ is the total water depth at the sill crest (the sum of the upper and lower layer depths, y_{1o} and y_{2o} respectively). The depth of the channel, $-h(x)$ is referenced to the depth of the sill crest, where $h_0 = 0$ (Figure 2.05).

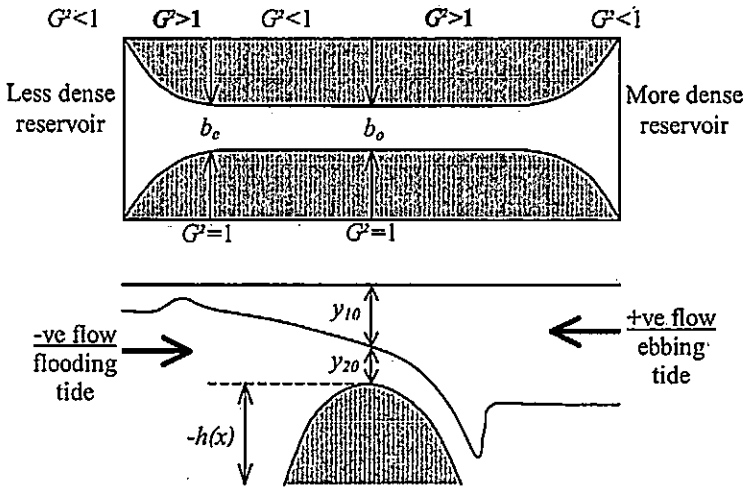

Figure 2.05. Schematic diagram illustrating two layer flow through a contraction in a channel and over a sill. Composite Froude number values (G^2)are shown (supercritical values are bold) in relation to the channel exit (b_e) and the sill crest (b_o). The depth of the upper and lower layer (y_{1o} and y_{2o} respectively) are also shown, along with flow conventions. Adapted from Farmer and Armi (1986).

The dimensionless depth can be expressed as:

$$h' = \frac{h}{(y_1 + y_2)_o} \tag{2.11}$$

with a dimensionless layer thickness being:

$$y_i' = \frac{y_i}{(y_1 + y_2)_o} \tag{2.12}$$

Farmer & Armi (1986) justify the use of the rigid lid approximation as the external Froude number is very small, and it may be expressed as:

$$y_1' + y_2' + h' = 1 \tag{2.13}$$

If the dimensionless layer depth is expressed as:

$$y_i' = (q_i')^{2/3} F_i^{-2/3} \tag{2.14}$$

and the ratio of the flow rates in each layer defined as:

$$q_r = \frac{q_1}{-q_2} \tag{2.15}$$

with a negative value of q_i indicating a (flooding) inflow of water from the dense reservoir. A value of $q_r = 1$ indicates that a steady flow between the two homogeneous reservoirs (without barotropic forcing) is occurring. If the flow rates (q_i) are regarded as being quasi-steady, *i.e.* unaffected by position along the channel, the flows through the system can be examined in terms of the continuity condition. Values of q_r will vary with the degree of barotropic forcing, being at a maximum on the ebbing tide, and approaching zero on the flooding tide.

Combining equations 2.14 and 2.15 allows the continuity condition to be expressed in Froude number space:

$$q_r^{2/3} F_1^{-2/3} + F_2^{-2/3} = \left[\frac{q_2'}{(1-h')^{3/2}} \right]^{-2/3} \tag{2.16}$$

Plotting lines of constant $q_2'/(1-h')^{3/2}$ as a function of F_1^2 and F_2^2 for a given q_r facilitates the analysis of flows through the contraction/sill system. Two-layer horizontal exchange flow may be maximal or submaximal, and expressing solutions to this exchange flow in terms of a Froude number plane solution (preserving continuity throughout) allows the important distinction between these two conditions to be made.

Maximal exchange flow, previously investigated by Stommel & Farmer (1953), exists for a certain set of flow conditions when a constriction or sill does not serve to limit the exchange of water between the two reservoirs. Expressing maximal exchange flow in terms of the Froude number plane solution when $q_r = 1$ (Figure 2.06), the two hydraulic control points at the sill crest (b_o) and the system exit (b_e) where $G^2 = 1$ can be distinguished. A region of subcritical flow (shaded area) exists between the crest of the sill and the exit. F_2^2 is supercritical downstream of the sill due to the higher flow speeds in the lower layer as the fluid accelerates down the lee side of the sill. If the reservoir of dense water is assumed to be of infinite depth, then F_2^2 collapses to zero upstream of the system exit.

Farmer & Armi (1986) use the Bernoulli equations for each layer in combination with the continuity equation (2.16) to derive the interface height (y_{2o}') for maximal exchange flows over a sill:

$$y_{2o}' = 0.375 \qquad (2.17)$$

It should be noted that this replaces the solution ($y_{2o}' = 0.5$) postulated by Stommel & Farmer (1953) and Armi & Farmer (1986) for flows through a horizontal contraction only.

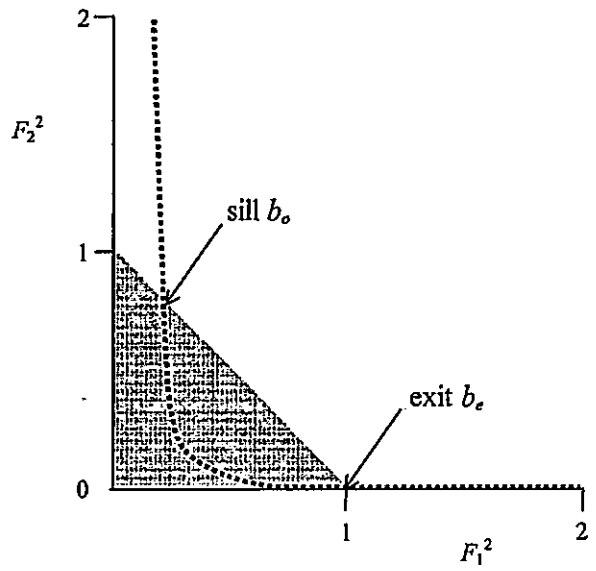

Figure 2.06. Froude number plane solution for maximal two-layer flow over a sill (dashed line). The shaded region represents subcritical flows between the sill and the system exit. Adapted from Farmer and Armi (1986).

Sub-maximal exchange flows are also possible. These may occur if one of the hydraulic control points at the entrance become flooded, either by a deep interface level in the left-hand (coastal) reservoir, or overridden by a shallow interface level in the right-hand (estuarine) reservoir. Solutions to sub-maximal exchange flows may also be expressed in terms of a Froude number plane solution. If the exit control is flooded by a deep interface in the coastal reservoir (Figure 2.07), subcritical conditions will not be achieved at the sill exit, but may still develop at the sill crest. Conversely, if the sill control is flooded by a shallow interface in the estuarine reservoir (Figure 2.08), the solution indicates critical flow at the exit ($F_1^2 = 1$, $F_2^2 = 0$), with critical conditions not being met at the sill crest.

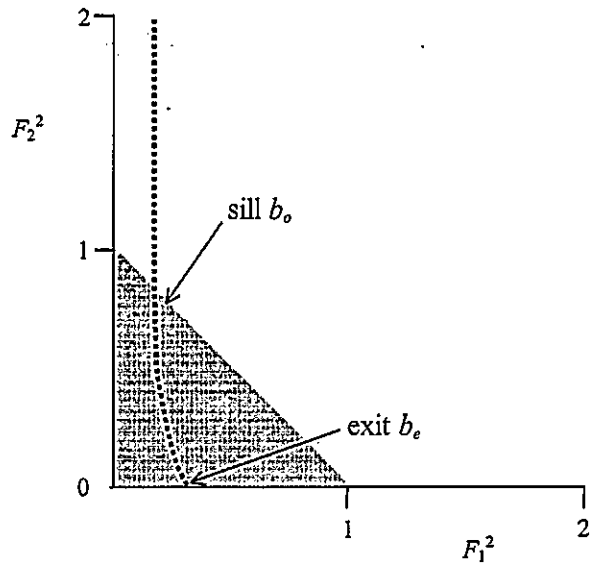

Figure 2.07. Submaximal exchange flow without exit control. Adapted from Farmer and Armi (1986).

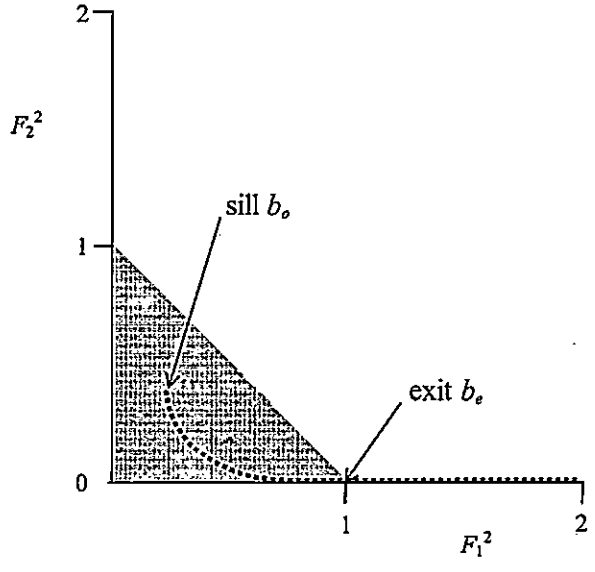

Figure 2.08. Submaximal exchange flow without sill control. Adapted from Farmer and Armi (1986).

The individual effect of a contraction on the two layer flows needs to be taken into account only if the contraction lies between the sill and the reservoir containing the denser fluid. In

this situation, the contraction will have a greater effect on positive (ebbing) flows, and a relatively smaller effect on negative (flooding) flows (Farmer & Armi, 1986). Therefore, in the common situation of the two morphological features being coincident, it is convenient to treat them as a single *constriction* (Dyer, 1997), with a control existing at the shallowest, narrowest section.

As the ratio of the flow rates, q_r (equation 2.15) is varied, the rate of horizontal exchange flow through the constriction will vary, along with the surface position of the interface, or front between the two reservoirs (Figure 2.09). The limiting condition, U_l, as would occur on a flooding tide, is reached when U_o is sufficient to arrest or 'block' the outflow from the estuarine reservoir (Figure 2.09e). At this point, the inflow plunges beneath the blocked layer where $F_1^2 = 0$. The flooding, coastal water is slightly subcritical ($F_2^2 < 1$) just before encountering the sill, is critical at the sill crest, and is supercritical as it accelerates down the lee side of the sill. Farmer & Armi (1986) have found the (non-dimensional) limiting flow value at the plunge point to be:

$$-U_o = -U_l = 0.81 \qquad (2.18)$$

As barotropic forcing (U_o) increases further, these flows are described as 'intermediate', and refer to a single moving layer. As U_o increases further into a 'strong' regime, buoyant outflow remains blocked, frontal location moves further downstream and the depth over which the plunge point occurs must increase to satisfy the continuity equation (equation 2.16). Such variations in plunge depth over a *gradually* increasing bed slope have been examined theoretically by Akiyama & Stefan (1984), and in the field by Huzzey (1982). Findings

indicate that a front forming in such a manner is arrested at a critical depth for a time, as the system adjusts to the increase in U_o. The influence of the contraction in the channel remains small for negative values of U_o (flooding tide) as the critical flows ($F_2^2 = 1$) are generally found in the lower layer which interacts more directly with the sill. The interaction of the *sill* with negative flows is, therefore, likely to be the dominant control on frontal formation and dynamics.

Further insights on the control exercised by topography at the mouth of a bar-built estuary have been gained by the use of an inflow Froude number (Largier, 1992):

$$F_o^2 = \frac{Q^2}{g'\overline{h}^3 b^2} \tag{2.19}$$

Where Q is the volume flow rate at the constriction ($Q=VA$, where V is the mean velocity and A is the flow cross-sectional area normal to the direction of the flow), g' is the reduced gravity, $\overline{h}$ is the mean water depth, and b is the width of the estuary. This parameter is applicable to both a sill and a contraction, but with a different critical value of F_o^2 for each case (1.0 and 0.3 respectively). Therefore, for net inflows, blocking of the surface waters commences at the constriction where $1.0 > F_o^2 > 0.3$. This condition is equivalent to the *intermediate* inflow stage (Figure 2.09e-g), and in this situation a virtual control exists upstream of the constriction, and the plunge point will occur upstream of this control section (Armi & Farmer, 1986; Farmer & Armi,1986). The flow plunges at the most constrictive section when $F_o^2 = 1$, and at a virtual control point downstream when $F_o^2 > 1$, known as *strong* inflow (Figure 2.09h). For net outflows, no seawater can intrude into the estuary where

$F_o^2 \geq 1$ at the constriction. G^2 should still exhibit a critical value of unity at the plunge point, irrespective of where the control is located in relation to the constriction.

The stability of the *vertical* interface in the frontal zone has been described by the shear Froude number, F_Δ^2, (Largier, 1992):

$$F_\Delta^2 = \frac{(u_1 - u_2)^2}{g'h} \tag{2.20}$$

Where u_1 and u_2 are the flow speeds in the upper and lower layers respectively, g' is the reduced gravity, and h is the water depth. F_Δ^2 has a critical value of unity, and in a strong inflow situation, h should increase (or Q decrease) downstream of the front, thus rendering $F_\Delta^2 < 1$ and the tidal intrusion front stable. However, if Q does not decrease downstream of the front, then F_Δ^2 would remain critical or supercritical and the two layers would mix. The front becomes unstable in this instance, and therefore, would be unlikely to be temporally or spatially persistent.

Although the work of Farmer & Armi (1986) has provided the basis for some further theoretical development of the behaviour of two layer flow through the combination of a sill and contraction (*e.g.* Baines, 1995), few researchers have attempted to combine this theory together with field measurements to yield a comprehensive explanation of frontal formation and dynamics. Farmer & Armi themselves attempt a brief investigation into the exchange flows through the Strait of Gibraltar, although appropriate field data is not presented to validate the findings. Largier (1992) has employed some of the basic theoretical

developments, and applied successfully a Froude number analysis in a bar-built estuary, where a transient tidal intrusion front was noted. Valle-Levinson *et al.* (2001) have analysed the flows at the mouth of a fjord using hydraulics theory with some success. There is a notable absence in the literature, however, of field data analysed in conjunction with this internal hydraulics approach to frontal formation in a partially mixed estuarine environment.

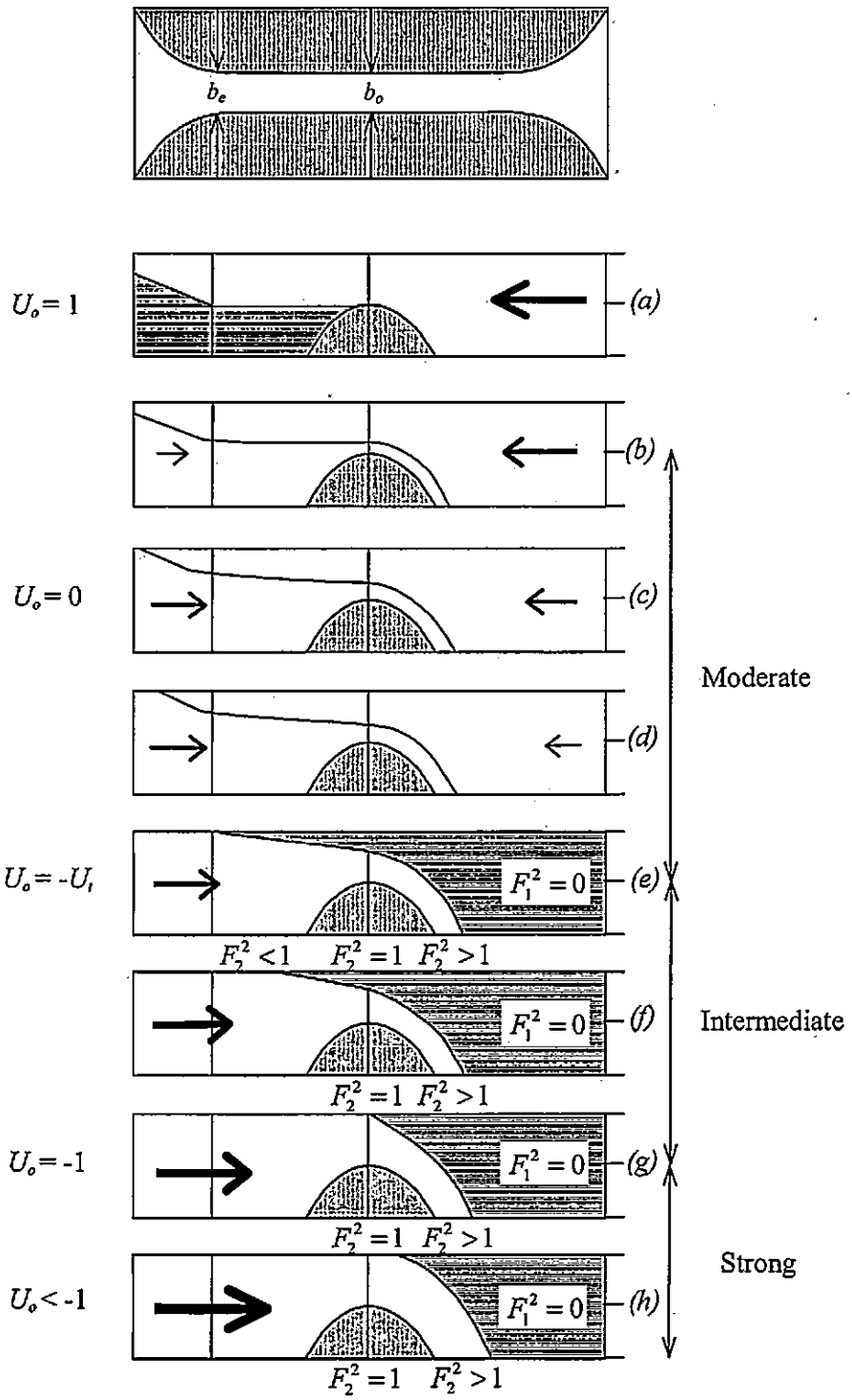

Figure 2.09. Schematic diagram of two layer flow over the combination of a sill and a contraction with varying degrees of barotropic forcing (U_o). The estuarine reservoir is on the right-hand side, coastal waters on the left. The limiting condition ($-U_t$) occurs when U_o is sufficient to block the buoyant estuarine outflow to form a tidal intrusion front (*e*). As U_o increases further, the plunge point occurs downstream of the critical section (*h*). Adapted from Farmer and Armi (1986).

2.5.2. Key field studies of tidal intrusion fronts

Early work examined fronts on the continental shelf as a zone between robust stratification and vertically homogeneous water columns created by vigorous tidal stirring (Simpson & Hunter, 1974; Simpson & Pingree, 1977; Bowman & Iverson, 1977; Bowman & Esaias, 1981; Simpson & James, 1986). A stratification parameter was developed at this time to predict frontal location:

$$\chi = \frac{h}{\overline{U}^3} \qquad \text{m}^{-2}\,\text{s}^3 \qquad (2.21)$$

where h is the total water depth and $\overline{U}^3$ is the depth mean velocity vector taken over an entire tidal cycle. Frontal locations in coastal seas were found to agree closely with contours of constant χ, evidenced by satellite imagery and salinity measurements. It is suggested that this parameter may be of use in locating estuarine fronts (Simpson & James, 1986), however, it is likely to be a significant oversimplification for use in such environments. It is assumed that stratification will vary linearly with changes in $\overline{U}$, which is unlikely to be the case when examining tidal flows through changes in topography, as would be experienced in an estuary.

One of the first reports of an estuarine tidal intrusion front was in the River Seiont, a macrotidal estuary in Wales (Simpson & Nunes, 1981). A clear V-shaped convergence was noted to form on the flooding tide, at two hours after low water (LW+2) and move downstream until LW+3. It was then observed to move back down the estuary as the flooding tide weakened, presumably as no hydraulic control was being exercised by the flat, straight sided channel at this point. The following expression was used in the analysis of the front,

defined as the speed of propagation (c) of the arrested plume relative to the inflowing seawater:

$$c = (g' h_1)^{1/2} \tag{2.22}$$

where g' is the reduced gravity, and h_1 is the speed of the upper layer relative to the lower layer. This expression, derived from the expression for the propagation of a density current (Benjamin, 1968) was used to locate $u = c$, defined as the point at which the inflow would plunge beneath the less dense estuarine water. More recent hydraulics theory suggests, however, that the arrested layer does not influence the dynamics of the plunging flow (Armi & Farmer, 1986; Largier, 1992), and therefore this expression is not appropriate.

Huzzey (1982) investigated a tidal intrusion front in Port Hacking, Australia, a microtidal estuary with a relatively small freshwater discharge. The front in this estuary was noted to form as the flood tide current flowed as a homogeneous layer across a shallow delta, and then down a steep bottom slope into a deeper basin of relatively fresh, stagnant water. At a critical depth on the slope, the flooding tide was observed to plunge underneath the brackish water to form a tidal intrusion front (Figure 2.10). Importantly the front was noted to remain static for the duration of the flooding tide, presumably as the system was able to hydraulically accommodate the moderate tidal inflows experienced in this region. Analysed in terms of a densimetric Froude number, the flow was found to be supercritical prior to plunging.

Pelegri (1988) also employed a Froude number analysis in the study of three macrotidal estuaries in Wales. Tidal intrusion front-like features were observed in each estuary on a flooding tide, although frontal dynamics were analysed in terms of a propagating density

current. This density current approach has since been shown to be incorrect (Armi & Farmer, 1986; Largier, 1992), and interestingly, results from two of the estuaries studied displayed a near total lack of agreement between observations and density current predictions.

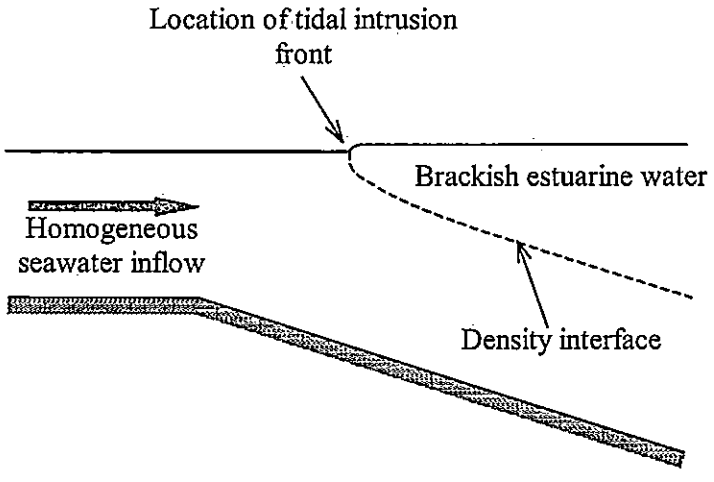

Figure 2.10. Sketch of the formation of a tidal intrusion front noted to form over a gradually increasing bed slope (after Huzzey, 1982).

Several studies have been conducted of a tidal intrusion front in the James River estuary, a partially mixed estuary forming part of the Chesapeake Bay system. The front was noted to develop on an early stage of the flooding tide, moving up-estuary over an increasing bottom slope as the tidal current increased, before dissipating as the flooding current waned (Kuo *et al.*, 1990; Marmorino & Trump, 1996; Brubaker & Simpson, 1999). Recording an across front salinity difference of between 2.5 and 4, early experiments used dye-release techniques to confirm the existence of plunging flow at the frontal interface (Kuo *et al.*, 1990). Further analysis within the same study was conducted in terms of a two-layer flow regime using a densimetric Froude number. Modelling studies using this approach indicated the formation of a front at a critical densimetric Froude number of unity. Importantly, the plunging flow at the

frontal interface was found to inject the surface waters to a depth where the estuarine gravitational circulation induced net upriver movement. From a biological perspective, this was found to be significant in the transport and retention of oyster larvae within the estuary.

High density ADCP (acoustic doppler current profiler) data collected across this frontal system found that the progression of the front up-estuary was occurring in the form of an internal hydraulic jump, to accommodate the increasing tidal flow (Marmorino & Trump, 1996). Convergent flows of between 30-50 cm s^{-1} were recorded across the frontal interface, with the width of the frontal zone found to be approximately 6 m, corresponding to a region of enhanced acoustic backscatter near the surface. The velocity gradient was found be an accurate frontal signature in this case. An inflow Froude number (F_o^2) was employed to parameterise the flow, with values of F_o^2 = 1.2 when the front was present indicating a hydraulic control being exercised on the flow. The front was noted to propagate along the estuary, over the gradually increasing bed slope, although this aspect of changing depth was not analysed in detail.

Further ADCP measurements taken across the James River estuary front noted maximum current flow speeds during the flooding tide of 50 cm s^{-1}, with a surface to bed density difference of 1.4 kg m^{-3} (Brubaker & Simpson, 1999). The stability of the flow was examined in terms of the gradient Richardson number as a signature of shear instability at the frontal interface. Whilst the results indicated shear instability at some frontal locations as the feature advanced up-estuary, the data were relatively sparse, and the results inconclusive. Modulations in frontal behaviour in terms of such shear instability were discussed, however, the authors did not analyse the adjustment of the front to flow changes associated with variations in bottom topography, although its importance was discussed

Bar-built estuaries have also been found to experience tidal intrusion fronts (Largier & Taljaard, 1991; Largier *et al.*, 1992; Largier, 1992). These studies have addressed the intrusion of seawater into a microtidal bar-built estuary using an inflow Froude number, F_o^2 (equation 2.19), and the composite Froude number, G^2 (equation 2.08). Considering the contraction and sill at the mouth of the Palmiet estuary, South Africa as a single constriction, the hydraulics theory developed to explain two-layer flows over topography (Armi & Farmer, 1986; Farmer & Armi, 1986) has been employed with much success to describe frontal evolution. A clearly apparent tidal intrusion front was noted to form on the flooding tide, with a single, mixed layer on the seaward side of the frontal interface, and a two-layer regime on the landward side. A Froude number analysis indicated hydraulic control of the flow with critical flow conditions ($F_2^2 \approx 1$) recorded at the constriction during the flooding tide. The flow was observed to plunge upstream of the hydraulic control section during the early part of the flood, typical of the intermediate inflow regime (Figure 2.09e-g). As the velocity of the tidal inflow increased, the plunge point was observed to move slightly landward. A value of $F_o^2 \approx 1$ was recorded at the constriction at this time, and therefore, the plunge point occurred directly above the hydraulic control section. The front was observed to move further downstream as the flooding tide reached its peak flow rate, when $F_o^2 > 1$. The plunge line, therefore, occurred downstream of the hydraulic control section, consistent with the strong flow regime (Figure 2.09h) described by Farmer & Armi (1986). Studies throughout the year in this area (Largier & Taljaard, 1991) indicated a robustness of the tidal intrusion front to seasonal changes.

3.0. The Dart Estuary

The Dart estuary (Plate 3.01), a ria, is situated in the south west of England and provides one of the deepest natural harbours in south Devon. It is used regularly by commercial vessels, fishing boats, naval shipping and a wide variety of pleasure craft. Activities carried out within the estuary include boatyards, marinas, ferry operators and training of naval officer cadets from Britannia Royal Naval College. An important tourist destination, the Dart estuary contains two Sites of Special Scientific Interest, with much of the region being a designated Area of Outstanding Natural Beauty. The outer estuary is part of the South Devon Heritage Coast, and a Coastal Preservation Area.

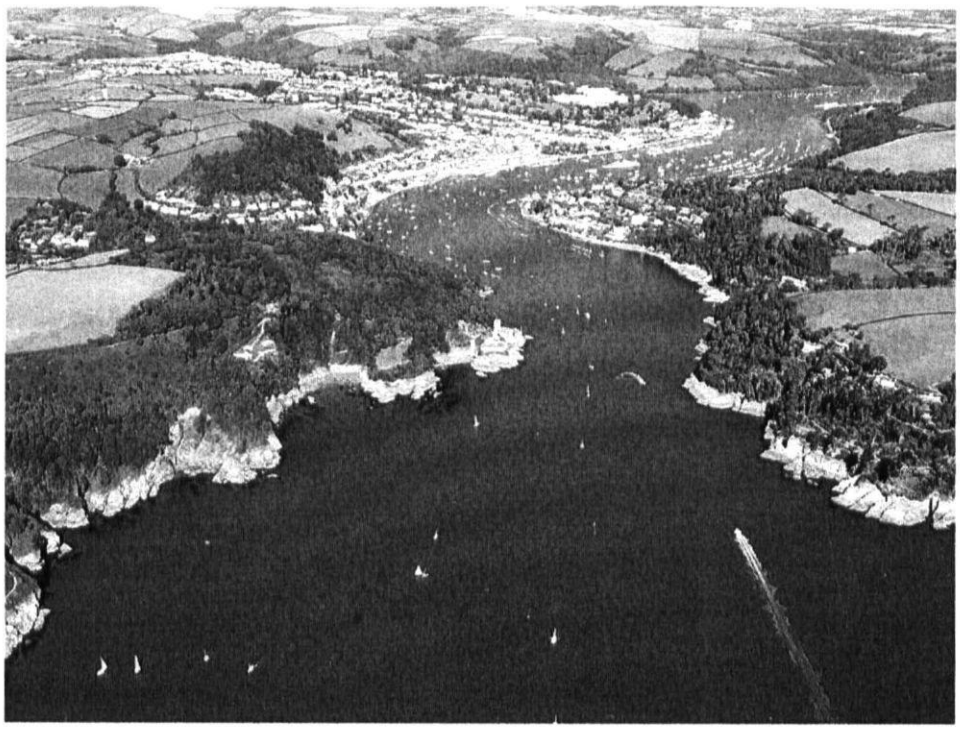

Plate 3.01. Aerial view of the mouth of the Dart estuary.

The source of the Dart is at Cranmere Pool on Dartmoor, approximately 65 km from its mouth at Dartmouth. Much of the fresh water entering the estuary originates on the granite moorland of Dartmoor, where rainfall averages in excess of 2000 mm per annum. The estuary has several small tributaries and drains a catchment area of 475 km^2 (Environment Agency, 1998). The upper tidal limit of the estuary occurs at Totnes weir (Figure 3.01), approximately 17 km from the mouth at Dartmouth.

The Dart is macrotidal, with a range of 5.2 m during spring tides, and 1.8 m during neap tides. The semi-diurnal tidal regime is asymmetrical, with the flooding spring tide typically having a duration of 6 h 30 m, and the ebb tide a duration of 5 h 40 m. Tidal flows thus display a marked ebb-dominance. Characteristic flow velocities during spring tides are 0.6 ms^{-1} and 1.0 ms^{-1} on the flood and the ebb respectively. During neap tides, typical flood and ebb velocities are 0.3 ms^{-1} and 0.6 ms^{-1} respectively (Priestley, 1998). Wave action at the entrance to the estuary can be strong, particularly during periods of prolonged easterly winds, although high sea states are experienced rarely beyond Dartmouth itself, due to the bends in the channel.

In the middle estuary, there are intertidal mudflats, narrow shingle shores and some bedrock outcrops, the immediate surrounding area dominated by agriculture in the form of improved pasture. The shores of the lower estuary are predominantly rocky and steep, with ancient deciduous woodland in many areas. The lower estuary is relatively narrow, being 200 m across at the mouth, where the water depth is approximately 10 m (Figure 3.02). The width increases to over 350 m just landward of the mouth, where there is an elongated depression in the seabed, around 200 m in length, in the centre of the channel where the depth increases to 25 m. The narrow, relatively shallow estuary mouth, between Castle Point on the western bank, and Kettle Point on the eastern bank thus forms a constrictive section (Figure 3.03).

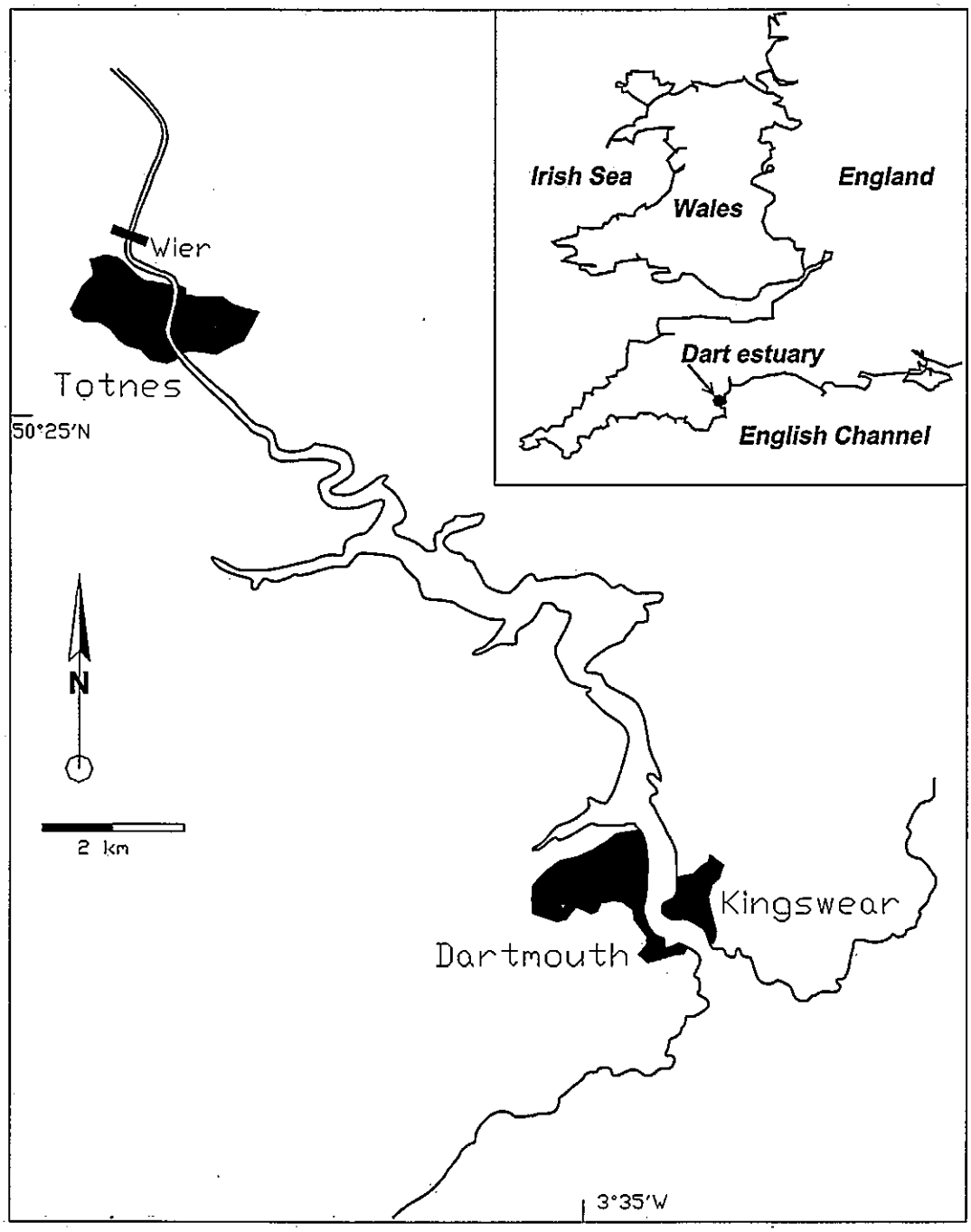

Figure 3.01. Map showing the Dart estuary from the mouth at Dartmouth, to the tidal limit at Totnes

The estuary supports a small number of wildfowl and waders, a bass nursery area, and is home to a large crab fishing fleet. Oyster farming has diminished due to tributyl tin pollution and water quality degradation, although recent efforts have been made to restore the industry (DEEM, 2004). Water and sediment quality within the estuary are generally good at the present time, although sewage pollution is still an issue in the upper reaches (Environment Agency, 1998).

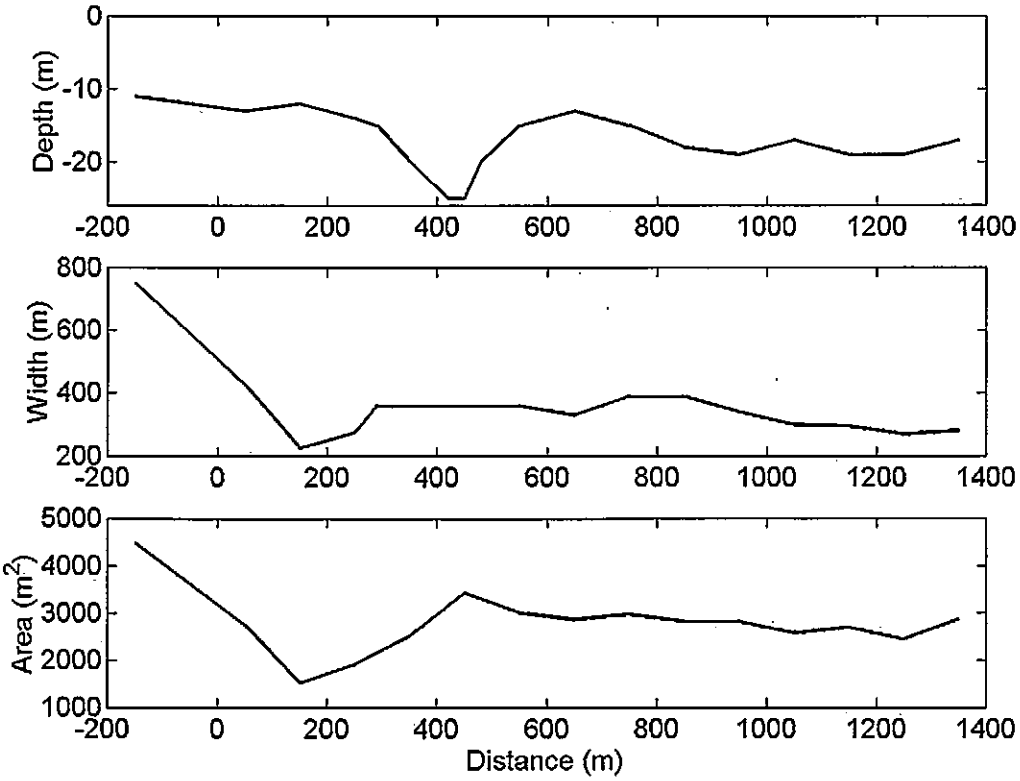

Figure 3.03. Changes in depth, width and cross-sectional area of the Dart estuary, from Checkstone buoy just outside the mouth (0 m), to the Lower Ferry (1350 m). Note the channel constriction at the mouth (150-275 m), and the depression in the seabed just inside the mouth (350-500 m) with the associated increase in cross-sectional area.

The holistic environmental management of the Dart estuary is relatively well-advanced, with both a Local Environment Agency Plan (LEAP), and a Dart Estuary Management Plan being published in 1998 (Environment Agency, 1998; DEEM, 1998). Dart Estuary Environmental Management (DEEM) is entrusted with day to day responsibilities for facilitating and implementing the management plan. To date, however, there have been relatively few scientific investigations conducted in the estuary. Background information has been obtained principally from the Dart Observatory, an estuarine monitoring system established by Britannia Royal Naval College in January 1997. Providing continuous, remote monitoring of the meteorological and oceanographic variables within the Dart estuary, the system was located 2 km landward of the mouth, at 50°20.52′ N, 3°34.53′ W (Figure 3.02). Consisting of a converted navigation buoy, sensors measuring temperature, conductivity and flow velocity sensors were mounted at the surface, at mid depth and on the bed. Data was telemetered from the buoy at hourly intervals for a period of two years. Analysis of data from this system (Priestley, 1998) found that the Dart is a partially mixed estuary which experiences a complete stratification/destratification cycle with the spring-neap transition (Figure 3.04). This is similar to that found in the Columbia river by Jay & Smith (1990), and in Chesapeake Bay by Haas (1977). Salinity variations were found to dominate the density distribution in the Dart estuary, with temperature variations making a negligible contribution (Priestley, 1998).

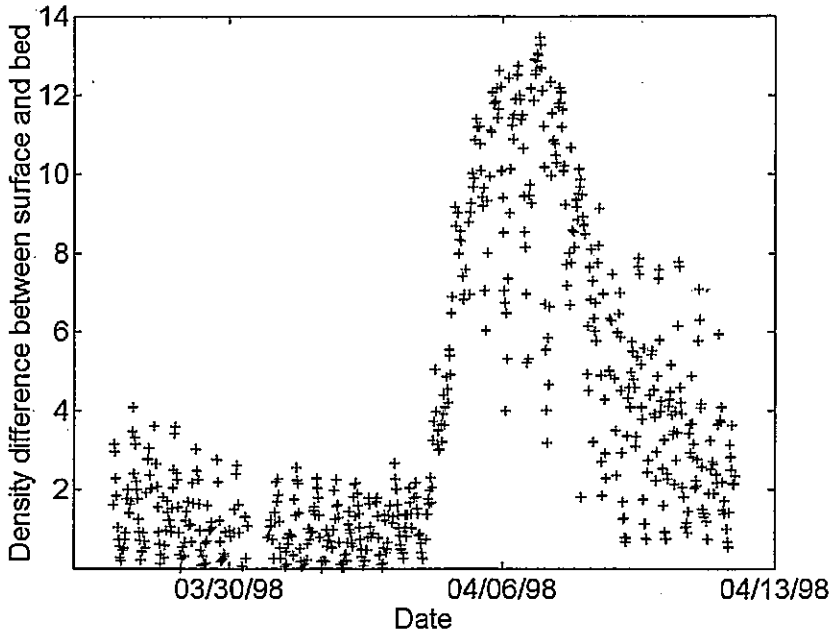

Figure 3.04. Difference between near bed and surface density (kg m^{-3}) in the Dart estuary. There is little difference between surface and bed density during spring tides (03/30/98) indicating a homogeneous water column. During neap tides (04/06/98) however, the large difference between surface and bed density indicates a stratified estuary.

A V-shaped tidal intrusion front has been observed to form at the mouth of the estuary around low water during periods of spring tides (Plate 3.02), remaining in position for several hours before disappearing abruptly. A clear foam line demarcates the frontal boundary, with a notable colour change evident on either side of the front.

4.0. Methods

4.1. Rationale and chapter overview

In order to fulfil the aims of this research, there was a requirement to collect and analyse a significant quantity of high-quality field data at the mouth of the Dart estuary. It was recognised at an early stage that the quality of this data set would be critical to the successful outcome of this project. Settings and calibrations of all instruments have, therefore, been investigated and conducted with some care. An acoustic doppler current profiler (ADCP) and conductivity temperature depth (CTD) probe were deployed from a survey launch using custom designed and built frames. A gross error check of the ADCP was performed prior to the survey, using an InterOcean S4 electromagnetic current meter deployed in the survey area. The CTD had been factory calibrated prior to the commencement of the data collection. Positioning was provided by a GPS (global positioning system) receiver interfaced to the ADCP equipment. Using this equipment, detailed field measurements have been undertaken of the flow and density structure at spring and neap tides across a stationary tidal intrusion front at the mouth of a the Dart estuary.

Survey lines were commenced from Checkstone buoy, approximately 300 m to seaward of the mouth of the estuary. Heading and speed changes of the survey vessel were kept to a minimum, thus ensuring that the ADCP data collected were as free from any vessel induced influences as possible. On reaching a location abeam of the Lower Ferry route, approximately 1 km landward of the mouth of the estuary, a new survey line was commenced immediately in the opposite direction, this time taking rapid CTD casts at 150 m intervals. Each pair of ADCP and CTD survey lines was conducted hourly, from one hour before low water (LW-1) to three hours after low water (LW+3), and combined to provide a quasi-synoptic snapshot of

the flow and density structure of the estuary for that hour of the tidal cycle. The maximum time offset for each pair of survey lines between the first ADCP reading and the last CTD dip was typically around 30 minutes. A further identical survey was conducted one week later, during a period of neap tides, when the tidal intrusion front was not present.

Data from the CTD and ADCP have been merged onto a coincident spatial grid in *X, Y* and *Z* dimensions using a Matlab routine, and minimally smoothed where appropriate. In this way, a detailed and accurate picture of the flow and density structure at the mouth of the Dart estuary has been recorded, from LW-1 to LW+3 during both a spring and a neap tide, with a well-developed example of a tidal intrusion front present during the spring tidal phase. This final output thus represents a high-quality data set, which can be processed further to fulfil the aims of this project.

Significant efforts have been expended to ensure that the data collection programme was meticulously planned and executed, including careful selection, calibration and integration of the equipment used. This chapter examines in some detail the methodology used to ensure the quality of the data, with due regard to the limitations of time in terms of vessel, equipment and personnel.

4.2. The survey area

Visual observations had been undertaken of the tidal intrusion front at the mouth of the Dart estuary over several months prior to the planning of this field data collection exercise. These observations indicated that all visual manifestations of the front occurred over a relatively small area, between Kettle Point and the Lower Ferry (Figure 3.02). There was no perceived

benefit, particularly in terms of the extra vessel and equipment time required, in surveying the entire estuary. Therefore, it was deemed sufficient to take measurements in the estuary mouth area only, from abeam Checkstone buoy to abeam the Lower Ferry route. Concentrating on a small area in this way, allowed for the recording of high density measurements, temporally and spatially, in order to develop a detailed understanding of the hydrodynamics responsible for frontal formation, evolution and decay.

4.2.1. Development of a suitable charting system

The Admiralty Chart for Dartmouth harbour (chart number 2253) was found to be unsuitable for the task at hand at a relatively early stage of this work. The desired survey area could not be extracted readily from the chart, which covers a relatively large area. The small scale of the chart (1:6250) hindered the presentation of the survey area on an A4 sheet, and there were data on the chart extraneous to the scope of this project, the locations of numerous small craft moorings, for example. Development of an electronic chart of the survey area was thus undertaken. Using an AutoCAD 2000 platform, a base map was created using much of the information from the Admiralty Chart. This was digitised incorporating three datum marks, and inserted into the AutoCAD software using real-world coordinates. This provided the distinct advantage that distances measured between points on the electronic chart could be resolved in actual units, metres in this instance. The chart has been rotated 37.5° clockwise, and the scale changed to 1:6500 in order to present the survey area more clearly.

Geographical data have been arranged in discrete layers within the AutoCAD chart as follows:

1. Bathymetry
2. Buildings
3. Coastline
4. Contours (land)
5. Contours (marine)
6. Graticule
7. Grid (UTM)
8. Land hatch
9. Sea hatch
10. Text
11. Title
12. Miscellaneous

Individual layers may be activated or deactivated for various data presentation purposes. Most usefully, the GPS (Global Positioning System) location of each recorded data collection point may be displayed on the AutoCAD chart. An AutoCAD 'lisp' routine was created to import comma-delimited geographical positions, and a position circle representing the data point location, together with an appropriate identification number may then be displayed on the chart. Each survey line has been stored in a discrete layer, thus maximising the flexibility of the charting system. The AutoCAD chart with the majority of the base layers activated (Figure 4.01) illustrates the flexibility that such a system allows.

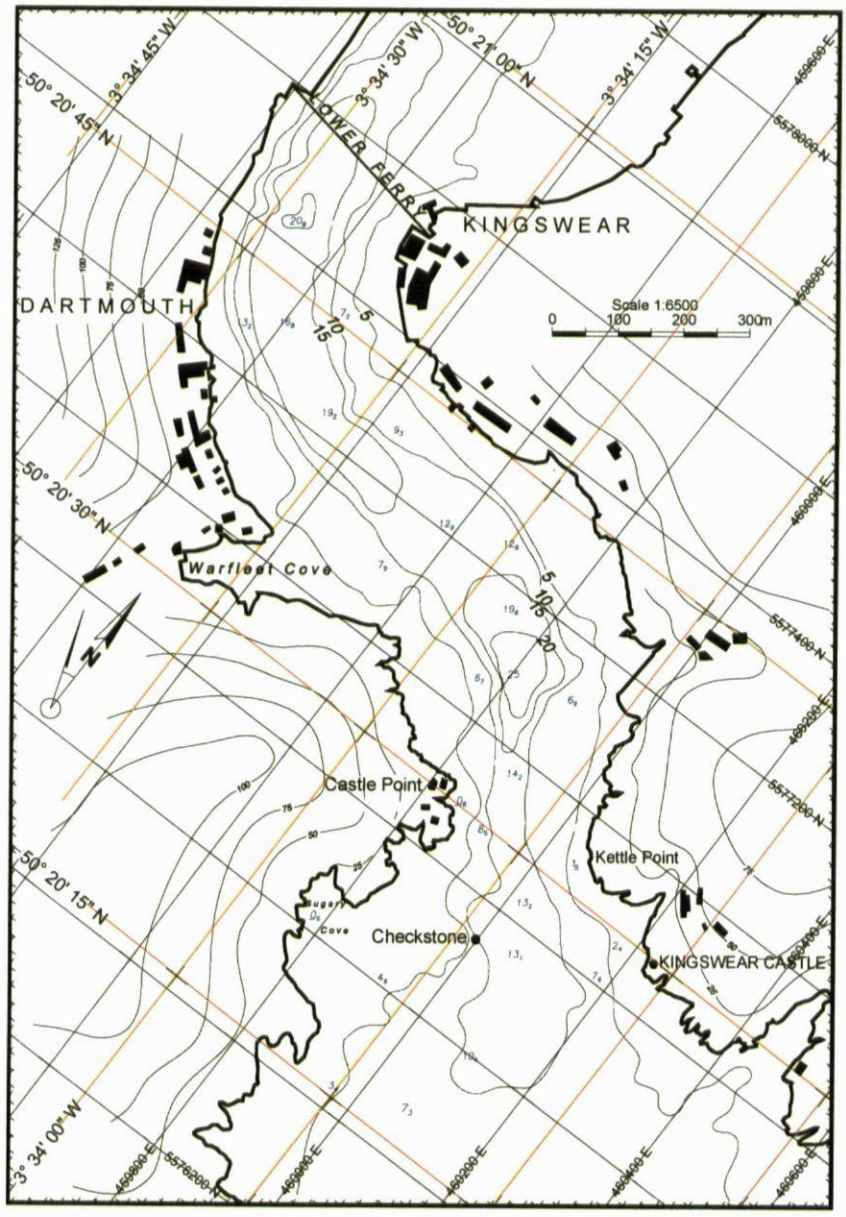

Figure 4.01. AutoCAD chart developed for use at the mouth of the Dart estuary.
All base layers have been activated, demonstrating the information available within this system.

4.3. Field data collection – survey vessel and instrumentation

4.3.1. Survey vessel

Picket boat eight (PB8) was the survey vessel used throughout the field data collection (Plate 4.01). Used primarily as a training vessel for Royal Naval officers under instruction at Britannia Royal Naval College, Dartmouth, it is a twin screw, 13.7m craft, constructed from glass reinforced plastic (GRP), with two six cylinder Perkins diesel engines. Outline drawings of PB8, including the field equipment deployment frames may be found in Appendix 1.

A laptop computer for the acoustic doppler current profiler (ADCP) was installed in the after cabin together with the GPS receiver (Plate 4.02). This provided a weatherproof area for this delicate equipment, and all the surveys were managed from this location. Unfortunately, no 240 volt power sockets were available on PB8, and this necessitated the use of a separate portable petrol generator to supply power for the laptop computer and GPS receiver. The generator was installed on the after deck for safety reasons, with an isolated extension lead providing power to the after cabin.

at which the sensor moves through water of changing temperature in attaining this response level. Response times may be slowed further as heat must dissipate through the viscous boundary layer set up around the probe, and the protective coatings on the sensor itself. Total response times of platinum resistance thermometers may therefore be as great as 0.6 s (Emery & Thompson, 2001).

In the complex case of water changing temperature rapidly as the sensor descends, the temperature response may be described by equation 4.01 (Emery & Thompson, 2001).

$$\frac{\Delta T}{\Delta T_o} = e^{-t/K} \tag{4.01}$$

Where ΔT is the temperature resolution, ΔT_o is the initial sensor temperature, t is the time in seconds, and K is the response time of the temperature sensor.

An early pilot study for this field experiment (Section 4.6.1) suggested that temperature was not a major component in density driven circulation in the Dart estuary. In March, the temperature gradient was only in the order of 0.1° m^{-1}. Therefore, to detect this change with an accuracy of 0.01°, using a typical total response time for such an instrument of 0.6 s (Emery & Thompson, 2001), t = 1.4 s. Hence a sensor drop rate of (1.0 m/1.4 s) 0.7 ms^{-1} could be considered ideal for accurate temperature data collection in the Dart estuary.

The conductivity sensor on the Valeport 604 is an oil-filled inductive coil. The sensor is pressure-balanced, to eliminate variations in sensor volume as the pressure increases. As

seawater conductivity is dependent on the ion content of the water; therefore it is directly proportional to salinity. The difference in voltage between two conductivity elements is measured at each end of a seawater 'passageway'. As the conducting elements are contained within the sensor housing material, little biofouling is likely (Emery & Thompson, 2001). It is a noted problem, however, that the response time of the conductivity sensor of a CTD instrument may be significantly slower than that of the temperature sensor. It is possible in this situation, therefore, that calculated salinity (as derived from measured temperature and conductivity) may 'spike' due to a mismatch between sensor response times. This is likely to be less of a problem with this particular instrument as salinity is calculated by PC software when downloading the recorded data, not when actually taking the readings of temperature and conductivity. This facilitates rapid, continuous measurements of salinity. A typical salinity accuracy of ± 0.005 could be expected for such an instrument (Emery & Thompson, 2001).

4.3.2.2. Calculation of derived parameters

The depth at which temperature and conductivity readings are taken is derived from measured hydrostatic pressure. There is an almost linear relationship between pressure and depth in the top 1000 m of the ocean (1 dBar $\approx$ 1m), such that the values of pressure are within 1% of the geometric depth in this area. The Valeport 604 uses a 300 Bar strain gauge transducer, an instrument which has a typical accuracy of $\pm 0.5\%$ of depth (Emery & Thompson, 2001).

The density of seawater is a parameter derived from both temperature and salinity. The Valeport software uses UNESCO standard formulae (equation 4.02) for the calculation

(Valeport Ltd, 1999), with the output being in the density anomaly (γ) form. This is defined as being:

$$\gamma = \rho - 1000 \tag{4.02}$$

where ρ is water density in kg m^{-3}.

Sound speed in seawater is usually calculated using one of a number of empirical equations which have been developed based on experimental measurements of a range of parameters (Korman, 1995). These yield direct measurements of sound velocity by the use of laboratory techniques under carefully controlled conditions. Urick (1967), Korman (1995) and Valeport (1999) examine the different common equations in detail, and a summary of their application (Table 4.01) indicates clearly those that are unsuitable for use in estuarine environments.

The Wilson formula (Wilson, 1960) is now regarded as being somewhat outdated and inaccurate following the adoption of the practical salinity scale and the international equation of state for seawater (Valeport Ltd, 1999). Superseded by the Chen & Millero formula (Chen & Millero, 1977), encompassing a wide range of temperature and salinity variations, this formula is now used commonly in shallow water. The Del Grosso equation (Del Grosso, 1974) is used more frequently in deep water environments. As the MacKenzie (MacKenzie, 1981) and Medwin (Medwin, 1975) formulae are both too limited in terms of the scope of temperature and salinity, the Chen & Millero equation was used exclusively throughout this work to calculate sound speed. It is an elaborate empirical equation using 42 coefficients, the

calculations being performed within the supplied Valeport Datalog PC software when downloading raw data from the instrument.

Equation	Date	Ranges of Validity		
		Temperature (°C)	Pressure (bar)	Salinity
Del Grosso	1974	0 to 15	<1034*	33 to 38
Wilson	1960	-4 to 30	<1000*	0 to 37
MacKenzie	1981	0 to 30	0 to 800	30 to 40
Medwin	1975	33 to 38	<100	33 to 38
Chen & Millero	1977	0 to 40	<100	0 to 40

Table 4.01. Comparison of equations in common use for calculating sound speed in seawater (from Urick, 1967; Korman, 1995; Valeport, 1999). (Note: the * refers to a unit of kg cm^2, this being the unit required in the calculation.)

4.3.2.3. Calibration and deployment

All sensors fitted to the Valeport 604 CTD were fully calibrated prior to the field data collection exercise (Table 4.02). The calibration process is usually completed in a laboratory by fitting a polynomial to the reference temperature data in order to define a calibration curve (Emery & Thompson, 2001).

	Depth (m)	Error in seawater
Conductivity (m sv)		0.000
Temperature (°C)		0.003
Pressure (dBar)	0	-0.002
	40	-0.008
	80	-0.015

Table 4.02. Sensor errors on Valeport 604 CTD following manufacturer's calibration.

The Valeport 604 has a weight of 12.5 kg in air, and 9.0 kg in water, and it was foreseen as a problem for one person to complete upwards of 50 CTD casts in a few hours with an instrument of such weight. No suitable winch system is fitted to the survey launch (PB8), and during previous exercises using this equipment, the CTD was lowered on a rope over the rubbing strake on the side of the vessel. Wishing to avoid the frictional additions inherent in this method, a deployment frame was designed by the author to lock into existing deck fittings and project approximately 0.5m over the port side of the vessel. Incorporating a large, low-friction turning block, this apparatus allowed for the rapid deployment and recovery of the CTD with minimal human effort. In addition, projecting the frame beyond the side of the vessel reduced the likelihood of the CTD swinging into the vessel during the critical, near-surface stages of deployment and recovery, particularly in higher sea-states. Constructed from aluminium tubing by a local boatyard, the frame was employed with great success (Plate 4.04). It was a simple matter to swing the CTD from the deck out over the water's surface. The instrument was held just under the surface and allowed to 'soak' for around 10 seconds to allow the sensors to adjust. It was then lowered by hand, as close to the prescribed drop rate of 0.7 ms^{-1} as could be estimated. Slackness in the line indicated the probe resting on the seabed, and recovery was a simple matter of pulling in on the line. It is estimated that each

process (Appendix 3). This program looks for zero values in the depth column as an indicator of the start of a new cast. Once the start of a new cast has been identified, the routine strips out the corresponding environmental variables for both the down-column and the up-column readings during that particular cast.

Problems can be encountered with data accuracy when using the up-column data. As the sensors are mounted on the downward-looking face of the instrument (Plate 4.03), water column properties may be modified by the upward passage of the probe towards the surface. Temperature may be changed by water carried along in the wake of the probe, and a turbulent wake may overtake the probe as it decelerates, leading to a false temperature reading (Emery & Thompson, 2001). These effects are minimised by using down-column data only, as the sensors are on the leading face of the instrument. In processing the CTD data, the Matlab routine ignores data points between the maximum recorded depth (the seabed) and the surface.

A further problem with CTD deployments from a vessel is the non-uniform descent of the probe, due to the effects of the ship's pitch and roll (Emery & Thompson, 2001). The applied Matlab routine effectively edits out these effects, by looking for a negative depth change between successive values on the down-cast, then removing these data points. Following the separation and processing of each dip in this way, the program asks for an appropriate user input, and produces the required graph of either temperature, salinity or density against depth for each cast.

4.3.3. Global Positioning System

The Global Positioning System (GPS) is a satellite-based radio navigation network administered by the United States Department of Defence. Using 24 satellites in circular orbits above the Earth's surface, approximately five of them should be in view of the user's antenna at any one time (Dixon, 1994). The satellites broadcast codes on two frequencies, a C/A-code (coarse acquisition) for civilian users, and a P-code (precision) for military users (Logsdon, 1992). A receiver which is P-code enabled can provide the precise positioning service (PPS), which is only currently available to the U.S. military, allied military forces and some other U.S. government agencies. The standard positioning service (SPS) is available to all users world-wide, and virtually all civil-use GPS receivers determine their positions by tracking the C/A-code (Tiberius, 2003).

When the GPS network was first initialised, the SPS was purposely degraded, termed 'selective availability', by the operators. At this time, the system was able to provide a positioning accuracy of 100 m at the 95% confidence level. However, selective availability was removed in May 2000, improving the SPS accuracy to near PPS levels. This was quoted by the U.S. Government in 2001 to be 13 m horizontally at the 95% level (Tiberius, 2003). Recent work has shown that this estimate is likely to be fairly pessimistic, even using a low-cost hand-held GPS receiver. For example, data collected statically over 14.5 hours had a standard deviation of 1.79 m for latitude, and 1.82 m for longitude, with no outlying position samples (Tiberius, 2003).

Following the removal of selective availability, ionospheric delay of the radio signal from the satellite and multipath are likely to be the largest sources of error (Tiberius, 2003). These can be minimised by careful antenna siting and design (Logsdon, 1992), or using a Differential

GPS (DGPS). This system uses a remote, land-based station to measure errors in the GPS signal. The received position at the station is compared with the known position, and the error quantified. This correction is then sent to the user on a separate VHS frequency or satellite channel and applied in the user's GPS receiver. A VHF-based differential correction service is provided free in the UK by the General Lighthouse Authorities of the United Kingdom and the Republic of Ireland. This comprises a network of 12 ground-based reference stations which provide transmissions with a coverage of at least 50 nautical miles around the coast of the UK. Dartmouth harbour is around half-way between the two nearest stations providing corrections, with St Catherine's Point Lighthouse and the Lizard lighthouse both being approximately 100 nm distant. The quoted range of the correction signals is 100 nm (Hydrographer of the Navy, 2000) and, therefore, Dartmouth is at the limit for both stations. Anecdotal evidence from local river users suggests that differential corrections are not received reliably in Dartmouth harbour, degraded by the masking effects of the VHF signal by the high-sided banks surrounding the entrance to the Dart. The option of satellite-provided differential corrections was explored and rejected on the grounds of cost, being in the order of several thousand pounds for the rental of a receiver and a subscription to the corrections.

A trial was conducted with the GPS and ADCP installed on PB8, which was moored alongside a static pontoon in the Dart estuary. A Trimble 4000SE single frequency 9 channel GPS receiver was interfaced to the ADCP acquisition software. Fixes were logged at 1 Hz for approximately 60 minutes (Figure 4.02). The majority of the 3617 fixes were found to be within an area of 4 m^2, apart from a brief GPS 'wander' to the south of around 3 m. The standard deviation of the latitude and longitude was found to be 0.3 m and 2.0 m, respectively (Table 4.02).

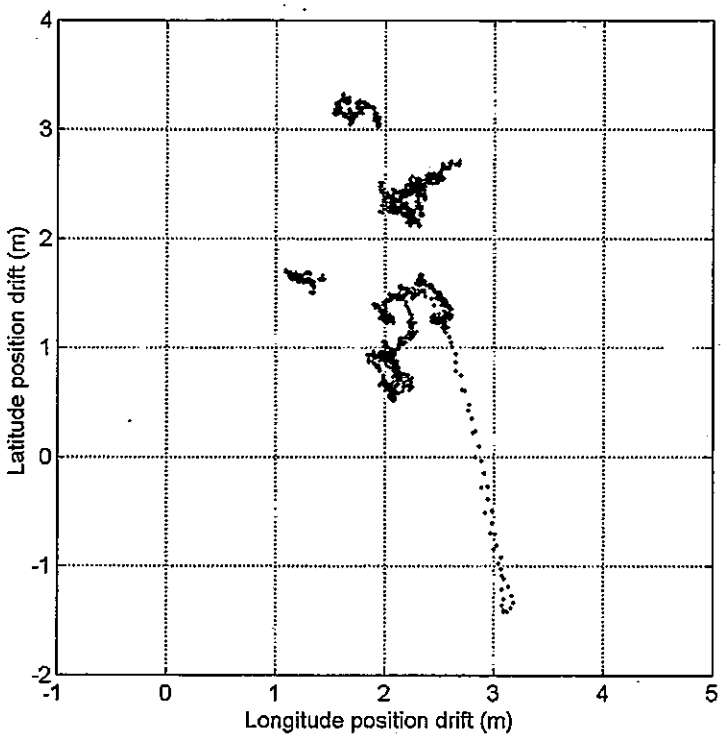

Figure 4.02. 3617 1 second GPS fixes logged over a period of approximately one hour. Vessel alongside Sandquay pontoon in the Dart estuary.

Re-processing the data and averaging into 20 s 'ensembles', very similar data accuracy to the 1 s fixes was apparent (Figure 4.03). Such an averaging process should act to reduce noise in the data and improve accuracy. As the averaging process within the software has not reduced the noise significantly, it is likely that the ADCP software uses one single fix within each ensemble, rather than averaging the position data over the ensemble time. No further information on this subject was forthcoming from the literature supplied with the ADCP equipment. However, with a horizontal accuracy of approximately 3.5 m, with a standard deviation of 0.5 m for latitude and 1.4 m for longitude (Table 4.03), DGPS was not deemed a requirement during the field data collection for this project.

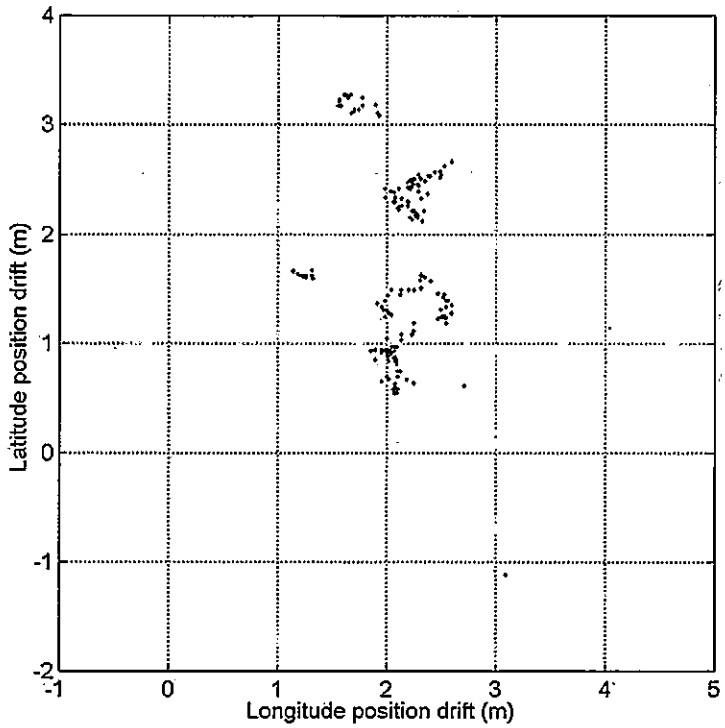

Figure 4.03. 3617 GPS fixes averaged into 183 20 second ensembles. Logged over a period of approximately one hour whilst alongside Sandquay pontoon

	Mean latitude variation (m)	Latitude variation standard deviation (m)	Mean longitude variation (m)	Longitude variation standard deviation (m)
1 second fixes	3.01	0.30	3.82	2.00
20 second averages	3.49	0.54	2.89	1.39

Table 4.03. Comparison of the standard deviation of GPS position fixes. The 1 second fixes are from raw GPS data, the 20 second averaging is carried out within the ADCP software.

Position data were recorded to the ADCP data files, and extracted using further Matlab routines, 'ctdpos.m' for the CTD cast positions, and 'latlong.m' for the ADCP ensemble positions (Appendix 3). The latitude and longitude data were then transformed from geodetic coordinates to a UTM grid for presentation on the prepared electronic chart. This transformation was undertaken using 'Geocalc' proprietary software. Once this datum transformation was complete, the bespoke AutoCAD 'lisp' enabled the rapid importing and presentation of the position data.

4.3.4. Acoustic Doppler Current Profiler

4.3.4.1. Principles of operation

The Acoustic Doppler Current Profiler (ADCP) is a well-tested and proven oceanographic tool (Gilboy *et al.*, 2000). Four separate small acoustic transducers are arranged in one transducer head in a Janus[1] configuration (Plate 4.05) with the beams pointing at an angle of 20° to 30° to the plane of the transducers (Emery & Thompson, 2001). There is some flexibility in the deployment configuration of the equipment as the transducer head can be vessel mounted, seabed deployed, or in some instances has been deployed horizontally on a towed float (e.g. O'Donnell *et al.*1998).

[1] Janus was a Roman god who looked backwards and forwards at the same time.

shortcomings, particularly in the accurate resolution of the vertical velocity vector. The latest 'broadband' instruments measure currents by determining the phase shifts of backscattered echoes from a series of multiple transmitted pulses (Emery & Thompson, 2001). Broadband ADCP's have a further advantage over the narrowband type of having a much lower level of random fluctuations in the data. These fluctuations are always present to some extent due to the random position of the scatterers within the ADCP footprint. Typically, the random fluctuations for a narrowband system are 5.6 dB, and for a broadband ADCP are usually under 1 dB (Deines, 1999).

The use of four acoustic beams allows the determination of velocity in three dimensions, with one pair of beams measuring in the north/south orientation, the other pair in the east/west orientation, with both pairs measuring vertical velocity (Wewetzer *et al.*, 1999). The redundancy provided by two measurements of vertical velocity allows the determination of an 'error velocity'. If the two separate measurements of vertical velocity differ markedly, there are likely to be errors in the measurement, and a high error velocity will be recorded to reflect this. ADCP software also uses the error velocity in the calculation and display of a 'percent good' value to provide an indication to the user of the data quality.

Each current profile is divided into uniform depth cells. This is achieved by range-gating the echo signal, which breaks the received signal into segments, or 'bins' for individual processing (RDI, 1996). Bin size can be set by the user, and has a typical selectable range of 0.2 m to 8.0 m. The larger bin sizes are usually used for averaging in deep water applications. Conversely, the smaller bin sizes tend to be selected in shallow water, where a greater resolution is required. If an extremely small bin size is selected in a highly variable environment, it is probable that a high level of random fluctuations in each bin will be

experienced. Some depth averaging of the signal is, therefore, useful to improve data quality. Typically, in estuarine operations, the majority of users have opted for a bin range of 0.5 m (Table 4.04), a sensible compromise between data quality and resolution. It should be noted that each bin is comparable to one individual current meter. Within the bin, maximum sensitivity to measured velocities is at the centre of each bin, with sensitivity reducing progressively towards the edges (Wewetzer *et al.*, 1999). Broadly, each bin represents an average of the flow velocity and direction over the length of the selected bin size.

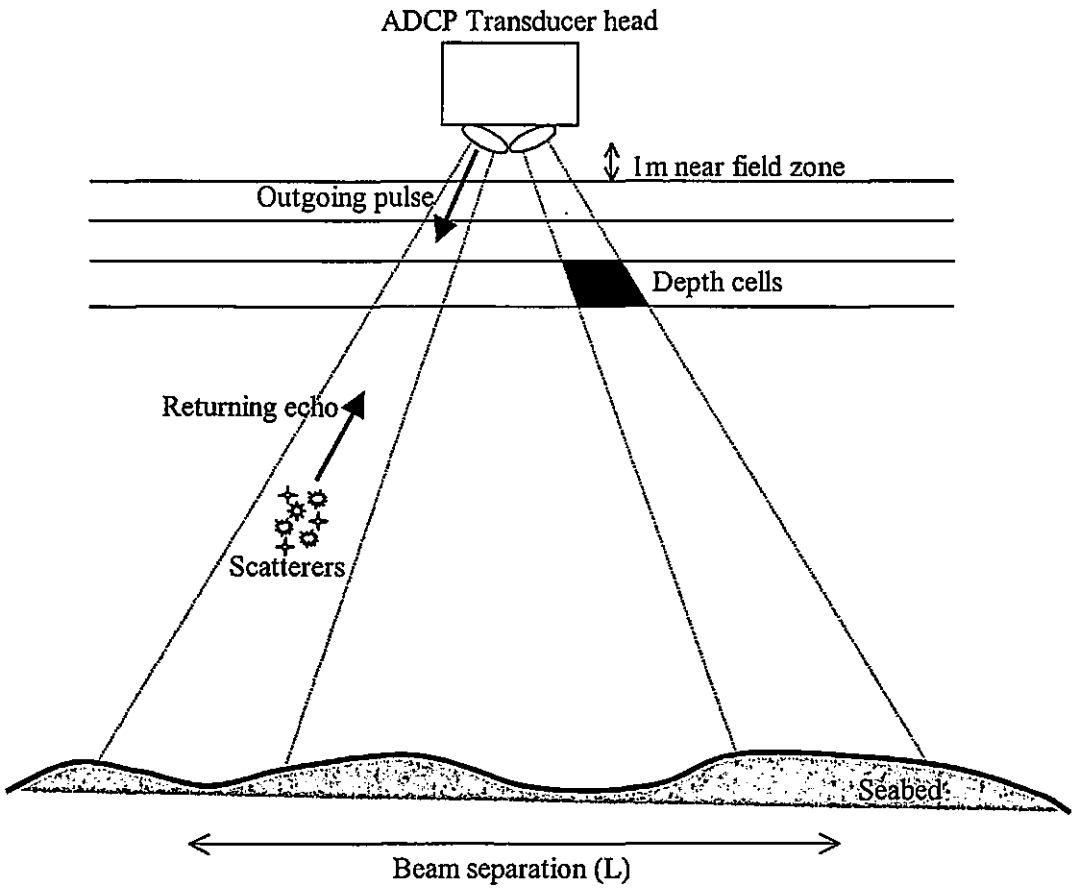

Figure 4.04. ADCP principle of flow measurement from a vessel-mounted configuration. Flow is assumed to be homogeneous across the beam separation distance (*L*).

Data derived from a single ping are likely to contain significantly more errors than data averaged over several pings. Time averaging can, therefore, reduce the relatively large errors contained within a single ping, and an 'ensemble' or time interval for averaging is selected when collecting the data. Ensemble length typically varies from 5 seconds to 30 minutes, and can be modified on post processing. Section 4.3.5.4. contains further details on the criteria on which ensemble length should be selected.

The depth over which an ADCP can measure flow vectors successfully is limited by some fundamental physical constraints. 'Ringing' occurs where a proportion of the energy from the transmitted pulse remains close to the transducer head for a time after the completion of the pulse cycle. The ADCP processing software must wait for the ringing to die away, before it can receive the returning echoes (RDI, 1996). This delay results in a blanking distance, sometimes called the 'near-field zone' common to all sonar transducers (Coates, 2002). For an ADCP operating at a transmit frequency of 600 KHz, the blanking distance is 1 m from the transducer. Thus, it is not possible to collect data in the top 1 m of the water column when using such an instrument. Ringing and contamination of the signal may be exacerbated by mounting the transducer loosely, or leaving it exposed on a metal hull. Deploying the ADCP in a transducer well, or moon pool through the ship's hull can reduce this effect (e.g. Murphy *et al.*, 1992).

Flow measurements near the bed can also present a problem. As the transducer face is mounted at an angle to the horizontal (typically 20°), it is possible to receive a stronger return from the sidelobes interacting the seabed (RDI, 1996). The maximum depth for acceptable data (R_{max}) may be calculated as follows:

$$R_{max} = D\cos(\theta) \qquad (4.03)$$

where D is the distance in metres from the head of the ADCP to the seabed, and θ is the angle of the beam relative to the vertical. Thus for operations in the Dart estuary, where the maximum water depth is likely to be in the order of 25 m, the maximum range for ADCP data will be 23.5 m.

4.3.4.2. Derivation of true coordinates

In order to determine the flow velocity in 'earth co-ordinates' from a moving vessel, the ADCP software has to correct for the velocity of the instrument over the sea floor. There are three methods of achieving this (RDI, 1996):

1. External navigation input
2. Assuming a reference water layer of no motion
3. Bottom tracking

The external navigation method (1, above) is usually achieved by interfacing a Global Positioning System (GPS) to the ADCP. This method is usually applicable in deep water, where the seabed is likely to be out of acoustic range. As flow speed is measured relative to vessel speed, it is essential to have a high quality navigation input if no bottom tracking is possible (Gargett & Moum, 1995). Using the 'reference layer' method is again usually undertaken in deep water, particularly where highly accurate Differential GPS (DGPS) corrections may not be available. Bottom tracking is a sensible method for use in shallow water, as it tends to be more accurate than the recorded current, typically in the order of 'a few

mm/s' (RDI, 1996). This method utilises a separate bin in the transmit pulse, to provide a more accurate method of gauging relative velocity than other bins. Bottom tracking has a further advantage in that many of its greatest errors are matched by exactly the same errors in the current profile. These 'common mode' errors cancel exactly when bottom tracking velocity is subtracted from the current profile data (RDI, 1996).

Once bottom tracking has been applied, true north, east and vertical velocity components may be computed using compass and tilt corrections (Gilboy *et al.*, 2000). The former is usually achieved using the ADCP's own internal fluxgate compass, or by interfacing the current profiler with an external gyrocompass. Tilt corrections are supplied by an internal or external pitch and roll sensor. The pitch, roll and heading measurements are then used to correct the measured velocities and ensure that the data is binned into the correct depth ranges (Emery & Thompson, 2001).

4.3.4.3. Mountings and calibrations

The standard configuration of the survey launch, PB8, presented some unique challenges when attempting to deploy the ADCP. Murphy *et al.* (1992) warn that any flex in the transducer mounting hardware during normal operations will lead to errors in the acoustic data. Peters (1997) used an ADCP mounted in a well in the aft section of a survey vessel. Encountering significant problems with bubble sweepdown below the ADCP transducer generated by the interaction of the hull with breaking waves, notable distortions were evident in some of his processed data. Additionally, wash from the screws is likely to affect significantly the recorded flow velocities when using such a mounting location.

An over-the-side mounting solution was also considered for PB8. To minimise flexing in the mounting system as discussed above, the apparatus would have to be designed to be as small, and close to the hull as possible. However, the flow field near the vessel's hull is likely to be contaminated by the motion of the vessel itself through the water. In particular, there is a potential for over-reading flow speeds near the hull, due to Bernoulli flows around the vessel when underway.

Consideration was given to mounting the transducer head on a towed device, such as that employed by Marmorino & Trump (1996). They mounted the ADCP on a cylindrical float, approximately 5 m long, which was towed alongside the survey vessel. Brubaker & Simpson (1999) have also employed this method with some success in Chesapeake Bay, mounting the ADCP horizontally on the float to reduce the blanking distance near the surface. Although this method of deployment does have some clear advantages, there may be significant contamination of the returning signal by sidelobe energy. Additionally, such a small mounting platform would be subject to large magnitudes of pitch and roll when operating in more disturbed water. Mindful of the fact that the entrance to the Dart estuary can experience swell of up to 1 m in certain conditions, the larger mounting platform of a survey vessel was deemed more satisfactory. Furthermore, changing the orientation of the instrument by 90°, outside its design parameters, would place the internal pitch and roll sensors out of range. As accurate inputs from these sensors are essential to correct the raw recorded data, it is likely that data quality would be poor, especially if operating in anything other than a flat calm environment. Most importantly, however, the budget for the fieldwork equipment for this survey would not allow for the fabrication of such a float.

An over-the-bow mounting system was thus deemed most appropriate for PB8, to fulfil the data accuracy requirements of the fieldwork. This mounting position has a number of clear advantages. The ADCP transducers are placed as far away from the screws as possible. Additionally, the instrument is on or near the centre-line of the vessel, thus minimising pitch and roll effects, as advised by Murphy *et al.* (1992). Even when operating on a vessel constructed from GRP (glass reinforced plastic) consideration must be given to magnetic deviation effects on the ADCP internal compass (or an external gyrocompass, if used). This deviation is likely to be significant near large metallic items, which in the case of PB8 are the two large diesel engines mounted amidships. The magnetic deviation was measured at various points around the vessel prior to commencement of the fieldwork, and found to be minimal in the bow area. Allowing the ADCP transducer to operate in 'clean', undisturbed water ahead of the vessel is also likely to improve the precision of the measurements.

Once the location of the ADCP had been confirmed, it was essential to conduct the design and installation of the mounting equipment with some care. The instrument requires mounting exactly vertically if possible, in order to minimise pitch and roll fixed offsets. Similarly, the orientation of the transducer in the horizontal plane should be noted, and should be accurately reproducible if the system is removed and re-installed (Murphy *et al.*, 1992). This potential transducer misalignment can introduce a significant error, if not accounted for. A 1° compass error can lead to a sideways velocity error of approx 10 cm s^{-1}, when a ship steams at 5 ms^{-1} (RDI, 1996). Plans for an mounting frame were drawn up and submitted to a local boatyard in late 2001, fitting the vessel extremely well on delivery in early March 2002 (Plate 4.06).

Calibration of an ADCP is not straightforward, and has been reported in very few studies to date. Gilboy *et al.* (2000) quote a velocity precision for a standard uncalibrated ADCP as ± 4

Joyce (1989) states that absolute accuracy in ADCP data is particularly important if using the instrument to estimate transport rates. If the ADCP is used as a reference level for geostrophic velocity calculations, then any uncalibrated bias can result in large errors in water column volume transport. In addition, Pollard & Read (1989) state that the transport bias due to misalignment errors is usually perpendicular to the vessel's track. As the instrument has been used purely to derive the longitudinal velocity structure of the Dart Estuary, *along* the track of the vessel, any bias in the data due to the transducer misalignment is likely to be in the form of a fixed offset. It will, therefore, be consistent throughout the entire data set, and is likely to affect the mixing calculations undertaken using the ADCP data to a minimal degree. In order to provide a gross error check of the ADCP data, however, an InterOcean S4 buoy was deployed in the survey area (Section 4.3.5). The results could then be processed and compared to the ADCP data post cruise. An error analysis of the data is undertaken in Section 4.6.3.

Surface salinity was measured regularly, and the data entered into the ADCP acquisition software. It should be noted, however, that the processing software makes the assumptions that salinity is constant until manually changed by the user, and that temperature and salinity are homogeneous with depth. A temperature sensor on the ADCP transducer head reduces these errors to some extent, although reducing salinity during survey transects up-river into fresher water is clearly not accounted for. An average value of salinity was manually entered for each transect, although there is the possibility of a slight over-estimation of flow velocity moving up-river, as sound speed reduces in fresher water. Haehnel (1990) noted a jump in velocity of 1.5% when traversing a temperature dominated front in the Greenland sea. This was due to the failure of the ADCP's temperature sensor in this case, which although increasing the bias in his data slightly, did not lead to substantial data rejection.

4.3.4.4. Deriving a suitable sampling strategy

Consideration must be given to the settings available for modification within the ADCP software and, in particular, the length of ensemble used for averaging. It is desirable to have some period of averaging to reduce the relatively large random errors present in single ping data. However, after a certain amount of averaging, the random error becomes smaller than the bias (due to transducer misalignment), and any further averaging will do little to reduce the overall error (RDI, 1996). In addition, there are likely to be notable dynamics across the narrow frontal zone, including convergent and supercritical flows, and almost immediate re-stratification downstream (Gargett & Moum, 1995). Measuring these inhomogeneities in velocity associated with frontal structures is a fundamental requirement of the field data collection, and therefore any averaging must not be of a length too great prevent accurate resolution of these events. The presence of such an inhomogeneity creates a finite limit to the statistical reliability of a sample, as increasing the averaging length eventually fails (Gargett & Moum, 1995). Lu & Lueck (1999) state that an ensemble length of 20 minutes reduces the standard deviation of the mean currents to 'low' levels. Even at a relatively slow vessel speed of 2 ms^{-1}, such a period would result in averaging single ping data over a horizontal distance of 2400 m, clearly too great to resolve the flow across a narrow frontal structure. In deep ocean surveys where the oceanographic parameters are more constant, such an averaging time may be more appropriate. In a dynamic, shallow water environment, however, flow resolution over shorter horizontal distances is required. There are a variety of methods to derive the ideal ensemble length, which clearly will always be a compromise between statistical data quality and resolution.

Brubaker & Simpson (1999) state that as the fundamental assumption is made that the flow across the area separating the acoustic beams is homogeneous (Figure 4.03), the beam

separation (L) of the longitudinal ADCP acoustic beams should be less than the ensemble length (Δx). If

$$\Delta x = U\Delta p \tag{4.07}$$

and

$$L = 2D(\tan\theta) \tag{4.08}$$

where Δp is the total number of pings per ensemble, U is the vessel speed (ms^{-1}), D is the water depth, and θ is the beam angle, the following relationship can be obtained (Table 4.1.).

Depth (m)	L (m)
10	7.2
20	14.6
25	18.2
33	24

Table 4.04. Relationship of water depth to beam separation (L).

If the relationship $L < \Delta x$ is to be maintained for data quality, then at a survey vessel speed of 2 ms^{-1}, and a Δp of 24 (an example 20 second ensemble containing 24 pings), Δx is 48 m (Table 4.05). At a maximum likely depth at the entrance to the Dart estuary of 25 m, L is 18.2 m, and the accuracy requirements are satisfied.

This horizontal averaging distance of 48 m was, however, considered too great to resolve accurately the flow across the frontal zone. This could either be resolved by reducing the

speed of the survey vessel (U), or reducing Δp. The latter was considered carefully and deemed to be undesirable. The more pings per individual ensemble (increasing Δp), the greater the accuracy of the velocity measurement, and hence data quality will improve. As the distance to be covered to traverse the frontal zone was not great (approximately 2 km transects) it was possible to reduce the speed of the survey vessel through the water. Following extensive trials during the fieldwork pilot study (Section 4.6.1) it was found that steerage way could be maintained at 1 ms^{-1} (2 knots) by the helmsman of PB8, using just one engine at very low revolutions. This was the minimum speed possible for safe navigation in the estuary.

Vessel speed	Δp	Δx (m)
0.5	24	12
1	24	24
1.5	24	36
2	**24**	**48**

Table 4.05. Effect of changes in vessel speed on ensemble length (Δx) whilst maintaining a constant ping rate (Δp).

Therefore, with a U of 1 ms^{-1}, and a Δp of 24, Δx is 24 m. As the relationship of $L < \Delta x$ has been maintained, data quality is acceptable statistically (Brubaker & Simpson, 1999), and the Δx (of each ensemble) of 24 m should ensure that flow changes across the frontal structure are recorded. It should be noted that to maintain the accuracy relationship, the depth of water should not exceed 33 m during the survey (Table 4.04).

Using the guidelines suggested by Lu & Lueck (1999) yields a similar result. They have derived the following relationship to calculate an ideal averaging time (τ):

$$\tau = \frac{L}{U} \tag{4.09}$$

where L is the beam separation (m), and U is the vessel speed (ms^{-1}). With a beam separation of 18 m (at a theoretical maximum operating depth in the Dart estuary of 25 m), and a speed of 1 ms^{-1}, the ensemble length should be approximately 18 s.

The final user settings for the ADCP as derived from the methods outlined above are similar to those used by other researchers working in estuarine environments (Table 4.06):

Researchers	Location	Depths	Settings
Brubaker & Simpson, 1999	James River estuary	<15 m	1.2 MHZ narrowband ADCP 1 m bins 20 s ensembles 40 m ensemble length
Gargett & Moum, 1995	Juan de Fuca Strait	<300 m	400 m ensemble length
Valle Levinson *et al.*, 2000	James River estuary	<15 m	600 KHz broadband ADCP 0.5 m bins 30 s ensembles 75 m ensemble length Calibration conducted
Haehnel, 1990	Greenland Sea	2000 m	8 m bins 5 min ensembles
Peters, 1997	Hudson river	<20 m	0.5 m bins 10 s ensembles
O'Donnell *et al.*, 1998	Connecticut river	<10 m	600 KHz broadband ADCP 0.25 m bins
Marmorino & Trump, 1996	James River estuary	<15 m	0.5 m bins 5 s ensembles

Table 4.06. ADCP settings used during the field data collection: Comparison with other recent work.

4.3.4.5. Extraction of the data

The acquisition software provided by RD Instruments for use with the ADCP is relatively flexible in terms of allowing the user to test and modify the instrument operating settings. Using 'VmDAS' (moving vessel Data Acquisition Software), it is possible to configure the

ping rate and ensemble length, make detailed changes to the methods of correcting the raw ping data, and configure external data sources, for example, an input from an external GPS or attitude sensor. Once raw ping data is being collected, transformation into earth co-ordinates is carried out along with any offset corrections and error velocity screening (RDI, 2001). The user displays of the data are quite basic, and include a tabular presentation, a flow profile or a ship track plot. Survey lines can be 'played back' after the event using the saved data files, although the software is limited by the quality of the displays, and the lack of a facility to export the data to other packages.

RD Instruments also supply a further software package designed to enable the user to visualise flows recorded by the ADCP. The 'WinRiver' software allows the user to replay recorded data files, and cannot be used effectively for setting up the instrument for deployment. Flow rates and directions are presented in the form of a contour plot. These plots have a serious limitation, in that only one flow parameter can be displayed on each pair of axes. For example, flow direction and magnitude require *two* separate contour plots. This makes it extremely difficult to visualise two- or three-dimensional flows, with any accuracy. A facility exists within Winriver, however, to export data in a complex ASCII format. The header for each exported ensemble of flow data includes a highly accurate time stamp and position information from the GPS. In order to reformat the data for further processing and analysis, with a separate column for each measured parameter, data from each survey line was exported from Winriver and then processed using the Matlab routine 'ADCP3.m' (Appendix 3). This routine reads the complex, exported ASCII file, and writes a text file in a logical format.

4.3.5. InterOcean S4 current meter

An InterOcean S4 current meter consists of a spherical, 25 cm diameter plastic housing containing all batteries, sensors and solid state electronics. The instrument uses Faraday's law of electromagnetic induction, to derive the true magnitude and direction of horizontal current flows. This law states that the voltage produced in a conductor is the product of the speed of the conductor, the magnitude of the magnetic field and the length of the conductor. In this case, a moving current behaves as a moving electrical conductor. Two pairs of exposed titanium electrodes, located on opposite sides of the equator of the S4, detect changes in the induced electrical potential associated with the ocean current, with the conductor length being the effective path between the sensing electrodes (Emery & Thompson, 2001). The magnetic field intensity is driven by an internal circular coil connected to a precisely regulated alternating current. The electric current measured by the electrodes are converted to the separate X and Y components of the flow velocity using the internal fluxgate compass and laboratory calibration factors. The manufacturer's stated accuracy for the instrument (Table 4.07) is slightly better in resolution terms than an RD Instruments ADCP (Section 4.3.5.3), and around the same in accuracy terms.

	Resolution	Accuracy
Speed (cm s^{-1})	0.2	2% of reading ± 1cm s^{-1}
Direction	0.5°	±2°

Table 4.07. Resolution and accuracy of an InterOcean S4 current meter (Manufacturer's Figures).

The InterOcean S4 was deployed in the Dart estuary on 12 March 2002, the day prior to the commencement of the fieldwork, in order to provide a first-order check of the ADCP data. The current meter was attached to a clump-weight by means of an acoustic release (Figure 4.05) to facilitate the recovery of the instrument. A further line was tied to a surface marker buoy. Following a function check of the S4's internal compass, this apparatus was then deployed from the survey vessel (PB8) in close proximity (approximately 1m) to the Dart Observatory data buoy (Section 3.0). The instrument was set to record a 10 s average every one minute, logging at 2 Hz. Having mobilised the ADCP equipment onto the survey vessel, PB8 motored past the S4's location at slow speed, passing as close to the surface marker buoy as safety would allow. Vessel time would only allow for two such passes to be completed, however, these were sufficient to confirm that the flow readings from the ADCP were of the correct order of magnitude (Table 4.08).

A difference in flow speed of 6.75 cm s^{-1}, between the S4 and the ADCP, was recorded during the first pass. There was, however, a slight difference in the depth at which the two instruments were recording, which may account for the difference. During the second pass, a difference of only 1.89 cm s^{-1} was noted. These measurements were recorded approximately 10 minutes later on a flooding tide, and the recording depths of the two instruments were, therefore, almost coincident at this time. On this second pass, the difference between the two recorded values amounted to only 3.6% of the ADCP's recorded flow speed.

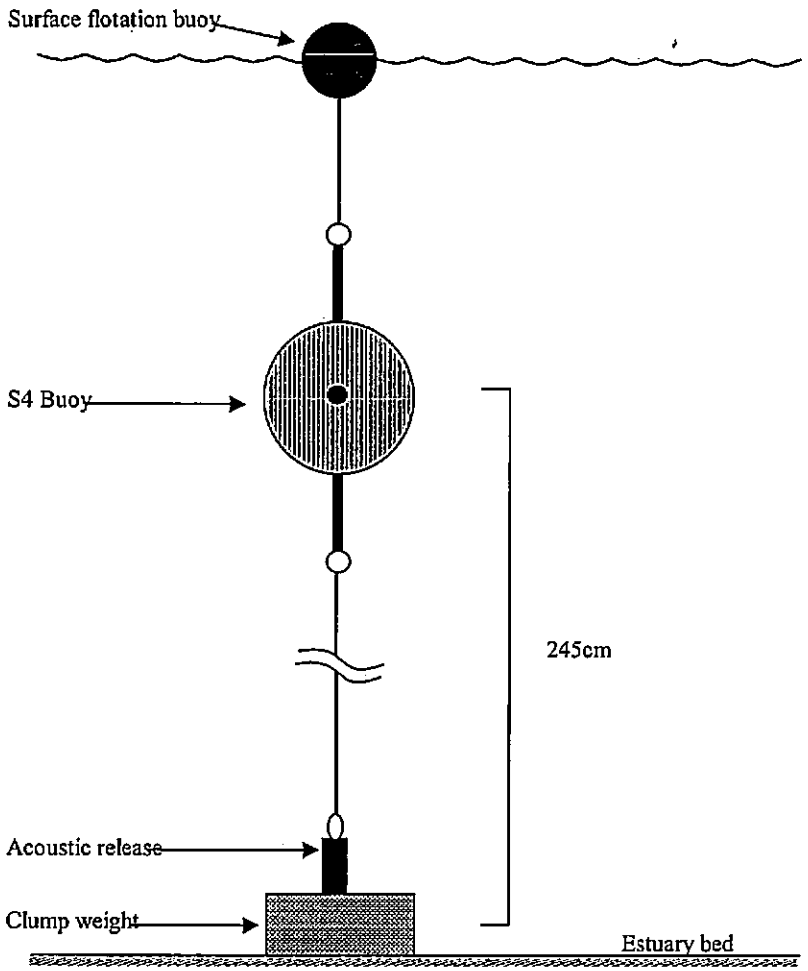

Figure 4.05. Schematic diagram showing the deployment of the InterOcean S4 current meter in the Dart Estuary

This exercise provided a first-order confirmation that the ADCP was recording 'sensible' flow velocity values. All the measurements taken during this deployment were broadly in line with the Manufacturer's quoted precision and accuracy specifications.

InterOcean S4				RD Instruments ADCP		
Depth (m)	Flow velocity (cm s^{-1})	Correction (cm s^{-1})	Corrected flow velocity (cm s^{-1})	Depth bin (m)	Flow velocity (cm s^{-1})	Difference (cm s^{-1})
4	51.5	-3.4	48.1	4.05	54.85	6.75
4.04	53.3	-3.4	49.9	4.05	51.79	1.89

Table 4.08. Comparison of measurements from InterOcean S4 and RD Instruments ADCP. The corrected flow velocity for the InterOcean S4 was derived from the calibration certificate supplied with the equipment.

4.6. Field data collection – methods employed

4.6.1. Pilot study

A pilot study for the main field data collection exercise was undertaken on 9 April 2001 with the following objectives, listed below.

1 To commission and check the mounting frame that had been designed and manufactured, to deploy the ADCP transducer head over the bow of PB8.

2 To commission and check the deployment frame that had been designed and constructed, to deploy the CTD probe from PB8.

3 To ascertain if the ADCP equipment functioned correctly and if the GPS equipment would interface successfully with the ADCP software.

4 To confirm the area that should be surveyed, to adequately characterise the tidal intrusion front.

5 To ascertain the approximate accuracy level of the stand alone (*i.e.* non-differential) GPS equipment.

6 To ascertain how many crew would be required to successfully collect environmental data using PB8 as a survey platform.

A survey was conducted starting at 1545, approximately one hour and 45 minutes after low water on a spring tide. Anecdotal evidence implied that the tidal intrusion front would be present at this point in the tidal cycle. The wind was negligible, with a swell height at the mouth of the estuary estimated to be 0.4 m. Survey lines were run across the front at the estuary mouth, commencing at Sandquay and ending at Castle Ledge buoy (Figure 3.02). Four survey lines were completed, two in a seaward direction and two in an landward direction, keeping as near to the centre of the channel as possible each time. ADCP data were recorded continuously during each survey line, and six CTD casts were made with the vessel stationary, during the second survey line. The survey was complete at 1700, approximately three hours after low water.

This study highlighted some very important aspects for consideration in the main survey. Firstly, it was apparent immediately that the ADCP data collected whilst taking CTD casts was of an extremely low quality. There were frequent spikes in the flow velocity readings, thought to be caused by the wash from the vessel's screws, as power was applied to stop the vessel prior to taking a CTD cast. It is also possible that this could cause some mixing of the water column, further skewing the readings. It was clear that data quality would be improved significantly by running each ADCP survey line in one direction, at a constant speed and without substantial changes in vessel heading. In this way, the effect of the passage of the

vessel through the water on ADCP readings should be minimised. CTD casts should then be undertaken on a returning survey line, with the coxswain attempting to minimise excess cavitation and wash from the screws at all times. Provided the ADCP was activated during the CTD survey lines, the GPS position of each CTD cast could be extracted from the ADCP data set.

Further, issues highlighted during the pilot study were as follows:

1. All watches used to be synchronised with GPS time at the commencement of the survey.
2. The positions of the CTD casts to be carefully recorded. Therefore, it should be possible to link the CTD data with the ADCP data, from the previous survey line.
3. Better recording proformas and documentation required. This would encourage better note-taking during the main survey.
4. It was apparent that a minimum of four personnel would be required for the main surveys, one coxswain, one CTD operator, one ADCP software operator, and one extra hand to accurately record and document the survey.

The objectives of the pilot study were met in full, with both deployment frames proving an immediate success, with no requirement for modifications in either case. The ADCP and GPS equipment was interfaced successfully, and provided a simple method of combining the vessel track, the ADCP data and the CTD data. From non-differential GPS data collected alongside the Sandquay pontoon, it was apparent that the Trimble GPS equipment used would provide adequate positioning precision (Section 4.3.3.).

From an analysis of the pilot study data, it was found that the hydrodynamic properties of the Dart estuary did not change considerably landward of the Lower Ferry, or seaward of Checkstone buoy (Figure 3.02). It would appear sensible, therefore, to concentrate the data collection area within these boundaries. The resulting survey lines would be approximately two kilometres long, which at a required survey speed of 2 knots, would be completed in around ten minutes. This compares favourably with the extended survey lines run during the pilot study. At 6 km in length, these would take 30 minutes to run one survey line. As visual observations of the front indicated it was present for only around two hours after low water, a ten minute survey line would clearly allow more survey lines to be run across the critical frontal zone.

4.6.2. Final sampling programme

The survey vessel Picket Boat eight (PB8) was mobilised on 12 March 2002. The ADCP equipment was installed and the heading offset carefully removed by conducting an alongside compass calibration, and rotating the ADCP head until the ADCP compass heading matched that of the pontoon alongside which the vessel was moored. A gross error check of the ADCP recorded data was conducted by deploying the InterOcean electromagnetic current meter in the Dart estuary as described in Section 4.3.5. A shielded GPS antenna was mounted on the foredeck of the vessel to ensure there was a minimal offset between the GPS and ADCP transducer positions. The CTD was set to record data at a depth increment of 0.2 m (for maximum data density), with a pressure trip at 0.2 m. The ADCP was set to record data in 0.5 m vertical bins (Section 4.3.4.4.).

Surveys were conducted at the mouth of the Dart estuary on the 13 March 2002 (spring tide), and on 22 March 2002 (neap tide). Predicted tidal ranges for the 13 March and the 22 March were 3.9 m, and 2.0 m, respectively (Figure 4.06). A low pressure system on 13 March made for relatively unfavourable survey conditions, with a Beaufort force 6 gusting 7 recorded in the log for most of the day. A 0.75 m swell was estimated at Checkstone buoy, just outside the estuary mouth. Due to the relatively large size of the survey launch, a stable platform was still provided for survey operations. All readings of horizontal flow velocity were reported as '100% good' by the ADCP software. The weather was more settled on 22 March, with a light force 2-3 wind, and a swell at Checkstone buoy of less than 0.3 m. It should be noted that there was little difference in freshwater runoff between the two survey dates (Figure 4.07). Data collection was commenced one hour before low water (LW-1) on each day, and completed three hours after low water (LW+3).

The generic survey procedure is now described. Starting approximately abeam of Checkstone buoy outside the estuary mouth, a survey line was commenced heading into the estuary (Figure 4.08). The vessel maintained a constant speed of approximately two knots ($\approx$1 ms^{-1}), with any heading changes kept to a minimum. A track up the centre of the channel was followed as closely as possible, the helmsman steering using a track pre-programmed in to the navigation suite GPS system on board. This ensured that the ADCP data collected at this time was as free from any vessel-induced influences as possible, such as sudden heading changes or excess wash from the screws. This survey line is represented on Figure 4.08 by the small black circles, with the ADCP ensemble numbers adjacent.

Once a location abeam of Dartmouth Yacht club was reached (just downstream of the Lower Ferry), a new survey line was commenced immediately in the opposite direction, this time collecting CTD data at pre-allocated dip locations. These locations are represented on the chart below by the larger numerals. Note that ADCP data was also collected during this survey line, mainly to facilitate the extraction of appropriate GPS positions for each CTD cast from the ADCP data header.

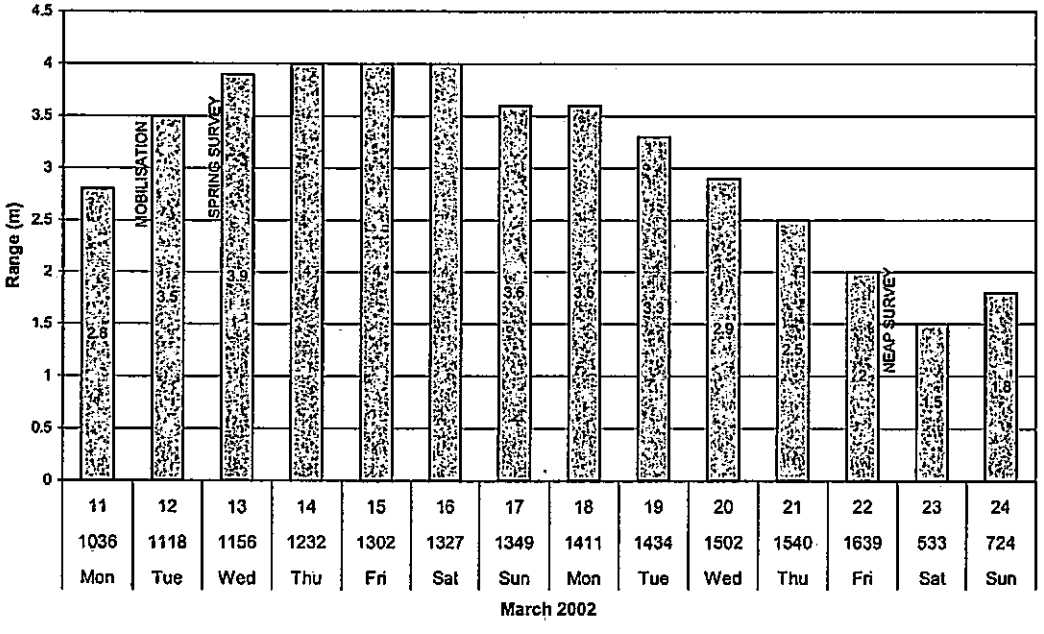

Figure 4.06. Date, time of low water, day and tidal ranges in the Dart estuary over a two week period in March 2002.

The high quality ADCP data from the initial run was combined with the CTD data from the second run down-estuary to form a quasi-synoptic snapshot of the flow and density conditions in the estuary for that hour of the tidal cycle. Each pair of ADCP and CTD survey lines was

conducted hourly, from one hour before low water (LW-1) to three hours after low water (LW+3). The maximum time offset for each pair of survey lines between the first ADCP reading and the last CTD dip was typically around 30 minutes.

In the majority of areas, the CTD positions and ADCP lines correspond very well (Figure 4.08); for example, at CTD cast 4 the offset to ensemble 81 is 12.3 m (estuary width 374 m) – a position offset of only 3.3% in the horizontal, across estuary plane. At CTD cast 5 the offset is 24.4 m (estuary width = 352 m), a position offset of 6.9% in the horizontal plane. The majority of the positions are well within the 10% zone, and can thus be regarded as representative of the flow and density at that location. It remains a fundamental assumption, therefore, that the flow and density characteristics are both steady and uniform at each CTD cast and corresponding ADCP location. For situations such as that occurring at cast 1, for example, the offset is 89.5 m along the axis of the estuary, which could lead to errors. The data from such positions have been rejected.

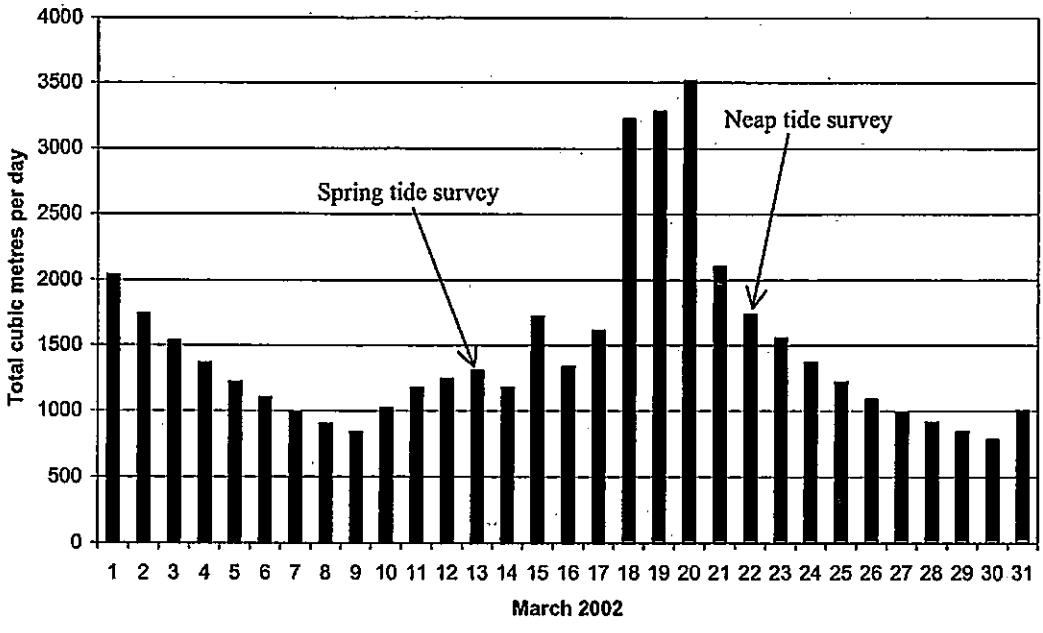

Figure 4.07. Freshwater runoff conditions during March 2002 at Austin's Bridge, 5 km upstream of Totnes at the head of the river Dart. Source: Environment Agency.

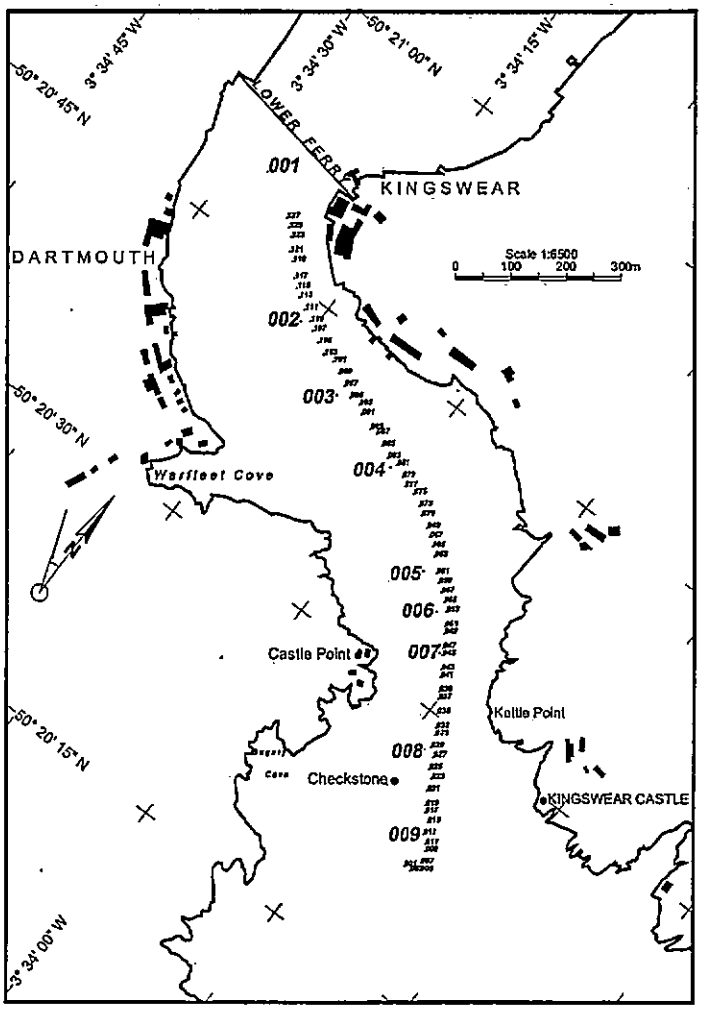

Figure 4.08. Survey area, and example ADCP survey line (small numerals) with corresponding CTD cast positions (large numerals). This example represents the tracks and positions two hours after low water (LW+2) on 13 March 2002.

4.6.3. Data quality summary

Emery & Thompson (2001) present the following method for calculating the random error of the horizontal velocity (σ) for each ensemble (ms^{-1}):

$$\sigma = \frac{(1.6\times10^{2})}{(FD\Delta p^{\frac{1}{2}})} \qquad (4.10)$$

Where F is the operating frequency of the ADCP (614 KHz) in hertz, D is the length of each ensemble (m) and Δp is the number of pings in the ensemble. The ADCP was set in 'ping as fast as possible' mode throughout, which is approximately 2 Hz. Typically, however, the ADCP managed to achieve only 6 pings in 5 s, with the remainder being processing time. This processing time is inherent to the system, and has therefore, been accounted for in these error estimates. With a selected bin size of 0.5 m and an ensemble length of 20 s , the random error is calculated to be approximately 5 cm s^{-1} with a standard deviation of $\pm$ 10%. Flows in the Dart estuary have been found to vary typically between 0.1 ms^{-1} and 0.7 ms^{-1} depending on the phase of the tidal cycle and location. At the higher flow velocities, the maximum random error potentially represents only 7% of the measured flow speed. Caution should be exercised when analysing lower flow speeds, however, as at 0.1 ms^{-1}, the random error could represent up to 50% of the recorded flow speed.

The GPS system accuracy was found to be 3.49 m in latitude and 2.89 m in longitude (Section 4.3.3.), a root mean square error of 4.53 m. At the scale of the chart used (1:6500) for the data presentation and analysis, such a positioning discrepancy would be difficult to resolve visually, and therefore such a positioning accuracy is deemed to be acceptable.

Provided the calculated sensor drop rate was adhered to as closely as possible when deploying the CTD probe, the measurements taken by this instrument are the most accurate in comparison with the other sensors. Typical accuracies for temperature measurement of $\pm 0.002°C$, and salinity of ± 0.005 provide ample resolution to fulfil the aims of this research.

4.7. Data processing

4.7.1. Data merging and initial processing

Although the CTD was set to take a reading every 0.2 m, it was apparent from the results that the instrument recorded at irregular depths throughout the water column. Typically the depth spacing of these data was from 0.2 m to 0.5 m. As the ADCP was set up to record flow data using 0.5 m bins, it was clear that the two data sets would have to be set on a similar depth grid in order to be combined for successful data analysis.

A Matlab routine, 'dataproc4.m', extracts the depth and density data from the raw CTD file, the flow data from the corresponding ADCP file, and writes one combined data file with all the information from that particular location (Appendix 3). A linear interpolation routine to re-grid the CTD data on to the ADCP 0.5 m bin spacing is incorporated. The data were then smoothed within 'dataproc4' using the following moving average routine:

$$(x_{n-1} \times 0.25) + (x_n \times 0.5) + (x_{n+1} \times 0.25) \qquad (4.11)$$

This routine has been highly successful in honouring the original data, whilst removing any spikes and noise (Figure 4.09).

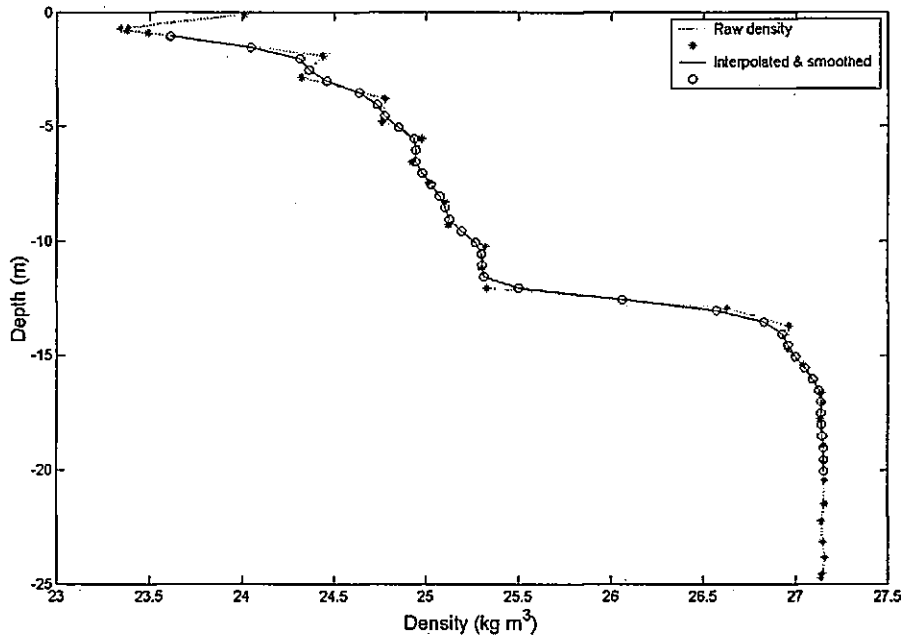

Figure 4.09. Example graphical output of Matlab routine 'Dataproc4'. This illustrates the smoothing and interpolation used in fusing ADCP and CTD data.

Finding the layer interface depth was accomplished using an interactive routine, 'n2_spline2.m', which enabled the final calculations to be made on the field data, this being accomplished using 'mixcalc2.m'. Graphical presentation of the data was facilitated by Golden Software's 'Surfer VII' package, velocity vectors being prepared for input to this program with a further Matlab routine, 'surfcurr2a.m'. A summary of the steps involved in the data processing, and the software and Matlab routines used highlights the care that was taken to ensure total data quality (Figure 4.10).

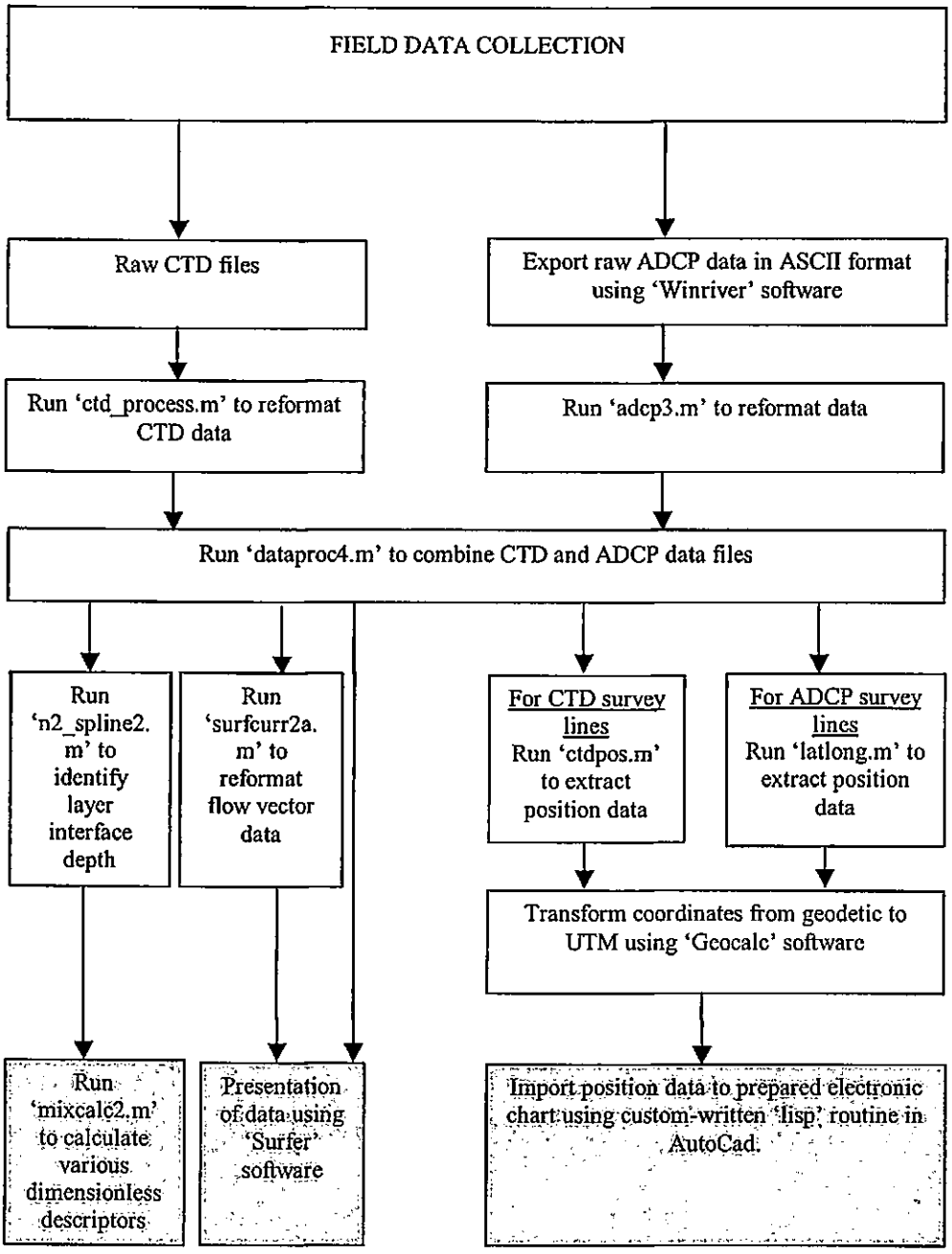

Figure 4.10. Flow diagram indicating the stages of data processing. The Matlab files and the 'lisp' routine referred to can be seen in Appendix 3.

5.0. Field data results

5.1. Chapter overview and summary

Field data results have been presented as longitudinal contour plots from one hour before low water (LW-1) to three hours after low water (LW+3) during both a spring and a neap tide. Horizontal flow vectors have been overlayed on contour plots of density, in order to represent the hydrodynamic interactions within the water column. Vertical profiles of density have been divided into two discrete layers, with recorded values of density and flow speed averaged within each layer, to facilitate the calculation of various frontal descriptors.

During spring tides (Figure 5.01), an exchange flow between estuarine and coastal waters was found to occur at LW. There was a visual manifestation of a tidal intrusion front for approximately two hours, starting at LW+1. A foam line marked the frontal interface at the surface, and a distinct colour change was noted on either side of the front. A homogeneous flow was recorded upstream of the frontal interface, with a two-layer, stratified regime present downstream. The location of the tidal intrusion front was characterised by a sharp discontinuity in density, this being driven almost entirely by changes in salinity. The front was noted to migrate landward as barotropic forcing increased further, remaining stationary for a time over the increasing depth caused by an elongated seabed depression just inside the mouth. By LW+3 the front had disappeared, with patches of foam and discoloured water distributed over much of the survey area at this time, and the water column being virtually homogeneous throughout.

No visual manifestation of the front was noted during neap tides. A well-developed, shallow pycnocline was recorded throughout the flooding tide, driven predominantly by a buoyant

outflow of low salinity water at the surface (Figure 5.02). This buoyant layer maintained its integrity from LW+1 to LW+2, although by LW+3, some erosion of this pycnocline had occurred. A corresponding thinning of the buoyant surface layer had taken place by this time.

A comprehensive set of dimensionless descriptors has been employed, to characterise the flow through the constricted entrance of the Dart estuary.

5.2. Data processing and presentation

5.2.1. Finding the layer interface depth

In order to define the interface between the layers of a two-layer flow, the Brunt Väisälä, or buoyancy frequency (N) can be calculated (Huzzey, 1982; Chen *et al.*, 1994).

$$N^2 = \frac{-g}{\rho}\frac{\partial \rho}{\partial z} \quad s^{-2} \tag{5.01}$$

Note that N^2 is exclusively used, as this avoids the use of imaginary numbers (the square root of a negative density gradient cannot be plotted). A Matlab routine (n2_spline2.m) has been developed in order to calculate and plot N^2 from the interpolated and smoothed density data for each CTD cast (Appendix 3). A cubic spline has been fitted to the calculated points of the N^2 plot, and as each graph is plotted, an interactive tool allows the user to pick the depth of maximum N^2 (Figure 5.03).

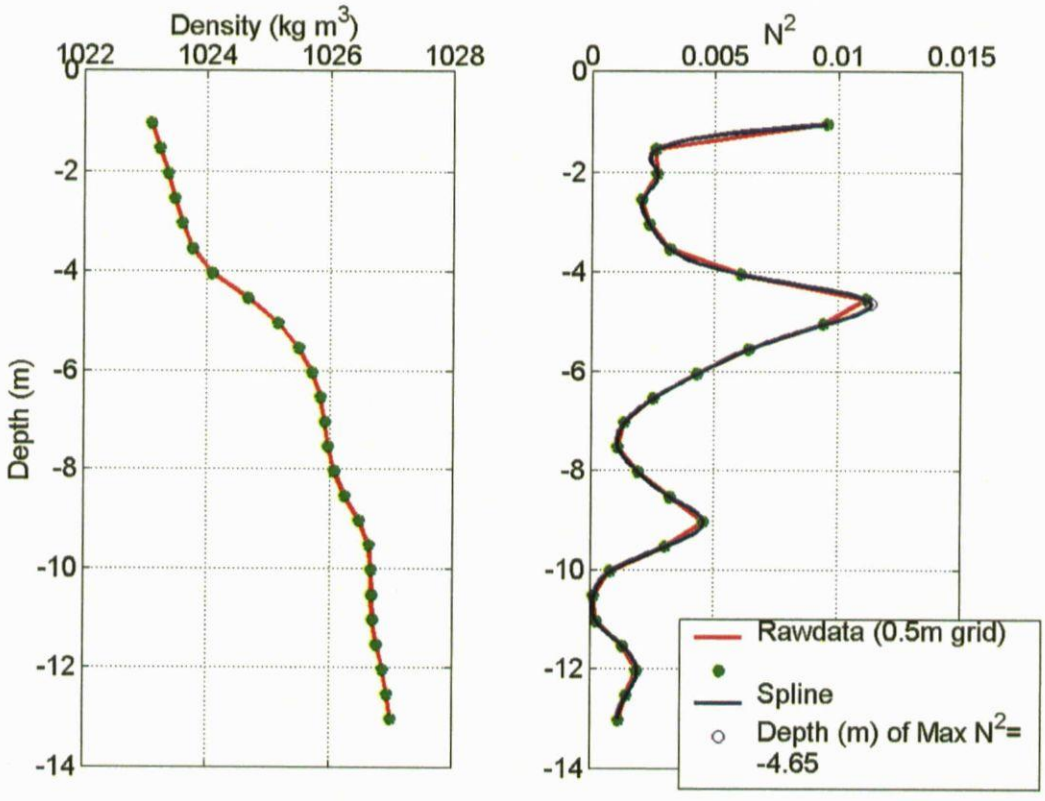

Figure 5.03. Example of the graphical output from 'n2_spline.2'. This routine calculates and plots N^2, and allows the user to graphically find the depth of maximum N^2. Note that the plotted N^2 values correspond to the higher depth value of the density gradient in all cases.

The user input facility in this routine allows the operator to select a zone around a desired data point, the program then picking the maximum value of N^2 from the selected area. The user input method has proved particularly useful in situations such as for Figure 5.04, where although the apparent N^2 maximum is at the surface, it may be more useful to pick off the layer interface at 3.05 m.

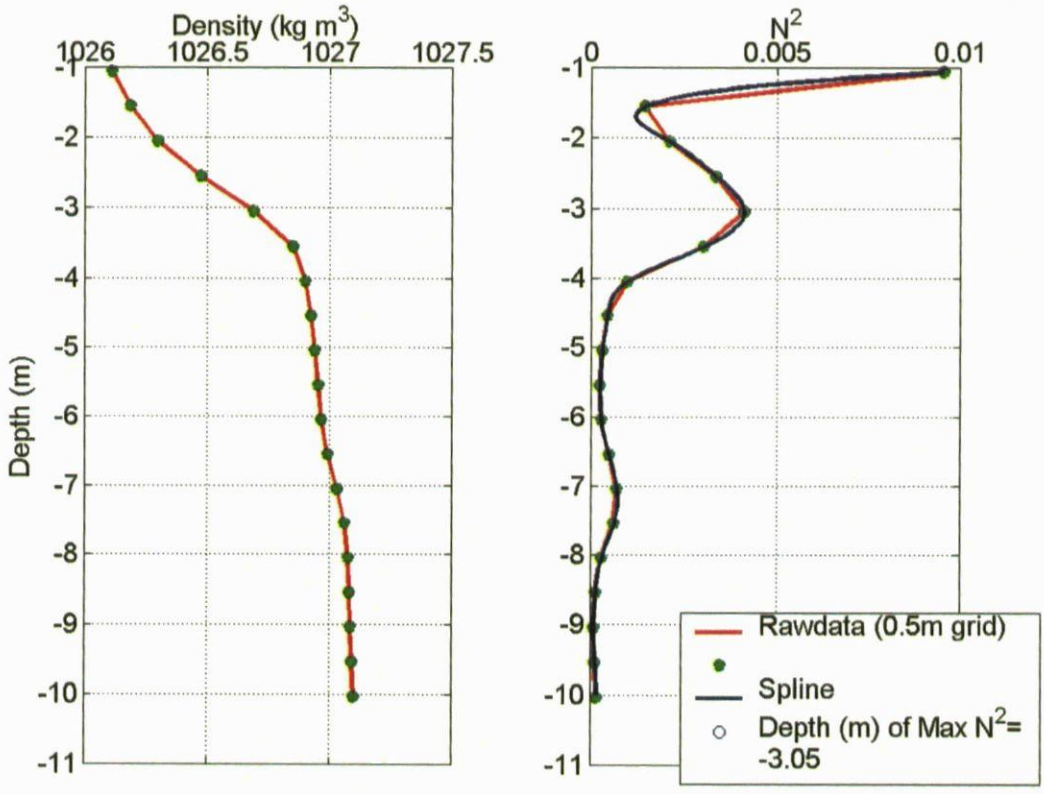

Figure 5.04. Graphical output from 'n2_spline2.m' highlighting the advantages in the 'user-input' method of quantifying N^2.

5.2.2. Removal of the vertical velocity component

Measurement of three-dimensional components of velocity using an acoustic doppler current profiler (ADCP) is hampered by the fact that the magnitude of the vertical flow velocity is significantly less than that of the horizontal flow. In addition, the pitch and roll of the vessel, particularly when operating in higher sea states, may be considerably greater than the vertical component of the flow. Although pitch and roll is effectively removed by the ADCP's internal sensors, the update rate of the pitch and roll sensor may not synchronise particularly well with the ping rate of the ADCP (Hughes-Clarke *et al.,* 2003). This is less of a problem in shallow water, when the ADCP ping rate is faster, or for the horizontal components of the

flow field, as the magnitudes of these parameters tends to be quite large. Errors may be introduced in vertical velocity, however, when attempting to resolve this component in higher sea states. As the sea state was in excess of force three when collecting the data during spring tides, with a swell of approximately 0.5 m, the vertical component of the flow was found to show considerable variability. The horizontal flow components appeared stable, with the ADCP software's internal algorithms reporting all the horizontal flow data as '100% good'.

The vertical velocity field has been removed from the processed data files, due to the uncertainties outlined above. As this component of the flow is recorded separately within the data telegram from the ADCP, it may be manipulated easily. A simple routine within the Matlab code 'surfcurr2a.m' (Appendix 3) used to prepare the ADCP files for presentation purposes reduces the vertical flow velocity to zero. The plotted flow velocity results presented in this chapter comprise, therefore, the horizontal flow magnitude and direction only.

5.2.3. Contouring and presentation of results

Once the raw data had been prepared, smoothed and interpolated onto a common grid (Section 4.7.1), visual presentation of the results was undertaken using Golden Software's Surfer VII package. Designed as a presentation tool for geographers and scientists, Surfer is highly flexible, enabling the contouring and clear presentation of complex three-dimensional data-sets.

Sparse and spatially irregular data, such as that represented by the CTD data sets, must first be interpolated onto a regularly-spaced grid within Surfer, before the contouring process is undertaken. Two fundamental assumptions are made during this interpolation and gridding

process. Firstly, the data fields are required to be stationary, or unchanging over the sample period of each plot. Secondly, the control point values should be related, or spatially autocorrelated over the distance between the data points (Swan & Sandilands, 1995). The latter point is important as a gridded surface based on control points which are too far apart may be totally misleading (Emery & Thompson, 2001). Choosing the locations of the CTD casts (Section 4.6.2.) with care has increased confidence in the autocorrelation of the plotted variables, and in the objectivity of the ensuing analyses. For example, CTD sampling density was increased slightly at the mouth of the Dart estuary, where the frontal system was believed to form. In addition, a horizontal anisotropy, or bias, has also been applied to the gridding and interpolation process within Surfer. As most physical processes have a preferred orientation, a degree of weighting along a preferred direction is defined by the anisotropy ratio (Swan & Sandilands, 1995). As the horizontal scale in the case of the data presented in this Chapter is two orders of magnitude greater than the vertical scale, a 'severe' anisotropy ratio has been applied to all contour plots, apart from those of gradient Richardson number. The implicit assumption is made that there is no longitudinal gradient in density in this parameter (Lewis, 1997).

Considerable care has been taken when gridding data using Surfer, to ensure that the gridded and contoured surface has remained an accurate representation of the longitudinal variations in each particular parameter. It was essential to choose an interpolation, or gridding technique that would honour the original, irregularly spaced data points closely, and interpolate between them without smoothing discontinuities in measured parameters which could indicate the presence of a front. There are a variety of methods available to achieve this gridding process, all accomplished using software subroutines within the Surfer package. The choice of method depends on the nature of the data, the degree of accuracy required and the computational cost

(deMoustier, 2003c). The two interpolation techniques used most frequently are kriging and triangulation.

Kriging was initially developed by D. G. Krige to estimate mining reserves in South Africa and, like most techniques, this method assumes some degree of continuity between interpolated variables. In this case, it is described by the semivariance calculated from data along a regular grid (Swan & Sandilands, 1995). Kriging interpolates irregularly spaced data onto a regular rectangular grid in order to define a smooth surface. Whilst this technique is relatively straightforward to implement computationally, is good for data with simple trends, and interpolates with a measure of error and confidence limits, it has the following disadvantages (deMoustier, 2003c).

- It does not necessarily honour the original data exactly.
- It may not deal with surface discontinuities in data very well, and may therefore, 'smooth out' any frontal system present.
- The selection of an appropriate region of influence is often difficult.
- The production of the regular rectangular grid requires a relatively evenly spaced grid of high-density isotropic data for optimum performance.
- It can lead to a bulls-eye effect of contours circling the control points.

Alternatively, the process of triangulation involves fitting a triangular irregular network, or TIN to the existing data set. Any number or distribution of control points can be tessellated by triangles, however randomly distributed. The result is that every point in an area is within, or on the edge of a triangle. The estimation of a new grid point value can then be undertaken using only the control points at the apices of the triangle within which it lies (Swan &

Sandilands, 1995). The preferred method of generating the TIN is Delaunay triangulation, a process in which the acuteness of the triangles is minimised. This function is available within the Surfer package.

Although triangulation requires a relatively large amount of storage space, and the generation of the TIN can be slow and computationally intense for large data-sets, it has the following advantages (deMoustier, 2003c):

- It fits all the data points exactly.
- Varying data densities are honoured more accurately than with regular rectangular grids, for example, kriging.
- Discontinuities in data are represented accurately.
- Contouring is nearly unambiguous.
- For contour map products, a better resolution of surface features is achieved as less low-pass filtering is applied compared with a regular rectangular grid.

Although each method of interpolation and gridding can produce its own brand of artefact, for example, the bulls-eye contours in the case of kriging, the best test of a method's validity is often whether the results make sense physically, and whether the variability is readily visible in the raw data (Emery & Thompson, 2001). Clearly, in representing visually the field data gathered for this study, there is a requirement to honour closely the original data with few artefacts. In particular, it is essential to be able to resolve water-mass discontinuities.

Triangulation has thus been chosen as the optimum gridding method in this case, as it will represent most accurately a frontal system on a two-dimensional contour plot.

All contour plots presented in this chapter have been prepared in the same way to allow a straightforward intercomparison of results to be undertaken (Figure 5.05). The grid spacing used for the gridding and interpolation process in Surfer was selected carefully to match that of the input data (the smoothed and interpolated raw data) as closely as possible. For example, the depth spacing of both the CTD and ADCP measurements had been fitted to a common 0.5 m depth grid (Section 4.7.1.) in the initial data processing stage, this same y-direction, or depth spacing being selected for the Surfer grid. In this way, minimal further data interpolation and smoothing has been undertaken, and control of the data quality has been maintained throughout. Contour plots have been produced using this methodology for each hour of tide, from one hour before low water (LW-1) to three hours after low water (LW+3), during both a spring and a neap tide.

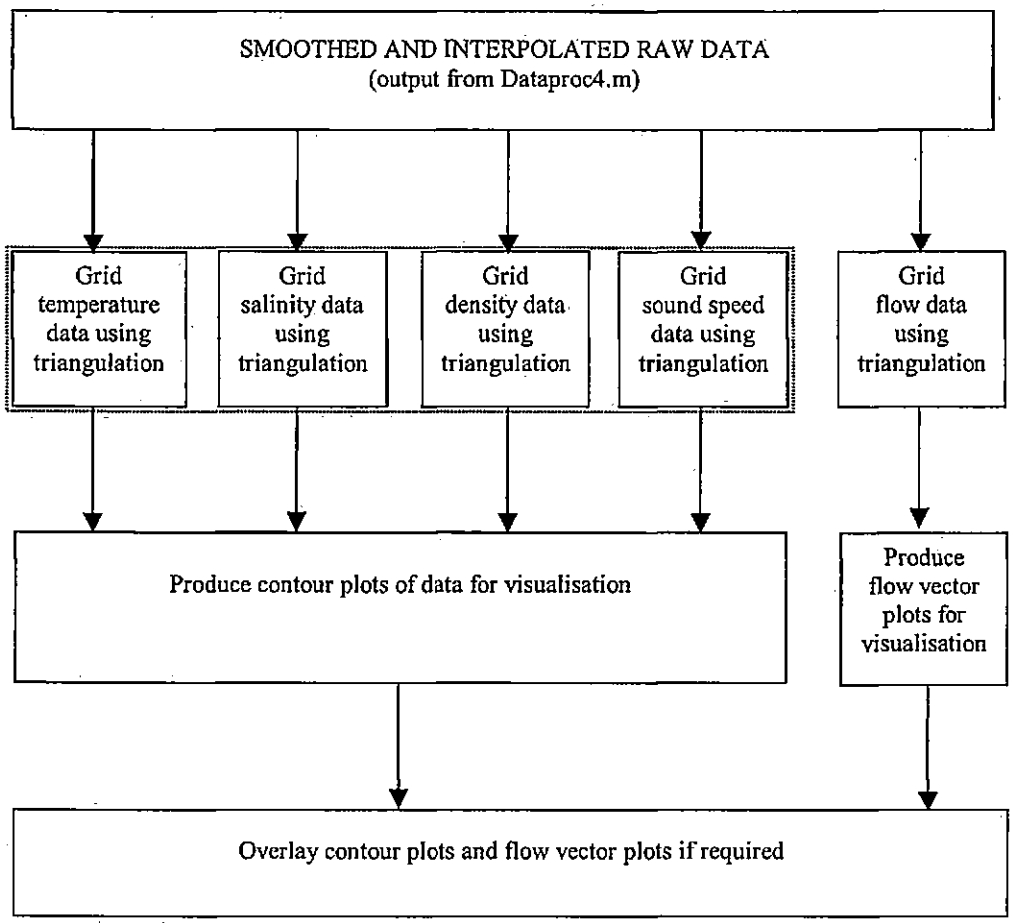

Figure 5.05. Flow diagram representing the gridding and contouring process involved in visually presenting CTD and flow velocity data using Surfer VII software.

For each hour of tide, a comprehensive selection of results is presented (Sections 5.3 and 5.4). Firstly, a bathymetric chart has been produced, illustrating the landward longitudinal track of the vessel whilst collecting the ADCP data. In addition, the CTD cast locations have been added to each chart, these being conducted on the return journey to seaward. Note that the chart has been rotated in this presentation, in order to orientate the channel in a direction similar to the longitudinal contour plots. It is straightforward, therefore, to correlate visually the data collection locations with the contoured data plots. Contour plots of temperature, salinity, density and sound speed are presented, each being colour coded for clear visual

assimilation, and again, linked to a bathymetric chart illustrating the data collection locations. The CTD cast number has been added above each contour plot in the correct location, this being the along-channel distance from Checkstone buoy, just outside the mouth of the Dart estuary. A final graphical plot overlays horizontal flow vectors on the contour plot of density to facilitate a detailed discussion of the hydrodynamics involved in frontal formation and decay. Positive vectors represent a flooding, landward flow, whilst negative vectors represent an ebbing, seaward flow. The constricted estuary mouth (narrowest point) is approximately 150 m from zero distance on each contour plot, with the seabed depression occurring between 350 m and 550 m. Finally, a data Table of the important hydrodynamic and dimensionless descriptors at each CTD cast location is presented.

5.2.4. Calculation of dimensionless descriptors

A comprehensive data Table is presented for each hour of tide, from one hour before low water (LW-1) to three hours after low water (LW+3), for a variety of important dimensionless descriptors, as discussed in Section 2.0. The calculation of these parameters has been undertaken using a Matlab routine, 'mixcalc2.m' (Appendix 3). Using smoothed and interpolated 'raw' data, this routine divides vertical profiles of density into two discrete layers, the interface between them being defined by the buoyancy frequency (N^2) maxima. Values of density and flow speed have been averaged within each layer using a Matlab trapezoidal integration routine to facilitate the calculation of the various frontal discriminators. A summary of the individual parameters presented for each hour of tide, their abbreviations, and the form of the equations used, is presented as a reference (Table 5.01).

Parameter	Abbreviation	Equation
Flow speed (upper layer) ms^{-1}	u_1	
Flow speed (lower layer) ms^{-1}	u_2	
Interface depth (m)	N^2_{max}	$N^2 = \frac{-g}{\rho}\frac{\partial \rho}{\partial z}$
Interfacial Froude number	Fi	$Fi = \frac{u}{\sqrt{(\Delta\rho/\rho)gh_1}}$
Layer Richardson number	Ri_L	$Ri_L = \frac{(\Delta\rho/\rho)gD}{u^2}$
Densimetric Froude number (upper layer)	F_1^2	$F_1^2 = \frac{u_1^2}{g'h_1}$
Densimetric Froude number (lower layer)	F_2^2	$F_2^2 = \frac{u_2^2}{g'h_2}$
Composite Froude number	G^2	$G^2 = F_1^2 + F_2^2$
Inflow Froude number	F_o^2	$F_o^2 = \frac{Q^2}{g'\overline{h}^3 b^2}$
Shear Froude number	F_Δ^2	$F_\Delta^2 = \frac{(u_1 - u_2)^2}{g'h}$
Density anomaly of upper layer	ρ_1	density ($kg\ m^{-3}$) -1000
Density anomaly of lower layer	ρ_2	density ($kg\ m^{-3}$) -1000

Table 5.01. Summary of individual parameters presented in results tables, their abbreviations, and the form of the equations used.

5.3. Spring tide

Contour plots of temperature, salinity, density and sound speed are presented from one hour before low water (LW-1) to three hours after low water (LW+3). Flow vector plots have also been produced for each hour of tide. In addition, a comprehensive Table of calculated dimensionless descriptors is presented.

Density and sound speed have been shown to be most affected by salinity, throughout the flooding spring tide. At LW-1 and LW, there was no visual manifestation of a frontal system. Density contours were relatively homogenous during this time, although a wedge of higher density water could be noted advancing towards the mouth of the estuary at LW. Flow vectors indicated a predominantly ebbing flow at LW-1, and an exchange flow occurring between estuarine and coastal waters at LW.

By LW+1, however, a tidal intrusion front had formed at the constricted mouth of the Dart estuary. This was clearly demarcated by a line of foam on the surface, and a change in colour and sea-surface roughness on either side of the frontal interface. The rougher, browner water, characterised by small breaking wavelets approximately 3-5 cm in height, was on the landward side of the tidal intrusion front. The greener, calmer surface waters were located on the seaward side (Plate 3.02). Density contours and flow vectors displayed a marked discontinuity across the frontal zone at this time, with a two-layer, stratified regime apparent landward of the frontal interface, and a homogeneous water column to seaward. At LW+2, the front had developed a more pronounced 'V'-shape, with the apex of the front having migrated downstream. The 'arms' of the front were still anchored to the shore at the narrowest part of the estuary (Figure 5.06). The density contours and flow vectors again showed a discontinuity

across the frontal zone, although there was some evidence of erosion of the pycnocline having taken place by this time. By LW+3, the visual manifestation of the front had all but disappeared, with only slight swirls and eddies of discoloured estuarine water being apparent at the surface, and two broken lines of foam apparent. The flow vectors and density contours had become relatively uniform throughout the transect at this time.

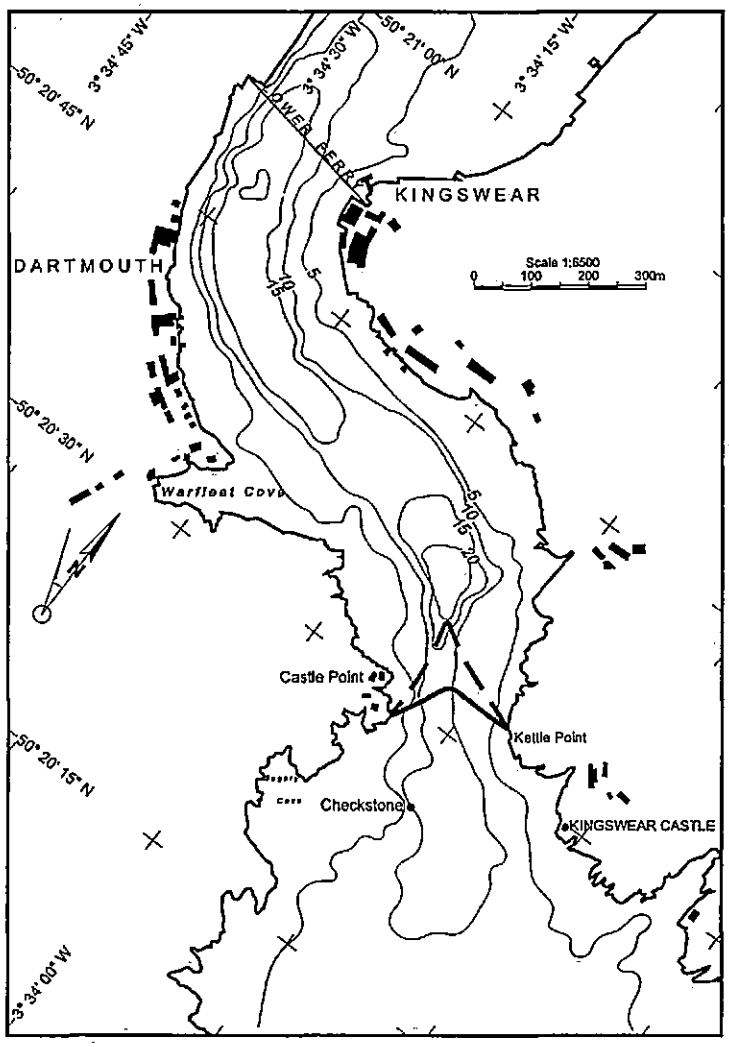

Figure 5.06. Visually observed positions of the tidal intrusion front at the mouth of the Dart estuary during a spring tide. Frontal positions on hour after low water (solid line) and two hours after low water (dashed line) are shown.

5.3.1. One hour before low water (LW-1)

There is very little change in temperature throughout the water column along the survey transect one hour before low water (LW-1), with only 0.25°C difference from one end of the transect to the other (Figure 5.07b). Contours of salinity (Figure 5.07c), however, indicate the beginnings of an intrusion of higher salinity water at depth, just outside the mouth of the estuary at distance -100 m. Density anomaly and sound speed contours (Figures 5.07d and 5.07e, respectively) are broadly similar in appearance to those of salinity. It is apparent, therefore, that salinity is the dominant factor affecting density and sound speed in the estuary at this time, as indicated in previous studies of the Dart at this time of year (Priestley, 1998). Flow vectors (Figure 5.07f) indicate a predominantly ebbing flow, with horizontal velocities of up to 0.6 ms^{-1} through the constricted mouth. A weakening of the outflow is apparent at depth just outside the mouth of the estuary at distance -100 m. This coincides with the intrusion of higher density seawater in this location, at the start of the flooding tide.

5.3.2. Low water

Temperature (Figure 5.08b) shows little change along the survey transect at low water (LW), with a negligible 0.25°C change over 1400 m. Salinity, however, displays a notable longitudinal gradient at the surface during this hour of tide (Figure 5.08c). A salinity of 34 is evident just seaward of Checkstone buoy, at distance -100 m, reducing progressively moving landwards along the transect, reaching a value of 30 near the Lower Ferry route. A basal intrusion of coastal water, with a salinity of 35 is apparent at the mouth of the estuary. Contours of density anomaly (Figure 5.08d) and sound speed (Figure 5.08e) are again similar in appearance to those of salinity, indicating that salinity predominates over temperature in affecting density at this time. Similarly to the salinity contours, sound speed reduces progressively to landward, with a value of 1488 ms^{-1} at Checkstone buoy, and 1482 ms^{-1} near the Lower Ferry. A vertical sound speed gradient of 5 s^{-1} is present just outside the estuary mouth. An artefact is evident in the sound speed contours (Figure 5.08e) just above the seabed, at distance +450 m, which is an example of the boundary effects which may sometimes occur when using a triangulation interpolation procedure to produce a grid for contouring (Section 5.2.3.). The flow vectors (Figure 5.08f) indicate the presence of an outflow in the surface layer, a basal inflow current, with net outflow at the mouth at this stage of the tidal cycle.

5.3.3. One hour after low water (LW+1)

By one hour after low water (LW+1) there is a notable discontinuity in the density anomaly contours (Figure 5.09d) just inside the estuary mouth, with a change in value from 26 kg m^{-3} to 24 kg m^{-3} in less than 100 m. This corresponds to the location of the visual manifestation of the tidal intrusion front. There was a narrow line of foam on the surface, and a change in colour and sea surface roughness on either side of the front noted when taking the field measurements. The coxswain of the survey vessel reported significant lateral shear when traversing the front, requiring considerable skill at the wheel to remain on course. The calmer waters, greener in colour and more transparent, were found on the seaward side of the front. Small breaking wavelets, approximately 3-5 cm in height were recorded on the landward side, where the water was browner in colour and more turbid. This colour and roughness change across the frontal zone is characteristic of such a system, and has been reported by numerous other researchers (e.g. Simpson & Nunes, 1981; Huzzey, 1982; Largier, 1992; Dyer, 1997; Brubaker & Simpson, 1999).

The density changes in the estuary are driven by changes in salinity (Figure 5.07c) as opposed to temperature (Figure 5.09b), a reduction in salinity from 34 to 31 being recorded across the frontal zone. The presence of this front at the mouth creates a well-mixed, homogeneous layer upstream of the mouth, and a two layer regime downstream (Figure 5.09f), with the shape of the contours downstream of the front mirroring the bathymetry. The flow in the surface layer is almost still upstream of the front, forming a deep 'pool' of brackish, eddying water at the surface. Flow speeds in the lower layer increase markedly to 0.7 ms^{-1} in the seabed depression underneath this buoyant surface layer. Contours of sound speed (Figure 5.09e) also reflect the discontinuity in flow speed and density across the frontal zone, with a difference of 4 ms^{-1}

across the narrow frontal zone at this stage of the tidal cycle. It should also be noted that there is a significant vertical gradient in density downstream of the front of 8 kg m^{-4}.

5.3.5. Three hours after low water (LW+3)

By three hours after low water (LW+3) the visual manifestation of the front had all but disappeared, with only slight swirls and eddies of discoloured estuarine water being apparent at the surface. Two broken lines of foam were noted, one at the landward end of the seabed depression, and one at the seaward end of the 15 m depth contour further downstream. Temperature remains uniform throughout the transect at this time (Figure 5.11b) with measurements of salinity (Figure 5.11c) also indicating a broadly homogeneous water column. There is a slight dip in the contours around 900 m from Checkstone buoy, which may be indicative of the remainder of the front. This corresponds to the area where patches of foam and discoloured water were noted. Contours of density anomaly (Figure 5.11d) and sound speed (Figure 5.11e) also reflect this 'dip' in salinity at distance +900 m, indicating an isolated area of lower density water at the surface in this location. Flow vectors (Figure 5.11f) are fairly uniform throughout the transect at this time, although they do reduce to near-zero at the surface, within the aforementioned mass of lower density estuarine water.

5.4. Neap tide

Contour plots of temperature, salinity, density and sound speed are presented from one hour before low water (LW-1) to three hours after low water (LW+3). Flow vector plots have also been produced for each hour of tide. In addition a comprehensive table of calculated dimensionless descriptors is presented.

Density and sound speed have been shown to be affected by both changes in salinity and temperature during a flooding neap tide. No visual manifestation of the frontal system occurred during the neap tide, although there was an indication in the density anomaly contours of a sub-surface front forming over the seabed depression one hour after low water (LW+1). An extremely well-developed vertical density gradient was in evidence throughout the neap tide survey period. An ebbing flow was recorded at LW-1, and by LW, a weak outflow remained at the surface throughout the transect with net inflow characterising the lower layer beneath. Slightly higher flow speeds at LW+1, although at 0.3 ms^{-1}, still about half those recorded during spring tides, appeared to cause some erosion and mixing across the pycnocline. There was still net outflow in the surface layer inside the estuary during this time. Both surface and bottom layers were flooding by LW+2, with a slight reduction in the thickness of the buoyant surface layer. By LW+3, the vertical density gradient was still in evidence, although was less pronounced than earlier in the tidal cycle, and some thinning of the surface layer had taken place by this time.

5.4.1. One hour before low water (LW-1)

A slightly warmer layer of estuarine water is lying above the colder coastal waters at one hour before low water (LW-1). The surface water is some 0.75°C warmer, and is due to the relatively rapid, preferential heating of the shallower areas further up-estuary at this time of year (Priestley, 1998). On an ebbing tide, these warmer waters are carried out of the mouth as a buoyant surface layer, resulting in a shallow, well-developed thermocline at the mouth of the Dart. Longitudinally, the change in temperature is not as pronounced, being 0.75°C over more than 500 m (Figure 5.12b). The presence of the estuarine water as a thin surface layer also gives rise to an extremely well-developed halocline at the estuary mouth. A change in salinity from < 24 at the surface, to 34 at < 4 m depth (Figure 5.12c) drives the vertical density changes (Figure 5.12d) in conjunction with the thermocline. Horizontal gradients of salinity and density are not particularly strong, a steady change occurring in the latter of 11.5 kg m^{-3} in total over a horizontal distance of 1 km. Sound speed (Figure 5.12e) also changes rapidly with depth, typically being around 1479 ms^{-1} at the surface, and 1489 ms^{-1} at 4 m depth. Similarly to those of density, horizontal gradients in sound speed are not as marked as the vertical gradients. Flow vectors reveal the highest ebbing flow velocities present in the upper layer of around 0.4 ms^{-1}, with uniform flows in the homogeneous lower layer of < 0.1 ms^{-1}.

5.4.2. Low water

Very little changes along the survey transect between LW-1 and LW. The warmer, buoyant surface layer remains in position (Figure 5.13b) with contours of salinity affirming the continuing presence of the lower salinity estuarine waters (Figure 5.13c). Density thus changes rapidly with depth (Figure 5.13d), this pycnocline causing a similarly dramatic change in sound speed with depth (Figure 5.13e). A vertical difference of 11 ms^{-1} is noted through most of the survey transect, although again, the horizontal gradients are less distinct than the vertical. The flow vectors record a weak outflow at the surface down to 2-3 m, corresponding to the calculated position of the density interface, N^2_{max}. There is a basal inflow of coastal waters below this interface throughout the transect.

5.4.3. One hour after low water (LW+1)

By one hour after low water (LW+1) during the neap tide, there are few differences in measurements of temperature (Figure 5.14b) and salinity (Figure 5.14c) in comparison with those taken at low water. Salinity contours indicate an increased intrusion of higher salinity coastal waters (salinity = 35) at depth from –200 m to +700 m. A strongly developed thermocline and halocline remain evident just below the surface, a layer of lower salinity (18) and higher temperature (11°C) estuarine water affecting the top 3 m of the water column. This buoyant estuarine water has again created a sharp pycnocline near the surface throughout the survey transect (Figure 5.14d). This vertical change in density anomaly (from 14 kg m^{-3} to 26.5 kg m^{-3}) creates a pronounced vertical gradient in sound speed, values changing from 1473 ms^{-1} at the surface to 1489 ms^{-1} at < 4 m depth (Figure 5.14e). Flow vectors at LW+1 (Figure 5.14f) illustrate a weakening of the outflow in the surface layer to around 0.1 ms^{-1}, with stronger up-estuary flooding waters in the lower layer; flow velocities being in the order of 0.2 ms^{-1} - 0.3 ms^{-1} in this region. There is an indication in the lower layer flow vectors of an sub-surface front forming over the seabed depression at distance +400 m (Figure 5.14f), although this did not manifest itself at the surface.

5.4.4. Two hours after low water (LW+2)

There is some evidence of mixing having occurred across the halocline by two hours after low water (LW+2). Salinity at the surface is now approximately 27 throughout the transect (Figure 5.15c), compared with a value of 18 recorded one hour previously. The interface depth, N^2_{max}, remains approximately the same, however, with a salinity value of 34 at the base of the halocline. Contoured temperature results (Figure 5.15b) are virtually identical to those recorded at LW+1, with a steep thermocline remaining present near the surface. This thermocline, in combination with the near-surface halocline influences density (Figure 5.15d), creating a thin, low-density layer near the surface and a marked pycnocline at 2-4 m depth. Density anomaly has increased to around 21 kg m^{-3} near the surface by this hour of tide, compared with 14 kg m^{-3} one hour previously. The entire flow is now landward at this time, with flow speeds having increased to 0.5 ms^{-1} in the lower layer through the constricted section. Flow velocities in the upper layer are less than 0.3 ms^{-1}.

5.5. Gradient Richardson number

Values of gradient Richardson number (*Ri*) are presented as contour plots, during both a spring and a neap tide (Figures 5.17 and 5.18, respectively). The location of each CTD cast is presented above each separate contour plot, and no inference should be made as to the values of *Ri* outside the local area of each of these data collection positions (Section 2.4.1.). No horizontal anisotropy has been applied, therefore, during the preparation and gridding process for these diagrams, and thus they are not biased in any direction. Ensemble averaged gradient Richardson numbers have been used (*i.e.* flow speeds have been averaged over the 20 s ensembles recorded by the ADCP) in a similar manner to Peters (1999), and therefore, values of *Ri* presented here can only be related loosely to flow instability and mixing.

The grey shading within each contour plot represents areas where $Ri < 0.25$ implying that the flow is unstable, with turbulent mixing taking place in these areas. The white areas are where $Ri > 0.25$ indicating a laminar flow, with mixing dominated by entrainment occurring in these regions (Dyer & New, 1986; New *et al.*, 1986). There are a variety of threshold values for *Ri* which may be used (Section 2.4.1.). A value of 0.25 is used widely when the time-scale used for averaging is short, compared with the buoyancy period, $2\pi / N$, where N is the buoyancy frequency (Brubaker & Simpson, 1999). The ensemble averaging length of 20 s, in this instance, is less than the typical buoyancy period of > 60 s recorded during this study, therefore, a threshold value of 0.25 is appropriate. Contours of density have been overlayed on each contour plot of *Ri* to assist in the spatial identification of the front during spring tides, and in the depth of the pronounced density interface during neap tides.

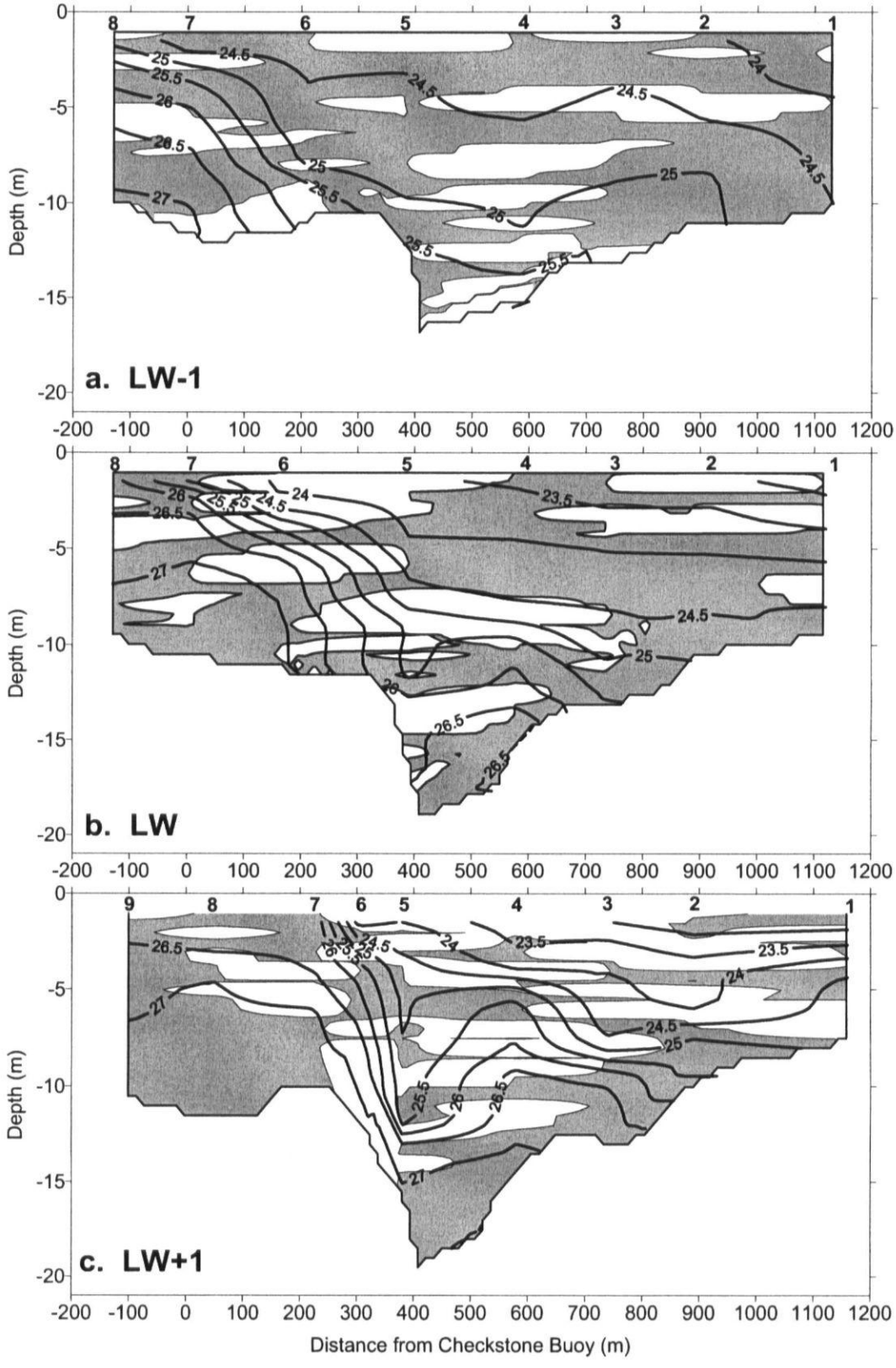

Figure 5.17 (a-c). Contours of gradient Richardson number (*Ri*) during spring tides.
Figure continues on the following page.

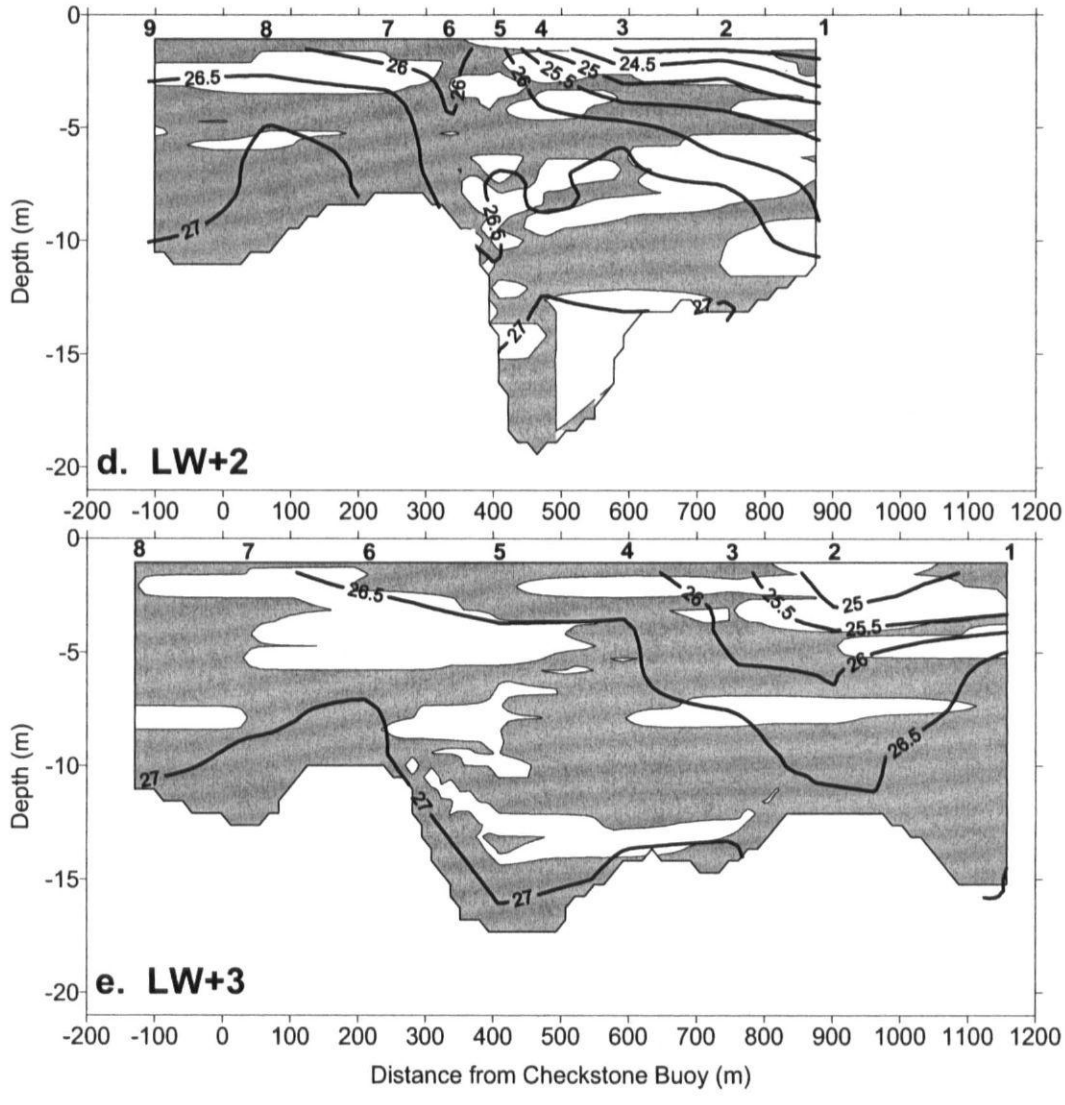

Figure 5.17. Contours of gradient Richardson number (Ri) during spring tides.
The grey shading represents areas where Ri <0.25, implying instability and mixing. Conversely, the white areas are where Ri >0.25 implying stability. Density anomaly contours (heavy black lines) are overlayed in intervals of 1 kg m^{-3} in each case.

During spring tides, estimates of the gradient Richardson number are highly variable (Figure 5.17). At LW (Figure 5.17b), there is evidence of stability near the surface around CTD casts five and six, and across the developing frontal interface at depth. By LW+1, when the tidal intrusion front is present, $Ri > 0.25$ across the frontal zone, indicating the relative stability of the front in the near-surface region. There are instabilities indicated across the frontal interface (where $Ri < 0.25$) at mid-depth, and again near the bed. The existence of a pycnocline downstream of the front is well-resolved, as $Ri > 0.25$ throughout this area at LW+1 and LW+2 (Figures 5.17c-d). By LW+3, when decay of the front had taken place, $Ri < 0.25$ at the majority of the measuring stations, indicating turbulent flow (Figure 5.17e). There are still areas of stability indicated during this hour of tide, particularly at the surface around CTD cast two, where the presence of a lower density pocket of water at the surface gives rise to a well-developed pycnocline beneath.

Estimates of Ri during neap tides indicate a highly stratified water column persisting from LW-1 to LW+3 (Figure 5.18). At the surface along the whole length of the transect, $Ri > 0.25$ identifying stable, laminar flows (with mixing dominated by entrainment) in the pronounced pycnocline in the first few metres of the water column. This stable area appears deepest at LW-1 (Figure 5.18a), becoming progressively shallower with the flooding tide. Below this stably stratified surface zone, results are somewhat mixed, with areas of stable, laminar flows indicated ($Ri > 0.25$) interspersed with well-mixed, turbulent zones ($Ri < 0.25$). Some contouring artefacts are present near the bed between casts one and five, an unavoidable side-effect at some boundaries when creating interpolated grids using triangular irregular networks.

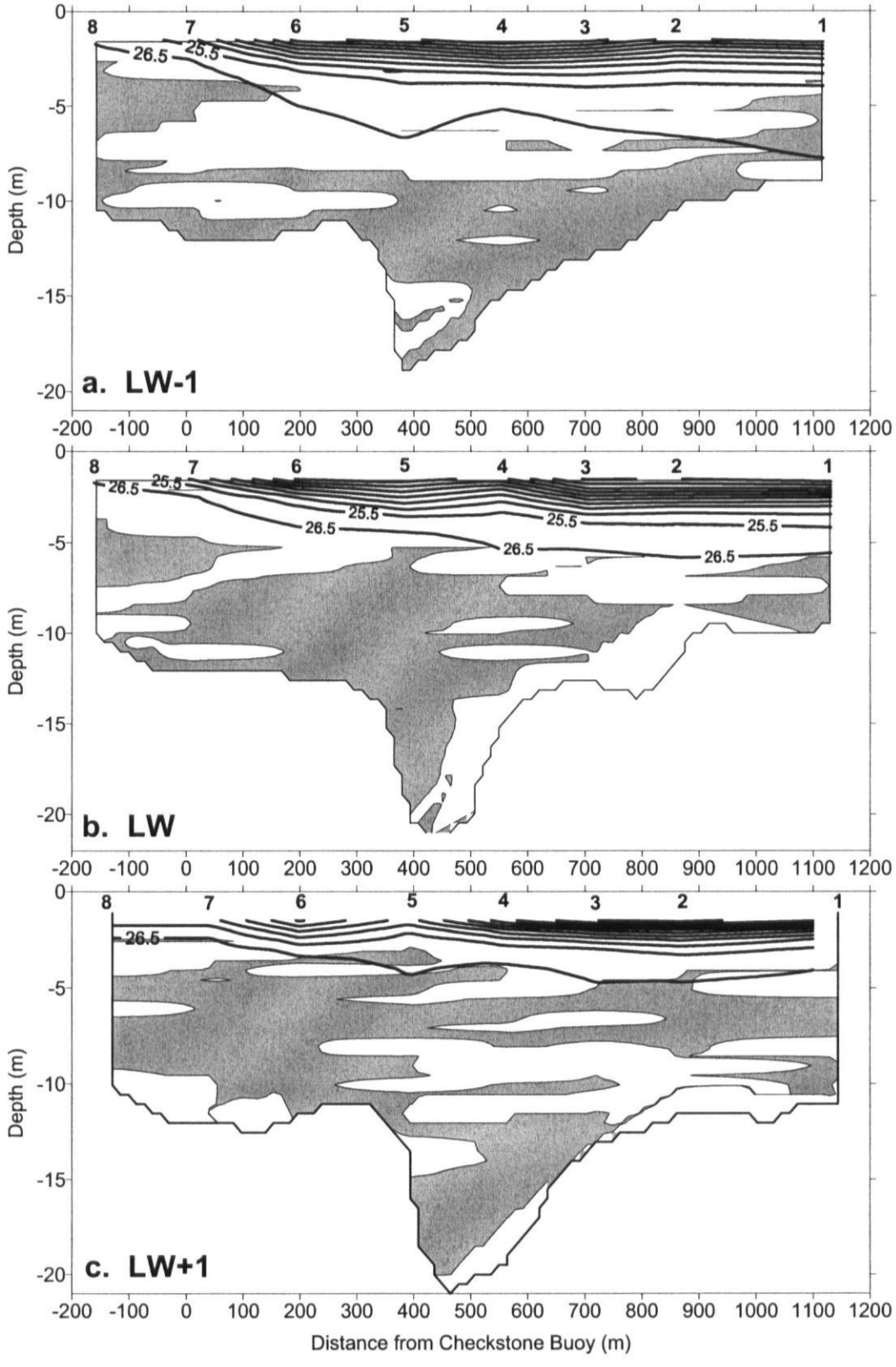

Figure 5.18 (a-c). Contours of gradient Richardson number (*Ri*) during neap tides.
Figure continues on the following page.

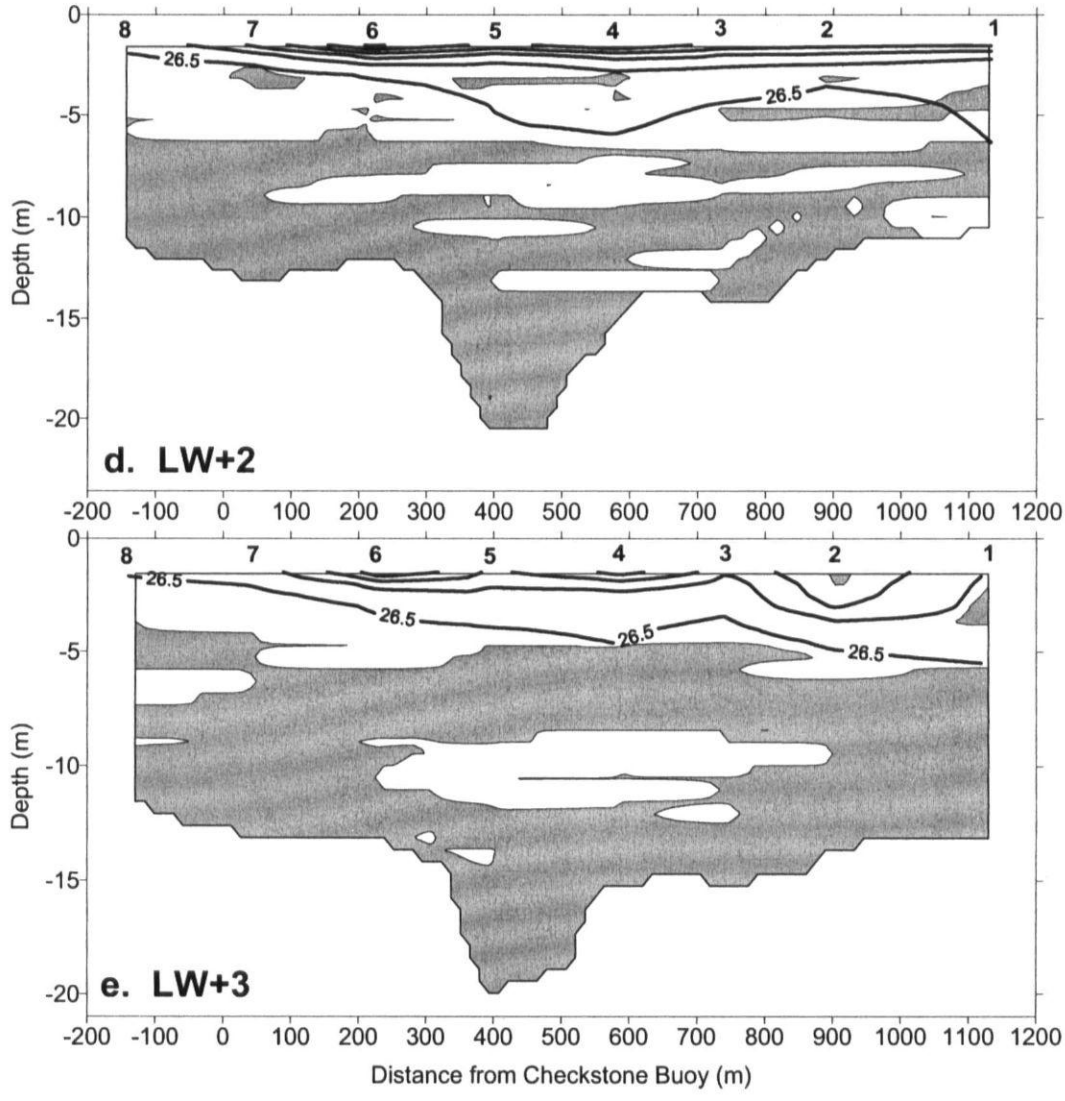

Figure 5.18. Contours of gradient Richardson number (*Ri*) during neap tides.
The grey shading represents areas where $Ri < 0.25$, implying instability and mixing. Conversely, the white areas are where $Ri > 0.25$ implying stability. Density anomaly contours (heavy black lines) are overlayed in intervals of 1 kg m^{-3} in each case.

6.0. Formation of a tidal intrusion front in the Dart estuary: A discussion

6.1. Chapter overview and summary

During spring tides, there is a visual manifestation of a tidal intrusion front at the mouth of the Dart estuary for approximately 2 hours, starting one hour after low water (LW+1). At LW, two-way horizontal exchange flow is present, although the thickness of the upper layer indicates that the buoyant outflow at the surface is partially arrested (but not blocked) at this time and, therefore, sub-maximal exchange flow is occurring. The front occurs at LW+1, as the morphology of the constricted mouth of the Dart estuary is such that a hydraulic control point is created. The flow becomes supercritical as it passes through the constricted mouth, undergoing a hydraulic jump as estuary cross-sectional area increases over a depression in the seabed. At this point, the buoyant estuarine outflow is arrested. In order to maintain continuity, the dense inflowing water plunges beneath this static surface layer, gaining velocity as it is compressed between the upper layer and the seabed. The critical flow speed required in order to arrest the buoyant outflow has been found to be identical to that predicted by hydraulics theory. The density stratification at, and downstream of the frontal interface is sufficient to suppress turbulent mixing, and hence the stratification persists for a time, with the front remaining spatially stable. As barotropic forcing increases at LW+2, the plunge depth increases, and the front migrates downstream, over the increasing depth of the seabed depression. As the tidal velocity increases further, exacerbated by enhanced baroclinic forcing due to the pronounced horizontal density stratification, interfacial shear dominates. The enhanced shear eventually overcomes the stratification, resulting in the rapid decay of the front.

During spring tides, the flow at the mouth is shown to exhibit similar behaviour as if flowing over a sill. The constriction at the mouth, followed by the abrupt increase in depth (and cross-sectional area) at the seabed depression creates a similar topographical situation to two-layer flow over the lee side of a sill at the mouth of a fjord, or bar-built estuary. The contraction at the narrow mouth is unlikely to influence the inflow greatly, as the flow in the upper layer is weak on the flooding tide, and therefore the control exercised by the contraction is weak. The seabed depression (the 'sill') will have the greater effect at this time, as the lower layer interacts directly with the changes in bathymetry which protrude into this active lower layer.

During neap tides, there is no visual manifestation of the front. Tidal straining exacerbates the stratification on the ebb, and lower flow velocities are not high enough to arrest the buoyant outflow from the estuary. Turbulence is highly suppressed by the pronounced stratification at this time, maintaining two-layer exchange flow intact for much of the flooding tidal cycle. The lower layer remains subcritical throughout the flooding tide and, therefore, no topographic control is exercised by the seabed in this case. The low flow velocities do not allow the formation of a hydraulic control point, and the front does not appear.

The composite Froude number (G^2) derived from the densimetric Froude numbers for each layer in a two-layer flow situation, has proved to be an accurate frontal discriminator. Additionally, the inflow Froude number (F_0^2) has proved to be invaluable in ascertaining the existence of a hydraulic control point, and quantifying whether the control occurred at the constriction, or upstream or downstream of it. The shear Froude number (F_Δ^2) was found to be the best and most accurate discriminator of frontal location, in addition to quantifying the magnitude of interfacial mixing. Conversely, the gradient Richardson number (Ri), interfacial

Froude number (Fi), and the closely related layer Richardson number (Ri_L) have not proved to be accurate frontal discriminators.

This chapter begins with a detailed analysis and discussion of the formation and dynamics of the tidal intrusion front in terms of the appropriate dimensionless descriptors. The latter part of this chapter (Section 6.3) combines the insights gained from this dimensionless analysis together with an examination of the hydrodynamic and mixing processes to form a comprehensive picture of frontal formation and decay in the Dart estuary during spring tides, and account for the non-appearance of the front during neap tides.

6.2. A dimensionless analysis of the Dart estuary tidal intrusion front

A clear tidal intrusion front was noted to appear at the entrance to the Dart estuary at one hour after low water (LW+1) on a flooding spring tide. The front was noted to move further downstream approximately 50 m by LW+2, before disappearing abruptly. The front was not observed to form during neap tides.

The entrance to the Dart estuary is characterised by a constriction in the channel, commencing approximately 150 m from the reference point of Checkstone buoy, moored just outside the entrance to the estuary. The constricted section is approximately 150 m in length, and is followed by an abrupt increase in bathymetry, caused by an elongated seabed depression, about 250 m in length (Figure 3.03). The apex of the front was noted to form at the seaward end of this seabed depression, with the 'arms' of the front being anchored to the estuary sides further upstream (Figure 6.01). As the flooding tide increased in magnitude, the apex migrated further downstream, over the increasing depth of the seabed depression. It appears,

therefore, that the formation of the front at spring tides is linked intimately with the bathymetric changes at the mouth of the Dart estuary. The constriction at the estuary mouth may be sufficient to provide a point of hydraulic control on the flow. An internal hydraulics analysis of the flow will enable the identification of any such control point, and will provide further insights into frontal formation and behaviour.

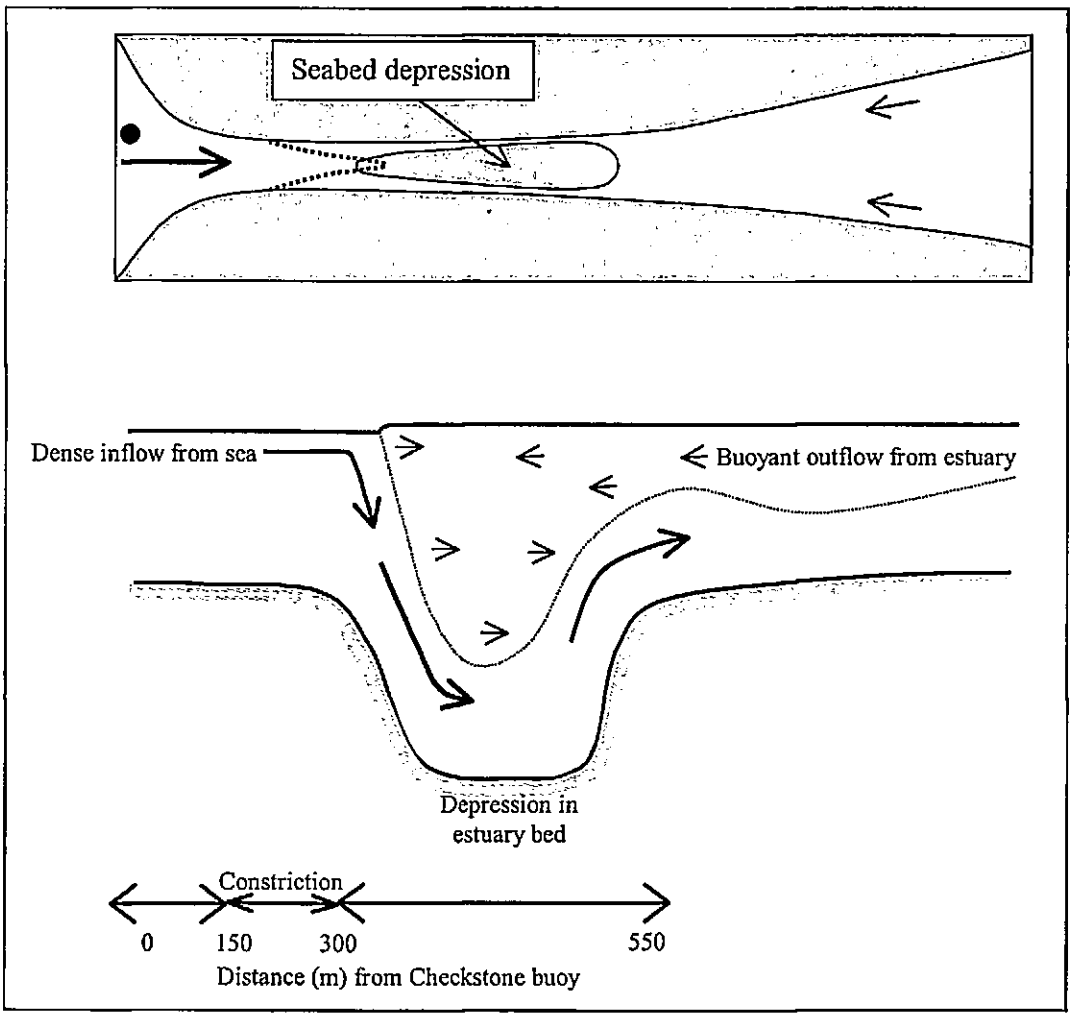

Figure 6.01. Schematic representation of the formation of a tidal intrusion front at the mouth of the Dart estuary. The plan view (top) shows Checkstone buoy (filled circle), and frontal interface shape referenced to the seabed depression (shaded). The elevation (bottom) shows the plunging inflow over the seabed depression.

6.2.1. Hydraulic control and mixing - spring tide

At one hour before low water (LW-1), the inflow Froude number, $F_o^2 = 3.5$ at the constriction (Figure 6.02), and as $F_o^2 > 3$, no denser water intrudes at this time (Farmer & Armi, 1986). It should be noted, however, that as F_o^2 is a squared parameter, it cannot discriminate that net *outflow* exists at this stage of the tidal cycle. The shear Froude number, F_Δ^2, is sub-critical throughout the majority of the transect (Figure 6.03). There must clearly be minimal shear occurring between the two layers at this stage of the tidal cycle, as they have very similar flow velocities and density values, and the interface between them is not well defined. The relatively shallow depth at the constriction does cause F_Δ^2 to become mildly supercritical in this area ($F_\Delta^2 = 1.2$), however, indicating a well-mixed water column. In addition, a critical value of F_Δ^2 at approximately 800 m, may indicate flow on the brink of instability just ahead of a further increase in bathymetry (Figure 5.07a).

The interfacial Froude number (Fi) is supercritical through the constricted mouth of the estuary, and generally subcritical landward of the constriction (Figure 6.04). This implies a broadly homogeneous flow through the narrow channel constriction, with the maintenance of a stratified regime inside the estuary mouth. Similarly, values of the layer Richardson number ($Ri_L < 2$) throughout the majority of the transect (Figure 6.05) indicate a relatively well-mixed water column, with further mixing dominated by bottom generated turbulence at this stage of the tidal cycle (Dyer, 1997).

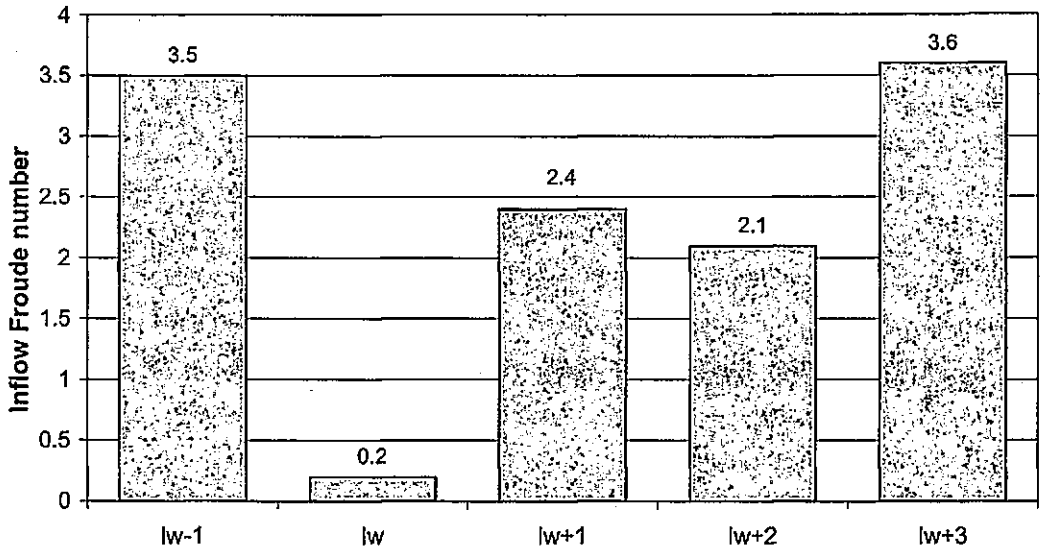

Figure 6.02. Variations in the inflow Froude number (F_o^2) at the constriction at the mouth of the Dart estuary during a spring tide.

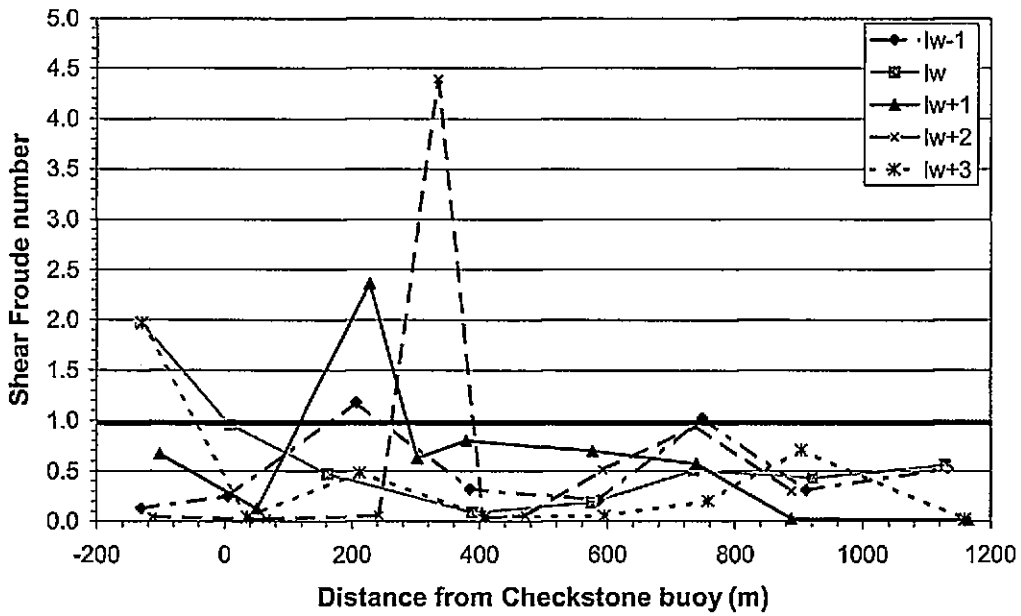

Figure 6.03. Variations in the shear Froude number (F_Δ^2) during a spring tide.
The constriction exists between 150 m and 300 m. The depression in the estuary bed exists from 300 m to 550 m.

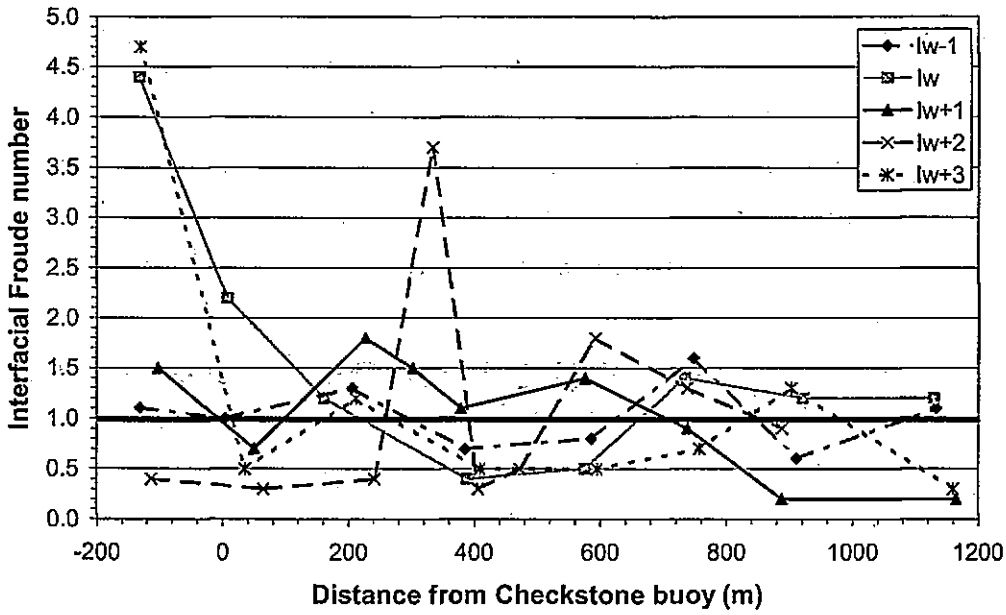

Figure 6.04. Variations in the interfacial Froude number (*Fi*) during a spring tide
The constriction exists between 150 m and 300 m. The depression in the estuary bed exists from 300 m to 550 m.

At low water (LW), $F_0^2 = 0.2$ at the constriction (Figure 6.02), therefore the outflow is not blocked, and two-way exchange flow (between estuarine and coastal water) is possible. Maximal horizontal exchange flows can only occur if the lower layer thickness, $y'_{2o} = 0.375$ of the water depth at the shallowest section over a sill, or $y'_{2o} = 0.5$ of the water depth through a contraction (Farmer & Armi, 1986; Chao & Paluszkiewicz, 1991). Here, $y'_{2o} = 0.33$, hence *sub*-maximal two-way flow is occurring, *i.e.* the seaward flow in the upper layer is partially arrested at this stage of the tidal cycle. This corresponds to Figure 2.09d, the 'moderate' inflow condition, where $-U_i < U_o$, where $-U_i$ is the limiting condition (where the buoyant outflow is blocked), and U_o is barotropic forcing. With regard to the vertical stability at this stage of the tidal cycle, $F_\Delta^2 = 0.5$ at the constriction, with supercritical values (implying

mixing) outside the mouth, and subcritical values (stratification) inside the mouth (Figure 6.03).

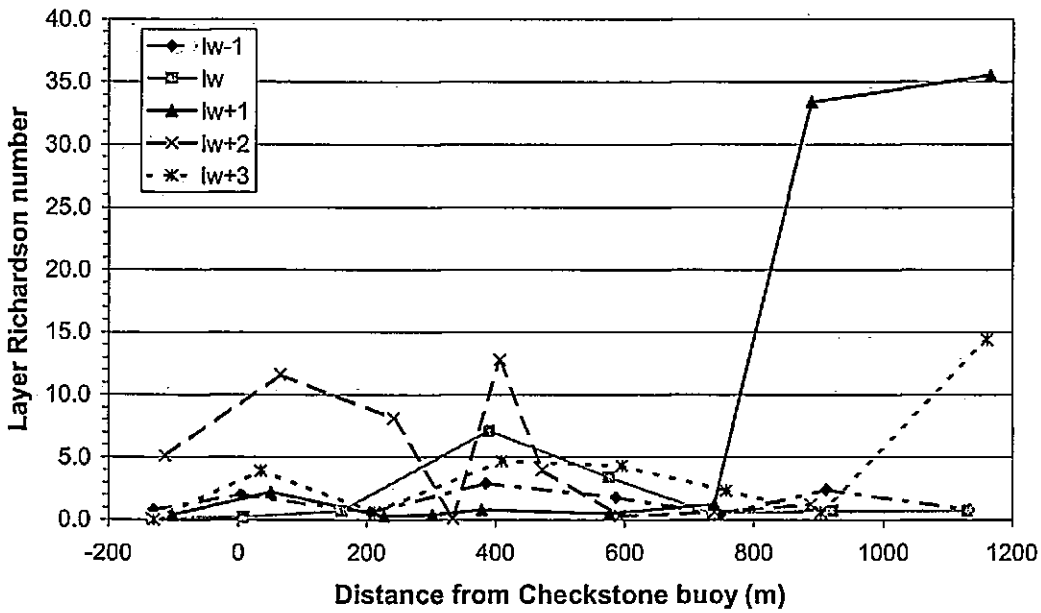

Figure 6.05. Variations in the layer Richardson number (Ri_L) during a spring tide
The constriction exists between 150 m and 300 m. The depression in the estuary bed exists from 300 m to 550 m.

Supercritical values of *Fi* at LW, apart from at the depth increase at casts five and four imply a broadly homogeneous flow (Dyer, 1997). Being related closely to *Fi*, it is unsurprising to find $Ri_L > 1$ over the bathymetric increase, and $Ri_L < 1$ elsewhere. The implication is of fully developed mixing in the shallower areas, dominated by bed shear, with less mixing in the deeper areas, these areas likely to be limited by interfacial shear (Lewis, 1997).

By one hour after low water (LW+1), when the tidal intrusion front is present, F_o^2 = 2.4 (strong inflow) at the constriction (Figure 6.02). The buoyant outflow is blocked, therefore, and as critical conditions can no longer be satisfied at the most constrictive section, a virtual control and plunge point must occur downstream. The apex of the front is thus found downstream of the mouth. This corresponds to Figure 2.09h, for two-layer flows over a sill and through a contraction. A value of F_Δ^2 = 2.4 at the constriction indicates that significant mixing is occurring in this location, just prior to the inflow plunging (Figure 6.03). Immediately downstream of the frontal interface, however, $F_\Delta^2 < 1$ implying stability in this area. This stability is controlled largely by the strong density difference between the upper and lower layers at, and downstream of the front. Thus, stratification is persistent in these areas, and the front is spatially stable.

Values of *Fi* at LW+1 are variable, becoming supercritical through the constriction as the flow speeds up in this area, with no change from supercritical to subcritical as the front is traversed (Figure 6.04). Only much further up the estuary, at about 700m from Checkstone buoy, is *Fi* < 1. Observed patterns in Ri_L are similar, with no clear indication in the data as to the presence of the front. The broadly subcritical values imply that fully developed mixing should be in evidence throughout the transect (Dyer, 1997). This is clearly not the case in this instance, as a two-layer, stratified regime is evident upstream of the frontal interface.

At LW+2, the front is still present, although it has migrated slightly further downstream by this time. F_o^2 = 2.1 at the constriction, still in the strong inflow regime, implying that a virtual control and plunging will continue to occur downstream of the constriction. F_Δ^2 is again supercritical (F_Δ^2 = 4.4) just upstream of the plunge point, and subcritical throughout the

remainder of the transect (Figure 6.03). This indicates continuing strong mixing and instability just upstream of the plunge point, with the stratification persisting elsewhere, resulting in a spatially stable front. It appears, therefore, that the reduction in flow speed at the depth increase just inside the mouth (due to the increase in cross-sectional area) leads to the formation of a stationary hydraulic jump, the attendant mixing at, and downstream of the jump driving the gradual erosion of the vertical density interface. Values of Fi and Ri_L are highly variable throughout the survey transect at this time (Figures 6.04 and 6.05 respectively). There is evidence of Fi changing from critical to subcritical across the frontal interface (between casts five and six), lending further credence to the existence of a hydraulic jump in this location. When viewed in isolation, however, the variability in this parameter along the remainder of the survey transect makes its reliability questionable. The maximum transect value of $Ri_L = 12.8$ just downstream of the frontal zone implies increasingly active mixing in this area, dominated principally by interfacial shear, and the presence of internal waves.

By LW+3, $F_o^2 = 3.6$ at the constriction, implying that the plunge point should be well downstream. Subcritical values of F_Δ^2 within the estuary imply that the estuary has become well-mixed at this time, with no further mixing taking place. $Fi > 1$ at the constricted mouth (cast six) and at cast two, suggesting a change in state of the flow, with intense mixing in these locations. $Ri_L < 1$ in these areas, highlighting the increasing role played by bed shear in promoting mixing at this stage of the tidal cycle.

6.2.2. A composite Froude number analysis – spring tide

One hour before low water (LW-1) the densimetric Froude number of the upper layer, F_1^2, is supercritical throughout the estuary entrance (Figure 6.06). These supercritical values are due to the rapid current flow, and minimal density difference between the two layers. The maximum $F_1^2 = 17.4$ at the seaward end of the transect (Table 5.02) is caused by a very shallow upper layer depth, combined with a rapid flow speed in this buoyant layer. The densimetric Froude number of the lower layer, F_2^2, shows greater variability than the upper layer, although it is supercritical at the constriction. The composite Froude number, G^2, is supercritical throughout the transect, due to the influence of F_1^2. The supercritical values of this parameter represent a broadly homogenous, well-mixed water column, with the upper layer controlling the flow at this point, due to the stronger flows in the upper region of the water column. At this stage of the tidal cycle, the end of the ebb, the flow in the lower layer is already weakening prior to the commencement of the flood (visible in the recorded flow vectors, Figure 5.07f).

At low water (LW), F_1^2 is supercritical throughout the constriction (Figure 6.07), with an abrupt change to subcritical over the seabed depression (at distance +389 m and +575 m). This change is due to the increased depth (increasing cross-sectional area, causing a reduction in flow speed) in these locations. Subcritical values of F_2^2 are notable throughout the transect, with many locations having values of zero, or near zero due to the low flow velocity in the flooding, basal layer. Values of G^2 are driven, therefore, by changes in the active, upper layer at this stage of the tidal cycle.

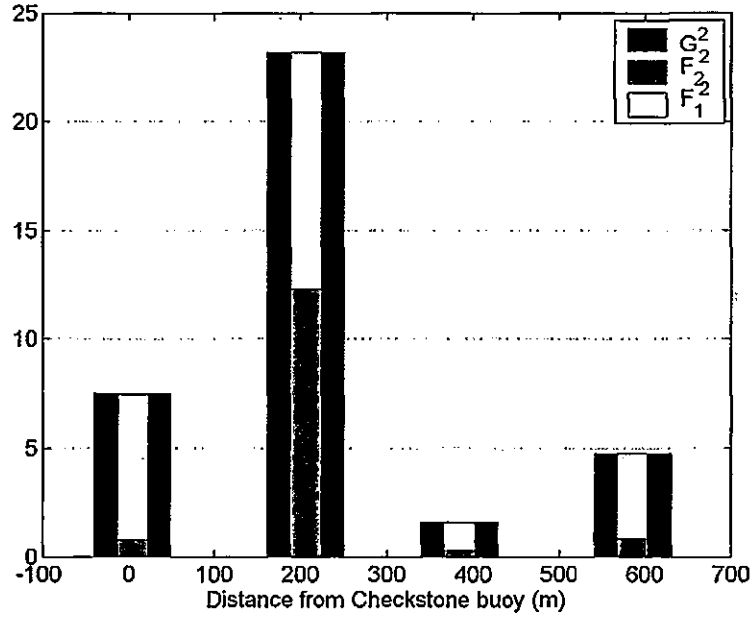

Figure 6.06. Variations in the composite Froude number, G^2 (comprising the densimetric Froude number for the upper and lower layers, F_1^2 and F_2^2 respectively) at the estuary entrance during a spring tide at LW-1. The constriction exists between 150 m and 300 m. The depression in the estuary bed exists from 300 m to 550 m.

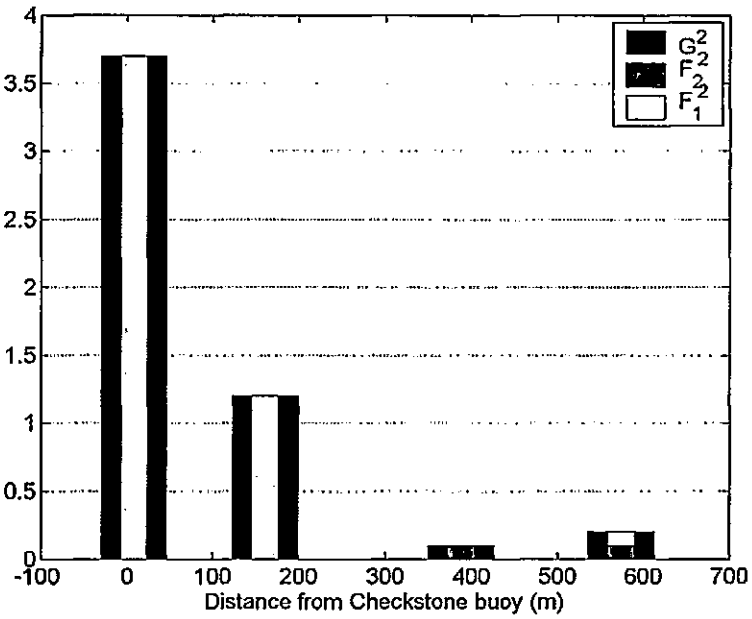

Figure 6.07. Variations in the composite Froude number, G^2 (comprising the densimetric Froude number for the upper and lower layers, F_1^2 and F_2^2 respectively) at the estuary entrance during a spring tide at LW. The constriction exists between 150 m and 300 m. The depression in the estuary bed exists from 300 m to 550 m.

By one hour after low water (LW+1) a supercritical value of G^2 at the constriction is driven largely by the higher flow speeds in the lower layer increasing the value of F_2^2 (Figure 6.08). At the seaward end of the seabed depression, G^2 reduces abruptly to a critical value of 1.0, with the upper layer being blocked ($F_1^2 = 0$) and the lower layer (F_2^2) thus also having a critical value of 1.0. The flow plunges at this point, with the abrupt decrease in the value of G^2 implying the presence of a hydraulic jump. The blocking of the upper layer increases its thickness, which correspondingly reduces the thickness of the lower layer. The velocity of the plunging inflow increases, therefore, as it is compressed between the upper layer and the seabed, in a similar manner to that described by Chen *et al.* (1994). It is possible that this is exacerbated by the transfer of kinetic energy from the arrested upper layer to the lower layer at the plunge point, further increasing the speed of the lower layer, and making it supercritical downstream of the constricted area. The plunging flow is therefore controlled mainly by the transition of the *lower layer* to a critical flow state at this location, with the upper layer being inactive ($F_1^2 = 0$) at this stage of the tidal cycle.

Two hours after low water (LW+2), F_1^2 is supercritical upstream (seaward) of the frontal interface (Figure 6.09) and generally subcritical downstream. A similar pattern is evident in the lower layer, with an abrupt reduction in flow speed at the seaward end of the seabed depression just inside the mouth. Hence G^2 is supercritical in all locations upstream of the plunge point, driven mainly by the high flow speeds in the lower layer. Across the frontal zone, G^2 reduces abruptly from supercritical ($G^2 > 80$) to zero, implying a strong hydraulic jump. This jump is likely to increase mixing across the two vertical layers and cause the erosion of the pycnocline evident in the density contours.

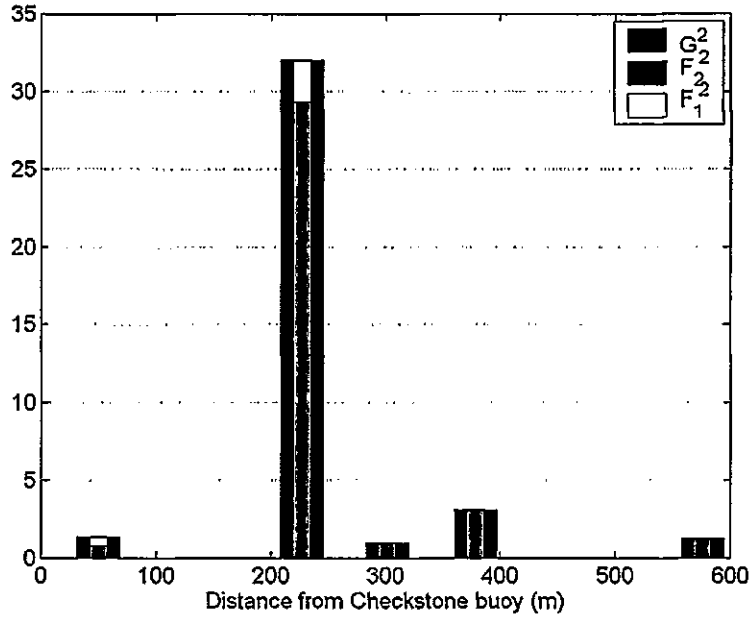

Figure 6.08. Variations in the composite Froude number, G^2 (comprising the densimetric Froude number for the upper and lower layers, F_1^2 and F_2^2 respectively) at the estuary entrance during a spring tide at LW+1. The constriction exists between 150 m and 300 m. The depression in the estuary bed exists from 300 m to 550 m. Note the reduction of G^2 to unity at 302 m, corresponding to the location of the tidal intrusion front.

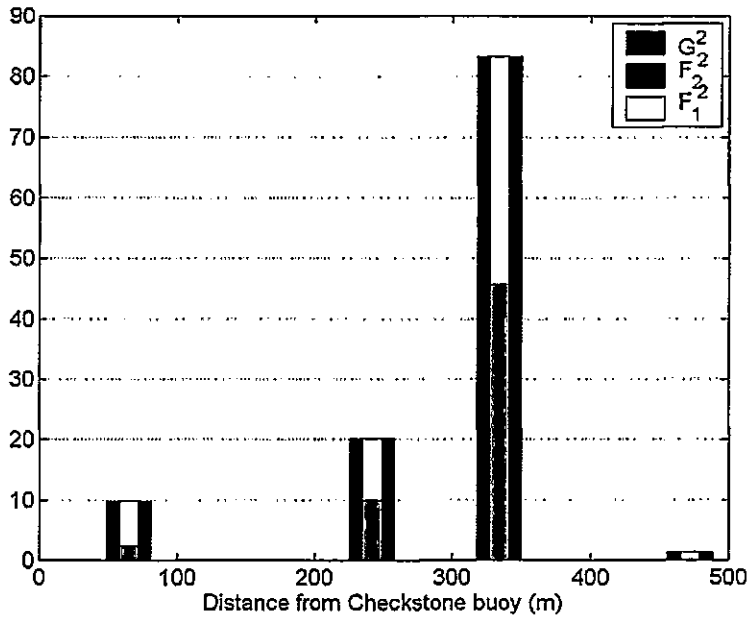

Figure 6.09. Variations in the composite Froude number, G^2 (comprising the densimetric Froude number for the upper and lower layers, F_1^2 and F_2^2 respectively) at the estuary entrance during a spring tide at LW+2. The constriction exists between 150 m and 300 m. The depression in the estuary bed exists from 300 m to 550 m.

By three hours after low water (LW+3), F_1^2 is supercritical throughout the estuary entrance due to the higher flow velocities at this stage of the tidal cycle (Table 5.06). F_2^2 is also supercritical, apart from $F_2^2 = 0.9$ at distance +409 m, where the increase in depth (and hence cross-sectional area) reduces flow speed. The generally supercritical values of G^2 (due to the higher flow rates) indicate that the hydraulic control point has become flooded and disappeared (Denton, 1987). It appears, therefore, that the estuary mouth area has become well-mixed at this time. The subcritical values of F_Δ^2 within the estuary (Figure 6.03) add further credence to this, implying that no further mixing is taking place.

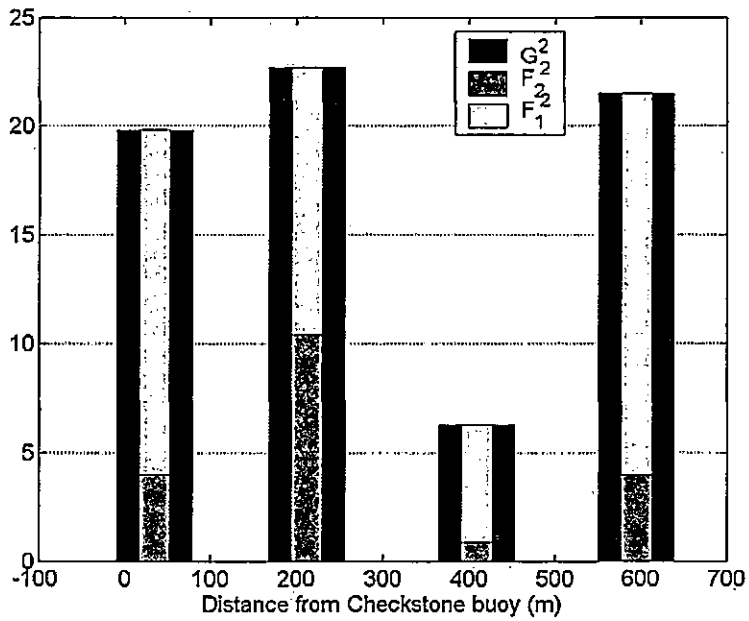

Figure 6.10. Variations in the composite Froude number, G^2 (comprising the densimetric Froude number for the upper and lower layers, F_1^2 and F_2^2 respectively) at the estuary entrance during a spring tide at LW+3. The constriction exists between 150 m and 300 m. The depression in the estuary bed exists from 300 m to 550 m.

6.2.3. Hydraulic control and mixing - neap tide

At one hour before low water (LW-1), the inflow Froude number, $F_o^2 = 0.02$ at the mouth (Figure 6.11). The outflow is not blocked, therefore, and two-way exchange flow is possible (Farmer & Armi, 1986). Subcritical values of the shear Froude number, F_Δ^2 range from 0 to 0.1 inside the estuary, increasing to a maximum of 0.5 just outside the mouth. This confirms a high degree of stratification present together with little shear or mixing between the layers (Figure 6.12). The interfacial Froude number, *Fi* is generally supercritical to seaward of the estuary mouth, and subcritical landward of the mouth (Figure 6.13). Well-mixed conditions outside the estuary are implied, therefore, with a stratified regime inside the mouth. The presence of a weak hydraulic jump between the supercritical and subcritical areas of *Fi* is suggested, although there is little evidence for this in the results from the other dimensionless descriptors presented here. The majority of the values of the layer Richardson number (Ri_L) through the constriction, and landward of the constriction are $20 > Ri_L > 2$, indicating that slight mixing is occurring at this time (Figure 6.14).

At low water (LW), little appears to change at the estuary entrance from the previous hour of tide, with $F_o^2 = 0.02$ at the constriction at this time (Figure 6.11). Again, as the outflow is not blocked, two-way exchange flow between estuarine and coastal waters is confirmed. As the lower layer thickness, $y'_{2o} = 0.9$ of the water depth, distinct sub-maximal two-way flow is occurring. Extremely low (subcritical) values of F_Δ^2 (Figure 6.12) affirm the high degree of stratification present at this time, indicating little shear or mixing occurring between the layers. *Fi* is generally supercritical through the constriction at this time, and subcritical further downstream (Figure 6.13). Again, this implies well-mixed conditions existing through the constricted section, with a stratified regime inside the mouth, and a weak hydraulic jump

between the two areas. The large vertical density difference between the layers inside the estuary, combined with lower flow speeds is again maintaining a stable density interface, with the supercritical Ri_L results to landward of the mouth (Figure 6.14) suggesting a degree of mixing dominated by interfacial shear.

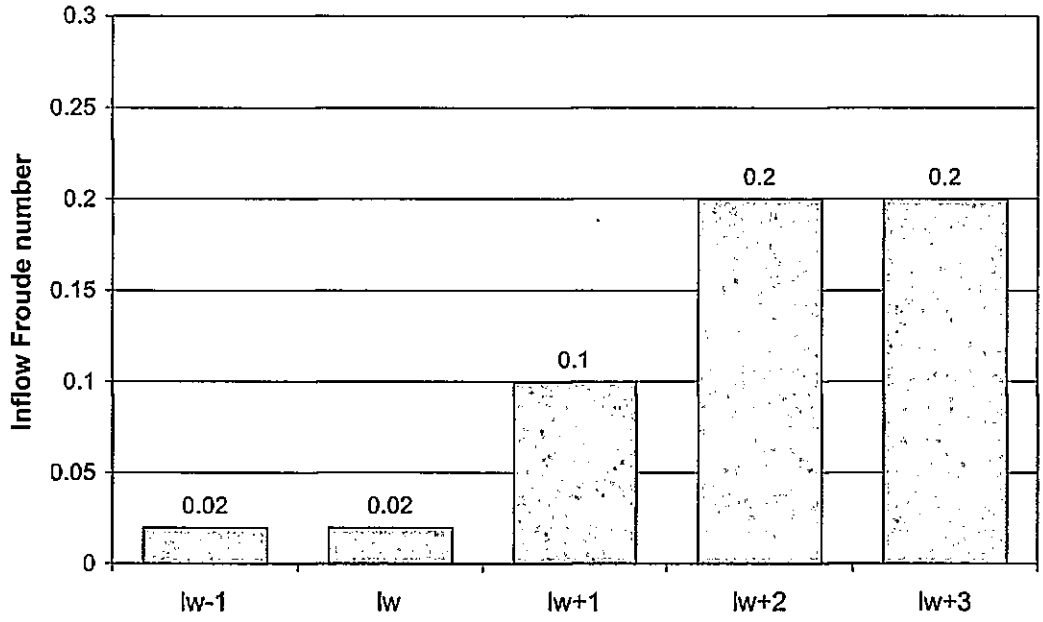

Figure 6.11. Variations in the inflow Froude number (F_o^2) at the constriction at the mouth of the Dart estuary during a neap tide. Note the expansion of the vertical scale in comparison with Figure 6.02.

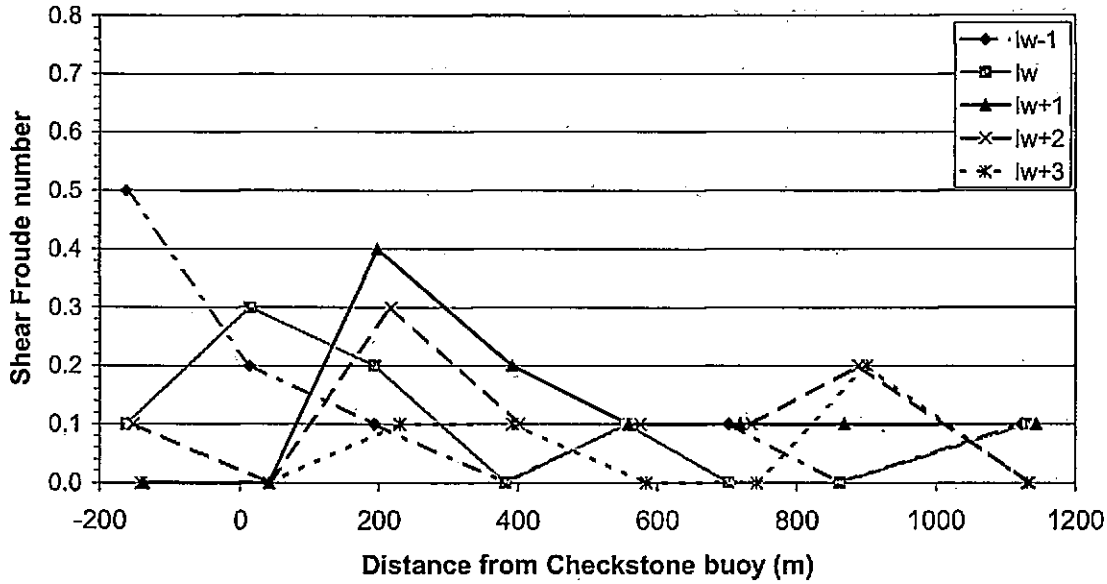

Figure 6.12. Variations in the shear Froude number (F_Δ^2) during a neap tide.
The constriction exists between 150 m and 300 m. The depression in the estuary bed exists from 300 m to 550 m.
Note the expansion of the vertical scale in comparison with Figure 6.03.

At one hour after low water (LW+1), $F_o^2 = 0.1$ at the estuary mouth (Figure 6.11). As the value of $F_o^2 < 0.3$, no hydraulic control point exists, and the outflow from the estuary is not blocked (Farmer & Armi, 1986). Two-way horizontal exchange flow remains possible, but is likely to remain sub-maximal due to the thin upper layer. Values of F_Δ^2 remain extremely low, a maximum $F_\Delta^2 = 0.4$ being achieved at the constriction (Figure 6.12). Thus, it is clear that the continuing density difference between the two layers is maintained in the presence of the low flow speeds, and corresponding low shear-induced mixing present at this time during a neap tide. Whilst the value of $F_\Delta^2 = 0.4$ indicates some shear and mixing occurring between the layers, it is at a much reduced rate in comparison to the spring tide situation. *Fi* is subcritical throughout the majority of the transect, although is supercritical through the constriction *and* over the start of the seabed depression (Figure 6.13). This is somewhat

unexpected, as the abrupt difference in depth between the two cast locations (10.6 m and 16.6 m respectively) should result in a change in state of the flow, as the inflowing waters encounter the deeper area, with its corresponding increase in cross-sectional area. Such a change of state over abruptly changing bathymetry is not indicated clearly in this case, using *Fi* as an identifier, potentially limiting its use in such situations. It is likely that the dependence of this parameter, and the related Ri_L (Figure 6.14) on the thickness of the upper layer only, results in this lack of resolution when traversing rapidly varying bathymetry.

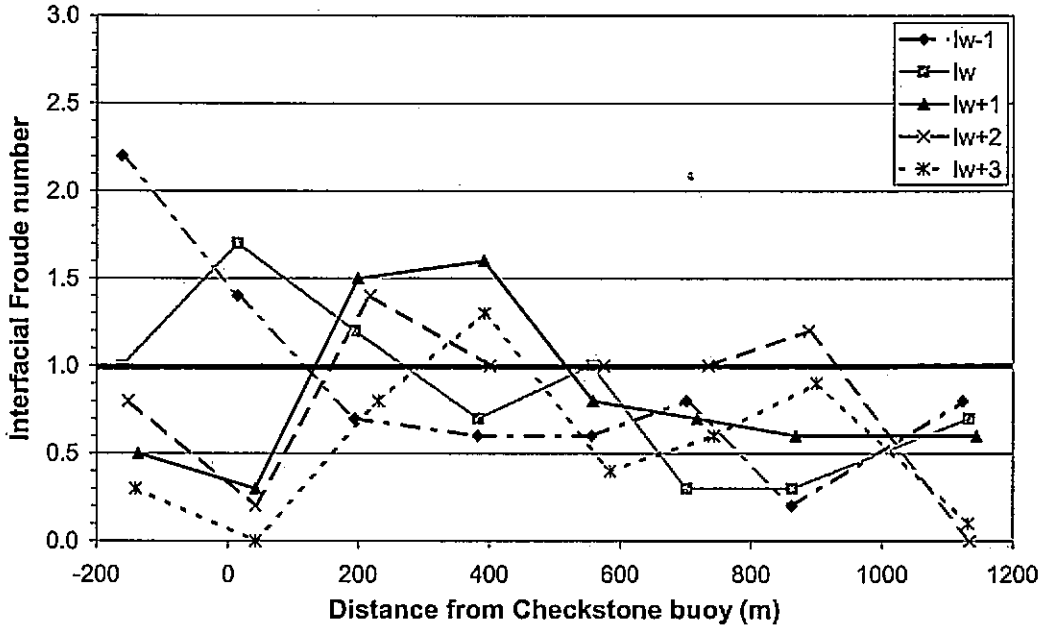

Figure 6.13. Variations in the interfacial Froude number (*Fi*) during a neap tide
The constriction exists between 150 m and 300 m. The depression in the estuary bed exists from 300 m to 550 m.
Note the expansion of the vertical scale in comparison with Figure 6.04.

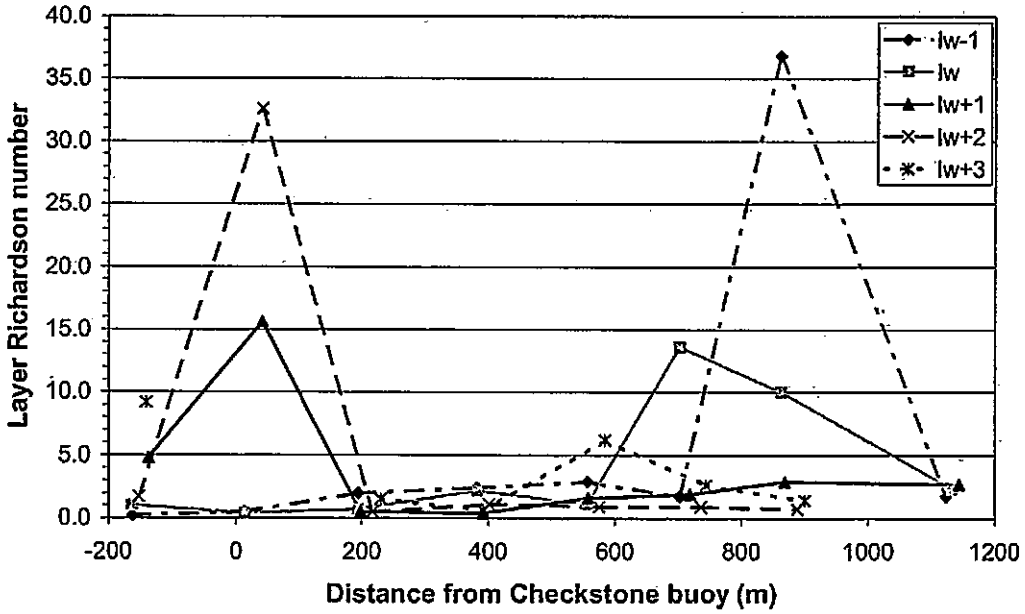

Figure 6.14. Variations in the layer Richardson number (Ri_L) during a neap tide
The constriction exists between 150 m and 300 m. The depression in the estuary bed exists from 300 m to 550 m.

Two hours after low water (LW+2) F_o^2 remains subcritical ($F_o^2 = 0.2$) at the constriction. This indicates the continuing absence of a hydraulic control point, but as the critical value of $F_o^2 = 0.3$ is approached, this indicates that only a slight further increase in flow speed would be required to create hydraulic control (equation 2.19). Values of F_Δ^2 remain subcritical throughout the survey transect (Figure 6.12). The low values do indicate *some* shear is occurring, however, and it is possible that Kelvin-Helmholz instabilities at the density interface are very gradually eroding the upper layer (Dyer, 1997). Evidence is provided to confirm this, as the calculated depth of the density interface is moving gradually closer to the surface throughout the flooding neap tide (N_{max}^2 values, tables 5.08 to 5.10). Both *Fi* and Ri_L are highly variable throughout the transect at this time (Figures 6.13 and 6.14 respectively). The broadly critical values of *Fi* over the seabed depression and inside the estuary mouth

could indicate significant mixing occurring across the density interface at this stage of the tidal cycle, although the persistence of the interface belies this to some extent. Variability in Ri_L at this time again makes it difficult to draw conclusions using this parameter, although $Ri_L > 20$ to seaward of the estuary mouth, implying a stable interface persisting in this area (New & Dyer, 1988).

Three hours after low water (LW+3), F_o^2 remains just subcritical ($F_o^2 = 0.2$) at the constricted mouth, and therefore, no topographic control is exercised on the flow. The very low values of F_Δ^2, the majority being zero, indicate a very low degree of shear-induced mixing taking place (Figure 6.12). The similarity in flow velocity and density between the two layers will not promote shear, and it is likely that any further erosion of the weak pycnocline would continue to occur relatively slowly. Fi and Ri_L remain highly variable throughout the transect at this time (Figures 6.13 and 6.14, respectively), although a change in Fi to supercritical above the seabed depression at cast five indicates the presence of a hydraulic jump in this area. No surface manifestation of the front was present, however, and this change in value of Fi is likely to have been caused by the small pocket of lower salinity water at the surface, in the region of the channel constriction.

6.2.4. A composite Froude number analysis – neap tide

One hour before low water (LW-1) the densimetric Froude number of the upper layer, F_1^2 is supercritical seaward of the estuary entrance, reducing to subcritical through the channel constriction and over the seabed depression (Figure 6.15). The subcritical values are driven by the great change in density ($\Delta\rho$) between the two flowing layers further landward of the

estuary entrance resulting in a large value for the reduced gravity, (g'). The depth of the upper layer also increases further landward, with flow speeds (u_1) remaining fairly constant throughout the transect, resulting in a large denominator in the F_1^2 equation (equation 2.09). The densimetric Froude number of the lower layer, F_2^2 is zero throughout, due to the negligible flow velocities in this lower layer and its significant depth. Changes in the composite Froude number, G^2 are, therefore, driven entirely by the ebbing upper layer, implying that the lower layer is inactive (*i.e.* does not interact with the bathymetry to control the flow) at this stage of the tidal cycle.

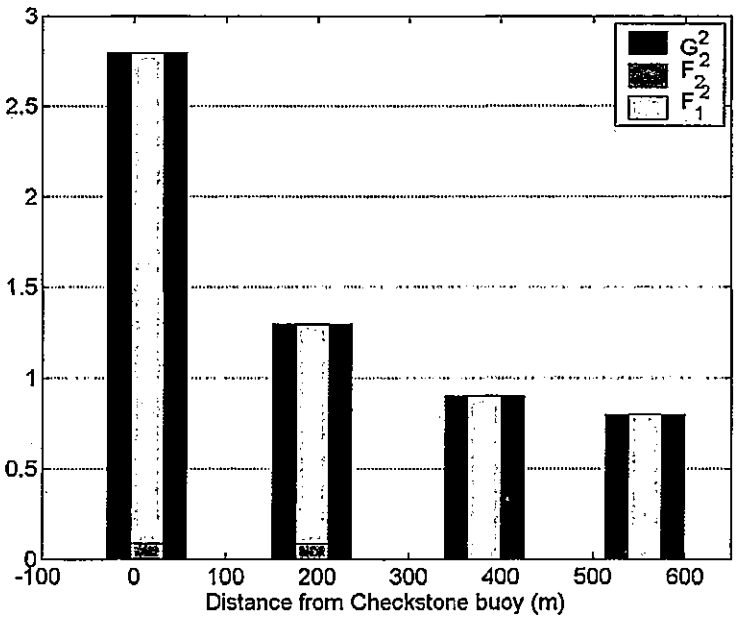

Figure 6.15. Variations in the composite Froude number, G^2 (comprising the densimetric Froude number for the upper and lower layers, F_1^2 and F_2^2 respectively) at the estuary entrance during a neap tide at LW-1. The constriction exists between 150 m and 300 m. The depression in the estuary bed exists from 300 m to 550 m. Note the change in the vertical scale in comparison with Figure 6.06.

At low water (LW), F_1^2 is supercritical at, and just outside the constricted mouth, due to a slight increase in flow velocity in these areas, and remains subcritical elsewhere due to the pronounced vertical density difference between the two layers (Figure 6.16). Values of F_2^2 are still zero at this time, therefore the lower layer remains inactive, and the flow does not interact with the bottom topography to provide a control point.

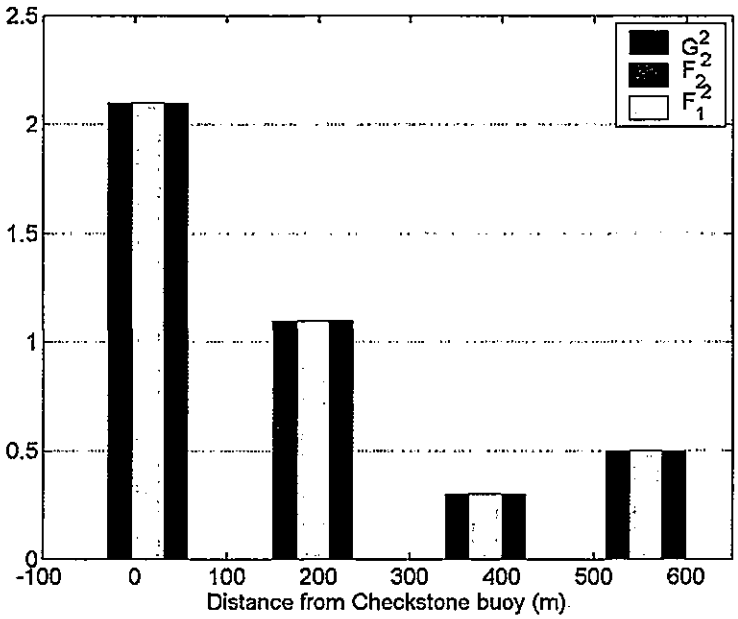

Figure 6.16. Variations in the composite Froude number, G^2 (comprising the densimetric Froude number for the upper and lower layers, F_1^2 and F_2^2 respectively) at the estuary entrance during a neap tide at LW. The constriction exists between 150 m and 300 m. The depression in the estuary bed exists from 300 m to 550 m. Note the change in the vertical scale in comparison with Figure 6.07.

By one hour after low water (LW+1), F_1^2 and F_2^2 are subcritical throughout the transect, with $F_2^2 = 0.2$ at the constricted mouth (Figure 6.17). As G^2 values are also subcritical, therefore,

and as $F_o^2 = 0.1$ at the constriction (Section 6.2.3.), no topographic control is exercised to form a hydraulic control point, and the front will not form.

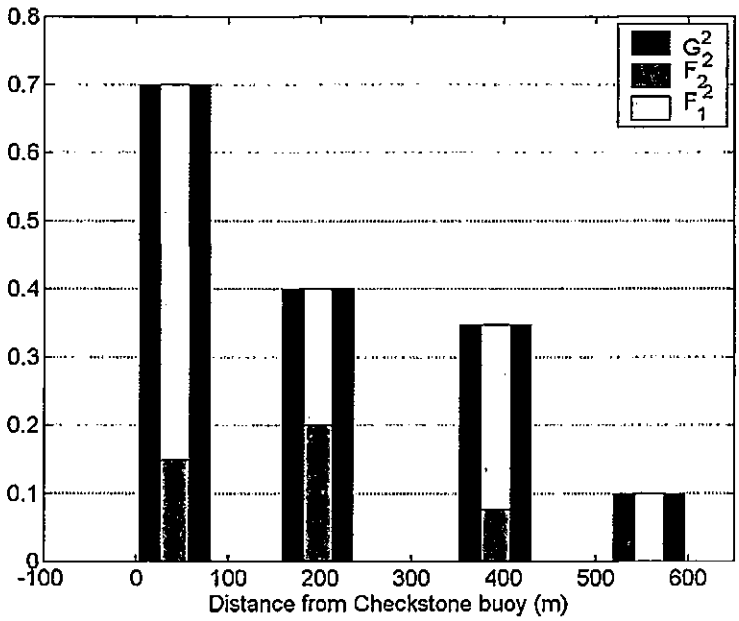

Figure 6.17. Variations in the composite Froude number, G^2 (comprising the densimetric Froude number for the upper and lower layers, F_1^2 and F_2^2 respectively) at the estuary entrance during a neap tide at LW+1. The constriction exists between 150 m and 300 m. The depression in the estuary bed exists from 300 m to 550 m. Note the change in the vertical scale in comparison with Figure 6.08.

At two hours after low water, G^2 is now supercritical outside the estuary mouth, and subcritical inside, with an implied hydraulic jump between these two areas (Figure 6.18). This flow transition is driven solely by the *upper* layer, with $F_1^2 = 1.5$ just seaward of the mouth, and $F_1^2 = 0$ just landward of the mouth. This transition to zero is driven by a reduction in flow speed in the constriction, presumably as the ebbing upper layer is stalled by the incoming, flooding tidal flow. F_2^2 remains subcritical throughout the transect during this time, and as

only the upper layer is active, no seabed topographic control exists. The passage of G^2 through unity at some point in the constriction does imply the existence of a hydraulic control point. However, the subcritical value of $F_o^2 = 0.2$ at the estuary mouth refutes this to a large degree, and it appears, therefore, that a hydraulic transition in the upper layer alone is not sufficient to allow frontal formation during neap tides.

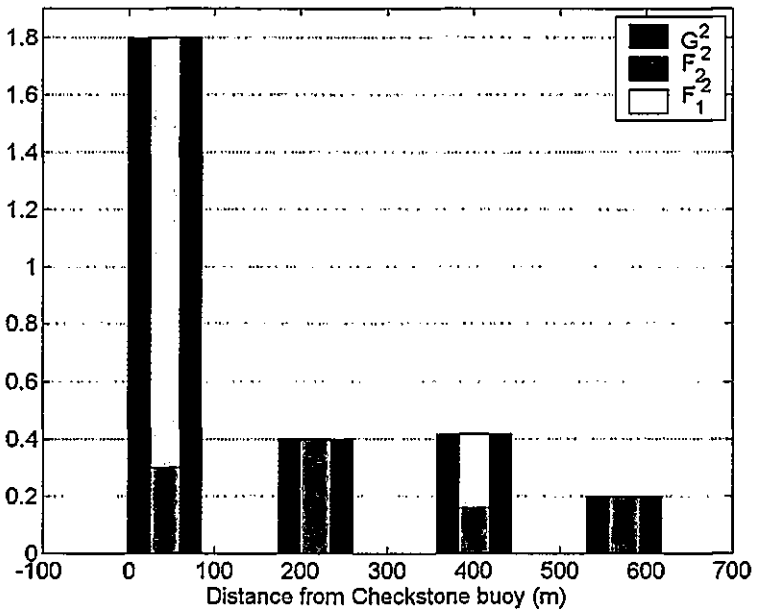

Figure 6.18. Variations in the composite Froude number, G^2 (comprising the densimetric Froude number for the upper and lower layers, F_1^2 and F_2^2 respectively) at the estuary entrance during a neap tide at LW+2. The constriction exists between 150 m and 300 m. The depression in the estuary bed exists from 300 m to 550 m. Note the change in the vertical scale in comparison with Figure 6.09.

Three hours after low water, G^2 again changes from supercritical to subcritical within the constricted section (Figure 6.19). This change is driven by changes in the upper layer, F_1^2,

similarly to that found during the previous hour of tide. The generally subcritical values of F_2^2 indicate that any control would still be exercised by the upper layer, the lower layer not interacting with changes in bathymetry at this time.

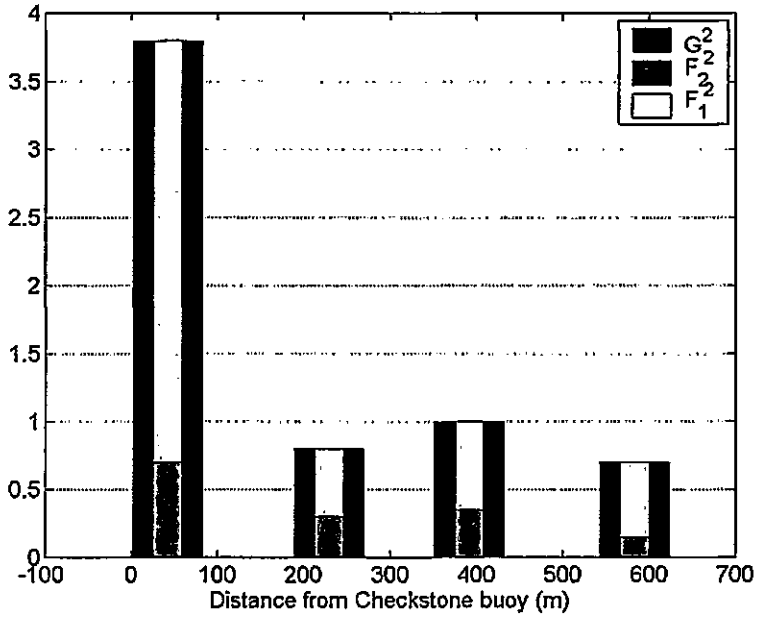

Figure 6.19. Variations in the composite Froude number, G^2 (comprising the densimetric Froude number for the upper and lower layers, F_1^2 and F_2^2 respectively) at the estuary entrance during a neap tide at LW+3. The constriction exists between 150 m and 300 m. The depression in the estuary bed exists from 300 m to 550 m. Note the change in the vertical scale in comparison with Figure 6.10.

6.2.5. A Froude number plane analysis

The two-layer, stratified flows at the mouth of the Dart estuary may be examined in terms of the Froude number plane. Comparisons may then be made with solutions for maximal and submaximal flow (Figures 2.06 to 2.08), derived from the continuity and Bernoulli equations (Section 2.5.1.1). In this way, hydraulic control points may also be identified clearly. This

analysis technique has been employed by Valle-Levinson *et al.* (2001), examining two-layer flows at the mouth of a fjord, with limited success. A hydraulic control point will exist when G^2=1, the area enclosed by the shaded triangle (Figure 6.20 to 6.27) representing subcritical values of G^2. The plotted points represent values of F_1^2 and F_2^2 calculated at the various CTD cast locations along each survey transect. Geographical locations for each numbered point are presented in the corresponding Figures in Chapter 5.

At low water (LW) during a spring tide, an exchange flow between estuarine and coastal waters was recorded at the mouth of the Dart estuary. A seaward transition from supercritical to subcritical is indicated to occur between CTD casts 6 and 5 (Figure 6.20). This corresponds to locations within the channel contraction and over the seabed depression respectively. A transition further downstream (landward), where G^2 changes from subcritical to supercritical, is noted between casts 4 and 3. These flow transitions are driven entirely by changes in flow in the upper layer, as F_2^2 is close to zero throughout the transect at this time. As the inflow is in the 'moderate' regime ($F_o^2 < 0.3$), the buoyant outflow is not blocked. The seaward control (the exit control) is fixed at the left hand exit of the system when $F_o^2 < 0.3$, and a virtual hydraulic control point will not, therefore, appear in this instance (Farmer & Armi, 1986). As the two intersections with the critical value of G^2 are coincident in this case, the implication is that the two controls are coincident, *i.e.* there is only one hydraulic control point at this time (Armi, 1986; Baines, 1995). The Froude number plane solution also aids visualisation of the hypothesis that the lower layer is inactive at this stage of the tidal cycle, as F_2^2 has collapsed to virtually zero throughout the transect. This is similar to the solution for submaximal exchange flow without sill control (Figure 2.08), presented by Farmer & Armi (1986).

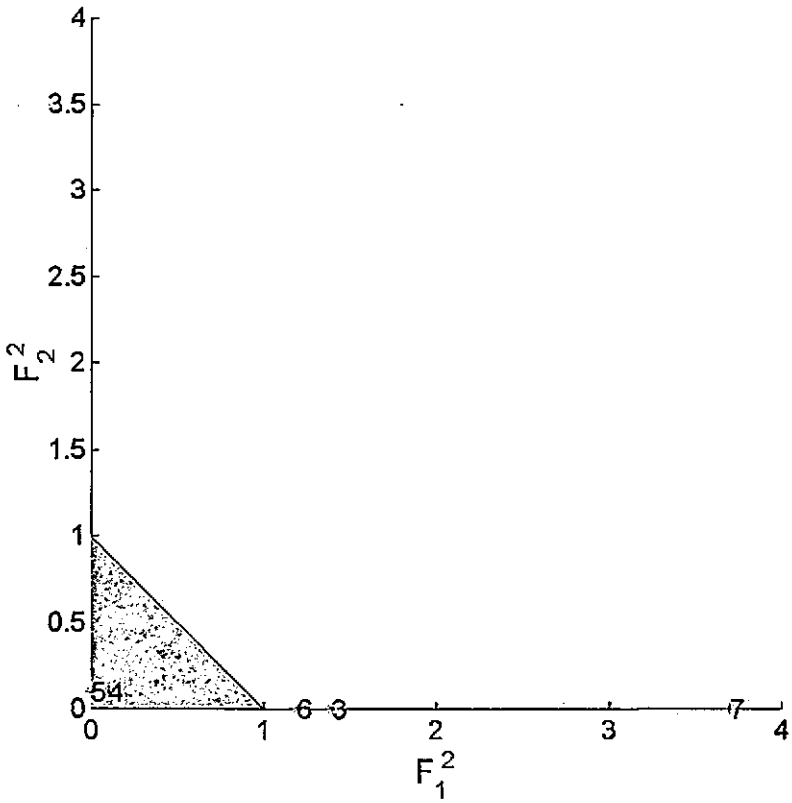

Figure 6.20. Froude number plane analysis at LW during a spring tide.
The numbered points correspond to the calculated values of F_1^2 and F_2^2 at CTD cast locations along the survey transect. The shaded area represents subcritical values of G^2. Refer to Figure 5.08a for the locations of each cast.

By LW+1 during a spring tide, when the tidal intrusion front was present at the entrance to the Dart estuary, the buoyant estuarine outflow is blocked and no exchange flow is possible. Plotted values of F_1^2 and F_2^2 have two intersections with the line of critical flow and two hydraulic control points are, therefore, apparent (Figure 6.21). Note that cast 7 has been plotted outside the axes, as it has an extremely high value. In this way the axes can be expanded to concentrate on the flow transitions at the critical level. The seaward, exit control appears between CTD casts 9 and 8, and the sill control appears at cast 6 (just before the flow encounters the seabed depression), where $G^2 = 1$. The flow is subcritical outside the

constriction (cast 9), and supercritical through the constriction (casts 8 and 7) as predicted by hydraulics theory for two layer flow over a sill and through a contraction (Farmer & Armi, 1986). As the inflow is in the 'strong' regime ($F_o^2 > 1$) at this time, the plunge point will occur at the virtual control point downstream at this time (Largier, 1992), corresponding to the observed plunge point between casts 7 and 6 (Figure 5.09f). This Froude number plane solution, with a kink at high Froude number values (CTD cast 7) is remarkably similar in shape to that achieved in the laboratory for unidirectional two-layer flows by Armi (1986), using a constriction in a small flume.

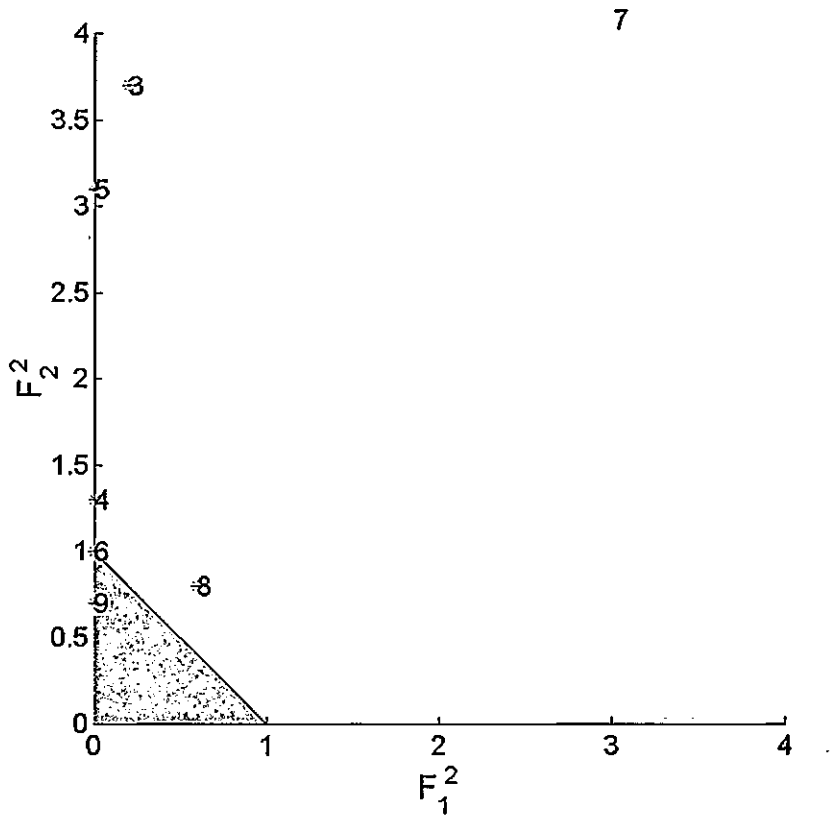

Figure 6.21. Froude number plane analysis at LW+1 during a spring tide.
The numbered points correspond to the calculated values of F_1^2 and F_2^2 at CTD cast locations along the survey transect. The shaded area represents subcritical values of G^2. Refer to Figure 5.09a for the locations of each cast.

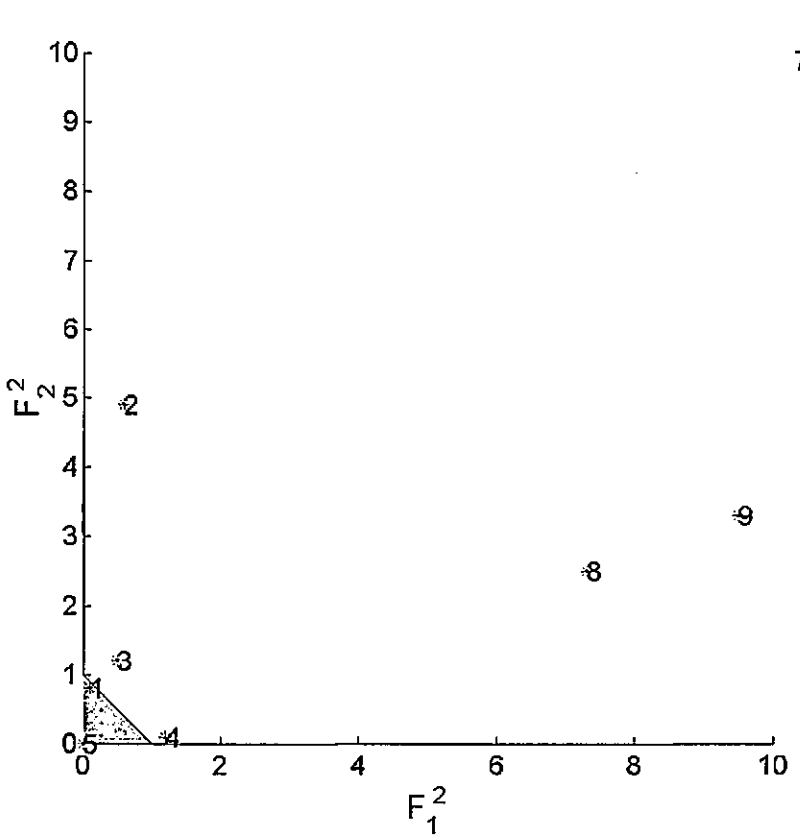

Figure 6.22. Froude number plane analysis at LW+2 during a spring tide.
The numbered points correspond to the calculated values of F_1^2 and F_2^2 at CTD cast locations along the survey transect. The shaded area represents subcritical values of G^2. Refer to Figure 5.10a for the locations of each cast.

At LW+2 during a spring tide, two intersections with the line of critical flow remain apparent (Figure 6.22). Again, casts 7 and 6 with high calculated values of F_1^2 and F_2^2 have been placed outside the axes to enable the transition area (shaded triangle) to be seen more clearly. Moving downstream, a control point is indicated between casts 6 and 5. This corresponds to the seaward end of the seabed depression, and the visual location of the plunge point at this time. The implication from the Froude number plane is that the plunge point is nearer to cast 5, corresponding to the visual observations and density contours (Figure 5.10f). A further hydraulic control point is found between casts 5 and 4, downstream of the frontal interface.

As the inflow is still in the 'strong' regime at this time ($F_o^2 > 1$), and barotropic forcing has increased further by this stage of the tidal cycle, the virtual control point has moved further downstream. By LW+3, no intersections are noted with the line of critical flow, where $G^2 = 1$ (Figure 6.23). This implies that the control points have become flooded and disappeared, in line with the theoretical predictions (Denton, 1987; Farmer & Armi, 1986).

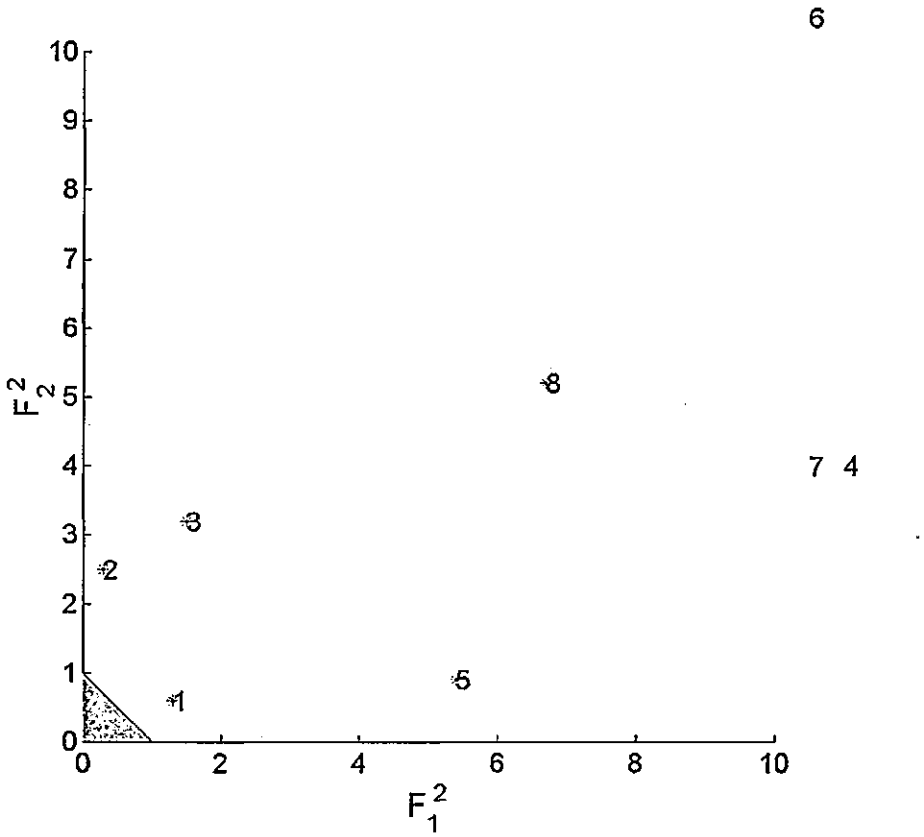

Figure 6.23. Froude number plane analysis at LW+3 during a spring tide.
The numbered points correspond to the calculated values of F_1^2 and F_2^2 at CTD cast locations along the survey transect. The shaded area represents subcritical values of G^2. Refer to Figure 5.11a for the locations of each cast.

At LW during a neap tide, an intersection with the line of critical flow is again noted, occurring between CTD casts 6 and 5 (Figure 6.24). This corresponds to a location at the end of the constriction, just before the seabed depression (Figure 5.11a). This control point is driven entirely by changes in the upper layer, as F_2^2 is zero throughout the transect at this time. This is very similar to the situation at LW during a spring tide (Figure 6.20). As the control exercised by the contraction is weak for two-layer flows when a sill and contraction is involved, this confirms that the lack of sill control, interacting with the lower layer will not allow the formation of a front during this stage of the tidal cycle. By LW+1 during a neap tide, all the solutions on the Froude number plane lie on the subcritical side of the shaded area (Figure 6.25). No hydraulic control exists at this time, therefore, confirming that the tidal intrusion front will not form.

Supercritical flows are evident seaward of the constriction (CTD casts 8 and 7) at LW+2 during a neap tide (Figure 6.26). An intersection of the line of critical flow is noted between casts 7 and 6, implying the presence of a hydraulic control point in this location. Again, this is driven primarily by changes in the flow in the upper layer, to form this exit control point. Similarly to the previous hour of tide, it appears that the subcritical lower layer prevents the formation of a control point at the sill, and therefore the front will not form.

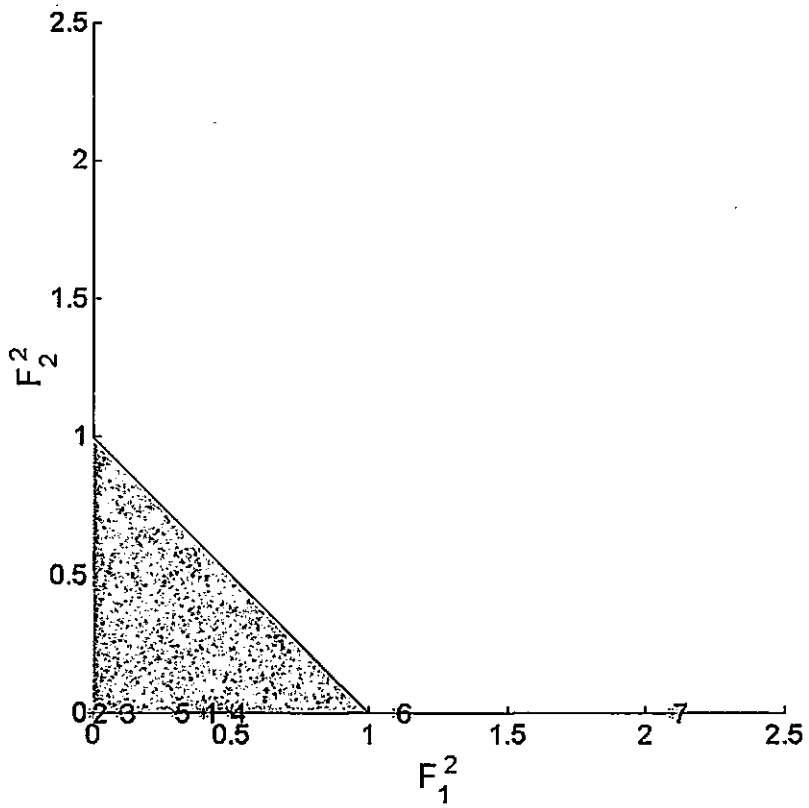

Figure 6.24. Froude number plane analysis at LW during a neap tide.
The numbered points correspond to the calculated values of F_1^2 and F_2^2 at CTD cast locations along the survey transect. The shaded area represents subcritical values of G^2. Refer to Figure 5.13a for the locations of each cast.

The results in the Froude number plane are somewhat variable at LW+3 during a neap tide (Figure 6.27). Moving from seaward, three intersections with the line of critical flow are apparent, between CTD casts 7 and 6, between casts 4 and 3, and between casts 2 and 1. These locations correspond to the contraction, a relatively shallow area downstream of the seabed depression, and a further bathymetric increase at the landward end of the survey transect respectively. Again driven principally by changes in flow in the upper layer, with F_2^2 remaining subcritical throughout the transect, the variable nature of Froude number plane

results at LW+3 does not provide any further insight into the hydraulic processes involved at this stage of the tidal cycle.

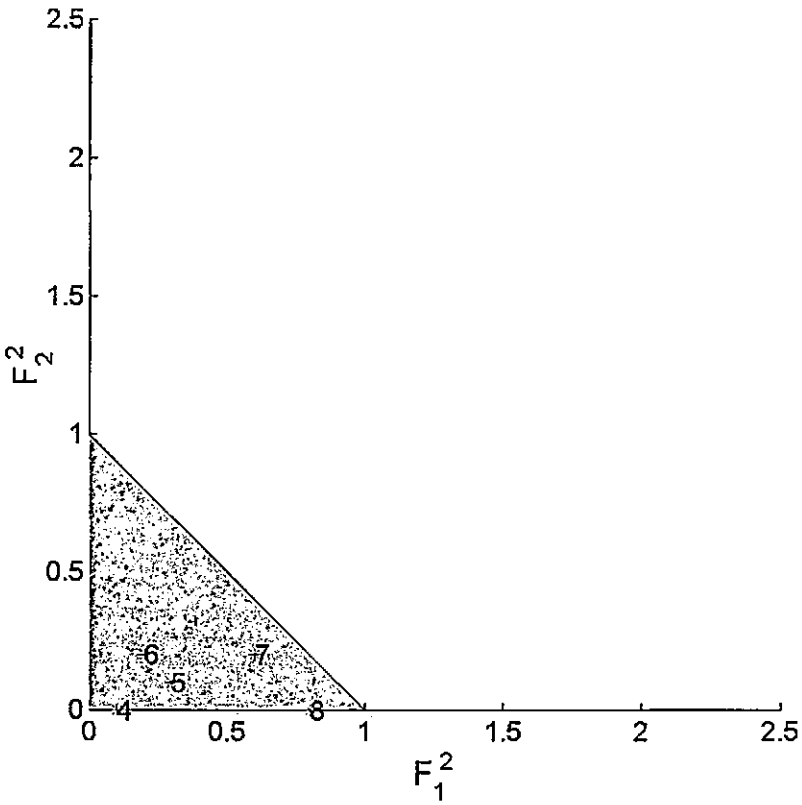

Figure 6.25. Froude number plane analysis at LW+1 during a neap tide.
The numbered points correspond to the calculated values of F_1^2 and F_2^2 at CTD cast locations along the survey transect. The shaded area represents subcritical values of G^2. Refer to Figure 5.14a for the locations of each cast.

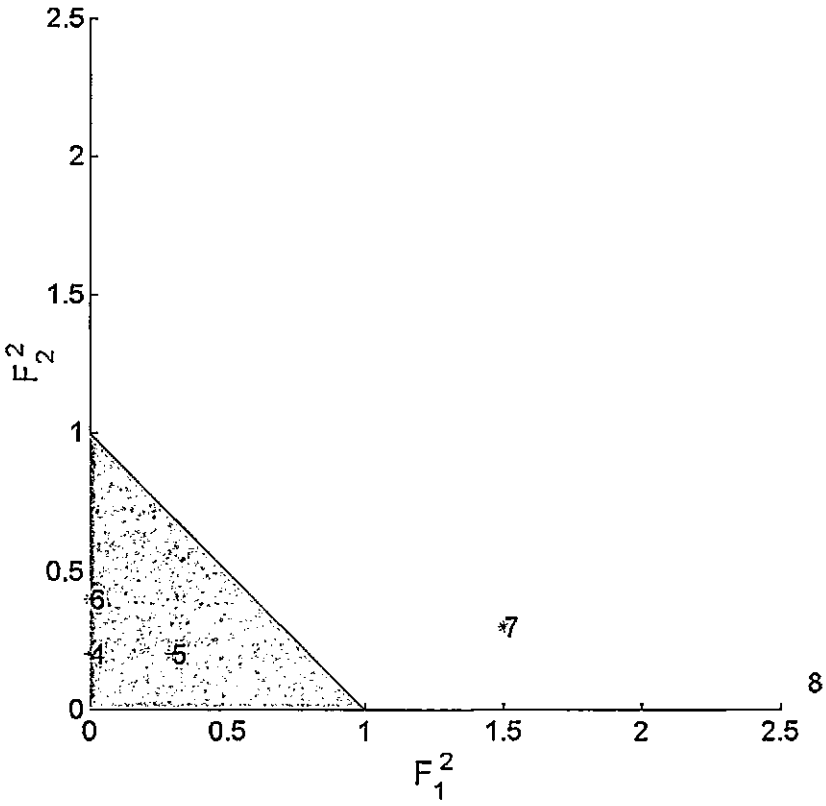

Figure 6.26. Froude number plane analysis at LW+2 during a neap tide.
The numbered points correspond to the calculated values of F_1^2 and F_2^2 at CTD cast locations along the survey transect. The shaded area represents subcritical values of G^2. Refer to Figure 5.15a for the locations of each cast.

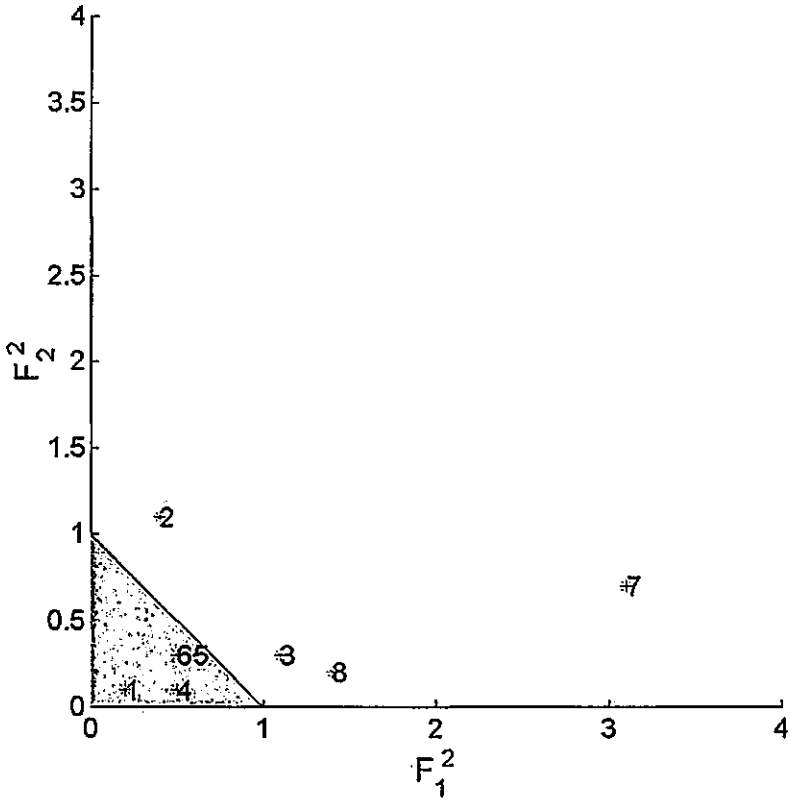

Figure 6.27. Froude number plane analysis at LW+3 during a neap tide.
The numbered points correspond to the calculated values of F_1^2 and F_2^2 at CTD cast locations along the survey transect. The shaded area represents subcritical values of G^2. Refer to Figure 5.16a for the locations of each cast.

6.2.6. Calculating the location of the frontal interface

In a strong inflow regime ($F_o^2 > 1$) through a constrictive channel section, Largier (1992) defines a solution for the depth at plunging (h_p) for flow over a sill:

$$h_p = \left(\frac{Q^2}{g' b^2} \right)^{\frac{1}{3}} \qquad (6.01)$$

This theory has been applied successfully by Largier (1992) in a shallow, bar-built estuary, to locate a tidal intrusion front spatially. This solution has also been employed with some success in a well-mixed micro-tidal estuary. Examining plunging flow over a gradually increasing bed slope in such an environment, predicted results of h_p using historical data were in close accord with field observations (Huzzey, 1982).

Calculating plunge depths during spring tides, using the field data gathered in the Dart during this time, yields a plunge depth of 12.3 m at LW+1 (Table 6.01). This corresponds favourably to the observed depth at the plunge point at this stage of the tidal cycle (Figure 5.09). At LW+2 the plunge depth is calculated to be 12.6 m, again corresponding to the approximate depth where the front was visually noted at that time (Figure 5.10), *i.e.* the front has migrated approximately 30 m further landward over the increasing depth of the seabed depression. At LW+3, the plunge depth of 16.0 m is consistent with the measured depth where the patches of foam and discoloured water were noted following frontal decay. During neap tides, calculated plunge depths are of the order of 4.5 m at LW+1, to 5.8 m at LW+3. This indicates that the flow is not topographically controlled by the seabed at any point during the neap tidal cycle, as

the water depth is well in excess of these figures throughout the transect at all stages of the flooding tide.

	Spring tide		Neap tide	
	h_p	Observed plunge depth (m)	h_p	Observed plunge depth (m)
LW+1	12.3	11.0	4.5	n/a
LW+2	12.6	12.0	5.6	n/a
LW+3	16.0	n/a	5.8	n/a

Table 6.01. Calculated values of h_p, channel depth at plunge point, together with approximate observed depths at frontal locations.

The channel width at plunging, for flow through a contraction, has been defined by Armi & Farmer (1986) as:

$$b_p = \frac{Q}{(g'h^3)^{\frac{1}{2}}} \qquad (6.02)$$

The predicted results of b_p compare favourably with frontal locations observed during spring tides at LW+1 and LW+2 (Table 5.13). At LW+3, b_p = 414 m, the approximate width where the patches of foam and discoloured water were noted. During neap tides, the estuary width is always greater than calculated values of b_p, and as a critical value is not reached (where b_p = channel width), the flow will not plunge at this time. This relationship should be viewed with some caution, however, as an average cross-channel depth (h) at the mouth has been used to derive the calculated result of b_p. As h is a cubed parameter in this instance, it will be highly sensitive to small changes or measurement errors.

	Spring tide		Neap tide	
	b_p	Observed plunge width (m)	b_p	Observed plunge width (m)
LW+1	343	340	74	n/a
LW+2	319	320	96	n/a
LW+3	415	400	94	n/a

Table 6.02. Calculated values of b_p, channel width at the plunge point, together with approximate observed widths at frontal locations.

6.3. Internal hydraulics, circulation and mixing in the Dart estuary

An internal hydraulics analysis of the stratified flows at the mouth of the Dart estuary has provided important insights into the mechanisms responsible for the formation and decay of a tidal intrusion front during spring tides, and the non-appearance of the front during neap tides. The constricted entrance to the Dart, with the seabed depression further landward of the constriction, facilitates the use of such an internal hydraulics analysis, if the assumption is made that the constriction consists of a both a sill and a contraction, acting as a single constriction on the flow. Whilst the Dart does not have a sill in the strictest sense, such an assumption yields explanations that are consistent with observations (Thain *et al.*, 2004). The narrow, constricted entrance to the Dart estuary, followed by an abrupt increase in depth over an elongated depression in the seabed (Figure 6.01) appears, thus, to create a similar topographic situation to flows over a sill at the mouth of a bar-built estuary or a fjord.

The supercritical inflow Froude number at the constriction ($F_o^2 = 3.5$) at LW-1 during a spring tide confirms that no seawater intrusion is possible (Largier, 1992). Supercritical values of the composite Froude number (G^2) throughout the transect at this time imply a broadly homogeneous water column, with the majority of the flow control exercised by the upper

layer. Subcritical values of the shear Froude number, F_{Δ}^2, confirm minimal shear occurring between two relatively homogeneous, unidirectional flowing layers at this stage of the tidal cycle.

By LW during a spring tide, two-way exchange flow between the estuarine and coastal reservoirs occurs through the constricted mouth of the Dart estuary. The subcritical value of the inflow Froude number ($F_o^2 = 0.2$) indicates that no hydraulic control is present at this time, although only a small increase in flow rate at the constriction would increase the value of $F_o^2 > 0.3$, to create hydraulic control (equation 2.19). Conversely, a Froude number plane analysis (Figure 6.20) implies the existence of one hydraulic control point at this time, an exit control at the boundary between the constricted mouth and the open sea. It appears this control is caused by flows in the upper layer only (represented by supercritical values of F_1^2), and therefore, no 'sill' control is present. The front is thus unable to form as no hydraulic control is exercised on the lower layer at this time, a requirement for flows through a combination of a sill and a contraction (Farmer & Armi, 1986). The horizontal exchange flow is noted to be sub-maximal at this time, as the interface height ($y'_{2o} = 0.33$) is less than the optimum interface height for maximal exchange flows (equation 2.17). Note that this flow is submaximal with respect to the upper layer, *i.e.* partial arrest of this layer had commenced by LW.

By LW+1 during a spring tide, a clear visual manifestation of the tidal intrusion front is present, corresponding with a remarkable discontinuity in the salinity and density field (Figures 5.09c-d). A relatively homogeneous inflow is recorded through the constriction, upstream of the frontal interface, with a marked two-layer, stratified regime apparent

downstream. The velocity field indicates the inflow speeding up through the constricted mouth, becoming supercritical as it passes through this region. A marked discontinuity in velocity is then apparent across the frontal interface (Figure 5.09f), consistent with field observations and theoretical studies suggesting plunging inflow and arrest of the upper layer occurring in this area (Farmer & Armi, 1986; Marmorino & Trump, 1996). A hydraulic control point is present ($F_o^2 > 1$), the supercritical value of F_o^2 indicating plunging flow should occur at a further virtual control point downstream of the constriction. The plunge point is recorded approximately 100 m downstream of the seaward end of the constriction (the exit control) at this time, thus validating this theoretical approach (Farmer & Armi, 1986). A Froude number plane analysis (Figure 6.21) also confirms the existence of two hydraulic control points at this time. A seaward, exit control is evident, together with a further 'sill' control appearing just prior to the plunge point.

Blocking of the buoyant estuarine outflow occurs at the plunge point, corresponding to Figure 2.09e for theoretical two layer flow over a sill and through a contraction. The limiting flow value (U_l) through the constriction sufficient to block the buoyant outflow is predicted by hydraulics theory to be 0.81 of the maximum flow speed (equation 2.18). Recorded values of flow speed in the constriction at LW+1 in the presence of the tidal intrusion front suggest $U_l \approx$ 0.47 ms^{-1}. Using equation 2.18, the maximum allowable flow speed to facilitate frontal formation is thus calculated to be 0.58 ms^{-1}. Provided peak flow is assumed to occur mid-way through the flood, i.e. at LW+3, these theoretical predictions are found to be identical to the observed flow speed (0.58 ms^{-1}) at LW+3 (Table 6.03). The value of U_l, as predicted by the hydraulics theory of Farmer & Armi (1986) is thus validated.

The blocking of the buoyant outflow is reflected accurately in the densimetric Froude number analysis of the upper layer, where $F_1^2 = 0$ at the plunge point. The flow reduces abruptly from supercritical to critical, with an implied stationary hydraulic jump, at the plunge point, where $G^2 = 1$. This flow transition is, therefore, driven entirely by a critical lower layer ($F_2^2 = 1$) at this point. Again, this calculated G^2 value at the 'sill' just prior to the plunge point corresponds exactly to the theoretical prediction of such hydraulically controlled flows (Farmer & Armi, 1986). This change of flow state and implied hydraulic jump occurs, therefore, as the supercritical inflow encounters the increased depth over the seabed depression. At this point, the inflow does not have sufficient velocity to push back the buoyant estuarine outflow, and arrest of the upper layer, corresponding to plunging of the lower layer occurs.

	Spring tide		Neap tide	
	Flow values (ms^{-1})	**$\Delta\rho$ (kg m^{-3})**	**Flow values(ms^{-1})**	**$\Delta\rho$ (kg m^{-3})**
Low water	0.25		0.16	
Low water +1	0.47	0.6	0.32	5.6
Low water +2	0.54	0.8	0.43	6.0
Low water +3	0.58		0.42	

Table 6.03. Flow values (ms^{-1}) and $\Delta\rho$ (kg m^{-3}) recorded at the channel constriction at various times during the tidal cycle.

The blocking of the outflow increases the thickness of this layer, correspondingly reducing the thickness of the lower layer. The velocity of the inflow, plunging beneath the static, arrested buoyant layer is thus increased, this process potentially being exacerbated by a transfer of

kinetic energy from the arrested upper layer to the lower layer. A supercritical value of the shear Froude number (F_Δ^2) through the constriction adds further weight to the hypothesis of significant shear and mixing occurring in this area, implying a homogeneous inflow. The density stratification indicated downstream of the front ($F_\Delta^2 < 1$) appears resistant to shear induced mixing at this stage of the tidal cycle, and appears to render the tidal intrusion front stable for a time.

Estimates of eddy viscosity (N_z) across the density interface just downstream of the frontal zone highlight the resistance of the frontal interface to shear induced mixing. Using the widely accepted relationship between eddy viscosity and the gradient Richardson number (Ri) expressed by Munk & Anderson (1948), N_z may be derived from field data thus:

$$N_z = N_o(1+10Ri)^{-1/2} \qquad \text{m}^2\,\text{s}^{-1} \qquad (6.03)$$

where N_o is the value of N_z when the water column is homogeneous. If N_o is taken to be (Dyer, 1997):

$$N_o = 2.5\times10^{-3}U_o h \qquad \text{m}^2\,\text{s}^{-1} \qquad (6.04)$$

where U_o is the tidal current amplitude (barotropic forcing) and h is the water depth, $N_z = 1.9 \times 10^{-4}$ m^2 s^{-1} in the pycnocline just downstream of the tidal intrusion front at LW+1. This value of N_z is a significant reduction from the homogeneous water column value of $N_o = 1.5 \times 10^{-3}$

$m^2 s^{-1}$ in this location. Plotting changes of *normalised* eddy viscosity (N_z/N_o) with depth highlights the decrease of N_z at the base of the pycnocline (Figure 6.28). This is apparent at a depth of 3 m at CTD cast 5, just downstream of the frontal interface, and is likely to be representative of the change in N_z horizontally across the frontal interface. It appears, therefore, that the N_z values indicate a significant inhibition of mixing across the density interface, resulting in frontal stability for a time. In the more homogeneous water column outside the mouth of the estuary (CTD cast 9), N_z/N_o should equal unity, the data supporting this over the majority of the water column in this location (Figure 6.28).

The presence of the tidal intrusion front is also likely to enhance the magnitude of the baroclinic flows in frontal zone. This component of the flow, acts in the same direction as the barotropic pressure gradient on the flooding tide. The low values of N_z in the pycnocline at the frontal interface, however, imply that this flow component is also unable to act in a horizontal plane across the density gradient characterising the frontal zone. The enhanced barotropic flow is likely, therefore, to be directed into the lower flowing layer, further exacerbating the flow velocities in the compressed lower layer beneath the tidal intrusion front.

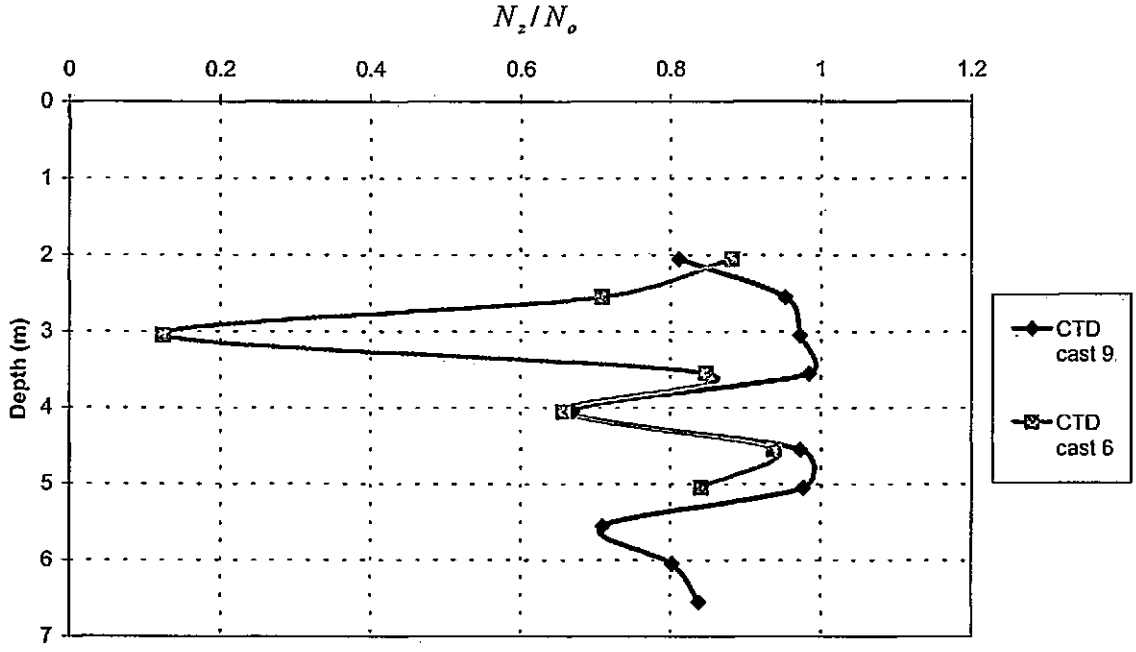

Figure 6.28. Variations in normalised eddy viscosity (N_z / N_o), with depth, at LW+1.
CTD cast 6 is just downstream of the frontal interface, where the location of the density interface is characterised by a sudden drop in eddy viscosity, implying stable stratification with inhibited mixing. A relatively homogeneous water column is indicated outside the estuary mouth at CTD cast 9.

By LW+2 during a spring tide, the tidal intrusion front is still present, although it has migrated approximately 50 m further downstream, over the increasing depth of the seabed depression. The increased barotropic forcing (U_o) increases the speed of the flow to 0.54 ms^{-1} at this stage of the tidal cycle. Therefore $U_o > U_i$, and the plunge point occurs further downstream, corresponding to Figure 2.09h for 'strong' inflows. Examining this stage of the flow in terms of the continuity condition (equation 2.16), if the ratio of the flow rate in each layer (q_r) is assumed to be steady, then increasing the flow rate in the lower layer (q_2') must be compensated for by an increase in depth (h'). The tidal intrusion front thus migrates over the increasing depth of the seabed depression to accommodate increasing U_o. The observed results in the plunge depth (h_p) confirm such an increase in depth at the plunge point (Table

6.01) and corresponds well to predicted values of h_p (Table 6.01). Additionally, supercritical F_o^2 values at the constriction, still in the strong inflow regime, indicate that the virtual control and plunge point will continue to occur downstream of the constriction. This hypothesis is augmented by the Froude number plane analysis, indicating two hydraulic control points at the estuary entrance, corresponding well to the observations recorded at this time.

The location of the plunge point at LW+2 is again reflected accurately by an abrupt reduction in G^2 from supercritical to subcritical across the frontal interface, with the calculated values of G^2 implying a strong hydraulic jump in this area. This change in flow state is driven by the lower flowing layer, with the blocked surface layer being described faithfully by $F_1^2 = 0$ at the plunge point. Density stratification downstream of the front is not as marked by this stage of the tidal cycle, and it appears that the formation of a stationary internal hydraulic jump over the seabed depression with the associated mixing is leading to a gradual erosion of the density interface. Values of F_Δ^2 are again supercritical upstream of the plunge point, and subcritical throughout the remainder of the transect. A homogeneous water column in the strong flows through the constriction is again implied, with stratification persisting downstream of the front, rendering the frontal system stable for a continuing period of time. Estimates of eddy viscosity (N_z) of 1.4×10^{-2} m^2 s^{-1} just downstream of the frontal interface also imply that the stratification is not as pronounced as at LW+1 (when $N_z = 1.9 \times 10^{-4}$ m^2 s^{-1}). It appears, therefore, that the density stratification is beginning to weaken, permitting some degree of mixing across the stratified frontal zone. The continuing horizontal density gradient across the frontal interface is likely to continue to enhance the baroclinic flows locally. This increased forcing cannot increase stratification further, as the salinity of the lower layer is already at a maximum of 35 by this stage of the tidal cycle. The enhanced flow is, however, likely to lead

to greater shear at the density interface, further reducing its intensity. The weakening interface allows more salt to be mixed upward into the upper layer of the water column, thus weakening the frontal density gradient, eventually facilitating the breakdown of the frontal system.

By LW+3 during a spring tide, the visual manifestation of the tidal intrusion front is no longer apparent. Swirls and eddies of discoloured estuarine water were noted at the surface during the survey, and two broken lines of foam were noted, one at the seaward end of the seabed depression, and one at the seaward end of the 15 m depth contour further downstream (Figure 5.06). The flow vectors are fairly uniform throughout the transect at this time, with the density contours indicating a homogeneous water column. A slight dip in the contours around 900 m from the start of the line may be indicative of the remainder of the front, and this corresponds to the area where patches of foam and discoloured water were noted. Supercritical values of F_o^2 at the constriction imply that the plunge point should be well downstream, although a Froude number plane analysis indicates that no control points are present. Supercritical values of G^2 throughout the transect add further credence to this, and subcritical values of F_Δ^2 suggest that no further mixing is taking place at this time. The implication is thus that the control points have become flooded and disappeared, in line with theoretical predictions for strong hydraulic flows (Denton, 1987; Farmer & Armi, 1986). Estimates of eddy viscosity have increased markedly by this stage of the tidal cycle, with a maximum value of $N_z = 1.2 \times 10^{-2}$ m^2 s^{-1} at mid depth, just downstream of the last recorded visual manifestation of the tidal intrusion front. The 'damping' effect on mixing caused by stratification is, therefore, absent following the breakdown of the density interface.

During a neap tide, no manifestation of the tidal intrusion front was recorded at the mouth of the Dart estuary. At LW-1, an extremely well developed vertical density gradient is apparent, with a shallow layer of buoyant estuarine water at the surface overlying a homogeneous lower layer. There is a pronounced density difference between the upper and lower layer (of up to 9.1 kg m^{-3}) with strong ebbing flows (about 0.4 ms^{-1}) apparent near the surface. Near bed velocities are of the order of just 0.1 ms^{-1}. Subcritical values of F_Δ^2 throughout the transect indicate a high degree of stratification together with little shear or mixing between the layers. F_2^2 is zero throughout the transect at this stage of the tidal cycle, implying that the lower layer is inactive. It does not, therefore, provide the required interaction with the bathymetry to provide a hydraulic control point. The absence of a control point is affirmed by a Froude number plane analysis. Whilst one control point is indicated, it occurs in the upper layer only, similarly to the situation at LW during a spring tide. The weak control provided by the contraction in two-layer flows is thus not able to provide sufficient hydraulic control to allow frontal formation. A subcritical value of F_o^2 at the constriction at this time confirms the presence of a two-way exchange flow between estuarine and coastal waters, although distinct submaximal exchange flow is noted to occur.

This situation appears to continue for several hours, through LW, up to LW+2. Values of F_Δ^2 remain subcritical throughout the survey transect, confirming the stability of the stratified system during neap tides. Estimates of eddy viscosity at LW+1 ($N_z = 2.9 \times 10^{-7}$ m^2 s^{-1}) imply that turbulence is highly suppressed in the presence of the well-developed stratification. By LW+3, $N_z = 3.6 \times 10^{-4}$ m^2 s^{-1}, indicating an increased level of turbulent mixing occurring at the base of the pycnocline. This appears consistent with the observations from the field data that

the depth of the density interface is eroded gradually upward, towards the surface throughout the flooding neap tide.

The enhanced stratification observed during neap tides is likely to be due to the effects of tidal straining. Advection of buoyant estuarine water at the surface during the ebb, combined with the lower flow rates during the flooding tide maintains a degree of stratification throughout the neap tidal cycle. This enhanced stratification is then sufficient to 'damp out' the majority of turbulent interfacial mixing (Lewis, 1997). Such a tidal straining process is similar to that recorded by Simpson *et al.* (1990), and Nepf & Geyer (1996).

A first-order approximation of the environmental forcing conditions responsible for frontal formation may be achieved using the inflow Froude number, F_o^2 (equation 2.19). If h and b are regarded as quasi-steady, together with a constant value of ρ_2 (the recorded value of 1027 kg m^{-3} in this case), then control on the flow will be exercised by variations in the flow velocity V, and in the density difference between the layers, $\Delta\rho$. For a critical value of $F_o^2 = 1$, re-arrangement of equation 2.19 allows critical values of $\Delta\rho$ to be obtained, as V is increased:

$$\Delta\rho = \left[\frac{(VA)^2}{h^3 b^2} \Big/ g\right]\rho_2 \qquad (6.03)$$

The results indicate clearly that as flow velocity increases, a greater $\Delta\rho$ is permitted (Figure 6.29). Similarly as $\Delta\rho$ increases, a correspondingly greater flow rate is required to achieve a critical value of F_o^2. During spring tides, the range of flow values recorded at the mouth

(Table 6.03) is sufficient to reach a critical value of F_o^2 given the density differences recorded between the layers at this time. In fact, at a maximum flow speed observed during the flooding spring tide of 0.58 ms^{-1} (Table 6.02), an increase in $\Delta\rho$ to 0.82 $kg\ m^{-3}$ would still allow the formation of the frontal system. The range of parameters within which the frontal system could form during a spring tide is represented on Figure 6.29 by the grey shaded area. Compared with the recorded value of $\Delta\rho$ at LW+1 of 0.6 $kg\ m^{-3}$, however, a further reduction in the density of the surface layer of 0.22 $kg\ m^{-3}$, corresponding to a reduction in salinity of only approximately 0.2 is permitted. This highlights the relatively critical balance between $\Delta\rho$ and V in frontal formation.

The non-appearance of the tidal intrusion front during neap tides can also be examined using F_o^2. The black shaded area on Figure 6.29 represents the range of flow values and $\Delta\rho$ values recorded during the early part of the flood during a neap tide. The high $\Delta\rho$ values at the mouth of the estuary at this time, caused by the presence of the buoyant surface layer (and exacerbated by tidal straining) do not correspond with the high flow speeds required for a critical value of F_o^2. Assuming the peak flow values during a neap tide would not exceed 0.43 ms^{-1} (Table 6.02), the required $\Delta\rho$ to allow frontal formation is found to be 0.5 $kg\ m^{-3}$ (equation 6.03). If the temperature is assumed to remain constant at its observed surface value, a surface salinity value of approximately 34.5 would be required to create a critical value of F_o^2, and allow frontal formation. As recorded salinity values were < 25 throughout the flooding neap tide, the front did not occur.

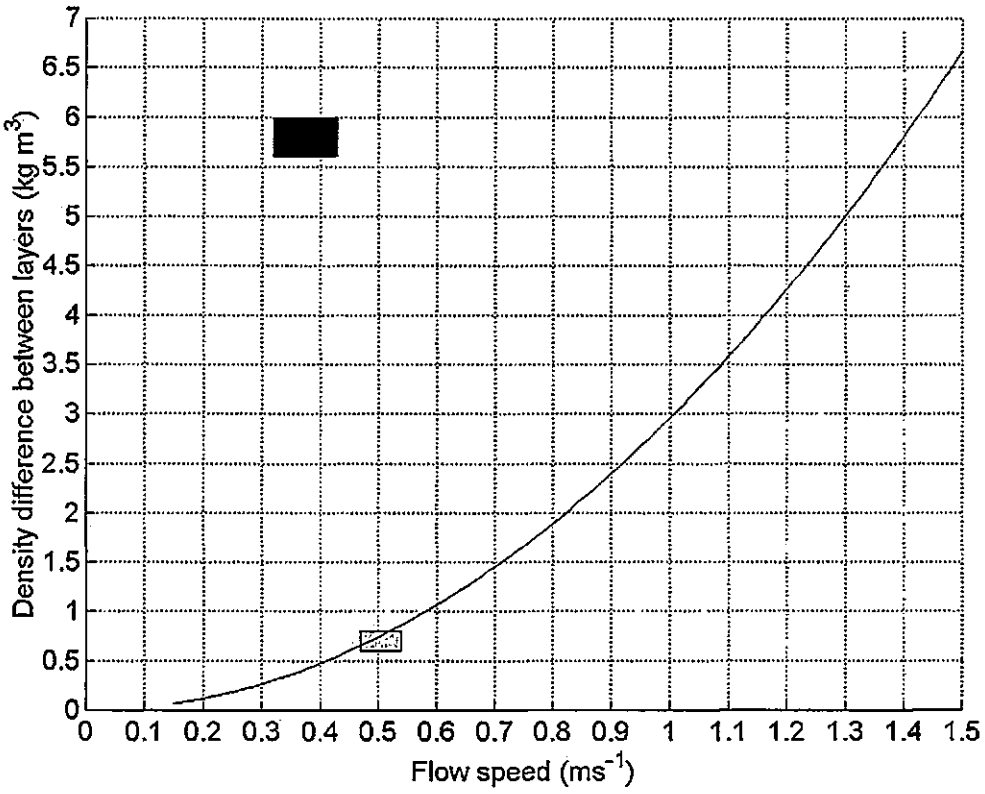

Figure 6.29. Critical values of the inflow Froude number (F_o^2), plotted in terms of flow speed (V) and $\Delta\rho$ in the constriction. The grey shaded area represents recorded parameters when the front was present during spring tides. The black shaded area represents recorded parameters during neap tides.

From the alternative perspective of flow speed, equation 2.19 can be re-arranged to yield a critical value of V, *i.e.* the flow velocity required in the presence of the pronounced stratification during a neap tide to arrest the buoyant outflow:

$$V = \frac{\sqrt{(g'h^3b^2)}}{A} \qquad (6.04)$$

yielding a required flow speed of 1.38 ms^{-1} during a neap tide. This value is clearly significantly greater than the actual flow velocity at this time (0.43 ms^{-1}). The non-appearance of the front during neap tides appears, therefore, to be due to the considerably greater stratification (due to tidal straining), combined with the slightly lower recorded flow speeds. The formation of the tidal intrusion front in the Dart estuary is thus caused by a constriction at the estuary mouth, followed by an increase in channel cross-sectional area caused by a seabed depression, in combination with a critical combination of $\Delta\rho$ and V. As V changes, therefore, through the spring-neap tidal cycle, and $\Delta\rho$ varies with freshwater runoff into the estuary, so the appearance and intensity of the frontal system is likely to vary on a tidal and seasonal scale.

6.4. Evaluation of frontal descriptors

6.4.1. Composite Froude number

The composite Froude number (G^2), comprising the sum of the densimetric Froude numbers for the upper and lower layers (F_1^2 and F_2^2 respectively) has proved to be invaluable in explaining the formation and behaviour of a tidal intrusion front. Supercritical values of G^2 have represented accurately a homogeneous water column, particularly notable in the rapid flows through the constriction at the entrance to the Dart estuary. Most usefully, a value of G^2 of unity was recorded at the plunge point during the spring tide evolution of the frontal system. Conforming exactly as predicted by hydraulics theory, and driven entirely by a change in the *lower* layer from supercritical to subcritical, the location where $G^2 = 1$ enabled the identification of the location of the hydraulic control point at the mouth of the estuary. In this way, the important interaction of the stratified flow with the seabed bathymetry was highlighted. The magnitude of the hydraulic jump occurring across the frontal interface has

also been estimated using G^2. This hydraulic jump was shown to become stronger at LW+2, as the strength of the barotropic forcing increased. The increasing intensity of this stationary hydraulic jump is likely to be a critical factor in frontal persistence, as the mixing in the area of the jump increases.

During the neap tide, when the tidal intrusion front did not form, G^2 again provided useful insights into the flow hydraulics. Values of G^2 were noted to undergo the transition from supercritical to subcritical in some areas, in a similar manner to that recorded during a spring tide. These changes were, however, found to be caused by flow transitions in the buoyant upper layer only (F_1^2). Importantly, the lower layer (F_2^2) was indicated to be subcritical throughout the flooding neap tide, thus not interacting with bathymetric changes to provide a hydraulic control point. The use of G^2 has, therefore, highlighted that changes in channel depth are more important than changes in width for tidal intrusion front formation at the entrance to the Dart estuary. A transition of G^2 from supercritical to critical or subcritical thus provides a clear indication of the existence of a front, and some indication of the magnitude of mixing occurring across the frontal zone (the intensity of the hydraulic jump). It should be highlighted, however, that the flow transition must be driven by the lower layer, particularly where bathymetric changes at the mouth are pronounced.

6.4.2. Shear Froude number

The shear Froude number (F_Δ^2) has proved to be an excellent frontal discriminator. During a spring tide, supercritical values of F_Δ^2 were noted through the constriction at the estuary mouth, indicating flows on the brink of instability and mixing prior to plunging. When the

tidal intrusion front had formed at LW+1, F_Δ^2 was noted to be supercritical upstream of the front, through the channel constriction, and subcritical immediately downstream of the frontal interface. This parameter thus differentiated clearly between the well-mixed water column upstream of the frontal interface, and the two-layer, stratified regime persistent downstream. The increasing depth over the seabed depression was enough to make F_Δ^2 abruptly subcritical, highlighting the importance of changes in bathymetry in frontal evolution. The extent of the change in F_Δ^2 across the frontal interface also provided some insight into the intensity of mixing occurring across the frontal zone. The increasing drop in F_Δ^2 across the frontal interface at LW+2 highlighted the increasing shear occurring, as the barotropic forcing increased by this time. During neap tides, F_Δ^2 remained subcritical throughout the transect. A degree of shear and mixing was indicated at LW+1 and LW+2, providing important evidence that the pronounced density interface was gradually eroding. The persistent stratification, combined with lower flow velocities ensured that F_Δ^2 remained subcritical despite the changes in the total water depth.

A spatial change in F_Δ^2, from supercritical to subcritical, indicated reliably the location of the inflow plunge point when the front was present. This parameter reflected accurately the required balance of flow and density differences across two layers, and the critical role that changes in the total water depth have been found to play in frontal formation. It was also possible to parameterise the mixing in the frontal zone using this descriptor, providing an indication of frontal stability.

6.4.3. Inflow Froude number

The inflow Froude number (F_o^2) has been found to provide a clear, first-order indication of the existence of a hydraulic control point at the mouth of the Dart estuary. During spring tides, at LW-1, a supercritical value of F_o^2 reflected accurately that no seawater intrusion was possible at this time. At LW, F_o^2 indicated clearly that two-way exchange flow was occurring between estuarine and coastal waters. By LW+1 and LW+2, when the tidal intrusion front was present, supercritical values of F_o^2 identified the existence of a hydraulic control point, and confirmed the blocking of the buoyant estuarine outflow. In addition, the location of the plunge point, or virtual hydraulic control was also indicated accurately to move further downstream as barotropic forcing increased. During neap tides, F_o^2 was subcritical throughout, and although a critical value was approached at LW+2, the flow speeds were not sufficient to block the estuarine outflow at this time. This identified correctly that no hydraulic control point was created, and the tidal intrusion front did not form. The subcritical values provided further evidence for the exchange flow prevailing through the channel constriction for the majority of the flooding neap tide.

A supercritical inflow Froude number has been found to provide a good indication of whether a tidal intrusion front will form near the estuary mouth. The magnitude of F_o^2 also indicated where the plunge point (and thus the location of the frontal interface) would occur in relation to the hydraulic control point at the channel constriction. In addition, this parameter provided some measure of the efficiency of exchanging estuarine and coastal flows through the mouth at some stages of the tide. This parameter may have even more use in such an estuary when

one considers that measurements need only be taken at one point (*i.e.* at the most constrictive section of the mouth) to ascertain whether, and approximately where a front will form.

6.4.4. Interfacial Froude number and layer Richardson number

The interfacial Froude number (*Fi*) displayed a marked variability throughout the flooding spring and neap tides. During some stages of the tidal cycle, *Fi* was found to be broadly supercritical through the constricted section of the estuary mouth and subcritical in other areas. Potentially useful in highlighting the homogeneous water column created by the rapid flows in the shallower areas, and the stratified flows allowed by the tranquil flows in deeper areas, the use of this parameter appears limited by its reliability. For example, when the tidal intrusion front was present at the estuary mouth, no change in *Fi* was noted across the frontal interface, *i.e. Fi* remained supercritical throughout this region of the survey transect. As there was an obvious change in state of the flow, and a hydraulic jump across the frontal interface indicated by other dimensionless descriptors, *Fi* was not capable of resolving adequately the presence of a tidal intrusion front.

The closely related layer Richardson number (Ri_L) also displayed a great deal of fluctuation throughout both the spring and neap tidal cycles. Whilst providing a degree of insight into the mixing processes during some parts of the tidal cycle, particularly the role played by interfacial shear in breaking down the frontal interface, the variability in Ri_L reduces confidence in the results. Both *Fi* and Ri_L have, therefore, been proved to provide results of an extremely unreliable nature, and be of relatively low resolution. It is likely that the dependence of both these parameters on the thickness of the upper layer only limits their use

when investigating topographically controlled flows, as other dimensionless descriptors have highlighted the critical role played by the lower flowing layer.

6.4.5. Gradient Richardson number

The gradient Richardson number (*Ri*) has not proved to be an accurate frontal discriminator. If the overlayed density contours were removed from Figures 5.17 and 5.18, it would not be possible to ascertain the location of the frontal interface. Some insights can be gained, however, into the state of the flow at some stages of the tidal cycle. When the tidal intrusion front was present during the spring tidal cycle, the existence of a pycnocline downstream of the front was well-resolved, as $Ri > 0.25$ throughout this area at LW+1 and LW+2. By LW+3, when decay of the front had taken place, $Ri < 0.25$ at the majority of the measuring stations, indicating turbulent flow, although there are still areas of stability indicated during this hour of tide. Across the frontal interface, $Ri < 0.25$, which could support the implications derived from results of F_{Δ}^{2}, indicating some shear-induced erosion of the density interface occurring at this time. During neap tides, the highly stratified water column, with its shallow pycnocline, was resolved adequately by *Ri*. Resolution in the lower layer beneath the pycnocline is not good, however, and the highly variable nature of *Ri* in this area reduces confidence in this parameter further.

Ri clearly does not resolve adequately the presence of a tidal intrusion front in this case. Values are generally variable throughout the survey transect, which may be a function of the critical value used, the ensemble averaging process, or the fact that shear instability may not be a particularly important process in tidal intrusion front formation. If the front is caused by an adjustment in flow associated with variations in bottom topography, it may not be spatially

well-described by this parameter (Brubaker & Simpson, 1999). It must also be borne in mind that the assumption must be made when using *Ri* that there is no longitudinal density gradient present. As a discontinuity in the density field is a frontal signature, *Ri* must, therefore be unsuitable as a frontal descriptor. Additionally, there may be a 'phase lag' in the results if used to infer mixing conditions, as it takes some time for mixing to take place, or an area of stratification to form (Lewis, 1997). The instability implied across the frontal zone at mid-depth during LW+1 may, therefore, not actually cause a breakdown in the density interface until some time later.

The dependence of eddy viscosity (N_z) on *Ri* also implies that caution should be exercised in the interpretation of N_z values in the analysis of stratified flows. If *Ri* is a relatively poor quantitative and qualitative indicator of mixing, then the Munk & Anderson (1948) parameterisations of the eddy coefficients using *Ri* (equation 6.03) must questioned (Peters, 1999). Alternative relationships have been examined (Dyer, 1988), although there appears to be no universally accepted solution at the present time.

7.0. Operation of a multibeam sonar system across a tidal intrusion front

7.1. Chapter overview and summary

Multibeam sonar systems, in use since the 1970's can reduce significantly the time required to conduct a bathymetric survey. The use of up to 120 separate, narrow acoustic beams enables the ensonification of a beamwidth, or 'swath' of around 150°. Present survey accuracy recommendations require 100% seabed coverage in shallow water, and have stringent depth error minimisation requirements. Depth errors caused by refraction of the sound rays through the water column are greatest at the outer beam angles, the traditional survey solution being to simply reduce the maximum swath width to remove the grossly refracted outer beams. This common approach is, however, rather rudimentary, and the reduced swath width usually requires the addition of more survey lines to be sailed by the vessel, reducing survey efficiency. Particular problems may be encountered when employing the traditional surveying approach of taking sound velocity profile measurements at the commencement of each survey line. This sound velocity information (the 'predicted' sound velocity profile) is then used by the multibeam sonar system software, to calculate and remove refraction artefacts. If the sound velocity is altered, for example, by sailing into a water mass different from that predicted (resulting in an 'observed' sound velocity profile), the refraction-induced depth errors would increase.

Three sonar refraction models have been developed and tested as part of this study, in order to quantify depth inaccuracies arising from such sound velocity profile errors. Model One imitates a cylindrical transducer array, where no electronic beam steering in utilised. Model Two mimics a flat transducer array, employing electronic beam steering to launch the narrow beams at the correct departure angle from the transducer face. Model Three is similar to

Model Two, but assumes that constant updates of surface sound velocity are received at the transducer face. Each model assumes the water column to be divided into two main layers, employing a constant sound velocity gradient solution in each layer for maximum accuracy. Following a comprehensive sensitivity analysis, sound velocity data derived from measurements in the Dart estuary during both a flooding spring and neap tide have been used to drive each of the three models. Contoured results of refraction-induced depth errors along the entire survey transect, from one hour before low water (LW-1) to thee hours after low water (LW+3), indicated that the use of Model Two provided the most accurate overall performance.

This depth error analysis indicated clearly that current sound velocity sampling practice when surveying in estuarine environments should be updated with immediate effect. The frequency of sound velocity sampling should be less than 50 m spatially, and less than one hour temporally. If such a sampling regime is not possible, the use of an appropriate multibeam sonar refraction model would facilitate the enhancement of both survey accuracy and efficiency.

7.2. Surveying in shallow water

Accurate hydrographic information is required to make informed decisions. These decisions may range from those taken during vessel navigation, military operations, coastal zone management, environmental monitoring, hydrocarbon and mineral exploitation, legal boundary delimitation, oceanographic modelling, or engineering and construction planning. The majority of users in these fields now require hydrographic data to be up-to-date, reliable, detailed, accurate and available in digital form. Surveying in shallow water has become the

focus of increasing attention recently. Naval emphasis and strategy is shifting towards the littoral zone, with the definition of littoral in the military sense referring to the continental shelf, coastal waters and estuaries. Commercial users of hydrographic data are demanding increasing accuracy of, and confidence in, shallow water bathymetric data. For example, the competitiveness of a particular harbour may be enhanced considerably by a high-specification bathymetric survey allowing the use of dynamic underkeel clearance management. In this way, extremely small margins under the keels of even the largest tankers can allow them port access. The performance and accuracy of commercially available surveying equipment is, therefore, critical in a wide variety of applications.

7.2.1. A historical perspective

Single beam echo-sounders have been in common hydrographic use for over 50 years. The technology involved is now at a mature level, and has been used with confidence in a full range of water depths. By simply measuring the time taken (t) for a short pulse of sonar energy (a 'ping') to travel from the transducer to the seabed and back, depth (D) can be derived from the following equation if the velocity of sound in seawater (c) is known:

$$D = \frac{vt}{2} \qquad (7.01)$$

The majority of general purpose hydrographic single beam echo sounders have beamwidths of between 10° and 30°, and depth measurements rely heavily upon the assumption that the seafloor is relatively flat. The minimum slant range is then a reasonable approximation of the

vertical depth of water at that point (Miller *et al.*, 1997). The orientation of the vessel upon which the transducer is mounted is not required, as the assumption is maintained that the main lobe of the transducer beam is vertical beneath the vessel. The assumption holds best with narrower beam systems in low sea states, as vessel movement, and thus the angular movement of the sonar beam is minimised. The obvious limitation is that no information is recorded outside the relatively narrow immediate beam footprint (Figure 7.01), and therefore, the bathymetry cannot be described between survey line spacing.

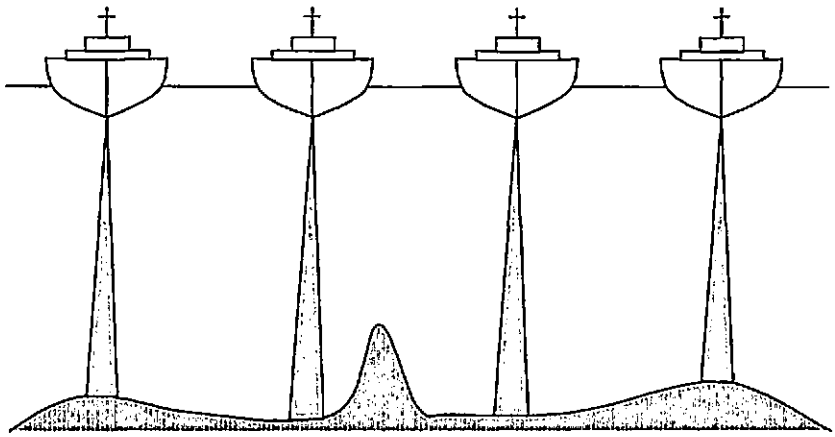

Figure 7.01. Consecutive survey lines using a single beam echo sounder.
The necessary distance intervals between the survey lines may result in important bathymetric information being missed.

The introduction of sidescan sonar in the 1950's did much to alleviate this limitation. Consisting of a towed body with a transducer on either side, a wide beamwidth ensonifies a correspondingly larger seafloor area (Figure 7.02). The changing intensity of acoustic backscatter, over changing seabed relief, provides a qualitative assessment of the bathymetry (Plate 7.01). Measurement of any shadows cast by the sidescan sonar can provide an

approximation of an object's height, however, as beam angle is not known accurately, an accurate calculation of depth cannot be made.

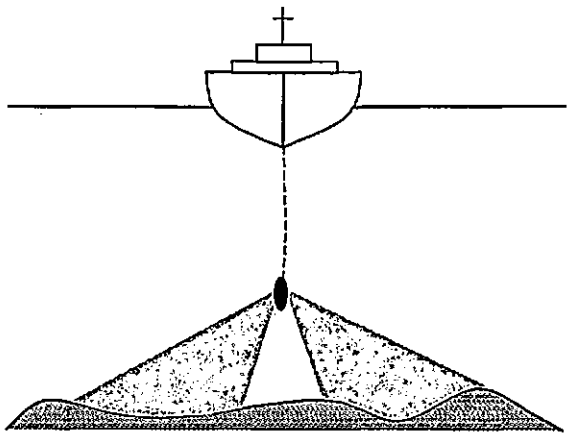

Figure 7.02. Operation of a side scan sonar system.
A towed body emits a wide beamwidth sonar pulse to either side. Measurement of the acoustic intensity of the returning signal allow a qualitative assessment of bathymetry to be made.

Multibeam sonar systems were first developed in the 1970's by the United States Naval Oceanographic Office to overcome this problem. The cold war drove a requirement for the ability to map the seabed with increasing accuracy, principally for submarine navigation and mine warfare purposes. Multibeam echosounders measure the slant range travel time of a short, narrow beamwidth acoustic pulse, travelling from the transducer to many points on the seafloor and back. Typically, up to 120 of these acoustic pulses, covering a beamwidth or 'swath' of 150° are sounded at one time. As both the beam angle and slant range of each pulse, or beam, is known accurately, an accurate measure of depth can be obtained from each beam (Hughes Clarke *et al.*, 1996). Providing quantitative bathymetric information (as opposed to the qualitative information provided by a sidescan system), a 150° beamwidth

Driven by the requirements of the oil industry operating in the Norwegian sector of the North Sea, and by improvements in technology and computer processing power, multibeam systems have been used more commonly over the last 10 years. Civilian and naval operators, attracted by the inherent efficiencies in multibeam surveying, have been using them increasingly in offshore engineering applications and in shallow water surveying (Plate 7.02). With the development of geographic information systems (GIS), hydrographic survey data are being used by an ever more diverse group. Data are now being required in digital form to highly prescriptive quality standards, which may specify that up to 100% of the seafloor is ensonified to within 0.3 m of the true depth. With such stringent requirements, it is becoming increasingly important to consider all the influences on multibeam sonar accuracy, including those of the environment.

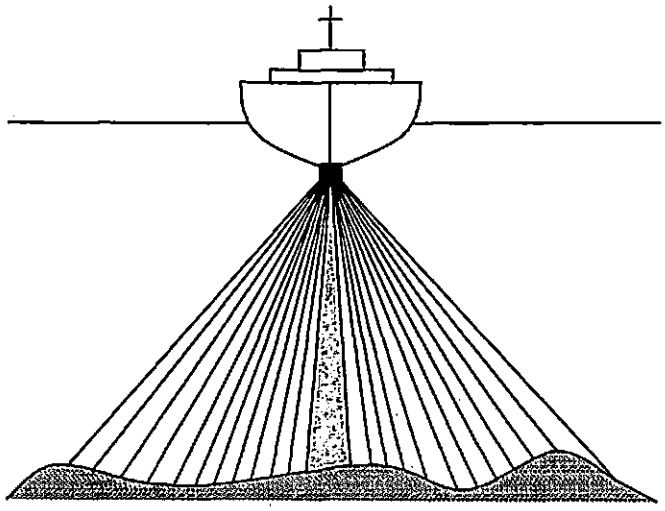

Figure 7.03. Comparison between a single beam echosounder (shaded area) and a multibeam system. The narrow, individual beams of a multibeam system, covering a wide seabed 'swath' enable greater survey efficiency.

The International Hydrographic Organisation (IHO) is responsible for setting standards for hydrographic surveys, world-wide. The IHO Special Publication No. 44 (referred to as IHO-S44) was first published in the 1960's, with a policy of revision every five years. The third edition of IHO-S44 was published in 1987 and, similarly to its predecessors, specified a single standard for hydrographic surveys. The single standard was based on the requirements for a nautical charting survey, and was based on the assumption of paper charts as the sole vehicle for data delivery. In addition, the assumption was made that data collection would be made primarily with a single beam echo sounder. At this time, a depth error of 0.3 m in depth of less than 30 m, and 10% of the depth in water depths greater than 30 m were the generic survey specifications. The latest edition of IHO-S44, the fourth edition, was finally published in 1998, taking into account the numerous recent developments in survey technology, including differential GPS, and multibeam sonar systems. The principle aim of this publication is:

> *"To specify the minimum standards for hydrographic surveys in order that hydrographic data collected according to these standards is sufficiently accurate and that the spatial uncertainty of the data is adequately quantified to be safely used by mariners (commercial, military or recreational) as primary users of this information"*

Recognising an increase in the number of different users of hydrographic data, and their differing accuracy requirements, the IHO (IHO, 1998) has now defined four categories, or 'orders' of survey (Table 7.01). Special Order hydrographic surveys are intended for use in specific critical areas, where bottom characteristics may be potentially hazardous to vessels, and where a minimum underkeel clearance exists. All error sources must be minimised, and

closely spaced survey lines must be used in order to ensure 100% sea floor coverage. Cubic features of a size greater than 1 m must be resolved clearly by the sounding equipment. Examples of Special Order survey areas are harbours, berthing areas and associated approach channels. The required horizontal positioning accuracy of seafloor features is 2 m (95% confidence level), with depth accuracy (95% confidence level) defined as:

$$\pm\sqrt{[a^2 + (\overline{b} * D)^2]} \qquad (7.02)$$

Where a is a constant depth error (sum of all constant errors), $\overline{b}$ is a the factor of depth dependent error, D is the water depth. Typically in 25 m depth, the required depth accuracy (equation 7.02) is 0.31 m.

Order 1 hydrographic surveys may be specified where underkeel clearances are less critical. Areas of high commercial shipping activity, including inland navigation channels and coastal areas, may still specify an Order 1 survey, provided the geophysical properties of the seafloor are less hazardous to vessels; for example, soft silt or sand beds. Order 1 surveys are generally restricted to depths of less than 100 m, and full seabed coverage is only required where the obstructions are potentially hazardous to vessels. Cubic features of a size greater than 2 m in depths up to 40 m, or greater than 10% of the depth in areas deeper than 40 m, must be resolved by the sounding equipment.

Order 2 surveys are intended for use in areas where the depth does not exceed 200 m, which are not covered by Special Order and Order 1 surveys. A general description of the

bathymetry is usually appropriate in an Order 2 area, ensuring that there are no obstructions which may present a danger to shipping. Similar to an Order 1 survey, full seabed coverage is only required in areas where the risk of obstructions may be a hazard to safe vessel navigation. Order 3 surveys are generally specified in water depths of greater than 200 m, and in all areas not covered by Special Order, Order 1 or Order 2 specifications.

	Special Order	Order 1	Order 2	Order 3
Examples of typical areas	Harbours, berthing areas, associated critical channels with minimum underkeel clearances	Harbours, harbour approach channels and some coastal areas with depths of up to 100 m	Areas not described by Special Order and Order 1, or areas up to 200 m water depth	Offshore areas not described by Special Order, Order 1 or Order 2
Horizontal accuracy	2 m	5 m + 5% of depth	20 m + 5% of depth	150m + 5% of depth
Depth accuracy for reduced depths	a=0.25 m b=0.0075	a=0.5 m b=0.013	a=1.0 m b=0.023	a=1.0 m b=0.023
Example depth accuracy required in 25 m depth	0.31m	0.6 m	1.15 m	1.15 m
100% bottom search	Compulsory	Selected areas	Selected areas	Not applicable
System detection capability	Cubic features > 1 m	Cubic features > 2 m in depths < 40 m; 10% of depth beyond 40 m	Same as Order 1	Not applicable
Maximum line spacing	Not applicable, as 100% search is compulsory	3x average depth, or 25m whichever is greater	3–4x average depth, or 200m, whichever is greater	4x average depth

Table 7.01. The four categories, or 'orders' of survey as currently defined by the International Hydrographic Organisation (IHO, 1998).

To create the required short acoustic pulse at the desired beam angle, two common multibeam transducer configurations are used, a cylindrical array or a flat array. Flat arrays are available in a variety of geometries, including uniform line, V-shaped and Mill's cross arrays. All flat arrays operate in a similar manner, with beam launch angle determined solely by phase-controlled beam steering (deMoustier, 2003a). The individual beams at varying departure angles from the array are created by triggering the elements further from the wave front at a later time (Figure 7.05). Note that all beam angles are defined as per sonar industry standards, with vertically down being 0° and a horizontal line towards starboard at +90°.

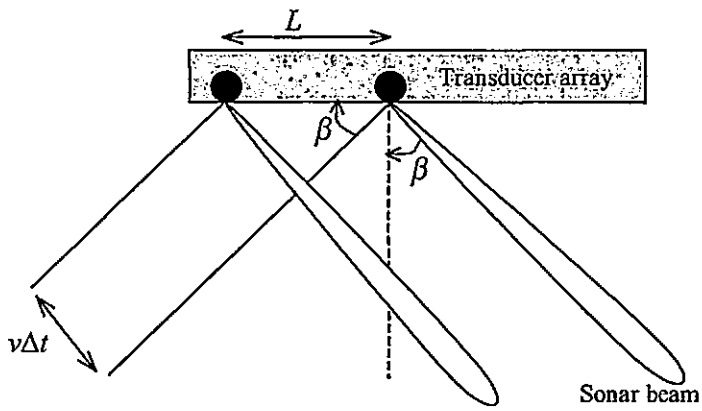

Figure 7.05. Principles of using phase controlled beam steering with a flat array to produce beams of varying departure angle.

For a flat transducer to steer a beam non-orthogonally to the transducer face by an angle β, the transducer element spacing (L) and the velocity of sound in seawater (c) can be used to calculate the time delay in seconds (Δt) thus (Hare *et al.*, 1995):

$$\Delta t = \frac{L \sin \beta}{f \lambda} \qquad (7.03)$$

With a multibeam system using a cylindrical array, the beams may be formed perpendicular to the tangent of the array curve with zero, or negligible beam steering required (Figure 7.06). The beam launch angle is determined by selecting the appropriate sector of the array at 90° to the desired launch angle.

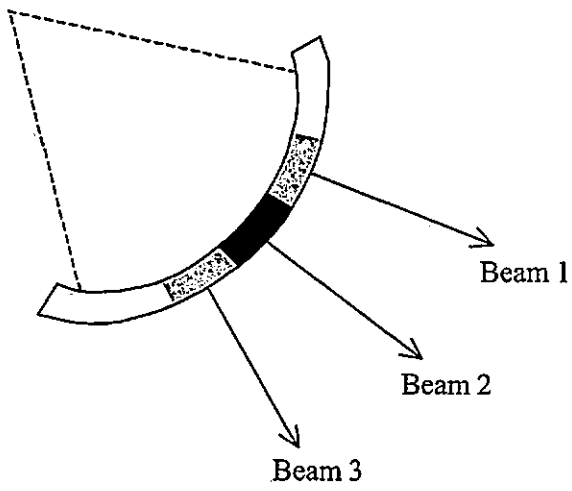

Figure 7.06. Operation of a cylindrical transducer array.
The beam launch angle is determined by selecting the appropriate sector of the array.

If the launch angle of each beam is known accurately, the measured two-way travel time of the sonar pulse (slant range) may be transformed into a geo-referenced depth (Figure 7.07). A number of parameters are required for this transformation, which is conducted separately for each beam. These include the position of the survey vessel (or more accurately, the

transducer), the pitch, roll and heading of the ship, and changes in the sound velocity with depth (Dinn *et al.*, 1997). Current multibeam sonar systems range in frequency from 12 KHz to 455 KHz, with the lower frequencies providing longer ranges, but a lower resolution.

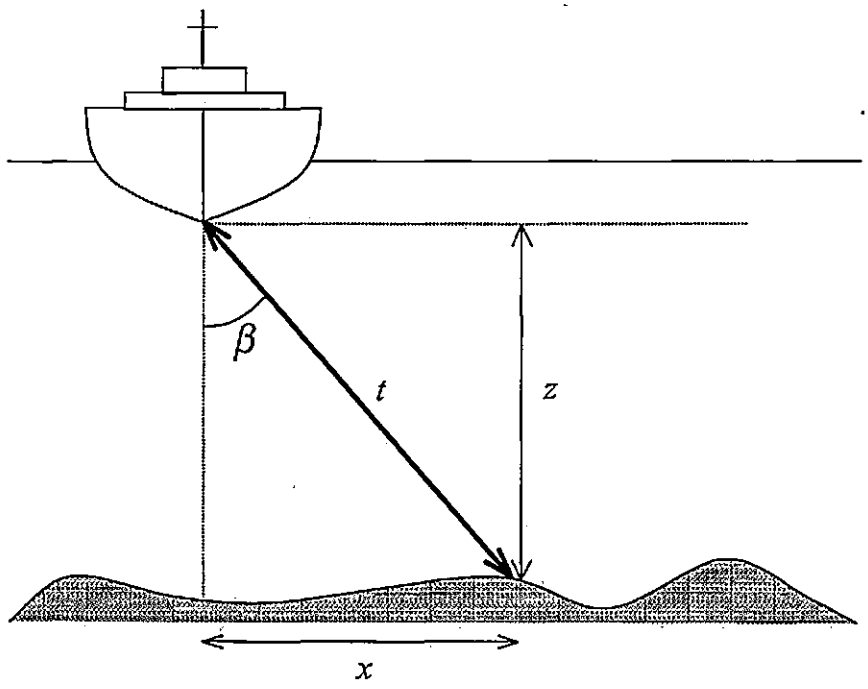

Figure 7.07. Measurement of bathymetry by a multibeam echo sounder.
Calculation of depth (z) and across track distance (x) is possible if the launch angle of the beam (β) and the two-way travel time (t) of the ray is known accurately.

7.3.2. Multibeam systems in common commercial use

The hydrographic surveyor has an ever-increasing choice of multibeam sonar system available on the open market, which can be grouped into three main categories (Lurton, 2002):

- Deep water systems. Typically operating at relatively low frequencies (around 12 kHz) for greater range. The large array dimensions involved limit their installation to large deep-sea vessels.
- Shallow water systems. These systems are designed for mapping continental shelves, and operate typically in the 100 kHz to 200 kHz band.
- High-resolution systems. These systems operate at high frequencies (typically 300 kHz to 500 kHz), and are used in shallow water for higher order surveys. Their small array size makes them suitable for installation on small coastal survey vessels or remotely operated vehicles (ROV's).

The three major manufacturers of multibeam sonar systems at the present time are Simrad AS in Norway, Reson AS in Denmark and L3 Elac Nautik GmbH in Germany. By 2001, over 700 multibeam echo sounders had been commissioned, with over two thirds of them supplied by the two Scandinavian manufacturers above (Lurton, 2002). All three companies offer an off-the-shelf, 'turn-key' approach to surveying, *i.e.* following installation of the survey transducers and equipment aboard a survey vessel, accurate bathymetric data can be collected with little more effort on the part of the surveyor other than turning on the equipment and steering a steady course. This is a significant oversimplification, however, and the numerous potential errors (Section 7.3.3.) need to be taken into account in order to record accurate bathymetric data.

The majority of multibeam sonar systems are broadly similar, with the choice of operating frequency, and the associated depth of operation being a prime consideration (Table 7.02).

Variations in transducer array configuration (cylindrical or flat arrays) and beam spacing are also worthy of attention.

Manufacturer	Simrad			Reson	L3 Elac
System	EM3000	EM1002	EM1000	Seabat 8111	SB1180
Year introduced	1999	1999	1998	1999	1997
Frequency (kHz)	300	95	95	100	180
Transducer type	Flat (*2)	Cylindrical	Cylindrical	Flat transmit Cylindrical receive	Flat
No. of beams	127	111	60	101	126
Approximate beam spacing (°)	0.9	0.5-1.5	2.5	1.5	1.25
Maximum swath width (°)	120	160	150	150	157

Table 7.02. Specifications of a selection of the most common commercially available multibeam sonar systems.

Three of the most popular systems by Simrad AS have been included for examination (Table 7.02). Most of these systems have numerous parameters which may be altered by the user, including a choice of equi-angular or equi-distant beam spacing. Equi-angular spacing, as the name suggests, spaces each consecutive beam at discrete, fixed intervals (Figure 7.08). The result is that the beam footprint spacing on the seafloor will vary with beam angle (Figure 7.09). The recorded depth measurement is a centrally-averaged point from the seafloor, ensonified within the larger beam footprint. The outer beams centres are spaced further apart than those directly underneath the transducer; thus, resolution of seabed objects will

deteriorate with increasing beam angle, as more averaging is undertaken across a larger area (Miller *et al.*, 1997). In addition, complete seabed coverage is not possible at the outer beam angles. This can be an important consideration for the surveyor, as some IHO survey specifications demand 100% seabed coverage (Table 7.01).

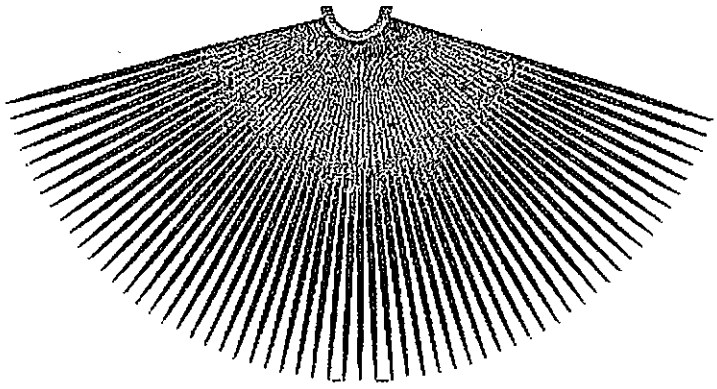

Figure 7.08. An example of a multibeam sonar system using equi-angular beam spacing. (Image courtesy of Hughes Clarke *et al.*, 2003)

Alternatively, equi-distant beam spacing (Figure 7.10) varies the angle between individual beams to produce a regular beam footprint spacing on the sea floor (Figure 7.11). Seabed coverage for the outer beam angles is improved in comparison to equi-angular spacing. This method also improves the resolution of targets ensonified by the outer beams, as they are spaced more closely together. Coverage directly beneath the transducer, however, is rather sparse, with fewer beam 'strikes' per target area. The choice between equi-distant and equi-angular operation is made by the operator, with consideration of the likely maximum swath width to be used.

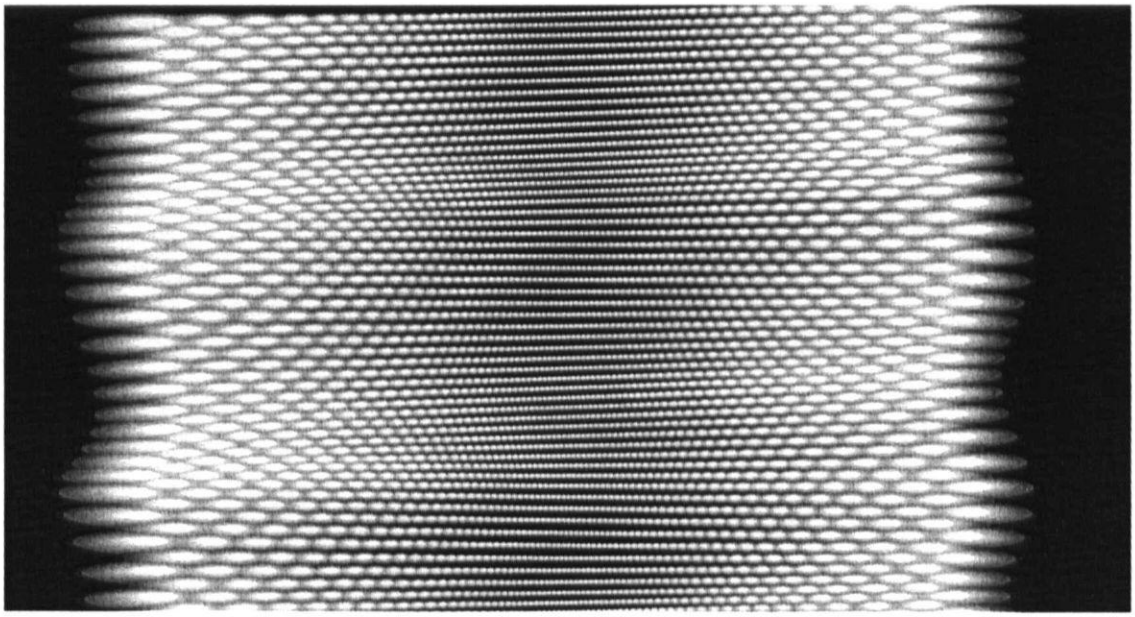

Figure 7.09. Sea floor footprints of each beam using equi-angular beam spacing.
Each white area represents an ensonified area of the seabed. Note that the outer beams are more widely spaced, reducing resolution. (Image courtesy of Hughes Clarke *et al.*, 2003)

Both cylindrical and flat transducer arrays are available from all the major manufacturers. Flat arrays are generally more limited in swath width, although their beamforming characteristics allow the creation of beams that are narrow in both the fore-aft and athwartships dimensions, thus improving resolution (deMoustier, 2003a). It should also be noted, however, that the beamwidth of the individual beams increases, with a corresponding reduction in resolution, with increasing beam angle (β) from the vertical. Cylindrical arrays (Plate 7.03) offer wider swath widths, and a constant beam width for all beam angles. The formation of each beam is computationally intensive, however, as the calculation must include the beam pattern of each element in the array sector of interest in order to compensate for the change in amplitude and phase from one element to the next around the curve (deMoustier, 2003a).

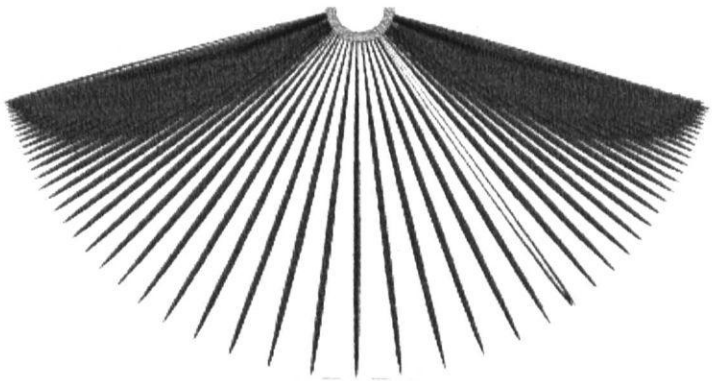

Figure 7.10. An example a multibeam sonar system using equi-distant beam spacing. (Image courtesy of Hughes Clarke *et al.*, 2003)

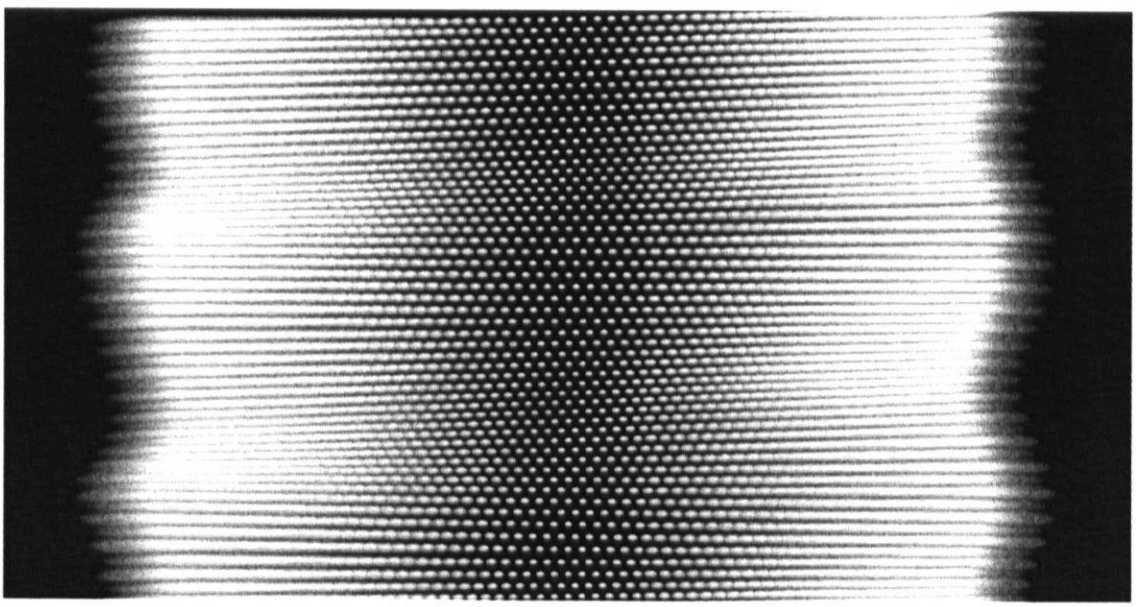

Figure 7.11. Sea floor footprints of each beam using equi-distant beam spacing. Each white area represents an ensonified area of the seabed. Note that the near-nadir beams are relatively widely spaced, reducing resolution. (Image courtesy of Hughes Clarke *et al.*, 2003)

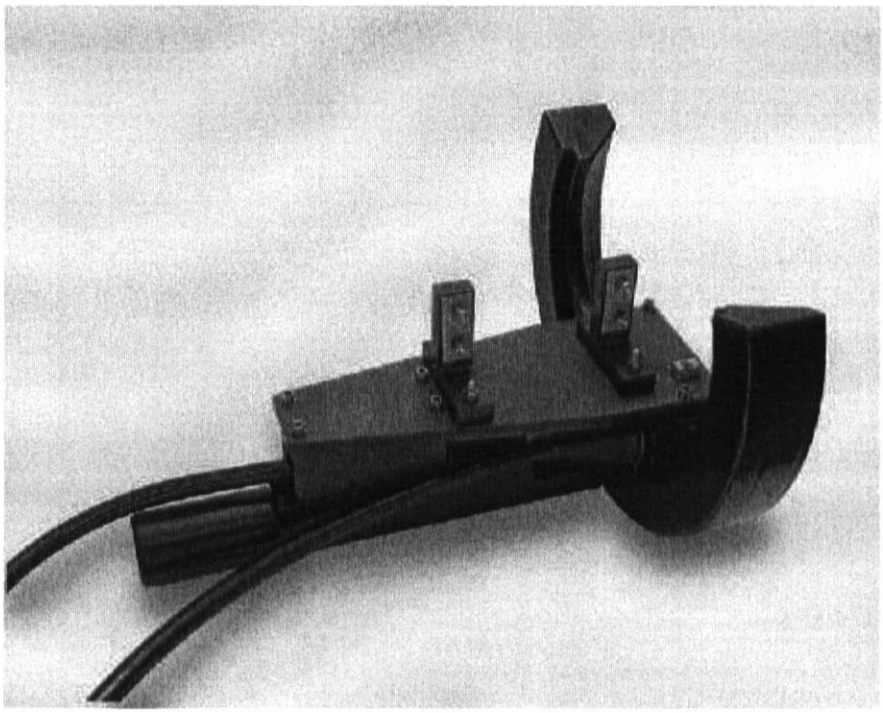

Plate 7.03. The cylindrical transducer of a Reson Seabat 8111 Multibeam sonar system.

7.3.3. Quantifying and controlling multibeam sonar errors

Multibeam sonar systems, with their capability to cover nearly 100% of the seabed, have been promoted heavily within the hydrographic community as the tool of the future (e.g. Hughes Clarke, 2000; Hogarth, 2003). If the entire beamwidth of a system could be utilised, allowing a swath width of up to 10 times the water depth, their rate of seabed coverage would be extremely high. Various system limitations, however, have limited survey line spacing to three or four times the water depth, with few hydrographic surveyors having the confidence to use the entire available beamwidth of their system.

A variety of errors, particularly apparent at higher beam angles from the vertical, serve to limit the efficiency of the multibeam sonar system. The measurement of the two way travel time undertaken by the multibeam system has to be made in the frame of reference of the ship on which the transducer is mounted. A number of parameters, many of which are measured at the time of the ping, are required to make the critical transformation from measured slant range travel times to accurate geo-referenced depths (Dinn *et al.*, 1995; Hughes Clarke *et al.*, 2003).

1. Geo-referenced position of the transducer
2. An accurate time measurement
3. The vector distance (x, y, z) in the ship frame of reference, between the transducer and the positioning sensor
4. Changes in average water level, due to tides and atmospheric effects
5. Vessel heave, or the vertical position of the transducer with respect to the average water level
6. Vessel attitude – pitch, roll and heading angles of the ship
7. Sound velocity changes with depth, a basic determinant of the launch angle using a flat transducer array, and path of the acoustic rays.

Even small errors in the measurement of any of these parameters can contribute significantly to the overall survey error budget; thus, they need to be addressed systematically and reduced (Hughes Clarke, 2003a).

The geo-referenced position of the transducer is almost always derived from the Global Positioning System (GPS). With differential corrections applied (DGPS), positioning can be obtained confidently to decimetre accuracy or better (Section 4.3.3.). The essential, highly accurate time stamp is generally also derived from the GPS receiver. The multiple sensors required for the transformation are often physically separated about the survey vessel. The relative location, orientation and time synchronisation of these sensors can be a problem, mitigated to a large extent by careful measuring and calibration by the field surveyor. Provided the location of each individual sensor about the vessel is determined with respect to a central reference point, and standard survey procedures are followed for field alignment of the sensors (the 'patch test', Hughes Clarke, 2003b), these systematic errors can be largely eliminated from the overall error budget.

Changes in local water level due to meteorological effects may be quantified accurately by the installation and careful monitoring of a local tide gauge. The change in the vertical position of the transducer relative to the reference surface of average water level derived from the tide gauge measurements is termed 'heave'. With conventional inertial sensors, heave can usually be measured to 10 cm in a frequency range of 0.05 Hz to 50 Hz (periods of between 20 s and 0.02 s). There can be problems, however, in keeping the heave error below 10 cm when encountering following seas with periods of longer than 20 s, and when there are changes in vessel squat and settlement at intervals longer than 20 s (Dinn *et al.*, 1997; Hughes Clarke *et al.*, 2003). These issues are now being addressed with the introduction of highly accurate DGPS. Resolution of the phase angle of the GPS carrier signal allows vertical position to be determined to within 5 cm with respect the Earth ellipsoid, making conventional heave sensors redundant.

The effects of not applying vessel pitch and roll corrections to each beam are two-fold. Firstly, as the vessel rolls, the entire multibeam footprint on the seabed 'wobbles' from side to side (Figure 7.12). The surveyor cannot be confident, therefore, that 100% seafloor coverage has been obtained, and significant survey line overlap (with a corresponding reduction in survey efficiency) is generally required to ensonify the entire survey area and satisfy the IHO-S44 requirements.

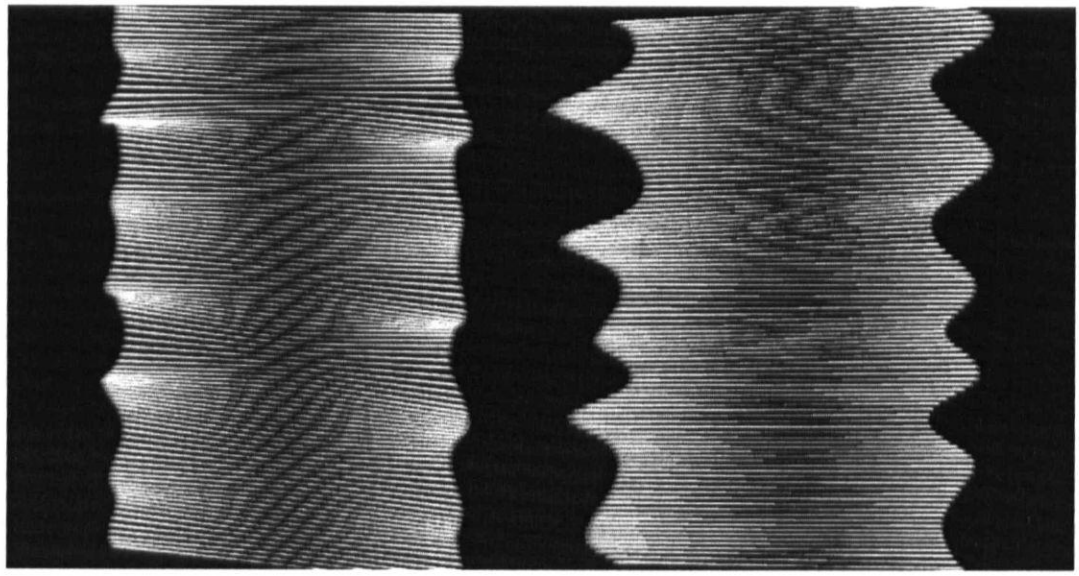

Figure 7.12. A multibeam echo sounder should compensate for the pitch and roll of the survey platform. The right-hand Figure represents no pitch and roll correction. The left-hand Figure represents a full correction applied to each ping cycle (Image courtesy of Hughes Clarke *et al.*, 2003).

Secondly, if the pitch and roll corrections are not applied at the time of the ping, the geo-referenced position of each individual beam will be incorrect. For example, if the steered beam angle (β) is increased by vessel roll, an uncorrected beam will strike a different part of the seabed to that intended (Figure 7.13). This error increases with increasing beamwidth, and

a multibeam sonar system with a beamwidth of 150° requires roll data to an accuracy of 0.05° to meet IHO-S44 standards (Dinn *et al.*, 1997). The latest generation of pitch and roll sensors, such as the POS-MV 320 and the Seatex AS from Norway enable extremely accurate, wide bandwidth (50Hz) position and attitude measurements to be made, determining pitch, roll, heading and yaw to within 0.05°, even on small coastal survey vessels. Thus, sensor technology has progressed to the point where vessel attitude no longer contributes significantly to the error budget, and the most significant limitation to wide-swath high quality data remains in imperfect water mass compensation (Hughes Clarke *et al.*, 2000).

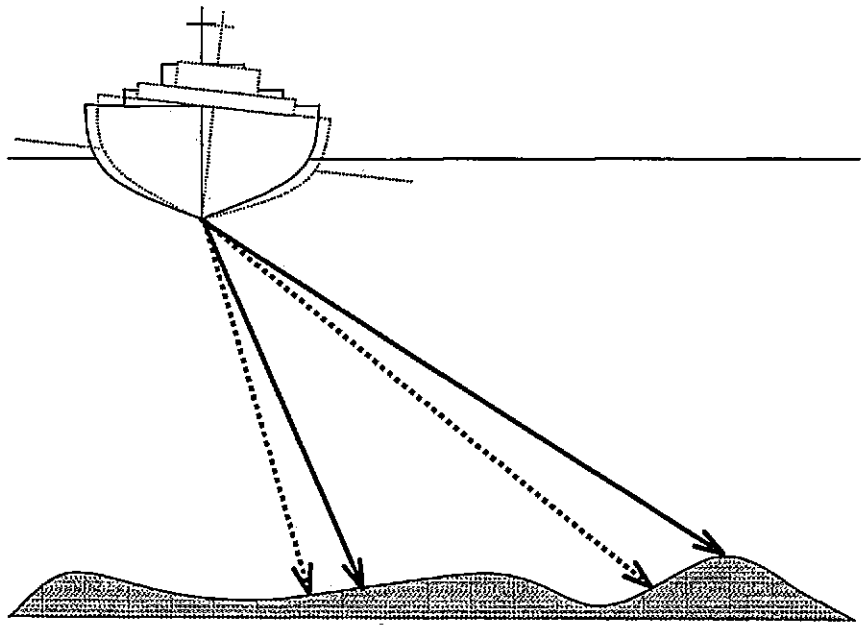

Figure 7.13. The effects of vessel roll on multibeam sonar accuracy.
As the vessel rolls, an uncorrected beam will strike a different are of the seabed to that intended. If roll is left uncorrected, depth errors can result.

The problem of not knowing, or under-sampling the water column variability is two-fold. Firstly, the launch angle (β) from the transducer of the acoustic beam may not be known accurately, due to poor knowledge of the sound velocity at the transducer interface. For any multibeam sonar system utilising a flat transducer array, individual acoustic beams are electronically steered to achieve the desired launch angles from the transducer face (Section 7.3.1.). In order to facilitate this electronic beam steering, it is necessary to know the transducer element spacing (L), the acoustic wavelength of the sound wave (λ) and the velocity of sound propagation in seawater (c). As:

$$c = f\lambda \qquad \text{ms}^{-1} \tag{7.04}$$

where f is the frequency of the acoustic signal in Hertz. Re-arranging equation 7.04 yields:

$$\lambda = \frac{c}{f} \qquad \text{m} \tag{7.05}$$

and therefore changing the speed of sound of seawater will clearly alter the wavelength of the sound wave. From equation 7.03:

$$\sin\beta = \frac{f\lambda\Delta t}{L} \tag{7.06}$$

When calculating the time delay between transducer elements, to achieve the required beam launch angle (β), the multibeam system assumes a fixed and constant value of sound speed at the transducer face. Altering c, therefore, (without an equivalent correction in f) will result in an error in λ, and a corresponding launch angle error. Such errors, caused by an incorrect sound velocity at the transducer face, will introduce an angular error independent of any subsequent ray tracing error. Some multibeam system manufacturers have attempted recently to reduce this beam steering error by mounting a time-of-flight sound velocity sensor near the sonar transducer (Hogarth, 2003). The sound velocity sensor continuously updates the multibeam software with the correct sound velocity, and therefore, launch angle errors should be negligible. In the case of a cylindrical type transducer array, the physical shape of the array determines the departure angle of the sound ray. No electronic beam steering is required, therefore, and changes in the sound speed at the transducer face will have no effect on the launch angle.

The second problem arising from not quantifying accurately the sound velocity changes in the water column is that of ray path deviation from the calculated path, due to errors in the sound velocity profile (SVP). Such SVP errors may arise either from inaccurate measurement, or by surveying into a new water mass without updating the original SVP. At each horizontal interface within the water column where the sound speed changes with depth, the sound wave will refract according to Snell's law (Figure 7.14):

$$\frac{\cos\theta_1}{c_1} = \frac{\cos\theta_2}{c_2} = \frac{\cos\theta_3}{c_3} = \frac{\cos\theta_4}{c_4} \qquad (7.07)$$

Where c_i is the sound velocity in layer i, and θ_i is the angle of incidence of the beam in layer i. Any errors in the measurement of the SVP will result in an error in c_i, and therefore, an angular error in refraction across the horizontal sound speed interface. This angular error can lead to horizontal positioning errors, and as the actual ray path differs from the predicted ray path, the travel time of the ray from the surface to the seabed may change. This altered travel time manifests itself as an error in depth (from equation 7.01). Both the horizontal and vertical positioning errors will increase from near-zero for the nadir beam (beneath the transducer), to a maximum at the outer beamwidths (deMoustier, 2003a).

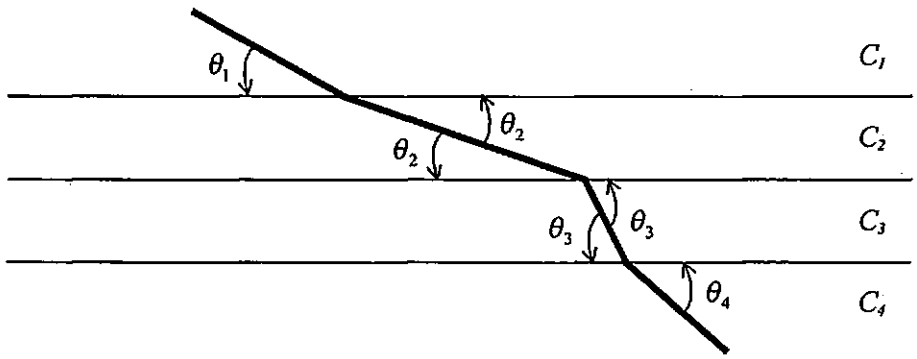

Figure 7.14. Refraction of a sound ray through several homogeneous layers, illustrating Snell's law.

Errors in the process of physically measuring the sound velocity profile can also contribute to the refraction error. At the present time, SVP's are collected using one of three techniques (Dinn *et al.*, 1997):

1. Sound velocity calculated from expendable bathythermograph (XBT) data, using one of several empirical sound velocity equations and a single salinity estimate.

2. Sound velocity calculated from CTD data, using one of several sound velocity equations.

3. Direct sound velocity measurement using a 'time-of-flight' sensor, whereby the travel time of an acoustic signal of known frequency, over a known (short) distance is used to derive the sound velocity through the medium at that time.

The first technique is used rarely in shallow water, as ignoring the influence of salinity when surveying on the continental shelf is likely to lead to significant errors. When using the second technique above, selecting the appropriate equation for the calculation of sound velocity from measured values of temperature and salinity needs to be undertaken with some care. Comparing the three most popular formulae in present use, Chen & Millero, MacKenzie and Medwin (Section 4.3.2.2.); differences in calculated sound velocity at the surface can be up to 0.3 ms^{-1} (Batton, 2004). With proper care taken in the design, calibration, deployment of the CTD, and in choosing the most appropriate equations, errors can be reduced to below 0.25 ms^{-1} (Dinn *et al.*, 1997). Direct measurement, or 'time of flight' sensors also experience a number of errors, including transducer ringing, multipath returns, and temperature effects on the path length and electronics. Proper design of the instrument can reduce many of these shortcomings, and the accuracy of these instruments can approach ± 0.1 ms^{-1} (Dinn *et al.*, 1997).

7.3.4. Present estuarine surveying practice – the time vs. accuracy problem

For the hydrographic surveyor operating a multibeam sonar system in shallow water, the principal barrier to survey accuracy remains that of sound velocity error. The oceanographic

conditions, principally salinity, temperature and density, which determine sound velocity are variable, both temporally and spatially. Traditional methods of monitoring such water column changes rely on stopping the vessel for periods of approximately 10 minutes, while a CTD sensor is lowered to the seabed. The sound velocity profile is then calculated using the most appropriate formula, and the data entered into the multibeam sonar system software prior to re-commencement of the survey. The time taken to conduct this entire exercise may be in excess of 30 minutes; thus, may appear prohibitively expensive in survey time. Survey agencies have traditionally been reluctant to take observations more frequently, and have thereby assumed implicitly that the spatial and temporal variability of the ocean could be described adequately using relatively sparse observations. If the water mass does change over time scales shorter than the sampling period, then significant errors in measured depths will result (Hughes Clarke *et al.*, 2000).

The problem of surveying to the required depth accuracy using a multibeam system is exacerbated in near-shore areas, where the competing influences of freshwater inflow and tidal mixing combine to result in rapid sound velocity changes over short time periods and distances (Dinn *et al.*, 1997). With the multibeam system software relying upon the most recently archived velocity profile to calculate the depth, departures from this profile will produce errors in both depth and horizontal position (Figure 7.15). Collection of a large number of spatially dense SVP's becomes critical in these near-shore areas, although there are no clear recommendations as to how frequent the sampling regime should be. Manufacturers of multibeam sonar systems still do not fully present, in a quantitative way, the implications of spatially or temporally under-sampling the sound velocity, and the majority of survey agencies do not appear to have well-researched guidelines on the frequency of sound velocity sampling, usually relying on the experience of the individual surveyor (Dinn *et al.*, 1995). Presently,

accepted industrial practice when surveying in an highly variable oceanographic environment, is to take a new SVP at the beginning and end of each survey line (Hughes Clarke *et al.*, 2003). This rudimentary methodology may not, however, be sufficient to collect bathymetric data which complies fully with the accuracy specifications of IHO-S44. Even in coastal areas, survey lines may be tens of kilometres long and take several hours of vessel time to complete. Clearly, significant water mass changes could occur within such an area, and recent instrument trials on the Georges Bank, Nova Scotia, noted a change in surface sound velocity from 1480 ms^{-1} to 1515 ms^{-1} over one 13 km long survey line (Hughes Clarke *et al.*, 2000).

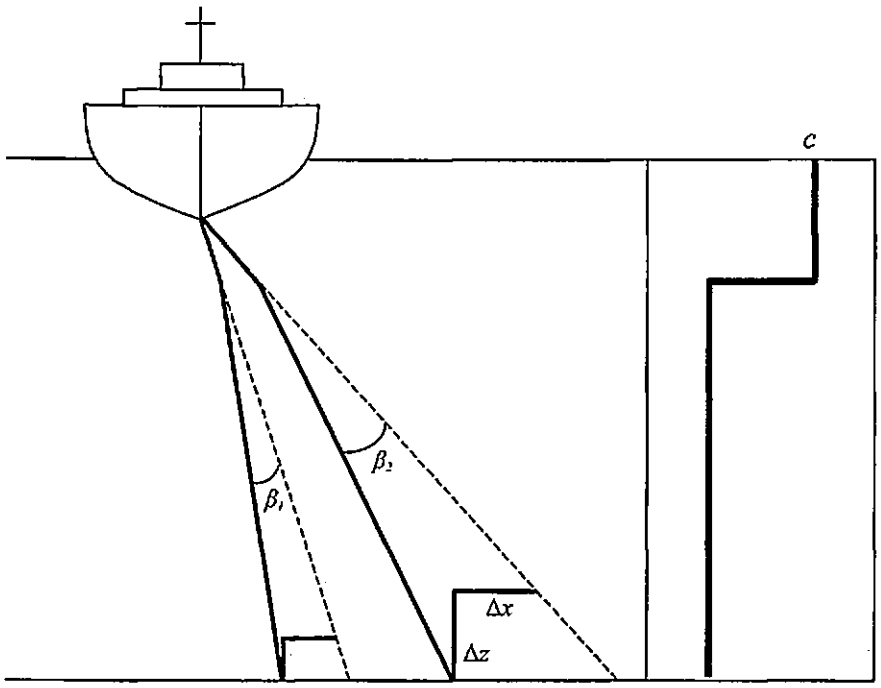

Figure 7.15. Refraction error caused by a discrete step in the velocity profile.
If this step in the profile remains uncorrected, horizontal (Δx) and vertical (Δz) errors will be produced. These errors increase with increasing beam angle (adapted from Hughes Clarke *et al.*, 2003).

Sound velocity has been noted to change significantly over extremely short temporal and spatial scales in estuarine environments. This variability has not been quantified adequately to date, and many surveyors remain relatively ignorant of the scale of the variability in shallow water, or choose to ignore it in order to expedite the survey results. Large estuaries, such as the Fraser River Delta in western Canada, with a considerable freshwater inflow, have yielded surface sound velocity variations of as much as 40 ms^{-1}, and vertical sound velocity variations of > 20 ms^{-1} during one survey period (Cartwright & Hughes Clarke, 2002). The Tamar estuary, UK, has been the subject of a recent study of sound velocity variability (Batton, 2004), although unfortunately, the measured values were not reported clearly. The presence of the tidal intrusion front in the Dart estuary has been noted to cause a change in surface sound speed of over 7 ms^{-1} across the frontal zone, a distance of less than 20 m (Thain & Priestley, 2002b; Priestley & Thain, 2003). The sudden change in water mass characterising the presence of a front usually manifests itself in the survey data in a fairly obvious way. To the experienced surveyor, a refraction artefact will usually present itself in the form of a 'smile' or 'frown' across display of the horizontal swath, with bathymetric errors increasing with increasing beam angle (Figure 7.16).

In order to overcome these issues, several techniques to improve the spatial density of SVP's have been proposed recently. These include using a continuously sampling, undulating sound velocity profiler (Cartwright & Hughes Clarke, 2002), or interpolation between discrete sound velocity profiles (Hughes Clarke *et al.*, 2000). The former, a relatively new development, remains subject to a number of problems, not least cost, and the regular loss of the undulating towed body. Attempts at post processing multibeam bathymetric data using SVP data interpolated from discrete profiles has improved accuracy, although a major limitation remains. If the sampling of the water column is relatively infrequent, there is little to be

gained by interpolating between SVP's, as the length scales of many oceanographic features, such as fronts are commonly smaller than the sampling distance. The installation of a continuously updating sound velocimeters at the transducer face in order to reduce beam launch angle errors has yet to become the industry standard.

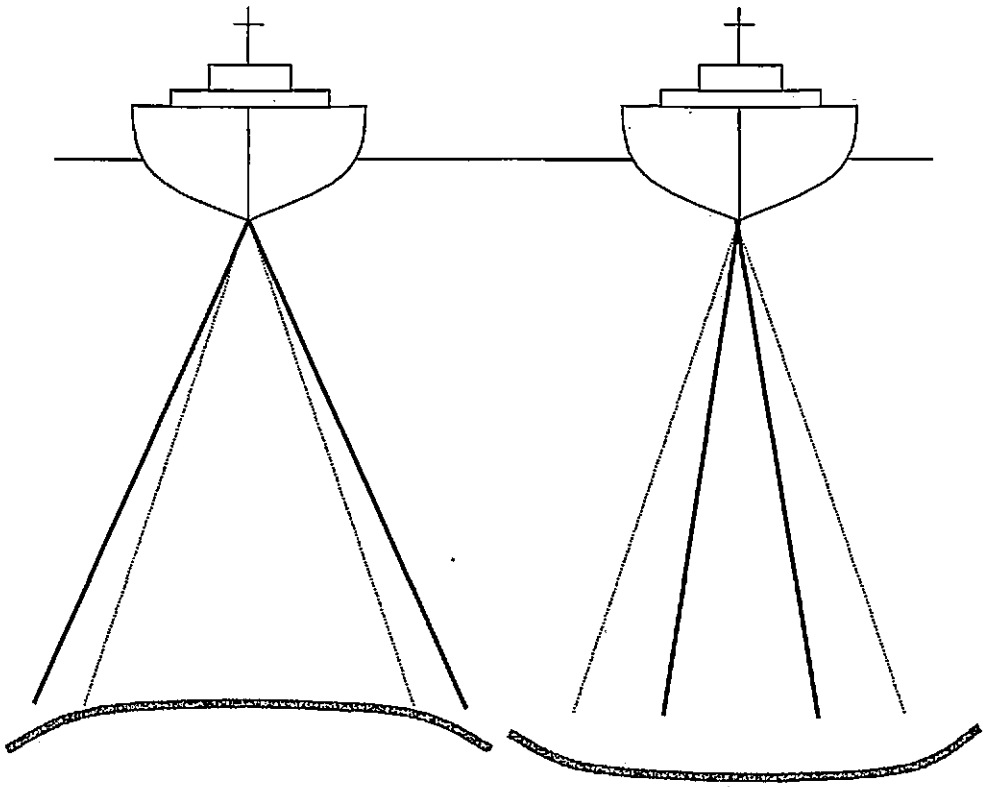

Figure 7.16. A refraction artefact will make a flat seabed either curve up (a 'smile') or down (a 'frown'). The refracted rays are represented by the solid lines. If a refraction artefact increases the beam angle, travel time to the seabed is increased, the depth appears to increase, and a 'frown' results. Conversely, a reduction in the beam angle caused by a refraction artefact will result in a shorter acoustic travel time to the seabed, the depth thus appearing to decrease resulting in a 'smile'.

With such limitations in mind, few survey agencies have considered using angular sectors (swath widths) greater than 120°. The shallow water hydrographic surveyor has traditionally dealt with refraction problems by reducing the swath width to around 100°, to ensure that the majority of beams will record bathymetric depths within IHO-S44 specifications (Hughes Clarke *et al.*, 2003). This solution is, however, a not a knowledge-based one, and although time may be saved in sound velocity sampling terms, the reduced swath width will require extra survey time to ensure 100% sea floor coverage. A modelling approach to the use of a multibeam sonar in a highly dynamic estuarine environment would enable the hydrographic surveyor to predict accurately the maximum beamwidth which could be used whilst still adhering to IHO-S44 specifications, thus maximising survey efficiency.

7.4. Development of a multibeam sonar refraction model

Modelling is an extremely efficient means of investigating sonar performance under varied environmental conditions. Both physical and mathematical sonar models are available, both of which have been used extensively to advance scientific understanding without expending resources on field observations. Physical, or analytical models pertain to theoretical or conceptual representations of the physical processes occurring in the ocean, and field measurement programmes and experimental field techniques. Mathematical models include both numerical models, based on mathematical representations of the governing physics, and empirical models, based on observations (Etter, 1991). In its most elemental form, a model is intended to generalise and abstract. A perfect model is one that represents reality in every way, although such a model would defeat its purpose, as it would be as complex as the problem it is attempting to represent. Even with the development of modern computing

power, modelling in the physical sciences normally has to be reduced to many easily managed components (Etter, 1991).

Many sonar propagation models exist, developed commercially and by the military. Due to national security concerns, military sonar models are not generally available for use by non-military personnel. Of the commercially-available sonar models, Wader-Hodgson, developed by Ocean Acoustic Developments Limited in 1993 is one of the most widely available. This model is, however, also aimed primarily at the deep water defence market. Attempts by the author to utilise this model were hampered by its inability to import sound velocity profiles spaced at variable intervals, and its extreme bias towards deep water use. Other deep water models, such as 'Kraken' are available to download from the Internet. Again, these models do not appear designed to function well in shallow water, and are usually limited to the propagation of a narrow, near-horizontal sonar beamwidth, such as would be found on a forward-looking military sonar. Many of these existing sonar models use predicted oceanographic data for the construction of the necessary sound velocity profiles. These data may be widely spaced, or unvalidated, and thus sonar models may become data limited, *i.e.* observational data may be lacking in sufficient quantity or quality with which to support model application and evaluation.

There have been several attempts, documented in the literature, to quantify the effects of refraction on a multibeam sonar system in shallow water using a modelling approach. Dinn *et al.* (1995) investigated the refraction of a single ray, at a launch angle (β) of 75° from the vertical, to highlight the potential errors when using wide swath widths. Note that the use of a 75° launch angle implies the use of a 150° multibeam swath width. Ray paths were calculated

for a number of transducer types assuming a 1 ms^{-1} measurement error present in a thin (0.3 m) surface layer at the face of the transducer. Water depth was assumed to be 30 m. Both flat arrays (with attendant electronic beam steering) and cylindrical arrays (with no electronic beamforming) were investigated. Interestingly, the cylindrical arrays were found to produce greater errors in depth than the flat arrays, the authors hypothesising that the beam steering error caused by the inaccuracy in surface sound velocity is nullified by the refractive effects at the first horizontal interface. Usefully highlighting the fact that errors in the sound velocity in the vicinity of the transducer face can lead to significant errors in depth calculation, no further analysis was undertaken for different beam angles. Cartwright & Hughes Clarke (2002) investigated multibeam refraction effects in the relatively deep Fraser River estuary in western Canada. Ray tracing for both a flat array and a cylindrical array in up to 70 m of water using archived profiles, results included the effects of updating the sound velocity at the transducer face in isolation from the remainder of the existing profile, as if a sound velocimeter was permanently installed in this area. The most significant errors appeared to be those from a cylindrical array, or from using an SVP with just the surface value corrected. Similarly to the results reported by Dinn *et al.* (1995), a *level* electronically beam steered array was found to partially harmonise the errors from using an archived sound velocity profile. The results of this study may not, however, be applicable to a shallower, partially mixed estuary. The assumption was made throughout that water column variability is confined to a very shallow region near the surface, which may not necessarily be the case in many areas. Most recently, Batton (2004) investigated the effect of sound refraction in an estuary on the accuracy of depths calculated from oblique swath angles. Predictably, the results indicated that the outer beams of the swath were refracted to a greater degree. Unfortunately, however, the focus of the study was on the horizontal positioning errors (Δx) rather than vertical (Δz) position errors, the latter being regarded as the most important issue by IHO-S44. In addition, the

work was conducted using an outdated version of the IHO specifications, quoting lower depth and horizontal positioning accuracy requirements.

The development of a multibeam-specific sonar model, supported by the extensive sound velocity data set from the Dart estuary, will be a valuable addition to this relatively sparse sonar model library. The presence of the tidal intrusion front in the Dart during spring tides will enable the quantification of both the temporal and spatial variability in the accuracy of bathymetry measurements taken at high beam angles. In addition, the availability of a data set from both a spring tide and a neap tide period will serve to highlight the temporal variability possible in such an estuarine environment.

7.4.1. Construction of the sonar model

As is required in all modelling in the physical sciences, some simplifications of the true environment are necessary in order to maintain a model's efficiency and practicality (Etter, 1991). In order to calculate a refraction solution, the water column is usually assumed to be horizontally stratified, with discrete layers of homogeneous fluid separated by distinct interfaces (Figure 7.14). Refraction across each interface thus occurs according to Snell's law (equation 7.07). As the sound velocity profile is sampled discretely, there will be an infinite number of interfaces over the entire water column, and thus some sort of approximation is required (Hare *et al.*, 1995). An accurate method of determining the layer boundaries, and the behaviour of the sound ray within each layer is critical to the performance of any ray tracing model.

Within each discrete, horizontal layer, it is possible to assume either a constant sound velocity, or a constant sound velocity *gradient* (deMoustier, 2003b). The constant sound velocity method is relatively simple, with the horizontal range of a ray being the sum of the horizontal ranges travelled in each layer, and the corresponding travel time along the ray being the sum of the time spent in each layer (Figure 7.17). The 'stair case' approximation of the profile may lead to inaccuracies in the ray tracing however, particularly if the number of steps used is relatively small (deMoustier, 2003b).

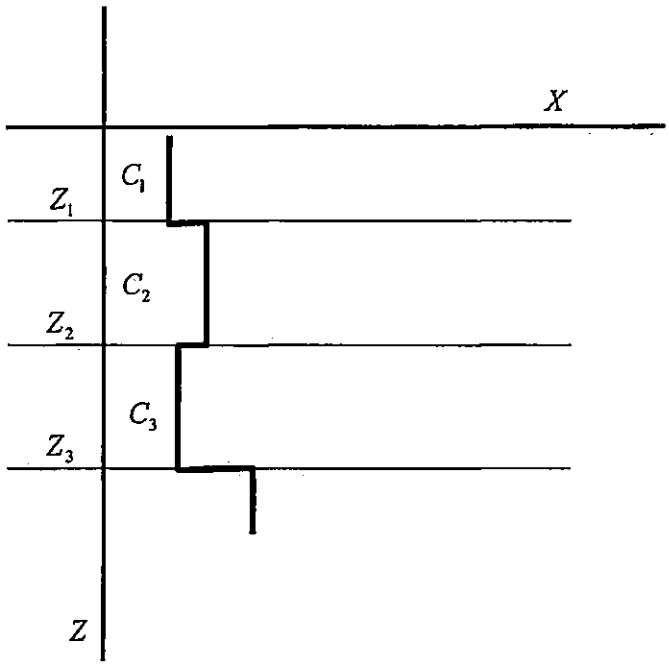

Figure 7.17. The constant sound velocity model. Sound velocity (c) is assumed to be constant within each depth layer (z_i)

The constant sound velocity gradient method is generally assumed to provide more accurate results, and has been used more widely in sonar modelling applications (e.g. Hare *et al.*, 1995; Cartwright & Hughes Clarke 2002; deMoustier, 2003b). In each layer, sound ray trajectories are arcs of circles, with the horizontal distance and arc length in each layer yielded by simple

geometry and trigonometry (Korman, 1995). The process is repeated through each layer, until all the horizontal layers within the water column have been traversed (Figure 7.18). The multibeam system then derives the bathymetric measurement from the total length of all the arcs (the distance travelled) and the time taken for the sonar ping to return from its seabed 'strike'. This entire ray tracing process is carried out individually for each beam, on each ping cycle during multibeam operation.

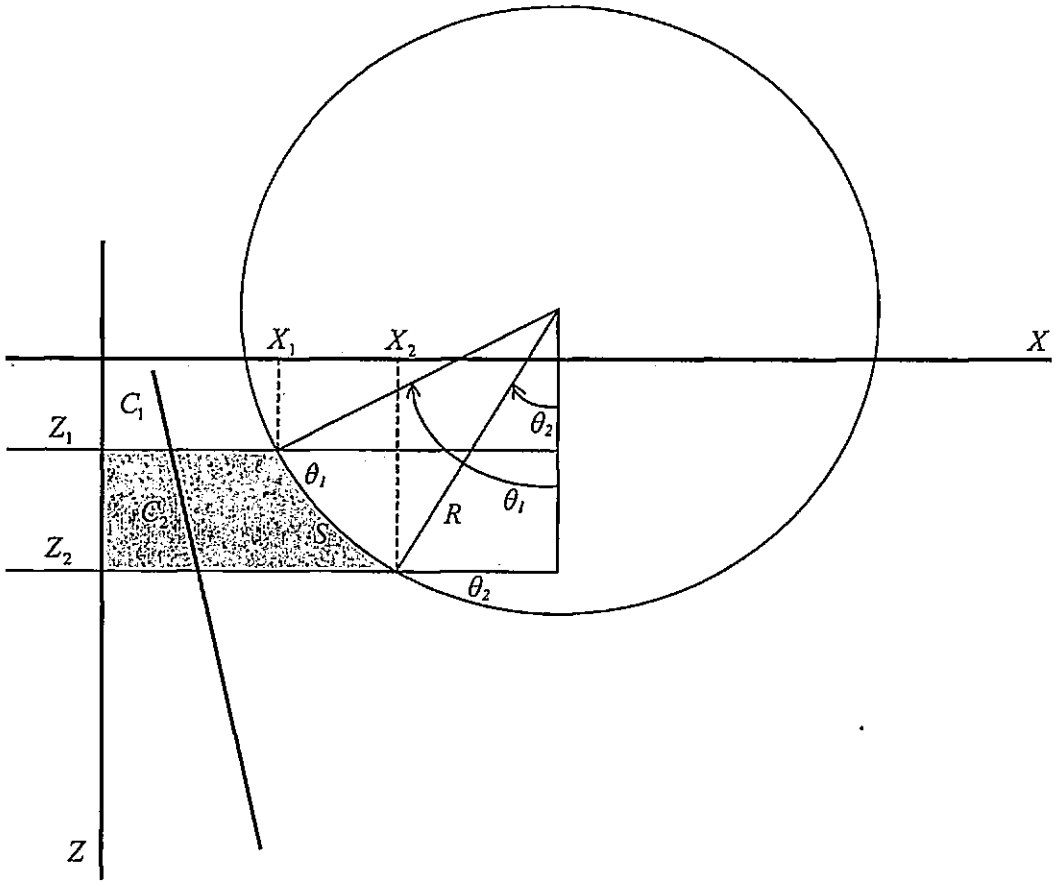

Figure 7.18. Sound ray path (S) in a constant positive sound velocity gradient. (After Korman, 1995)

In order to calculate the path of an individual ray through a stratified water column, assuming a constant sound velocity gradient within each stratified layer, the following equations may be defined (Korman, 1995), referring to Figure 7.18 throughout. The gradient of the sound velocity within each layer (c_z) is obtained from:

$$c_z = \frac{c_2 - c_1}{z_2 - z_1} \qquad s^{-1} \tag{7.08}$$

where c_i is the sound velocity in layer i, and z_i is the depth of the interface (i). The radius of the circle (R) in metres is derived thus:

$$R = \frac{c_1}{[c_z \cos\theta_1]} \tag{7.09}$$

where θ_i is the entering grazing angle. From Snell's law (equation 7.07):

$$\cos\theta_2 = \frac{c_2 \cos\theta_1}{c_1} \tag{7.10}$$

The horizontal displacement (Δx) in metres is:

$$\Delta x = x_2 - x_1 = -R[\sin\theta_2 - \sin\theta_1] \tag{7.11}$$

Additionally, the arc length (S) may be defined by:

$$S = R(\theta_1 - \theta_2) \tag{7.12}$$

Using the sound velocity data collected in the Dart estuary in spring 2002 (Sections 5.3 and 5.4), the horizontal stratification of the water column has been determined in exactly the same manner as for the hydrodynamic study. A two-layer regime within the estuary has been assumed throughout, with the interface between the two layers determined by the Brunt Väisälä frequency, N^2 (Section 5.2.1.). In order to ensure the widest possible application of the multibeam sonar propagation model, three variations of the model have been prepared, with each model variation representing one different type of multibeam sonar system (Table 7.03). The model code has been written using Matlab (Appendix 3), with each model designed to quantify the errors in depth (Δz) and horizontal distance (Δx) associated with surveying into a new (observed) water mass, whilst still using archived (predicted) water mass information from the last available sound velocity profile measurement (Figure 7.19)

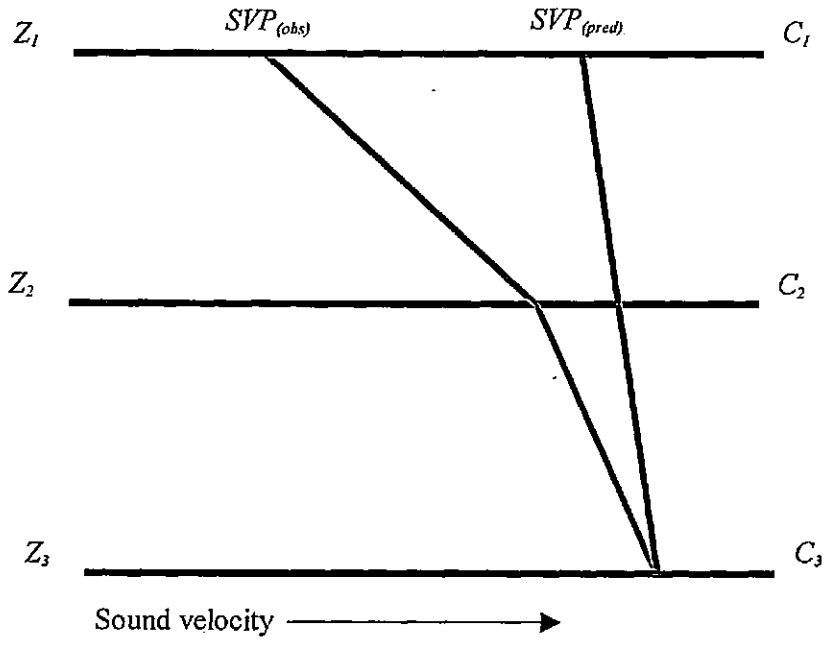

Figure 7.19. Change possible in sound velocity profile (SVP), when crossing a frontal zone. The predicted, or archived sound velocity profile ($SVP_{(pred)}$) may differ considerably from the observed, or new sound velocity profile ($SVP_{(new)}$)

	No of layers in water column	Assumptions	Sonar type represented by model
Model 1	2	No beam steering at transducer face	Cylindrical array with no beam steering error at the transducer face
Model 2	2	Beam launch angle error at transducer face	Flat array without surface sound velocity updates
Model 3	3	Sound velocity updated at transducer face only, no beam launch angle error	Flat array with surface sound velocity updates

Table 7.03. Summary of the three sonar models developed in order to quantify potential hydrographic surveying errors across a frontal zone.

7.4.1.1. Generic model variables and outputs

Assuming that the water column is stratified into two layers, as for the hydrodynamic studies, the model initialisation variables are defined as follows (Figure 7.20):

- Layer interface depth (z_2),
    - Predicted SV profile ($z_{2(pred)}$)
    - Observed SV profile ($z_{2(obs)}$)
- Sound velocities at the surface (c_1)
    - Predicted SV profile ($c_{1(pred)}$)
    - Observed SV profile ($c_{1(obs)}$)
- Sound velocity at the interface between the two layers (c_2)
    - Predicted SV profile ($c_{2(pred)}$)
    - Observed SV profile ($c_{2(obs)}$)
- Sound velocity at the seabed (c_3),
    - Predicted SV profile ($c_{3(pred)}$)
    - Observed SV profile ($c_{3(obs)}$)
- Depth of the seabed (z_3)
- Beam launch angle (β)

Each variable may be altered by the user, by following simple, on-screen instructions. For a given beam launch angle, the refraction in each of the two layers is calculated, with the

process being undertaken twice, tracing one ray for the predicted, or archived sound velocity profile (SVP), and conducting a separate ray trace for the observed, or new SVP. The 'predicted' ray path thus represents the path that a sound ray at a given beam angle would travel through the water column, as derived from a measured SVP. The observed, or 'actual' ray path represents the path the sound ray at a given beam angle would travel through a new water mass with different oceanographic properties. The difference between the two ray paths thus represents the error that would occur in measured depths and horizontal positions if the new water mass was not accounted for. The model presents both ray traces on one plot, for a simple visualisation of the deviation arising from the using the predicted SVP in a water mass with different oceanographic properties (Figures 7.21 and 7.22).

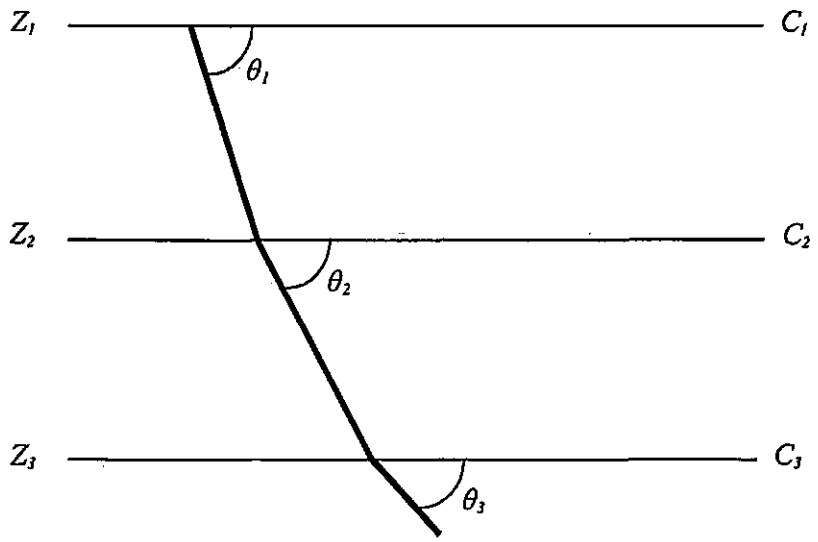

Figure 7.20. Illustration of the main variables in the generic multibeam propagation model. Interface depth (z_2), seabed depth (z_3), as well as the sound velocity at the surface, interface and bed (c_1, c_2, c_3 respectively) may all be altered by the model user, for both a predicted and observed sound velocity profile.

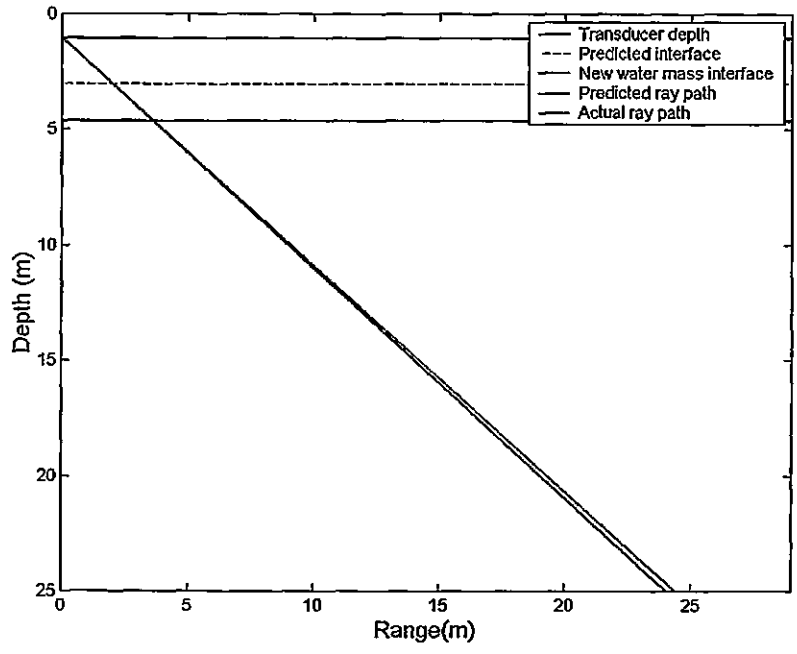

Figure 7.21. Basic function of the multibeam sonar model. One beam launch angle is presented for clarity. Ray traces are constructed using both a predicted sound velocity profile, and an observed, or updated sound velocity profile.

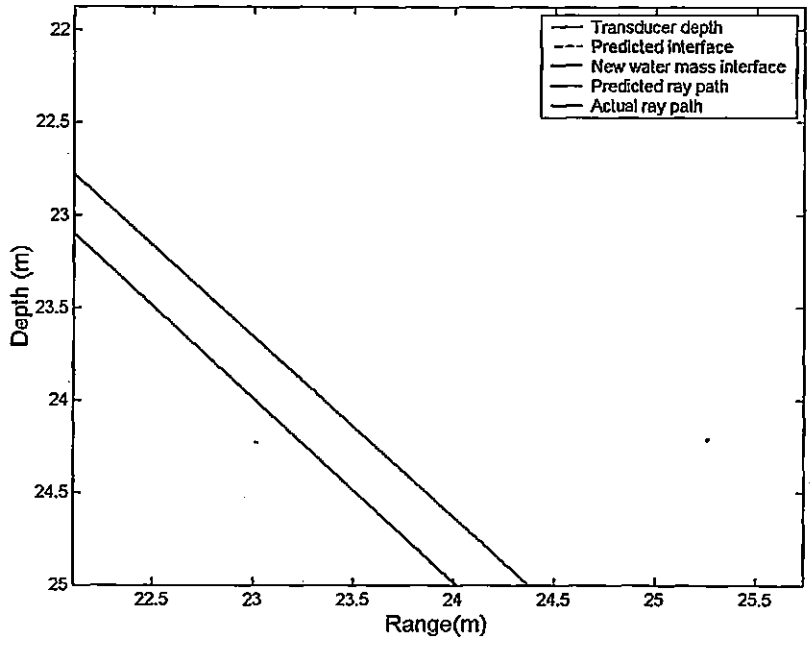

Figure 7.22. Zoomed image of the model output, illustrating the errors in depth (Δz) and horizontal distance (Δx) where the beam ray-traced using the observed profile strikes the seabed.

Calculation of the vertical displacement, or depth error (Δz) which would arise from surveying into a differing water mass cannot be derived directly from equation 7.13, as defined by Korman (1995):

$$\Delta z = R[\cos\theta_2 - \cos\theta_1] \qquad (7.13)$$

An increased sound velocity gradient in the observed SVP is compensated for by a decreased value of R, and a decreased value of θ_2. The net result is that the vertical displacement remains identical, for both the predicted and observed profiles. As the multibeam system relies on a time measurement to derive the depth, the simplest method of calculating the depth error arising from an incorrect SVP is to quantify the difference in arc length, S, (distance the refracted ray has travelled) derived from the ray traces of predicted and observed profiles, and to translate this into a vertical distance (Figure 7.23).

The difference in arc length (ΔS) may be used to derive Δz. The depth error caused by using the predicted SV profile when an updated, observed profile exists, is thus described by:

$$\Delta z = \Delta S \sin\theta_{2(obs)} \qquad (7.14)$$

1. A plot of the sound velocity profile for both the observed and predicted water masses; this allows a first-order check of the input data (Figure 7.24).
2. A visual display of the errors between observed and predicted, across half a swath width (Figure 7.25)
3. A plot of horizontal error, with increasing beamwidth (Figure 7.26).
4. A plot of depth error with increasing beamwidth (Figure 7.27), together with a numerical statement on the depth error plot of the beam angle at which the maximum permissible depth error is exceeded. A 'Special Order' survey specification is assumed.
5. In addition, the model code allows the user to save the depth error vs. beamwidth information to a delimited text file, again by the use of a standard Windows browser dialog box.

Note that only the critical depth error is calculated, this generally being regarded as a more important parameter than horizontal error, both by IHO-S44 and the majority of practising surveyors. Importantly, it should be noted that in a realistic scenario, only 50% of the total allowable depth error can be assigned to refraction effects (Dinn *et al.*, 1997; Hughes Clarke *et al.*, 2003). The remainder of the depth error budget is usually statistically used up by errors from other sources, such as the motion sensor. The critical depth error calculated by the model is, therefore, half that suggested by the IHO-S44 specifications. Finally, the model code allows the user to save the depth error vs. beamwidth information to a text file, again by the use of a standard Windows browser dialog box.

7.4.1.2. Model One

Model One assumes that the equipment in use is a cylindrical transducer array, with no electronic beam steering required at the array face. There is, therefore, no beam steering error at the transducer face to consider, and both predicted and observed beam launch angles are identical. The model thus operates exactly as described in the generic model construction section above, ray tracing over two layers, using both a predicted (archived) SVP, and an observed (new) profile. Refraction occurs at the layer interface only, and the calculated differences between the two ray traces thus provides the horizontal and vertical errors caused by using the predicted profile when surveying in a new water mass.

7.4.1.3. Model Two

Sonar Model Two assumes that the equipment in use is a flat transducer array, with electronic beam steering conducted at the array face. In order to electronically steer the beam departure angle correctly, the correct sound velocity at the transducer face is required (Section 7.3.1.). If the sound velocity at the transducer face is incorrect, or alters without the multibeam sonar system software being updated of the change, an error in the departure angle of the electronically steered beam may result. The actual departure angle (β_a) of the beam launched from an array in a water mass different to that predicted may be defined by (Cartwright & Hughes Clark, 2002):

$$\beta_a = \sin^{-1}\left[\frac{c_{(obs)}}{c_{(pred)}}\sin\beta\right] \tag{7.15}$$

Model Two calculates and plots the ray traces for both the predicted SVP and the observed SVP, taking into account this departure angle error due to watermass variability. The remainder of the model variables, and iterations are exactly as for Model One once the updated launch angle has been calculated.

7.4.1.4. Model Three

Sonar Model Three is the most sophisticated of the three models, assuming that a constantly updating sound velocimeter is mounted at, or near the transducer face. This scenario could be applicable to a flat array with constantly updating sound velocity information, which would negate the beam launch angle errors associated with a such an array design.

When receiving constant updates of *surface* sound velocity, the multibeam sonar software has to make some assumptions regarding the remainder of the SVP (Cartwright & Hughes Clarke, 2002). The sonar software would be unaware of any changes in the SVP below the updating surface value, and thus the profile would be modified by the presence of a thin, near-surface layer (Figure 7.28). Within this thin 'snapback' layer, the coincident surface sound velocities at the surface (due to the surface correction of the observed SVP) diverge rapidly. With the addition of the 'snapback' layer, the model now has three discrete layers, with ray tracing for both the predicted profile and the observed profile conducted within each layer, in an identical manner to that described for Model One and Model Two.

7.4.2.1. Effects of sound velocity changes

In order to understand the effects of changing sound velocity on each model output, suitable test input files were prepared. A predicted SVP, with fixed values, was compared with a changing observed profile. The sound velocity values in the observed profile files were reduced progressively, first at the surface, then at the layer interface and finally at the bed, before running each of the three models. The water depth was maintained at a constant 25 m, with the layer interface set at a depth of 10 m throughout the tests.

In order to quantify the effects of changing the surface sound velocity, the sound velocities at the interface and the bed were set at a constant 1490 ms^{-1} and 1495 ms^{-1}, respectively. The surface sound velocity was then decreased progressively from 1489 ms^{-1} to 1480 ms^{-1}, thus increasing progressively the sound velocity gradient in the upper layer. Comparing the results calculated by the three models, Model One suffered the greatest errors, with Model Two being the most accurate (Figure 7.29). The depth error calculated by Model Three appeared to increase as the surface sound velocity was reduced. The enhanced accuracy of Model Two is due to the 'self cancelling' effect of the refraction errors, which can occur when using a flat transducer array in a changing sound velocity environment (Dinn *et al.*, 1997). The beam launch angle for a flat transducer operating in a different water mass (β_a) is compensated for by the refraction error at the layer interface (Figure 7.30). The result of this effect is that the errors in the lower layer are constant (Figure 7.31). Provided that the upper layer forms only a small proportion of the entire water column, and the transducer in use is mounted both flat and level (flat transducers mounted at an angle from the horizontal do not benefit from this effect), the depth and horizontal position errors should remain relatively small (Cartwright & Hughes Clarke, 2002; Hughes Clarke *et al.*, 2003).

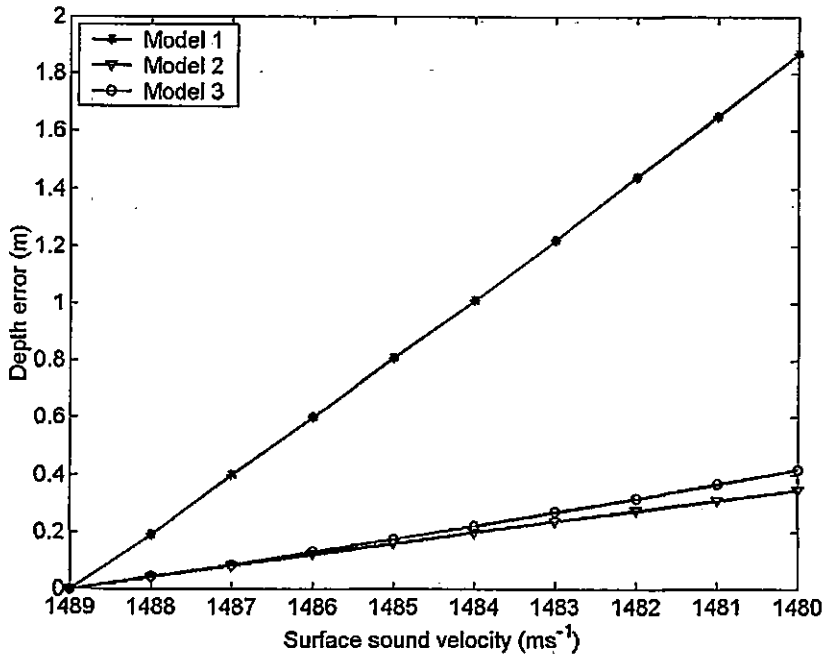

Figure 7.29. Comparison of model performance varying only surface sound velocity.

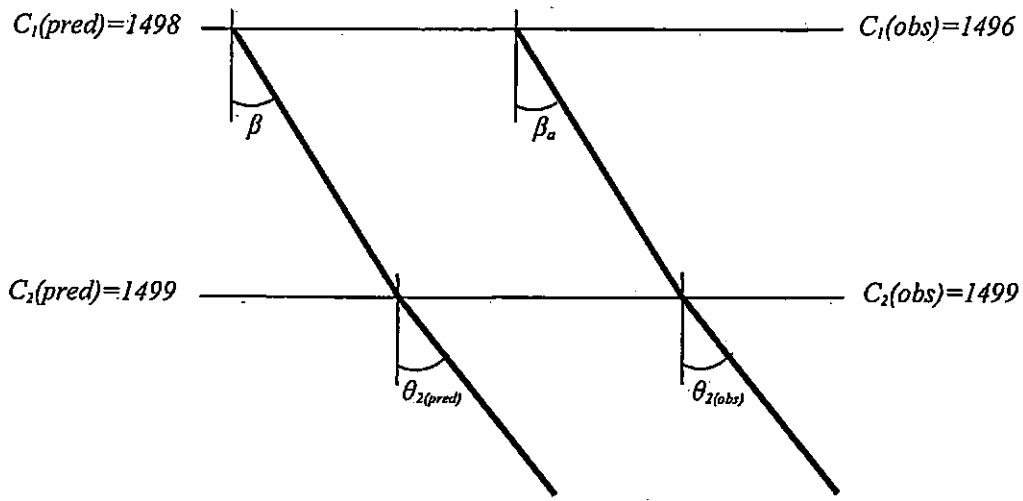

Figure 7.30. Harmonisation of the beam steering error occurs in the lower layer.
If β is 20°, from equation 7.15, β_a becomes 19.97°. Following refraction at the first interface (equation 7.06), both predicted ($\theta_{2(pred)}$) and observed ($\theta_{2(obs)}$) ray trace angles are refracted to 20.01°.

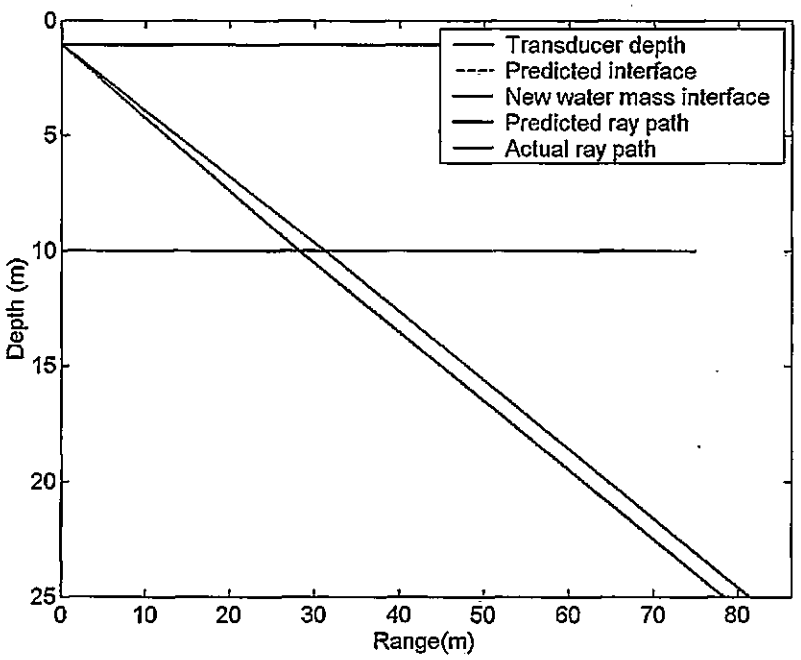

Figure 7.31. Example output of Model Two for just one refracted ray. The beam launch angle error is partially compensated for by the refraction at the layer interface, resulting in a constant error in the lower layer.

In order to quantify the effects of changing the sound velocity at the layer interface, the sound velocities at the surface and the bed were set at a constant 1488 ms^{-1} and 1495 ms^{-1} respectively. The sound velocity at the interface was then decreased progressively from 1493 ms^{-1} to 1488.5 ms^{-1}. Each comparison profile thus experienced a progressively reducing SV gradient in the upper layer, with a correspondingly increasing sound velocity gradient in the lower layer. A comparison of the results calculated by the three models illustrates that the use of Model Three resulted in the smallest calculated depth errors (Figure 7.32).

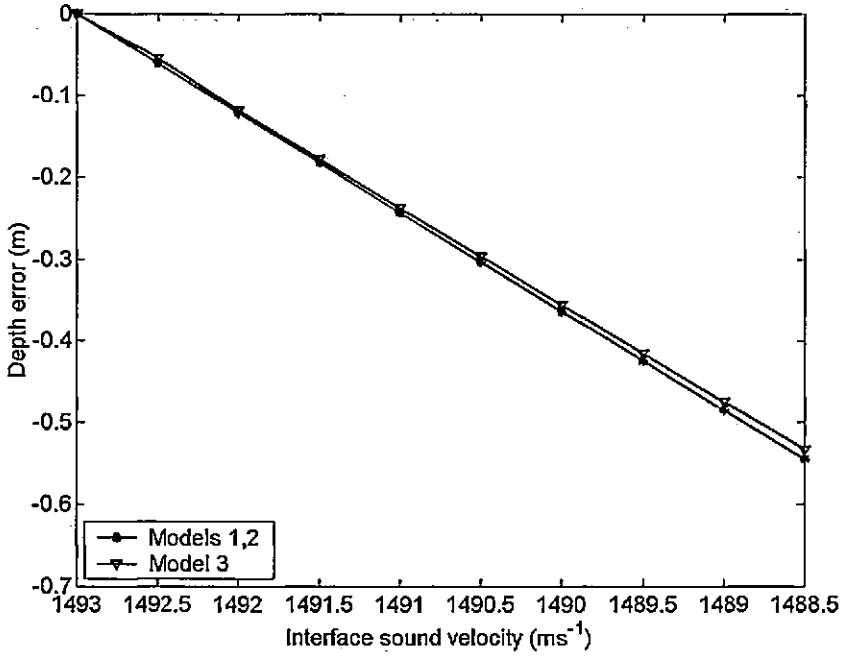

Figure 7.32. Comparison of model performance, varying only the interface sound velocity.

The recorded depth errors produced by the use of Models One and Two are identical. As only the sound velocity at the interface has been varied, no beam steering errors caused by a changing surface sound velocity have been recorded by the use of Model Two. This absence of a surface beam steering error does, therefore, remove the beneficial harmonisation of refraction errors at the first layer interface (illustrated by Figure 7.31). The depth errors recorded using Model Three with a changing sound velocity at the interface diverge from those produced by the use of Models One and Two. The presence of a shallow 'snapback' layer effectively reduces the thickness of the main upper layer of the water column (e.g. Figure 7.28). This has the effect of increasing the sound velocity gradient in that layer, increasing the upward refraction of the sound rays in that region. This slight refraction change is sufficient to reduce the errors arising from the separate paths followed by rays traced from

the observed and predicted SVP's. Note that any slight divergence from a straight line in the Model Three results are artefacts due to rounding errors only.

The effects of changing the sound velocity at the bed were investigated by altering progressively the bed sound velocities from 1495 ms^{-1} to 1491 ms^{-1}. The sound velocities at the surface and the layer interface remained at a constant 1490 ms^{-1} and 1495 ms^{-1} respectively. Each comparison profile thus experienced a progressively reduced sound velocity gradient in the lower layer, whilst the sound velocity gradient in the upper layer remained constant. Results produced by all three sonar refraction models were identical in this instance, with the magnitude of the error being generally less than when varying only the surface or the interface sound velocity (Figure 7.33). By changing the sound velocity at the bed, the only parameter which is altered is the sound velocity gradient in the lower layer. Model differences arise primarily due to changes in the upper layer or at the surface, and the magnitude of the refraction at the interface (equation 7.06) is not altered by changing the sound velocity at the bed.

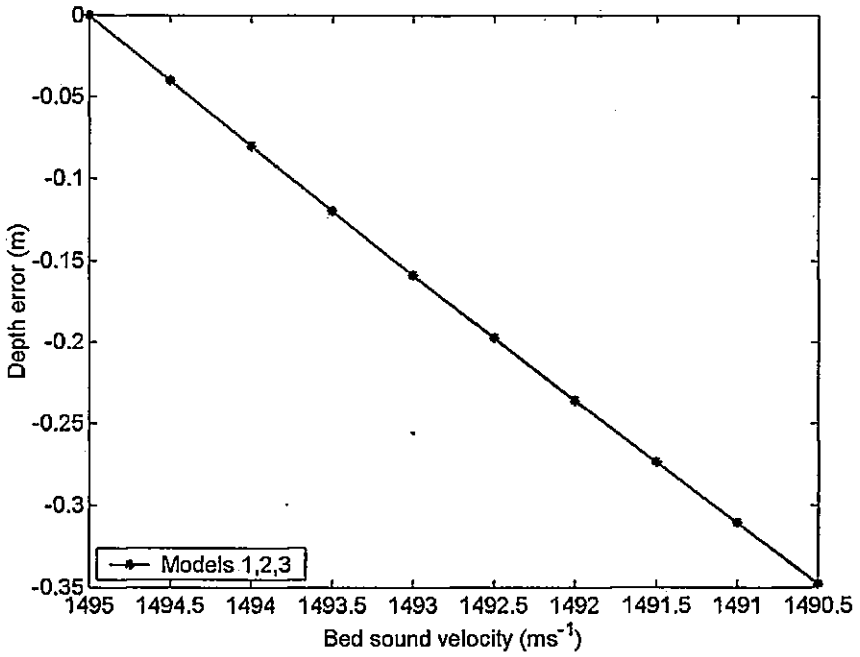

Figure 7.33. Comparison of model performance varying only the bed sound velocity.

7.4.2.2. Effects of depth changes

In order to quantify the errors arising from changing the depth of both the layer interface and the total depth of the water column, a predicted sound velocity profile, with fixed values, was again compared with a changing observed profile. The sound velocity values at the surface, interface and bed were set at 1488 ms^{-1}, 1490 ms^{-1} and 1495 ms^{-1} respectively, for both predicted and observed profiles, whilst the depths were changed progressively and the errors calculated by each of the three models recorded.

The effect on model performance of changing the layer interface depth was quantified by comparing a predicted sound velocity profile, with a layer depth of 19 m with observed profiles containing layer interfaces decreasing progressively from 18 m to 2 m. The total

water depth was maintained at a constant 25 m, throughout this test. Identical depth error results were recorded using Models One and Two (Figure 7.34). As the surface sound velocity of both the observed and predicted profiles was identical, no beam steering error occurred using the flat transducer array represented by Model Two. The behaviour of both models was, therefore, identical. The relative magnitude of the Model Three results decreases slightly as the interface depth approaches the water surface. As the layer interface becomes shallower in the observed profiles, the sound velocity gradient in the upper layer increases, increasing the upward refraction of the sound rays in this region. The use of Model Three reduces the overall effect of this upward refraction, due to a degree of extra downwards refraction provided by the shallow 'snapback' layer near the surface.

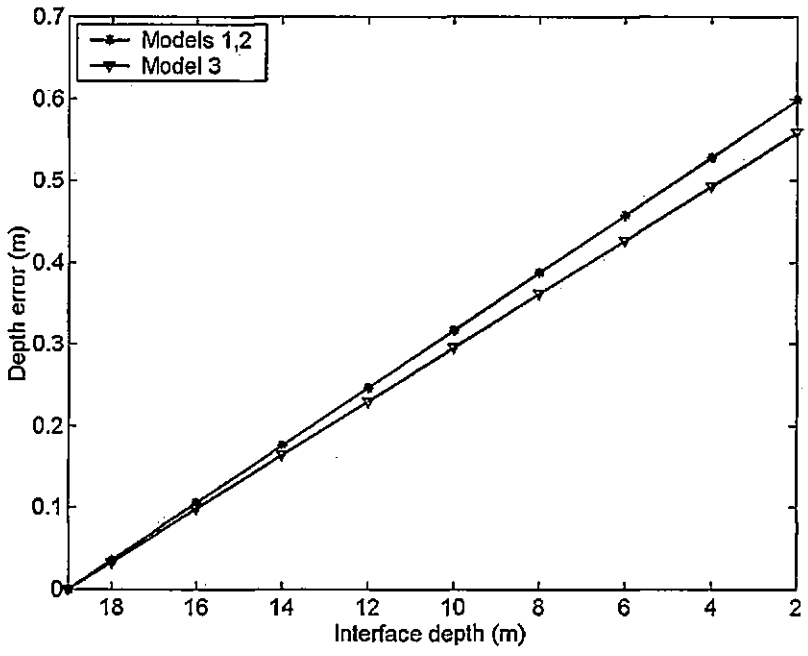

Figure 7.34. Comparison of model performance varying only the depth of the interface.

Lastly, in order to quantify the effects of changing the total water depth, a further test file was prepared, with the sound velocities at the surface, interface and bed maintained at set values of 1488 ms^{-1}, 1490 ms^{-1} and 1495 ms^{-1} respectively. Note that a surface sound velocity error of 1 ms^{-1} was introduced into all the observed profiles. In this way, it was possible to identify if the depth errors produced by such a change in surface sound velocity propagate with increasing depth. The interface depth of both the predicted profiles and the observed sound velocity profiles was fixed at 10 m, and the total depth of the observed profiles was increased progressively from 15 m to 90 m. The worst performance in this instance was achieved by the use of Model One (Figure 7.35). Clearly, any differences in refraction occurring between the ray traces conducted with the observed and predicted profiles will increase in magnitude with increasing depth (Figure 7.25). As expected, the depth errors recorded by the use of Model Two were constant with changing depth. The harmonisation at the layer interface of the beam steering error which occurs at the surface results in errors which remain constant with depth in the lower layer (Figure 7.31). The best performance was achieved using Model Three, with a measured depth error of virtually zero in all water depths. As the depth of water increases, the sound velocity gradient in the lower layer decreases, the gradient in the upper layer remaining the same. The effect of the sound velocity error introduced at the surface is reduced to a large extent by the extra upward refraction caused by the 'snapback' layer present in the Model Three observed sound velocity profiles. This upward refraction negates the effect of the extra downward refraction in the lower layer, caused by the reducing sound velocity gradient. The errors remain constant with depth as the increase in θ_2 (Figure 7.20) in the observed profile ray trace is compensated for by an increase in R (equation 7.08), due to the reduced gradient of the SVP in the lower layer of the observed profile. The net result is that the arc length (S, equation 7.11) travelled by the rays using the predicted and observed profiles, and hence the calculated depth, is the same.

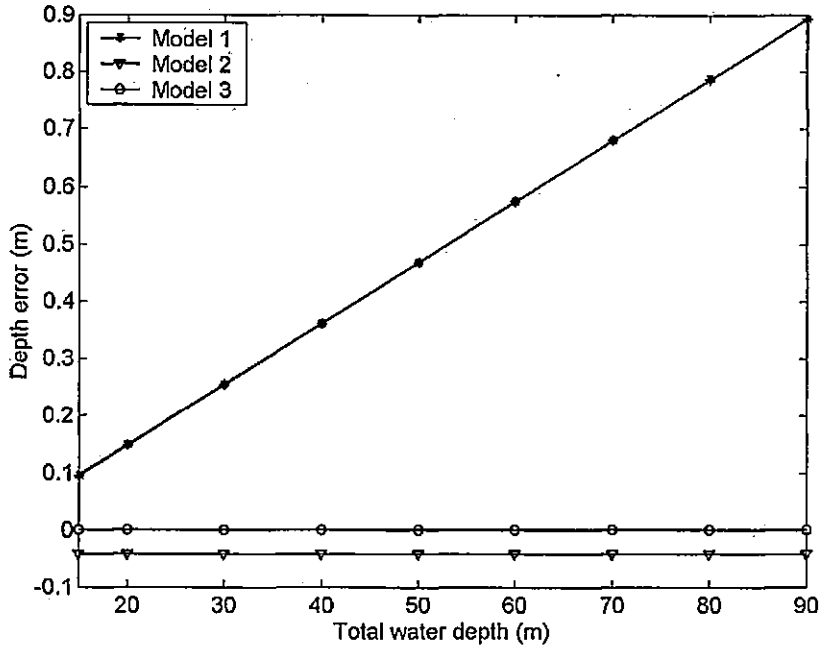

Figure 7.35. Comparison of model performance varying only the total water depth.

In summary, it appears that Model One (representing a cylindrical transducer array) is extremely sensitive to variations in surface sound velocity. The calculated depth errors using this model were relatively large in this scenario, rising to 1.87 m when the sound velocity at the surface was reduced by 9 ms^{-1} from that predicted. This model also returned the worst performance out of the three sonar refraction models as total water depth increased. Varying the depth of, or the sound velocity at the layer interface resulted in a reasonable performance in comparison with the other refraction models. Changes in sound velocity at the bed had relatively little effect on the calculated depth error, and all three sonar models produced identical performance when changing this parameter alone.

The depth errors calculated using Model Two (representing a flat transducer array, experiencing the inherent beam launch angle error) remained relatively small under all conditions. Variations at the layer interface, both in depth and sound velocity, contributed to the greatest recorded depth errors produced by this model. Particularly robust to changes in total water depth, reasonable performance was also returned with changes in surface and bed sound velocity.

Refraction Model Three (representing a flat array with an updating sound velocimeter at the transducer face) produced a very similar performance to Model Two. Marginally superior to the other sonar models when experiencing changes at the layer interface and in the total water depth, the presence of a 'snapback' layer in the Model Three observed sound velocity profiles (where the observed sound velocity at the surface is snapped to a value identical to the predicted sound velocity value) appears to reduce many of the inherent ray tracing errors.

7.5. Multibeam sonar refraction modelling in the Dart estuary

7.5.1. Model input: sound velocity variability in the Dart estuary

Derived field observations of sound velocity from the Dart estuary are intended to provide the input for the multibeam sonar refraction model. In this way, it will be possible to predict at what spatial locations in the estuary specific beam angles no longer meet the IHO-S44 specifications. Using the entire data set, from one hour before low water (LW-1) to three hours after low water (LW+3) during both spring and neap tides, will also facilitate an accurate description of the temporal variability in multibeam sonar accuracy within such an

estuarine environment. In particular, this approach will enable the effect of the presence of a tidal intrusion front to be ascertained and, by using the three sonar refraction models to represent different types of commercially-available sonar system, type-specific sonar performance will be examined.

7.5.1.1. Spring tide

The following plots represent the sonar model input variables for sound velocity, as recorded in the Dart estuary during a spring tide. The data are essentially the same as that presented in the contour plots in Chapter 5.3, (e.g. Figure 5.07.), although contouring of the data has not been undertaken for this application, for the purpose of clarity. In this way, small variations in sound velocity at the surface, the interface and at the bed, which may have an effect on sonar refraction can be highlighted. Note the reversal of the *y*-axis enabling the surface, interface and bed sound velocities to appear in the 'correct' order. The survey transect and CTD cast locations for each hour of the tide are identical to those plotted in Chapter 5.3.

One hour before low water (LW-1), sound velocity at the surface remains relatively constant, with a high degree of variability at the layer interface (Figure 7.36). The effect of a basal inflow of higher salinity water at the mouth, increasing sound velocity in this area may be identified clearly in the lower layer.

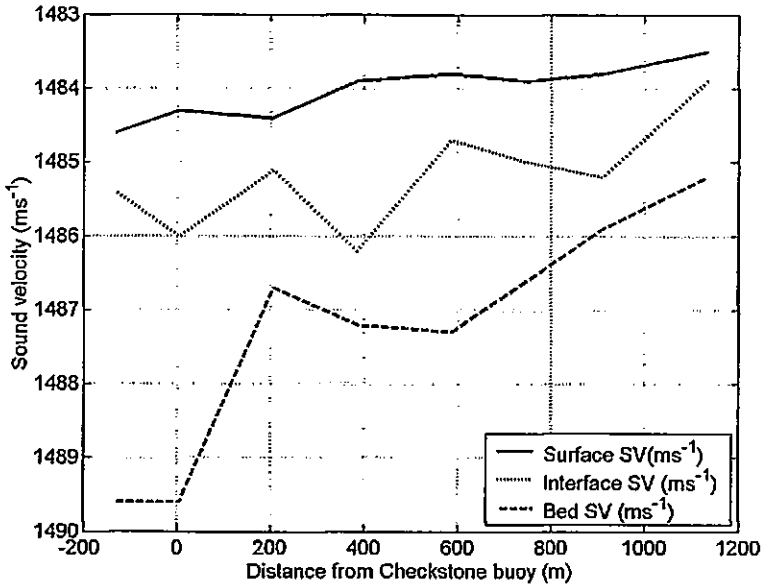

Figure 7.36. Variability of sound velocity (SV) in the Dart estuary, during spring tides at LW-1

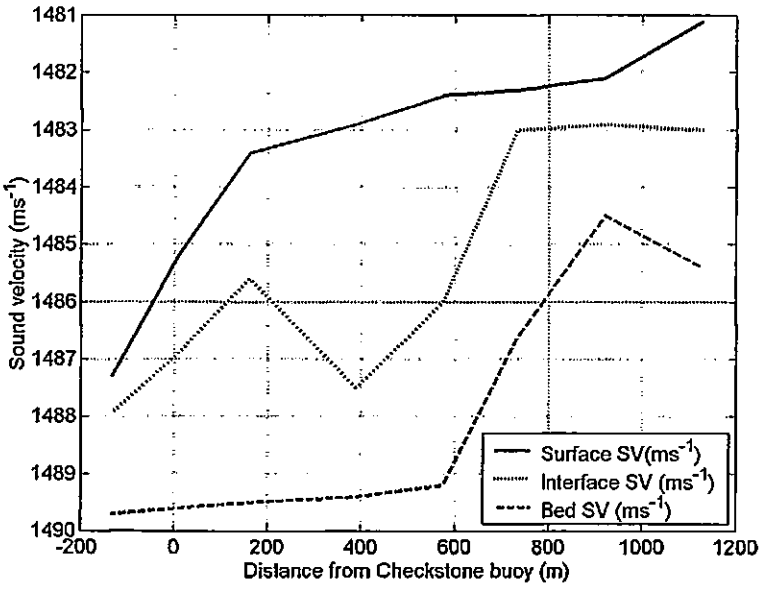

Figure 7.37. Variability of sound velocity (SV) in the Dart estuary, during spring tides at LW

At LW, this intrusion of higher salinity water on the flooding tide is increasing the sound velocity in the surface and interfacial areas; it is also apparent that this intrusion has travelled further landward in the lower layer (Figure 7.37). By LW+1, the presence of the tidal intrusion front can be seen clearly in the sound velocity values (Figure 7.38). The sudden decrease in sound velocity between 200 m and 300 m indicates that the frontal zone has been traversed, and lower salinity, with a correspondingly lower sound velocity is present. The variability present in the sound velocity at the layer interface is most likely due to density instabilities in this area.

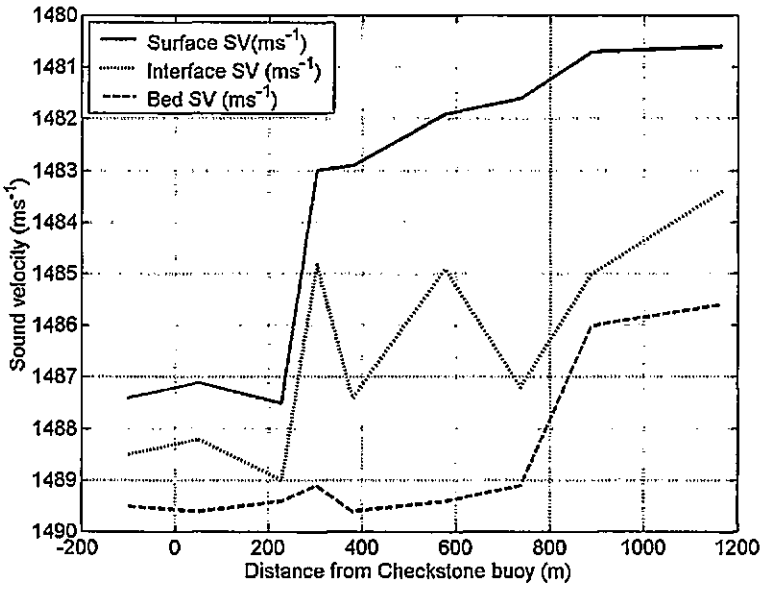

Figure 7.38. Variability of sound velocity (SV) in the Dart estuary, during spring tides at LW+1

By LW+2, the migration of the front further landward can be identified in the plotted sound velocity values (Figure 7.39). The frontal interface at this time occurs between 300 m and 400

m from Checkstone buoy, with a high degree of variability remaining evident in the interfacial sound velocity values. At LW+3, the front was no longer visually apparent, although the plotted values of sound velocity indicate a significant change at approximately 900 m (Figure 7.40). This corresponds with the area in the estuary where discoloured patches of water were noted following the decay of the tidal intrusion front.

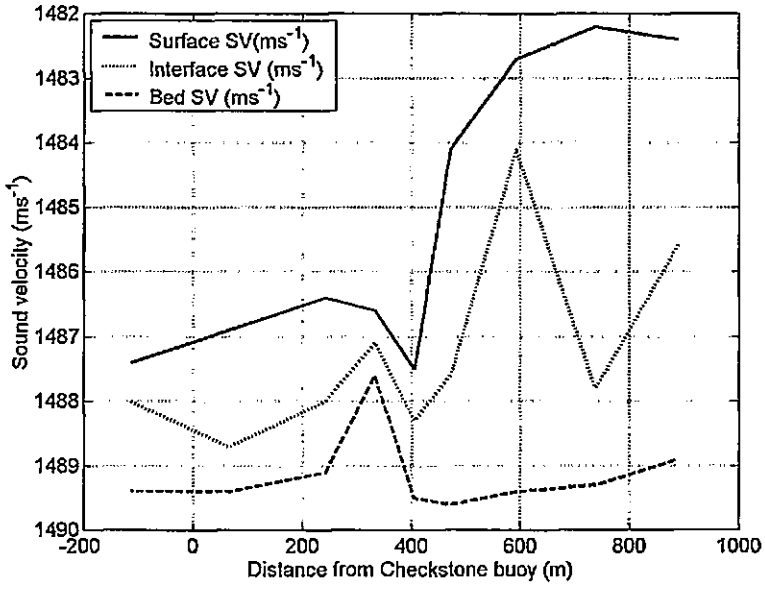

Figure 7.39. Variability of sound velocity (SV) in the Dart estuary, during spring tides at LW+2

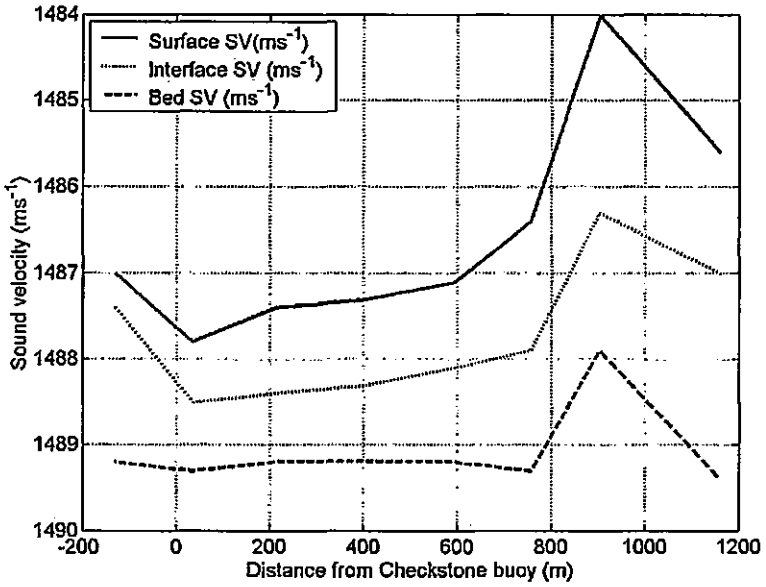

Figure 7.40. Variability of sound velocity (SV) in the Dart estuary, during spring tides at LW+3

7.5.1.2. Neap tide

The following contour plots represent the sonar model input variables for sound velocity, as recorded in the Dart estuary during a neap tide. The data are similar to that presented in the contour plots in Chapter 5.4, (e.g. Figure 5.12.) although again, are presented as line graphs in this application for clarity. The survey transect and CTD cast locations for each hour of the tide are identical to those plotted in Chapter 5.4.

At LW-1, there is an appearance of higher salinity water (with a correspondingly higher sound velocity) at the entrance to the estuary, with minimal vertical difference in sound velocity in this area (Figure 7.41). By 200 m landward of Checkstone buoy, the strongly stratified water column manifests itself clearly on the sound velocity, with a relatively constant value recorded

at the surface and bed. There is some variability in sound velocity at the interface, which again, may be caused by density instabilities in this area.

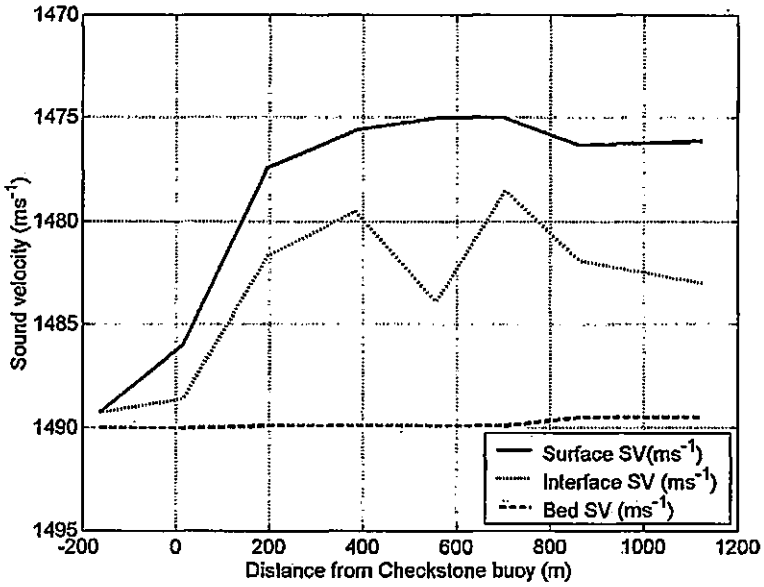

Figure 7.41. Variability of sound velocity (SV) in the Dart estuary, during neap tides at LW-1

The situation remains similar as the flooding tide progresses through LW (Figure 7.42) and LW+1 (Figure 7.43), with stratification increasing with increasing distance through the transect translating clearly into sound velocity values. During the LW+2 and LW+3 periods (Figures 7.44 and 7.45 respectively), variability in the surface and upper layers has increased, with the surface layer in particular experiencing large sound velocity variations. The progressive thinning of the lower density surface layer by LW+3 (Figure 5.16d) enhances the variability in this region of the water column.

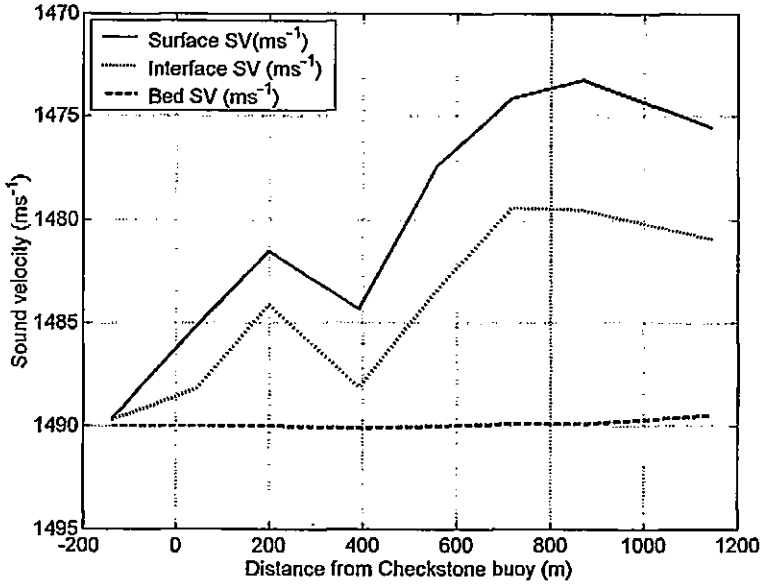

Figure 7.42. Variability of sound velocity (SV) in the Dart estuary, during neap tides at LW

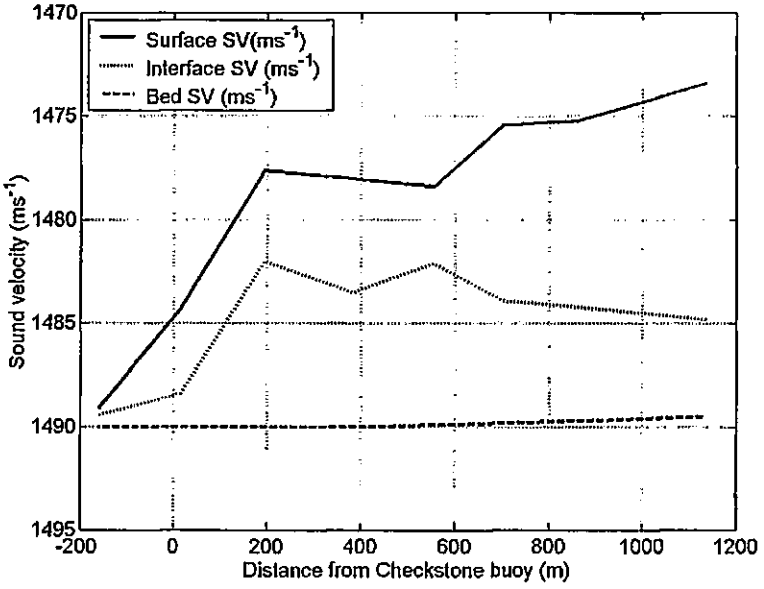

Figure 7.43. Variability of sound velocity (SV) in the Dart estuary, during neap tides at LW+1

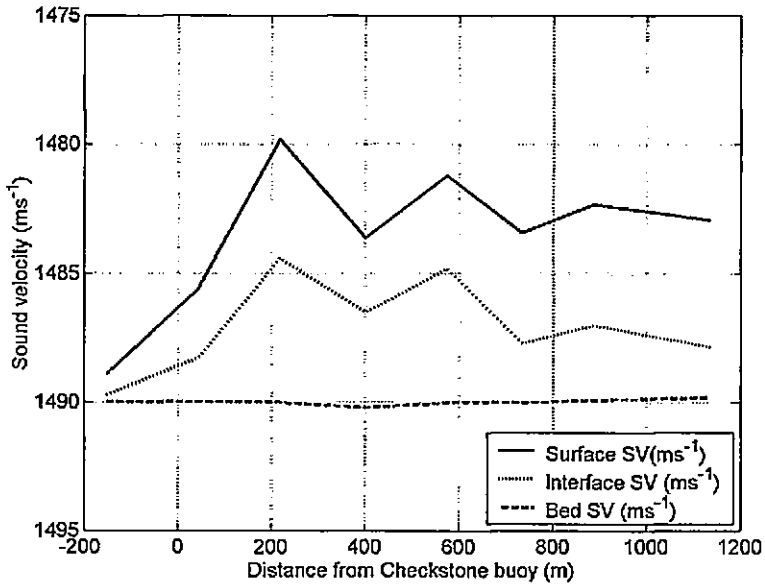

Figure 7.44. Variability of sound velocity (SV) in the Dart estuary, during neap tides at LW+2

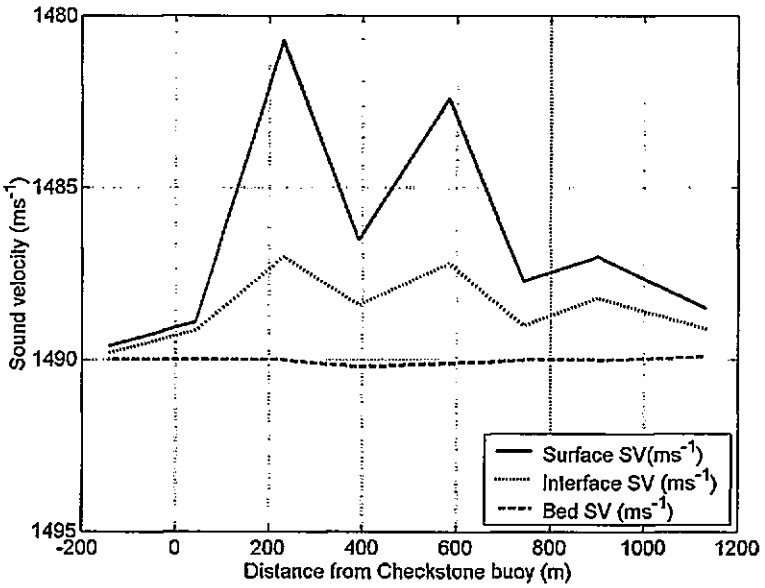

Figure 7.45. Variability of sound velocity (SV) in the Dart estuary, during neap tides at LW+3

7.5.2. Model output: application to Dart estuary data

Sonar Models One, Two and Three have been used in order to ascertain the effects of using different common types of multibeam sonar system in the Dart estuary, during a flooding spring and neap tide. The sound velocity information calculated from the most seaward CTD cast has been used as the reference or predicted sound velocity profile (Sections 7.5.1.1. and 7.5.1.2.), with information from each consecutive CTD cast to landward being used to construct an observed profile. Using a multibeam ray trace derived from the observed sound velocity profile, and comparing it with a ray trace derived from the predicted sound velocity profile, the critical beamwidth at which the allowable depth error is exceeded, according to IHO-S44 specifications, can be determined. This situation is intended to mimic a surveyor taking one CTD cast at the beginning of each survey line, to update the sound velocity profile within the multibeam system software, before surveying into the estuary, landward of an estuarine mouth. Such a surveying technique is presented as an extremely likely real-world surveying scenario (Dinn *et al.*, 1995; Hughes Clarke, 2000; Cartwright & Hughes Clarke, 2002; Hughes Clarke *et al.*, 2003).

Results from refraction calculations undertaken at each CTD cast location have been contoured for each hour of the tide, using a bespoke Matlab routine, 'contouring.m' (Appendix 3). This routine employs the technique of triangulation with linear interpolation, in order to ensure that spatially irregular original data are honoured as closely as possible (Section 5.2.3.). Each contour plot has been colour-coded, with the maximum permissible depth error, according to IHO-S44, added as a bold line for clarity. This visualisation of the results is intended to provide a 'birds-eye' view of the survey errors along the length of the survey transect, with the assumption maintained that the vessel keeps to a steady course on a

7.5.2.1. Spring tide

The use of sonar Model One, representing a cylindrical transducer array, during spring tides enables the time and spatial location of degraded sonar performance to be ascertained (Figure 7.47). Errors are experienced at LW-1, due to the presence of the thin, low salinity layer at the water's surface inside the estuary. This layer is not present at the most seaward CTD cast used to calculate the reference sound velocity profile; therefore, refraction errors occur when this ebbing layer is encountered. At LW, the errors are distributed more widely along the survey transect, as two-way horizontal exchange flow continues at the mouth, during this stage of the tidal cycle. The presence of the tidal intrusion front at LW+1 may be determined clearly at approximately 200 m from Checkstone buoy, where the depth errors measured by the outer sonar beams increase abruptly. Such a refraction artefact would manifest itself clearly to the surveyor as a 'frown' on the sonar display (Figure 7.16), with the refracted sonar beams in the observed water mass travelling a greater distance than those predicted using the original water mass information. The area where the error increases moves landward at LW+2, corresponding to the spatial migration of the tidal intrusion front described in Section 5.3. At LW+3, an area of slightly increased refraction error may be noted from 800 m to the end of the survey transect, corresponding to the area where patches of discoloured water were noted following the decay of the tidal intrusion front. The largest permissible beam angle for surveying within the prescribed depth specifications are at LW+1 and LW+2, at 59° and 57° respectively.

The performance of sonar refraction Model Two, representing a flat transducer array with attendant beam launch angle errors, appears broadly similar to that of Model One (Figure 7.48). Importantly, however, the acceptable beamwidth is increased in the majority of

examples. The presence of the tidal intrusion front may again be ascertained at LW+1 by the abrupt decrease in permissible beamwidth approximately 250 m from Checkstone buoy. Further similarities with the Model One results exist at LW+2, where the landward migration of the tidal intrusion front can be determined. The superior performance advantage in comparison with Model One is lost at LW and LW+1, where the maximum permissible beamwidth reduces to 53° and 55° respectively. By LW+2, performance is much improved, with the use of a 65° beam angle still providing acceptable bathymetry measurements.

The use of refraction Model Three, representing a flat transducer array with a continuously updating sound velocimeter near the transducer face, provides very similar performance to Model Two (Figure 7.49). The presence and migration of the tidal intrusion front at LW+1 and LW+2 is again reflected in the multibeam sonar accuracy results. The refraction solution displaying the most degraded performance was recorded at LW, permitting a maximum beam angle of 53°, identical to the Model Two performance. The performance of Model Three at LW+1 and LW+2 was also identical to the Model Two results, with beam angles of 55° and 65° respectively. Only at LW+3 did Model Three output deteriorate in comparison with Model Two, with a 69° maximum permissible beam angle compared with 67°.

Thain, 2003). Anecdotal evidence exists that the Royal Navy has already altered its shallow water hydrographic surveying methodology in order to take account of these specific recommendations.

The reduction in survey efficiency, resulting from such a stringent sound velocity sampling regime, is frequently too great to make commercial sense to many survey agencies. Continuous sound velocity sampling remains limited by equipment technology (Section 7.3.4.), and the use of a continuously-updating sound velocimeter at the transducer face, radically altering the upper region of the SVP with an updated surface value, makes considerable assumptions regarding the constancy of the remainder of the SVP. The traditional survey solution to reduce the swath width, thereby assuming that any grossly refracted outer beams are removed from the sounding solution is a rather 'hit and miss' affair. There can be little confidence placed in a solution made on the basis of such an arbitrary decision. The use of an appropriate sonar refraction model as a survey decision-aid improves survey efficiency, by maximising the available swath width, whilst still maintaining the quality of the bathymetric data. The resulting advantage in surveying time, together with the greater confidence which can be placed in the final depth solution, can also be used to significant commercial advantage. With the input of a few simple measurements, or even estimates, the most appropriate time to conduct the survey, the ideal sound velocity sampling frequency and density, and the sonar array type providing the most accurate solution may be determined.

For example, when undertaking a survey of a partially mixed estuary such as the Dart, the limitations of traditional surveying practice become readily apparent. By using only one SVP

derived from measurements taken at the beginning of a survey line, the presence of the pronounced stratification during the neap phase of the tidal cycle, produces extreme refraction of the outer beams. The use of a refraction model enables the identification and quantification of the spatial and temporal variability in the magnitude of the depth errors, caused by refraction. A few carefully-planned CTD casts, using the refraction model output, could be sufficient for several hours of continuous, accurate, surveying. Modelling the presence of the tidal intrusion front during spring tides suggests that either extremely frequent sound velocity sampling is necessary, or an appropriate reduction in swath width is required. The latter solution is suggested as most appropriate in this instance due to the highly dynamic nature of the frontal system. Using the models to investigate the effect of spatial and temporal variations in estuarine stratification in this way, the most effective solution would be to plan the time of the survey to coincide with periods of low stratification, with little temporal variability. In this way, swath width could be maximised and sound velocity sampling density reduced to a minimum.

The use of a sonar refraction model could also be used in the post-processing of bathymetric data (e.g. Cartwright & Hughes Clarke, 2002). A survey could be conducted taking sound velocity profiles as frequently as practicable. Any readily-apparent refraction artefacts could be removed at a later time, using refraction solutions calculated using an appropriate model. Whilst this does improve survey efficiency in terms of minimising vessel time, significant delays in post-processing and chart production could result.

Refraction modelling also facilitates the selection of the most appropriate equipment to use, in a particular hydrodynamic environment. The use of a flat sonar transducer array, without

surface sound velocity corrections (Model Two) has been found to provide the most consistent performance. The Simrad EM3000, or L3 Elac (Table 7.02) would, therefore, provide reasonable overall performance in an estuarine environment. Adding a continuously-updating sound velocimeter at the transducer face adds little to the accuracy of the bathymetric measurements (Model Three). The use of a cylindrical transducer array, such as that employed by the Simrad EM1000 and EM1002, would result in the recording of the greatest depth errors. The performance of a hybrid type transducer, such as the Reson Seabat would fall somewhere between the two other types.

This depth-error analysis indicates clearly that present sound velocity sampling practice when surveying in estuarine environments should be updated with immediate effect. The frequency of sound velocity sampling should be less than 50 m spatially; it should be less than one hour temporally. If such a sampling regime is not possible, the use of an appropriate multibeam sonar refraction model enables the identification of the period of the tidal cycle when a survey may be undertaken most efficiently. In addition, the areas where additional sound velocity profiles are required to maintain accuracy may be identified. In this way, survey accuracy and efficiency may be enhanced considerably.

8.0. Conclusions

A tidal intrusion front has been observed to form at the mouth of the Dart estuary during spring tides. The visual manifestation of the front is apparent for approximately two hours, starting one hour after low water (LW+1). At LW, two-way horizontal exchange flow between estuarine and coastal waters is present, although the thickness of the upper layer indicates that the buoyant outflow at the surface is partially arrested (but not blocked) at this time. Sub-maximal exchange flow at the estuary mouth is, therefore, occurring at this stage of the tidal cycle, consistent with theoretical predictions of such flows (Chao & Paluszkiewicz, 1991; Farmer & Armi, 1986). The front forms at LW+1, as two-layer flow interacts firstly with a constriction at the estuary mouth then, secondly, with a depression in the seabed, producing an hydraulic control point. As the flow enters the estuary, it speeds up and becomes supercritical as it passes through the constricted mouth. When it reaches the depression in the seabed, the inflow undergoes an internal hydraulic jump, due to the change in estuary cross-sectional area, becoming abruptly critical or subcritical. At this point, it no longer has sufficient velocity to push back the buoyant estuary outflow, which is arrested. In order to maintain continuity, the dense inflowing water plunges beneath the static surface layer, gaining velocity as it is compressed between this surface layer and the seabed. The critical flow speed required, in order to arrest the buoyant outflow, has been found to be identical to that predicted by hydraulics theory (Farmer & Armi, 1986). Estimates of eddy viscosity across the pycnocline, just downstream of the frontal interface, indicate a suppression of turbulence in this area; hence, density stratification remains persistent and resistant to shear-induced mixing at this stage of the tide (Section 6.3). The tidal intrusion front thus continues to be spatially stable for a time, remaining bathymetrically arrested, from LW+1 to LW+2, consistent with the findings of field studies and theoretical investigations (Huzzey, 1982; Akiyama & Stefan, 1984; Armi & Farmer, 1986; Farmer & Armi, 1986; Marmorino & Trump,

1996). As barotropic forcing increases, the plunge depth increases, and the front migrates downstream, over the increasing depth of the seabed depression. As the tidal velocity increases further, estimates of eddy viscosity indicate an increase in turbulence at the pycnocline, allowing interfacial shear to dominate. Enhanced baroclinic forcing across the frontal interface also increases the magnitude of the inflow in the lower layer, exacerbating the shear across the pycnocline at the base of the frontal system. This enhanced shear, combined with an increasing upward transport of salt across the weakening horizontal density interface, eventually overcomes the stratification, resulting in the rapid decay of the front.

It appears, therefore, that during spring tides, the flow at the estuary mouth is behaving as if flowing over a sill. The constriction at the mouth, followed by the abrupt increase in depth (and cross-sectional area) at the seabed depression, creates a similar topographical situation to two-layer flow over the lee side of a sill, at the mouth of a fjord or bar-built estuary. The contraction at the narrow mouth is unlikely to influence the inflow to a great degree, as the flow in the upper layer is weak on the flooding tide; therefore, the control exercised by the contraction is weak (Farmer & Armi, 1986). The seabed depression ('sill') will have the greater effect at this time, as the lower layer interacts directly with the changes in bathymetry which protrude into this active lower layer (Armi, 1986).

During neap tides, there is no visual manifestation of the front. Tidal straining exacerbates the stratification on the ebb, and lower flow velocities are not of a sufficient magnitude to arrest the buoyant outflow from the estuary (Sections 2.2.2 & 6.3). Estimates of eddy viscosity at this time indicate that turbulence is highly suppressed by the pronounced stratification present, maintaining two-layer exchange flow intact for much of the flooding tidal cycle. The lower layer remains subcritical throughout the flooding tide; therefore, no topographic control is

exercised by the seabed in this case. The low flow velocities do not allow the formation of a hydraulic control point, and the front does not appear.

The composite Froude number, G^2 (equation 2.08), derived from the densimetric Froude numbers, F_1^2 and F_2^2 (equation 2.09) for each layer in a two layer flow situation, has proved to be an accurate frontal discriminator in this case (Sections 6.2.2, 6.2.4, 6.4.1). An abrupt change in the value of G^2, from supercritical to subcritical, was found to be a good indicator of the presence of a front. This flow transition was found to be driven principally by changes in the lower layer when the front was present, highlighting the role played by bathymetric changes in frontal evolution. The inflow Froude number, F_o^2 (equation 2.19), proved to be invaluable in ascertaining the existence of a hydraulic control point, and quantifying whether the control occurred at the constriction, or upstream or downstream of it (Sections 6.3 & 6.4.3). F_o^2 also provided a measure of the efficiency of any exchange flow present between estuarine and coastal waters, which may have use in wider estuarine applications. The shear Froude number, F_Δ^2 (equation 2.20), was found to be supercritical just upstream of the front, and subcritical just downstream, in every realisation of frontal formation. The supercritical values of F_Δ^2 indicated flow on the brink of instability and mixing prior to plunging. Increasing water depth by a factor of two over the seabed depression was sufficient to make F_Δ^2 abruptly subcritical. During neap tides, the large density difference between the layers in the presence of lower flow velocities ensured that F_Δ^2 remained subcritical, despite the spatial changes in the total water depth. As this parameter was subcritical in every case, *apart* from when and where a front was present, it has proven to be the best and most accurate discriminator of frontal location, in addition to quantifying the magnitude of interfacial mixing (Sections 6.3 & 6.4.2).

The gradient Richardson number, *Ri* (equation 2.03), did not prove to be an accurate frontal discriminator. Whilst providing some insights into areas of mixing and stratification across the frontal zone (Sections 5.5 & 6.4.5), it did not indicate reliably the location of the front, nor its formation and decay. The interfacial Froude number, *Fi* (equation 2.07), and the closely related layer Richardson number, Ri_L (equation 2.04), were found to be extremely variable throughout surveys during spring and neap tides, and have not proven to be accurate frontal discriminators (Section 6.4.4).

The theoretical dimensionless parameters developed by Farmer & Armi (1986) and Largier (1992), for use with two-layer flow over a sill, have been found to have use in such a partially mixed estuary. Although not having a sill in the strictest sense, the Dart estuary, a ria, behaves rather like a fjord or bar-built estuary, due to dramatic changes in depth and width just inside the estuary mouth. Thus, two-layer flow in this region behaves in a similar fashion to that over the lee side of a sill, plunging inflow and the formation of a tidal intrusion front being hydraulically-controlled by the topographic changes (Thain *et al.*, 2004). This frontal system is likely to vary in intensity, at different stages of the spring-neap and seasonal cycle. For the front to form, a balance must exist (for a time, at least) between the tidal forcing and relative buoyancy of the estuarine waters. Anecdotal evidence suggests that, during equinoctial spring tides, when barotropic and baroclinic forcing are high, the front decays extremely quickly, or may not form at all. During periods of prolonged drought, the estuary may not be sufficiently stratified to promote the creation of a front.

The presence of a tidal intrusion front can prove problematical for the hydrographic surveyor utilising multibeam sonar equipment in such an environment. In order to obtain an accurate sounding solution, a multibeam sonar system requires up-to-date sound velocity profile

information, in order to calculate the paths of each individual sound ray through the water column (Dinn *et al.*, 1995; Hughes Clarke *et al.*, 2003). Additionally, flat sonar transducer arrays employ electronic beam-steering to launch each sound ray at the desired angle from the transducer face. The electronic beam steering angle is a function of the acoustic wavelength, itself, a function of the velocity of sound in seawater. Thus, if both the surface sound velocity, and the sound velocity profile are not measured at intervals appropriate to the variability, the final reduced soundings may not meet the challenging depth-accuracy standards demanded by the International Hydrographic Organisation (IHO, 1998).

Present estuarine surveying practice is based on limited research; it involves generally measuring the sound velocity profile only once, when commencing each new survey line (Dinn *et al.*, 1997; Hughes Clarke *et al.*, 2003). This profile is assumed then to remain constant, until the following update. Calculated values of sound velocity, derived from the data collected in the Dart estuary during both a spring and a neap tidal period, indicate a high degree of temporal and spatial variability. When traversing the tidal intrusion front at LW+1, for example, variations in surface sound velocity of 4 ms^{-1} have been recorded over a horizontal distance of less than 75 m (Section 5.3.1). Additionally, the change in the depth of the pycnocline, when crossing the frontal zone, may lead also to pronounced refraction artefacts. During periods of neap tides, the persistent low salinity layer at the surface may cause significant errors, if only a single sound velocity profile were to be taken outside the estuary mouth, where the layer is not present (Cartwright & Hughes Clarke, 2002).

Three sonar refraction models have been developed and tested, as part of this study, in order to quantify the effect of a tidal intrusion front in a partially mixed estuary on multibeam sonar accuracy; likewise to facilitate the identification of the optimum sound velocity sampling

methodology in such an estuarine environment (Sections 7.4 & 7.5). Simulating a cylindrical transducer array, a flat transducer array and a flat array receiving constant updates of surface sound velocity, the three models have used as inputs the sound velocity data collected in the Dart estuary, during both spring and neap tides. Model results indicated that surveying across a tidal intrusion front would require a typical reduction in swath width, from the maximum of 150° to 114°, to maintain depth accuracies acceptable to IHO specifications. During certain periods of the neap tidal cycle, the model results indicated that the presence of the pronounced low salinity surface layer would require a reduction in swath width to 90°, to maintain the integrity of the reduced depth soundings. The most effective overall performance would be provided by the use of the flat sonar transducer array (Model Two). Continuously updating the surface sound velocity to remove beam steering errors (Model Three), was found not to improve the accuracy of the depth soundings. The use of a cylindrical transducer array (Model One) was found to produce good survey results during a spring tide, however, the performance of this model was reduced dramatically during neap tides, reducing the mean overall effectiveness of such a transducer.

Therefore, it is apparent that generic sound velocity sampling procedures, as undertaken by the hydrographic surveyors in estuarine environments, are not sufficient to quantify adequately the variability in the sound velocity field, which occurs due to the presence of a tidal intrusion front. The frequently-employed solution, of reducing the swath width to remove refraction artefacts in the outer beams, compromises overall survey efficiency. The guidelines on sound velocity sampling in estuaries should, therefore, be updated with immediate effect. It is suggested that, in order to ensure maximum accuracy of reduced depth soundings and to improve survey efficiency, the frequency of sound velocity sampling should be less than 50 m spatially, and less than one hour temporally. If such a sampling regime were undertaken, the

full multibeam sonar swath width could be employed with confidence during hydrographic surveys. The use of a greater swath width would allow the surveyor to complete the survey using fewer survey lines, yielding corresponding improvements in efficiency. For example, assuming a water depth of 25 m and a survey line length of 2 km during a spring tide at LW+1 in the Dart estuary, employing the full sonar swath width would facilitate a reduction in surveying time of 62%. Such improvements are exacerbated in shallower water, where the maximum sonar footprint on the seabed is reduced (Figure 7.07). Assuming a 10 m water depth, for example, the ability to use the full swath width would result in an 82% reduction in surveying time, representing a time saving of almost 12 hours.

It is possible, however, that the dense sampling of the sound velocity field required to facilitate such improvements in surveying efficiency may not be practicable in terms of the time needed to conduct the measurements required. Employing a refraction modelling approach at the survey planning stage is likely, therefore, to provide the most useful information to the practicing surveyor. Potentially most useful, however, is the use of an integrated system, combining the appropriate dimensionless estuarine descriptors together with a sonar refraction model. In the common morphological situation of a constricted estuarine mouth, measurements of density and flow speed taken solely in the channel constriction could be related to a critical inflow Froude number (F_o^2). The use of a simple graph (e.g. Figure 6.29) would then enable the surveyor to ascertain the likely presence of a tidal intrusion front, and to plan the survey accordingly in order to maximise efficiency. This would allow the most effective sound velocity sampling locations and times to be quantified and, in combination with the use of a sonar refraction model, the maximum swath width of the multibeam system to be calculated. To improve survey efficiency further, the times during the tidal cycle when oceanographic conditions would facilitate the use of the maximum swath

width could be determined. Thus, an hydrographic survey could be scheduled to take place when the frontal system was likely to be absent, using an appropriate and efficient sound velocity sampling regime. In the case of the Dart estuary, surveying near times of high water during a spring tide, using a flat sonar transducer array, would be likely to provide the most effective results, with the minimum of post-processing required to remove refraction artefacts. A survey agency employing such an integrated planning approach would enjoy a considerable commercial advantage.

This programme of study has provided conclusions of practical use, to those investigating estuarine dynamics and to hydrographic surveyors. It is suggested that future work should concentrate on developing a simple two-dimensional numerical model, which would simulate accurately frontal formation and decay over changing bathymetry. Incorporating the dimensionless descriptors, which are most appropriate to frontal formation and development as identified in this study, would facilitate its use in other estuaries. Such a modelling approach would provide further useful insights into the dynamics of a tidal intrusion front, and would facilitate a comprehensive investigation into the formation and intensity of the front at stages of the tidal cycle, other than during the peak spring and neap phases. Ultimately, the combination of such an hydrodynamic model, together with a sonar refraction model, would provide a complete planning solution to the hydrographic surveyor. Additionally, further fine-scale field measurements, such as those provided by using the ADCP variance method or a high frequency echo-sounder, would enhance our understanding of the small-scale processes at work at the frontal interface; as such providing useful data for hydrodynamic model validation

In conclusion, it appears that tidal intrusion fronts may be a relatively common feature at the mouths of estuaries similar in morphology to the Dart. This research provides information of use in the prediction and analysis of such systems. Whilst it is enlightening to hear anecdotal reports that many survey agencies, including the Royal Navy, are considering sound velocity sampling in estuarine environments more carefully in light of the findings of this study (Priestley & Thain, 2003), it is apparent that a need remains to develop and inculcate an understanding of the complex relationships between estuarine hydrodynamics, frontal systems, sonar errors and the error in final reduced-depth value. A better understanding of these relationships will assist the hydrographic surveyor in effective planning, yield improvements in survey accuracy and efficiency, and may lead to more informed decisions regarding purchases or upgrades to multibeam sonar systems.

9.0. References

Akiyama, J. & Stefan, H. G. (1984). Plunging flow into a reservoir: Theory. *Journal of Hydraulic Engineering*, **110**, 484-499.

Armi, L. (1986). The hydraulics of two flowing layers with different densities. *Journal of Fluid Mechanics*, **163**, 27-58.

Armi, L. & Farmer, D. M. (1986). Maximal two-layer exchange through a contraction with barotropic net flow. *Journal of Fluid Mechanics*, **164**, 27-52.

Baines, P. G. (1995). *Topographic effects in stratified flows*. Cambridge University Press, New York, 482 pp.

Batton, D. (2004). The effect of refraction on oblique angles of multibeam echo-sounders due to sound speed changes through the water column. *The Hydrographic Journal*, **113**, 15-20.

Benjamin, T.B. (1968). Gravity currents and related phenomena. *Journal of Fluid Mechanics*, **31**, 209-248.

Bowman, M. J. (1988). Estuarine Fronts. In *Hydrodynamics of Estuaries Vol.I, Estuarine Physics*. (ed. B. Kjerfve), pp. 85-132. CRC Press, Boca Raton.

Bowman, M. J. & Esaias, W. E. (1981). Fronts, stratification and mixing in Long Island and Block Island Sounds. *Journal of Geophysical Research*, **86**, 4260-4264.

Bowman, M. J. (1977) Introduction and proceedings. In *Oceanic Fronts in Coastal Processes* (ed. M. J. Bowman & W. E. Esaias), pp. 2-16. Proceedings of a workshop held at the Marine Sciences Research Centre, May 25-27, 1977. Springer-Verlag, New York.

Bowman, M. J. & Iverson, R. L. (1977). Estuarine and Plume Fronts. In *Oceanic Fronts in Coastal Processes* (ed. M. J. Bowman & W. E. Esaias), pp. 87-104. Proceedings of a workshop held at the Marine Sciences Research Centre, May 25-27, 1977. Springer-Verlag, New York.

Brandt, S. B. (1993) The effect of thermal fronts on fish growth: A bioenergetics evaluation of food and temperature. *Estuaries*, **16**, 1, 142-159.

Brubaker, J. M. & Simpson, J. H. (1999). Flow convergence and stability at a tidal estuarine front: Acoustic Doppler current observations. *Journal of Geophysical Research*, **104**, C8, 18257-18268.

Bryden, H. L. & Kinder, T. H. (1991). Recent progress in Strait dynamics. *U. S. National Report to International Union of Geodesy and Geophysics, 1987-1990. Reviews of Geophysics, supplement*, **29**, 617-631.

Cartwright, D. & Hughes Clarke, J. E. (2002). Multibeam surveys of the Fraser River Delta, coping with an extreme refraction environment. *Canadian Hydrographic Conference proceedings*, CDROM.

Chao, S. Y. & Paluszkiewicz, T. (1991). The hydraulics of density currents over estuarine sills. *Journal of Geophysical Research*, **96**, C4, 7065-7076.

Chen, C. T. & Millero, F. J. (1977). Speed of sound in seawater at high pressures. *Journal of the Acoustical Society of America*, **62**, 1129-1135.

Chen, P., Grant Ingram, R. & Gan, J. (1994). A numerical study of hydraulic jump and mixing in a stratified channel with a sill. In *Estuarine and Coastal Modelling III.* (ed. M. L. Spaulding, K. Bedford, A. Blumberg, R. Cheng & C. Swanson), pp. 119-133. American Society of Civil Engineers, New York.

Ciannelli, L. (2002). Effects of spatial variability, associated with a frontal structure, on predictions of age-0 walleye pollock (*Theragra chalcogramma*) growth around the Pribilof Islands, Bering sea. *Estuarine, Coastal and Shelf Science*, **55**, 151-165.

Coates, R. (2002). Underwater acoustics, short course notes. Seiche.com Ltd., Imperial College, London.

Cudaback, C. N. & Jay, D. A. (2001). Tidal asymmetry in an estuarine pycnocline 2: Transport. Journal *of Geophysical Research*, **106**, C2, 2639-2652.

DEEM. (1998). Dart estuary environmental management plan. Dart Estuary Environmental Management, Dartmouth, Devon.

DEEM. (2004). Tidelines, Autumn 2004. Newsletter of Dart Estuary Environmental Management, Dartmouth, Devon.

Del Grosso, V. A. (1974). New equation for the speed of sound in natural waters (with comparison to other equations). *Journal of the Acoustical Society of America*, **56**, 1084-1091.

deMoustier, C. (2003a). Multibeam sonar methods. In *31st Coastal Multibeam Sonar Training Course.* (ed. J. Hughes Clarke, C. deMoustier, L. Mayer & D. Wells). Ocean Mapping Group, University of New Brunswick.

deMoustier, C. (2003b). Sound refraction in the water column. In *31st Coastal Multibeam Sonar Training Course.* (ed. J. Hughes Clarke, C. deMoustier, L. Mayer & D. Wells). Ocean Mapping Group, University of New Brunswick.

deMoustier, C. (2003c). DTM generation methods and pitfalls. In *31st Coastal Multibeam Sonar Training Course.* (ed. J. Hughes Clarke, C. deMoustier, L. Mayer & D. Wells). Ocean Mapping Group, University of New Brunswick.

Deines, K. L. (1999). Backscatter estimation using Broadband Acoustic Doppler Current Profilers. *Oceans 99 MTS/IEEE*, 13-16 Sept 1999.

Denton, R. A. (1987). Locating and identifying hydraulic controls for layered flow through an obstruction. *Journal of Hydraulic Research*, **25**, 281-299.

Dinn, D. F., Furlong, A., Loncarevic, B. D., Penny, M. & Dakin, D. T. (1997). Controlling multibeam sonar errors. *Sea Technology*, **38**, 8, 75-80.

Dinn, D. F., Loncarevic, B. D. & Costello, G. (1995). The effect of sound velocity errors on multibeam sonar depth accuracy. *Proceedings of the IEEE Oceans 95 Conference*, San Diego, California, pp. 1001-1010.

Dixon, C. (1994). *Using GPS.* Adlard Coles Nautical, London, 90 pp.

Duck, R. W. & Wewetzer, S. F. K. (2001). Impact of frontal systems on estuarine sediment and pollutant dynamics. *The Science of the Total Environment*, **266**, 23-31.

Durazo, R., Harrison, N. M. & Hill, A. E. (1998). Seabird observations at a tidal mixing front in the Irish sea. *Estuarine, Coastal and Shelf Science*, **47**, 153-164.

Dyer, K. R. (1979). Estuarine hydrography and sedimentation: A handbook. Cambridge University Press, Cambridge, 230 pp.

Dyer, K. R. (1997). *Estuaries: a physical introduction.* John Wiley, Chichester, 195 pp.

Dyer, K. R. (1988). Tidally generated estuarine mixing processes. In *Hydrodynamics of Estuaries Vol.I, Estuarine Physics.* (ed. B. Kjerfve), pp. 41-57. CRC Press, Boca Raton.

Dyer, K. R. & New, A. L. (1986). Intermittency in estuarine mixing. In *Estuarine Variability*, (ed. D. A. Wolfe), pp. 321-339. Academic Press, Orlando.

EOS. (1978). Oceanic fronts: a summary of a Chapman Conference (ed. C. N. K. Mooers), *Trans American Geophysical Union*, **59**, 484-491.

Emery, W. J. & Thomson, R. E. (2001). Data Analysis methods in Physical Oceanography. Elsevier Science Ltd, Oxford, 638 pp.

Environment Agency. (1998). Local Environment Agency Plan: River Dart Action Plan July 1998. Environment Agency, Miller Way, Exeter.

Etter, P. C. (1991). *Underwater acoustic modeling.* Elsevier, Barking, 305 pp.

Farmer D. M & Armi, L. (1986). Maximal two-layer exchange over a sill and through the combination of a sill and contraction with net barotropic flow. *Journal of Fluid Mechanics*, **164**, 53-76.

Gargett, A. E., & Moum, J. N. (1995). Mixing efficiencies in tidal fronts: Results from direct and indirect measurements of density flux. *Journal of Physical Oceanography*, **25**, 2583-2608.

Garvine, R. W. (1977). River plumes and estuary fronts. In *Estuaries, geophysics and the Environment,* pp. 30-35. National Academy of Sciences, Washington DC.

Geyer, W. R. & Smith, J. D. (1987). Shear instability in a highly stratified estuary. *Journal of Physical Oceanography*, **17**, 1668-1679.

Gilboy, T. P., Dickey, T. D., Sigurdson, D. E., Yu, X., & Manov, D. (2000). An intercomparison of current measurements using a vector measuring current meter, an acoustic Doppler current profiler, and a recently developed acoustic current meter. *Journal of atmospheric and oceanic technology*, **17**, 4, 561-574.

Griffin, D. A. & LeBlond, P. H. (1990). Estuary/ocean exchange controlled by spring/neap tidal mixing. *Estuarine, Coastal and Shelf Science*, **30**, 275-297.

Haas, L. W. (1977). The effect of the spring-neap tidal cycle on the vertical salinity structure of the James, York, and Rappahannock Rivers, Virginia, USA. *Estuarine and Coastal Marine Science*, **5**, 485-496.

Haehnel M. (1990). Employing an Acoustic Current Profiler in Surveys of the Arctic Front in the Greenland Sea. In *Proceedings of the IEEE Fourth Working Conference on Current Measurement*, pp. 173-179, Clinton, Maryland.

Hansen, D. M. & Rattray, M. (1966). New Dimensions in Estuary Classification. *Limnology and Oceanography*, **11**, 319-326.

Hare, R., Godin, A. & Meyer, L. (1995). *Accuracy estimation of Canadian swath (multibeam) and sweep (multitransducer) sounding systems.* Canadian Hydrographic Service internal report.

Heathershaw, A. D., Richards, S. D. & Thorne, P. D. (1996). Acoustic absorption and scattering by suspended sediments in turbid coastal waters. *Journal of Defence Science*, **1**, 2.

Hogarth, P. (2003). Achieving high accuracy using wide swath bathymetry systems. GeoAcoustics Ltd, Yarmouth, internal report.

Hughes Clarke, J. E., Meyer, L. A. & Wells, D. E. (1996). Shallow water imaging multibeam sonars: A new tool for investigating seafloor processes in the coastal zone and on the continental shelf. *Marine Geophysical Research*, **18**, 607-629.

Hughes Clarke, J. E. (2000). Acoustic seabed surveying - meeting new demands for accuracy, coverage and spatial resolution. *Geomatica*, **54**, 4, 473-413.

Hughes Clarke, J. E. (2003a). Dynamic motion residuals in swath sonar data: Ironing out the creases. *International Hydrographic Review*, March 2003.

Hughes Clarke, J. E. (2003b). Field Calibration: The patch test and the reference surface. In *31st Coastal Multibeam Sonar Training Course.* (ed. J. Hughes Clarke, C. deMoustier, L. Mayer & D. Wells). Ocean Mapping Group, University of New Brunswick.

Hughes Clarke, J., deMoustier, C., Mayer, L. & Wells, D. (2003). *31st Coastal Multibeam Sonar Training Course.* Course notes, Ocean Mapping Group, University of New Brunswick.

Hughes Clarke, J. E., Lamplugh, M. & Kammerer, E. (2000). Integration of near-continuous sound speed profile information. *Canadian Hydrographic Conference,* Montreal, Canada.

Huzzey, L. M. (1982). The dynamics of a bathymetrically arrested estuarine front. *Estuarine, Coastal and Shelf Science*, **15**, 537-552.

Hydrographer of the Navy. (2000). Admiralty list of Radio Signals 8, NP 288, Satellite Navigation systems. United Kingdom Hydrographic Office, Taunton.

International Hydrographic Organisation. (1998). *IHO standards for hydrographic surveys, Special Publication no. 44, 4th edition.* International Hydrographic Bureau, Monaco.

InterOcean. (1996). S4 Current Meter Family. InterOcean systems, inc., San Diego.

Jay, D. A. & Smith, J. D. (1990). Circulation, density structure and neap-spring transitions in the Columbia river estuary. *Progress in Oceanography*, **25**, 81-112.

Jay, D. A. & Smith, J. D. (1988) Residual Circulation in and Classification of shallow, stratified estuaries. In *Physical Processes In Estuaries*, (ed. J. Dronkers, W. van Leussen), pp. 21-41. Springer- Verlag, Berlin.

Joyce, T. M. (1989). On in situ 'calibration' of shipboard ADCPs. *Journal of Atmospheric and Oceanic Technology*, **6**, 169-172.

Klemas, V. & Polis, D. F. (1977). Remote sensing of estuarine fronts and their effects on pollutants. *Photogrammetric Engineering and Remote Sensing*, **43**, 599-612.

Korman, M. S. (1995). Underwater acoustics and sonar: the preliminary edition. Kendall/Hunt, Iowa, 245 pp.

Kranenburg, C. (1988). On internal waves in partially mixed and stratified tidal flows. In *Physical Processes In Estuaries*, (ed. J. Dronkers, W. van Leussen), pp. 213-238. Springer- Verlag, Berlin.

Kuo, A. Y., Byrne, R. J., Brubaker, J. M. & J. Posenau. (1988) Vertical transport across an estuary front. In *Physical Processes In Estuaries*, (ed. J. Dronkers, W. van Leussen), pp. 93-109. Springer- Verlag, Berlin.

Kuo, A. Y., Byrne, R. J., Hyer, P. V., Ruzecki, E. P. & Brubaker, J. M. (1990). Practical application of theory for tidal intrusion fronts. *Journal of Waterway, Port, Coastal and Ocean Engineering*, **116**, 341-361.

Largier, J. L. (1992). Tidal intrusion fronts. *Estuaries*, **15**, 26-39.

Largier, J. L. (1993). Estuarine Fronts: How Important Are They? *Estuaries*, **16**, 1-11.

Largier, J. L. & Taljaard, S. (1991). The dynamics of tidal intrusion, retention, and removal of sea water in a bar-built estuary. *Estuarine, Coastal and Shelf Science*, 33, 325-338.

Largier, J. L., Slinger, J. H. & Taljaard, S. (1992). The stratified hydrodynamics of the Palmiet – a prototypical bar-built estuary. In *Coastal and Estuarine Studies 40. Dynamics and exchanges in estuaries and the coastal zone*, (ed. D. Prandle), pp. 135-153. American Geophysical Union, Washington, D.C.

Lee, C. & Beardsley, R. C. (1974). The generation of long nonlinear internal waves in a weakly stratified shear flow. *Journal of Geophysical Research*, 79, 3, 453-462.

Lewis, R. E. (1996). Relative contributions of interfacial and bed generated mixing in the estuarine energy balance. In *Mixing in estuaries and Coastal Seas*, (ed. C. Pattiaratchi), pp. 250-266, Coastal and Estuarine Studies Series, **50**, American Geophysical Union, Washington DC.

Lewis, R. (1997). *Dispersion in Estuaries and Coastal Waters*, John Wiley, Chichester, 312 pp.

Linden, P. F. & Simpson, J. E. (1988). Modulated mixing and frontogenesis in shallow seas and estuaries. *Continental Shelf Research*, **8**, 1107-1127.

Loder, J. W. & Greenberg, D. A. (1986). Predicted Positions of Tidal Fronts in the Gulf of Maine region. *Continental Shelf Research*, **6**, 397-414.

Logsdon, T. (1992). *The Navstar Global Positioning System.* Van Nostrand Reinhold, New York, 256 pp.

Lu, Y. Y. & Lueck, R. G. (1999). Using a broadband ADCP in a tidal channel. Part I: Mean flow and shear. *Journal of atmospheric and oceanic technology.* **16,** 11, 1556-1567.

Lurton, X. (2002). An introduction to underwater acoustics: principles and applications. Praxis Publishing, Chichester, 347 pp.

MacKenzie, K. V. (1981). Nine-term equation for sound speed in the oceans. *Journal of the Acoustical Society of America,* **70,** 807-812.

Madirolas, A., Acha, E. M., Guerrero, R. A. & Lasta, C. (1997). Sources of acoustic scattering near a halocline in an estuarine frontal system, *Scientia Marina,* **61,** 4, 431-438.

Marmorino, G. O. & Trump, C. L. (1996). High-resolution measurements made across a tidal intrusion front. *Journal of Geophysical Research,* **101,** C11, 25661-25674.

Maxworthy, T. (1979). A note on the internal solitary waves produced by tidal flow over a 3-D ridge. *Journal of Geophysical Research,* **84,** C1-6, 338-346.

McManus, J. (2000). Sedimentation associated with frontal systems. In *Coastal and estuarine environments: sedimentology, geomorphology and geoarchaeology* (ed. K. Pye, & J. R. L. Allen), Geological Society, London, Special Publications, **175,** 5-11.

Medwin, H. (1975). Speed of sound in water: A simple equation for realistic parameters. *Journal of the Acoustical Society of America*, **58**, 1318-1319.

Mehrotra, S. C. (1973). Boundary contractions as controls in two-layer flows. *Journal of the Hydraulic Division ASCE* **99**, HY11, 2003-2012.

Mendes, S., Turrell, W., Lutkebohle, T. & Thompson, P. (2002). Influence of the tidal cycle and a tidal intrusion front on the spatio-temporal distribution of coastal bottlenose dolphins. *Marine Ecology Progress Series*, **239**, 221-229.

Miller, J. E., Hughes Clark, J. E., Paterson, J. (1997). How effectively have you covered your bottom. *The Hydrographic Journal*, **83**, 3-10.

Monismith, S. G. & Fong, D. A. (1996). A simple model of mixing in stratified tidal flows. *Journal of Geophysical research*, **101**, C12, 28583-28598.

Munk, W. H. & Anderson, E. R. (1948). Notes on a theory of the thermocline. *Journal of Marine Research*, **7**, 276-295.

Murphy, D. J., Biggs, D. C. & Cooke, M. L. (1992). Mounting and Calibrating an Acoustic Doppler Current Profiler, *Marine Technology Society Journal*, **26**, 34-38.

Nepf, H. M. & Geyer, W. R. (1996). Intratidal variations in stratification and mixing in the Hudson estuary. *Journal of Geophysical Research*, **101**, C5, 12079-12086.

New, A. L. & Dyer, K. R. (1988). Internal Waves and Mixing in Stratified Estuarine Flows. In *Physical Processes In Estuaries*, (ed. J. Dronkers & W. van Leussen), pp. 239-254. Springer-Verlag, Berlin.

New, A. L., Dyer, K. R. & Lewis, R. E. (1986). Predictions of the Generation and Propagation of Internal Waves and Mixing in a Partially Stratified Estuary. *Estuarine, Coastal and Shelf Science*, **22**, 199-214.

Nunes, R., Lennon, G. & de Silva Samarasinghe, J. (1989). The negative role of turbulence in estuarine mass transport. *Estuarine, Coastal and Shelf Science*, **28**, 361-377.

O'Donnell, J. (1993). Surface Fronts in Estuaries: A Review. *Estuaries*, **16**, 12-39.

O'Donnell, J., Marmorino, G. & Trump, C. L. (1998). Convergence and downwelling at a River Plume Front. *Journal of Physical Oceanography*, **28**, 1481-1495.

Pelegri, J. L. (1988). Tidal Fronts in Estuaries. *Estuarine, Coastal and Shelf Science*, **27**, 45-60.

Peters, H. (1997). Observations of stratified turbulent mixing in an estuary. Neap-to-spring variations during high river flow. *Estuarine Coastal and Shelf Science*, **45**, 69-88.

Peters, H. (1999). Spatial and temporal variability of turbulent mixing in an estuary. *Journal of Marine Research*, **57**, 6, 805-845.

Pinckney, J. & Dustan, P. (1990). Ebb-tidal fronts in Charleston Harbor, South Carolina: physical and biological characteristics. *Estuaries*, **13**, 1-7.

Pollard, R. T. & Read, J. F. (1989). A method for calibrating ship-mounted Acoustic Doppler Current Profilers, and the limitations of gyro compasses. *Journal of Atmospheric and Ocean Technology*, **6**, 859-865.

Postma, H. (1988). Physical processes in estuaries; some evaluating remarks. In *Physical Processes In Estuaries*, (ed. J. Dronkers & W. van Leussen), pp. 547-550. Springer-Verlag, Berlin.

Priestley, A. D. (1998). The Dart Observatory: an estuarine monitoring system. *International Ocean System Design*, **2**, 5-9.

Priestley, A. D. & Thain, R. H. (2003). Water column variability at an estuarine mouth: Implications for multibeam sonar surveys. In *Proceedings of Third International Conference on High Resolution Surveys in Shallow Water*, Sydney, Australia, 17-21 November 2003.

RDI. (1996). Acoustic Doppler Current Profilers. Principles of operation: A practical primer. R. D. Instruments, California.

RDI. (2001). VmDas User's Guide. R. D. Instruments, California.

Salvadores, S. R. & Milou, M. I. E. (2004). Multimodal analysis of the acoustic field at the Rio de la Plata estuary. *Journal of Coastal Research*, **20**, 3, 655-661.

Sharples, J. & Simpson, J. H. (1993). Periodic frontogenesis in a region of freshwater influence. *Estuaries*, **16**, 1, 74-82.

Simpson, J. H. & Hunter, J. R. (1974). Fronts in the Irish sea. *Nature*, **250**, 404-406.

Simpson, J. H. & Pingree, R. D. (1977). Shallow sea fronts produced by tidal stirring. In *Oceanic Fronts in Coastal Processes* (ed. M. J. Bowman & W. E. Esaias), pp. 29-43. Proceedings of a workshop held at the Marine Sciences Research Centre, May 25-27, 1977. Springer-Verlag, New York.

Simpson, J. H. & Nunes, R. A. (1981). The Tidal Intrusion Front: An Estuarine Convergence Zone. *Estuarine, Coastal and Shelf Science*, **3**, 257-266.

Simpson, J. H. & James, I. D. (1986). Coastal and estuarine fronts. In *Baroclinic Processes on the Continental Shelf* (ed. C. N. K. Mooers), pp. 63-92, American Geophysical Union, Washington, D.C.

Simpson, J. H. & Turrell, W. R. (1986). Convergent fronts in the circulation of tidal estuaries. In *Estuarine Variability* (ed. D. A. Wolfe), pp. 139-151. Academic Press, Orlando.

Simpson, J. H., Brown, J., Matthews, J. M. & Allen, G. (1990). Tidal straining, density currents and stirring in the control of estuarine stratification. *Estuaries*, **13**, 125-132.

Stigebrandt, A. (1988). Dynamic control by topography in estuaries. In *Hydrodynamics of Estuaries Vol.I, Estuarine Physics* (ed. B. Kjerfve), pp. 18-26. CRC Press, Boca Raton.

Stommel, H. & Farmer, H. G. (1953). Control of salinity in an estuary by a transition. *Journal of Marine Research*, **12**, 13-20.

Sturley, D. R. & Dyer, K. R. (1992). A topographically induced internal wave and mixing in the Tamar estuary. In *Coastal and Estuarine Studies 40. Dynamics and exchanges in estuaries and the coastal zone* (ed. D. Prandle), pp. 57-74. AGU, Washington, D.C.

Swan, A. R. H. & Sandilands, M. (1995). Introduction to geological data analysis. Blackwell Science Ltd, Oxford, 446 pp.

Thain, R. H., Priestley, A. D. & Davidson, M. A. (2004). The formation of a tidal intrusion front at the mouth of a macrotidal, partially mixed estuary: a field study of the Dart estuary, UK. Estuarine, Coastal and Shelf Science, **61**, 161-172.

Thain, R. H. & Priestley, A. D. (2002a). The importance of tidal intrusion fronts for sonar Operations. In *Proceedings of XIIIth International Scientific Conference*, Naval University of Gdynia, Poland, 14-15 November 2002.

Thain, R. H. & Priestley, A. D. (2002b). Sound speed variability across an estuarine front. *Proceedings of the Undersea Defence Technology conference, La Spezia, Italy.*

Tiberius, C. (2003). Handheld GPS receiver accuracy. *GPS World*, **14**, 2, 46-51.

Urick, R. J. (1967). Principles of underwater sound. McGraw-Hill, New York, 384 pp.

Valeport Ltd. (1997). Model 604 CTD Probe, installation and 8008 CDU operation manual. Document ref: 0600822a, Valeport Ltd, Totnes, Devon.

Valeport Ltd. (1999). DataLog operation manual. Document ref: 0300849a, Valeport Ltd, Totnes, Devon.

Valle-Levinson, A., Jara, F., Molinet, C. & Soto, D. (2001). Observations of Intratidal Variability of Flows Over a Sill/Contraction Combination in a Chilean Fjord. *Journal of Geophysical Research*, **106**, C4, 7051-7064.

Valle-Levinson, A., Wong, K. C. & Lwiza, K. M. M. (2000). Fortnightly variability in the transverse dynamics of a coastal plain estuary, *Journal of Geophysical Research*, **105**, C2, 3413-3424.

Van Leussen, W. & Dronkers, J. (1988). Physical processes in estuaries: An introduction. In *Physical Processes In Estuaries*, (ed. J. Dronkers & W. van Leussen), pp. 1-21. Springer-Verlag, Berlin.

Wells, D. (2003). Hydrographic performance standards. In *31st Coastal Multibeam Sonar Training Course*. (ed. J. Hughes Clarke, C. deMoustier, L. Mayer & D. Wells). Ocean Mapping Group, University of New Brunswick.

Wewetzer, S. F. K., Duck, R. W. & Anderson, J. M. (1999). Acoustic Doppler current profiler measurements in coastal and estuarine environments: examples from the Tay Estuary, Scotland. *Geomorphology*, **29**, 1-2, 21-30.

Wilson, W. D. (1960). Equation for the speed of sound in seawater. *Journal of the Acoustical Society of America*, **32**, 1357.

Wood, I. R. (1968). Selective withdrawal from a stably stratified fluid. *Journal of Fluid Mechanics*, **32**, 209-223.

Wood, I. R. (1970). A lock exchange flow. *Journal of Fluid mechanics*, **42**, 671-687.

Yih, C. (1969). A class of solutions for steady stratified flows. *Journal of Fluid Mechanics*, **36**, 1, 75-85.

Appendix one. Picket Boat 8 Drawings

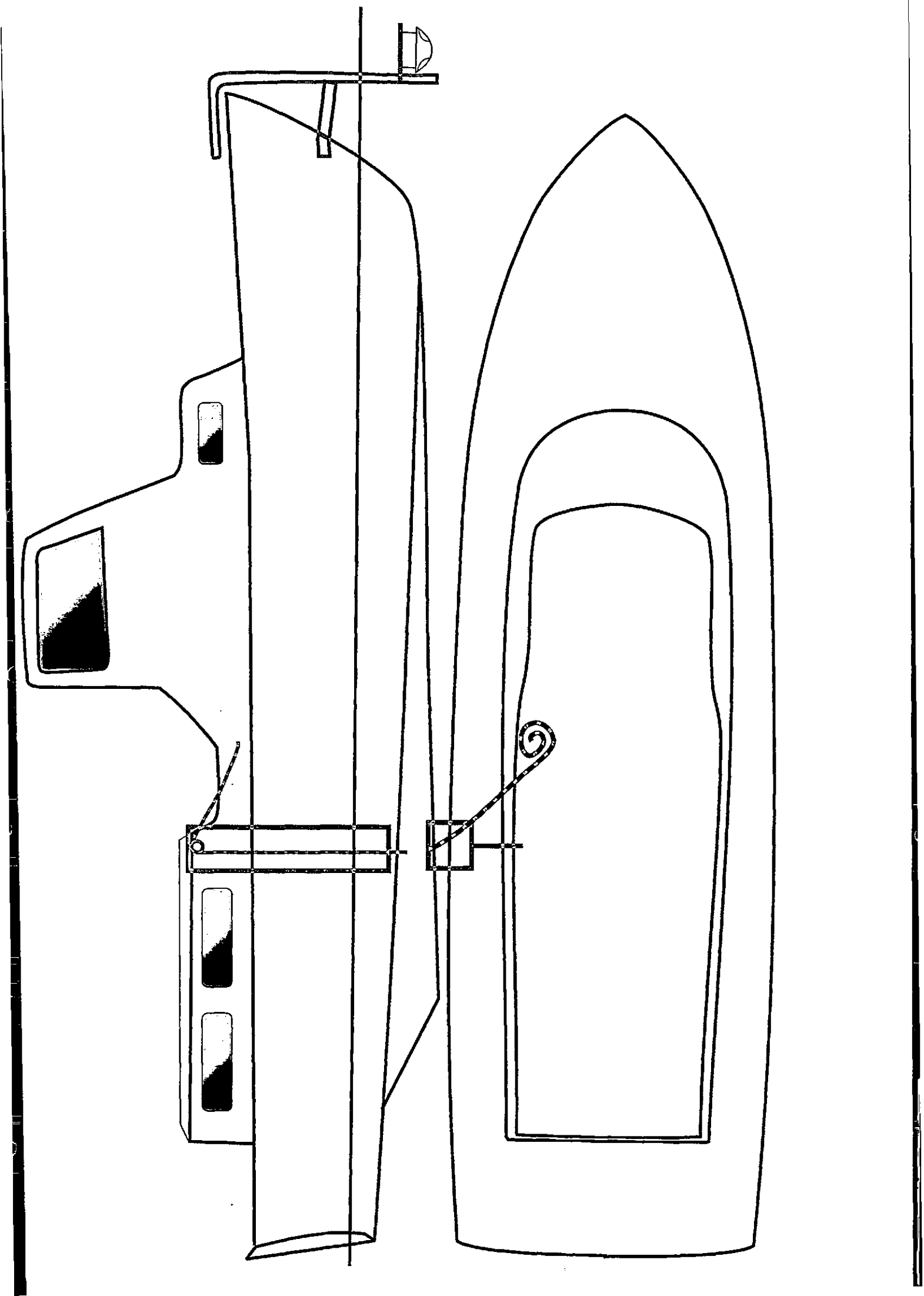

Appendix two. Publications

Thain, R. H., Priestley, A. D. & Davidson, M. A. (2004). The formation of a tidal intrusion front at the mouth of a macrotidal, partially mixed estuary: a field study of the Dart estuary, UK. *Estuarine, Coastal and Shelf Science,* **61**, *161-172.*

Priestley, A. D. & Thain, R. H. (2003). Water column variability at an estuarine mouth: implications for multibeam sonar surveys. *Third international conference on high resolution surveys in shallow water, Sydney, Australia,* 17-21 November 2003.

Thain, R. H. & Priestley, A. D. (2002). Sound speed variability across an estuarine front. *Proceedings of the Undersea Defence Technology conference, La Spezia, Italy.*

Available online at www.sciencedirect.com
SCIENCE DIRECT®
Estuarine, Coastal and Shelf Science 61 (2004) 161–172
ESTUARINE COASTAL AND SHELF SCIENCE
www.elsevier.com/locate/ECSS

The formation of a tidal intrusion front at the mouth of a macrotidal, partially mixed estuary: a field study of the Dart estuary, UK

R.H. Thain[a,*], A.D. Priestley[a], M.A. Davidson[b]

[a]Department of Marine Environment, Britannia Royal Naval College, Dartmouth, Devon TQ6 0HJ, UK
[b]School of Earth, Ocean and Environmental Sciences, University of Plymouth, Drake Circus, Plymouth, Devon PL4 8AA, UK

Received 19 November 2003; accepted 13 April 2004

Abstract

High-resolution measurements of density and velocity were made before, during and after the formation of a transient tidal intrusion front at the mouth of a narrow, partially mixed estuary during spring tides. Detailed Acoustic Doppler Current Profiler (ADCP) and density measurements throughout 1 km longitudinal transects at hourly intervals during spring tides indicated that the front formed when the barotropic inflow was sufficient to arrest the buoyant outflow from the estuary. This has been shown to be driven by a constriction of the channel at the mouth and a depression in the seabed just landward of the mouth, with these changes in topography shown to interact with the flow in a similar manner to theoretical two-layer flow over the lee side of a sill. A detailed analysis of the flow and stratification across the narrow frontal interface found a high degree of shear and mixing just prior to the plunge point, which together with a hydraulic jump at the seabed depression, eventually led to the destruction of the density interface and the total intrusion of seawater as the flooding tide strengthened. There was no surface manifestation of this front during neap tides, and further measurements have confirmed that the relatively weak barotropic flow at this time was not sufficient to overcome the stratification in a two layer regime. An evaluation of the key frontal discriminators has confirmed the validity of their use in such an estuary.

Keywords: estuaries; internal hydraulics; intrusion front; morphology; stratification; observations; Dart estuary

1. Introduction

Tidal intrusion fronts are a common feature at or near estuary mouths throughout the world. When buoyant outflow at an estuary mouth becomes blocked by a strong tidal inflow of dense seawater, the inflowing water plunges below the estuarine water as a negatively buoyant gravity current, often forming a distinctive V-shape of foam and debris at the surface (Simpson and Nunes, 1981; Dyer, 1997). These fronts are commonly static, with a control point associated with a topographical feature such as a sill or width constriction (Armi and Farmer, 1986; Farmer and Armi, 1986; Uncles, 2002), or may be formed over a gradually increasing bottom slope (Huzzey, 1982; Akiyama and Stefan, 1984; Marmorino and Trump, 1996). They are likely to occur frequently in bar-built estuaries (Largier and Taaljard, 1991; Largier, 1992), but have also been observed in fjord-like systems (Lavelle et al., 1991) and in partially mixed estuaries (Marmorino and Trump, 1996).

Tidal intrusion fronts are often transient, only appearing for a few hours of a tidal cycle (e.g. Brubaker and Simpson, 1999). Some studies, however, have found tidal intrusion fronts which have proved to be persistent throughout a tidal cycle, moving up and down the estuary with the flood and ebb respectively (Simpson and Nunes, 1981; Pelegri, 1988), although the estuaries in which these persistent, mobile fronts occurred changed little in width or depth to provide a hydraulic control point.

The presence of a tidal intrusion front may influence horizontal dispersion and residual circulation throughout

* Corresponding author.
E-mail address: rthain@plymouth.ac.uk (R.H. Thain).

0272-7714/$ - see front matter

Nomenclature

A	cross sectional area
b	estuary breadth
b_p	width at plunge point
F_i^2	densimetric Froude number for layer i
F_Δ^2	shear Froude number
F_0^2	inflow Froude number
g	gravitational acceleration
g'	reduced gravitational acceleration
G^2	composite Froude number
h	height above bed
h_p	depth at plunge point
$\bar{h}$	mean water depth
h_i	depth of layer i
ρ	density
N^2	Brunt Väisäla frequency
Q	net volume flow rate at the constriction
u_i	flow speed for layer i
V	mean flow velocity
z	depth

the estuary (O'Donnell, 1993), have impacts on local biological processes (e g Kuo et al , 1990) and the differing water masses on either side of the front may profoundly affect sonar propagation patterns (Thain and Priestley, 2002, Priestley and Thain, 2003) Whilst direct observations of such fronts have been rare (O'Donnell, 1993), particularly in terms of the velocity field, hydraulics theory has been well developed to explain plunging flow in a two layer regime, particularly with the influence of topographic effects Most of these studies have concentrated on sills (e g Huppert, 1980, Farmer and Armi, 1986), contractions in the channel width (Armi and Farmer, 1986) or gradually increasing bed slope (Huzzey, 1982, Akiyama and Stefan, 1984) Topographic effects of two-layer flow over seabed depressions have been investigated by Sturley and Dyer (1992) However, although internal waves were observed to form at the interface between two-layer flow, no front appeared to form in this case

This paper presents detailed field measurements of the flow and density structure at spring and neap tides across a stationary tidal intrusion front at the mouth of a partially mixed estuary The study aims to use these high-density measurements to ascertain the controlling parameters in frontal formation and evolution during spring tides, and importantly, explain the absence of the front during neap tides Furthermore, by setting this work within the context of previous, largely theoretical studies of frontal systems, the most appropriate dimensionless descriptors may be identified for incorporation in further numerical and practical studies of such environments

1 1 *Internal hydraulic control*

The internal hydraulic theory of Farmer and Armi (1986) and Armi and Farmer (1986) is well established, and has been applied successfully to identify the controls on exchange flows over a sill and through a constriction at the mouths of estuaries (Largier and Taljaard, 1991) Farmer and Armi (1986) treat the sill and contraction separately. However, in the common situation of the two morphological features being coincident, it is convenient to treat them as a single constriction (Dyer, 1997), with a control existing at the shallowest, narrowest section

Plunging flow can be evaluated and described in terms of a composite Froude number (G^2) of two layers, F_1^2 and F_2^2 (Farmer and Armi, 1986)

$$G^2 = F_1^2 + F_2^2 \tag{1}$$

where F_i^2 is the densimetric Froude number for layer i

$$F_i^2 = \frac{u_i^2}{g' h_i} \tag{2}$$

u_i is the flow speed of layer i, g' the reduced gravity ($g\Delta\rho/\rho_2$), where $\Delta\rho$ is the density difference between the two layers, and h_i is the depth of layer i The two-layer flow is assumed to be inviscid, with each layer being homogeneous and unsheared The effect of channel friction is neglected, and is assumed not to affect hydraulic control Where $G^2 = 1$, this indicates the existence of a hydraulic control point, where the flow undergoes an internal hydraulic transition from subcritical to critical The inflow plunges at this control, and as the upper buoyant layer should be blocked ($F_1^2 = 0$) at this point, the flow is controlled by the transition to a critical densimetric Froude number of the lower layer F_2^2 of unity

In order to define the interface between the layers of this two-layer flow, and to quantify stratification, the Brunt Väisälä frequency (N^2) can be calculated (Huzzey, 1982, Chen et al , 1994) The interface is taken as being at the point of maximum N^2 (the point of maximum buoyancy)

$$N^2 = \frac{-g}{\rho}\frac{\partial \rho}{\partial z}\ s^{-2} \tag{3}$$

An inflow Froude number can be used to describe control exercised by topography at the mouth of a bar-built estuary (Largier, 1992)

$$F_0^2 = \frac{Q^2}{g' \bar{h}^3 b^2} \tag{4}$$

where Q is the volume flow rate at the constriction ($Q = VA$, where V is the mean velocity and A is the flow cross-sectional area normal to the direction of the flow), g' is the reduced gravity, $\bar{h}$ is the mean water depth, and b is the width of the estuary. This parameter is applicable to both a sill and a contraction, but with a different critical value of F_0^2 for each case (1.0 and 0.3, respectively). Therefore, for net inflows, blocking of the surface waters commences at the constriction where $1.0 > F_0^2 > 0.3$. This condition is termed intermediate inflow, and in this situation a virtual control exists upstream of the constriction, and the plunge point will occur upstream of this control section (Armi and Farmer, 1986; Farmer and Armi, 1986). The flow plunges at the most constrictive section when $F_0^2 = 1$, and at a virtual control point downstream when $F_0^2 > 1$ (strong inflow). For net outflows, no seawater can intrude into the estuary where $F_0^2 \geq 1$ at the constriction. G^2 should still exhibit a critical value of unity at the plunge point, irrespective of where the control is located in relation to the constriction.

The shear Froude number, F_Δ^2, is a good descriptor of the stability of the vertical interface in the presence of the shear between the layers (Largier, 1992):

$$F_\Delta^2 = \frac{(u_1 - u_2)^2}{g'h} \tag{5}$$

where u_1 and u_2 are the flow speeds in the upper and lower layers, respectively, g' is the reduced gravity and h is the water depth. F_Δ^2 has a critical value of unity, and in a strong inflow situation, h should increase (or Q decrease) downstream of the front, thus rendering $F_\Delta^2 < 1$ and the tidal intrusion front stable. However, if Q does not decrease downstream of the front, then F_Δ^2 would remain critical or supercritical and the two layers would mix. The front becomes unstable in this instance, and therefore would be unlikely to be temporally or spatially persistent.

This paper details the formation of a tidal intrusion front at the mouth of a narrow, partially mixed estuary using detailed measurements of density and velocity at both spring and neap tides. The abrupt appearance of the front (frontogenesis) for several hours on a flooding spring tide is shown to be related to the interaction of two-layer flow over the local topography, and this is examined in terms of a densimetric Froude number. An inflow Froude number analysis provides an insight into the efficiency of exchange flow present during some stages of the tidal cycle, and the use of these descriptors enables the identification of a topographic control at the mouth of the estuary. The rapid decay (frontolysis) of the front several hours later, and subsequent mixing across the frontal interface is analysed using a shear Froude number. An evaluation of the application of these Froude numbers is presented, and further work during a neap tide highlights the importance of the strength of barotropic forcing and the relative buoyancy provided by freshwater runoff in front formation and integrity.

1.2. Study area

The Dart estuary, Devon, in the south west of England is a ria which lies between the small towns of Dartmouth on the western bank and Kingswear on the eastern bank (Fig. 1). The estuary is not dredged regularly, and the mean depth of water in the lower reaches is less than 14 m (relative to chart datum). The lower estuary is relatively narrow and steep-sided, being 200 m across at the mouth, where the water depth is approximately 10 m. The width increases to over 350 m just landward of the mouth where there is an elongated depression in the seabed, around 200 m in length, in the centre of the channel, where the depth increases to 25 m.

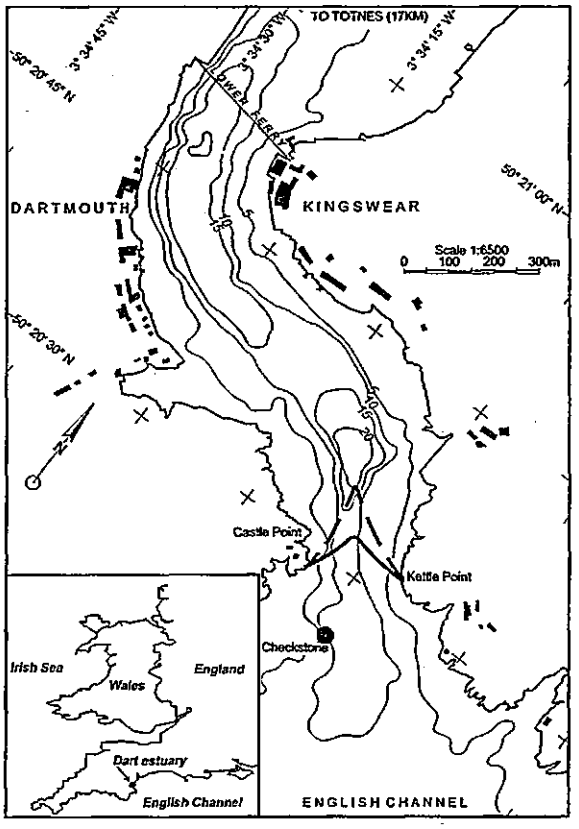

Fig. 1. The Dart estuary mouth, in the south west of England (inset). Survey lines were from Checkstone buoy just outside the estuary mouth, to the lower ferry. Note the depression in the seabed just inside the mouth. Visually observed positions of the tidal intrusion front 1 h after low water (solid line) and 2 h after low water (dashed line) are shown. The BRNC data buoy is approximately 1400 m upstream from the Lower Ferry.

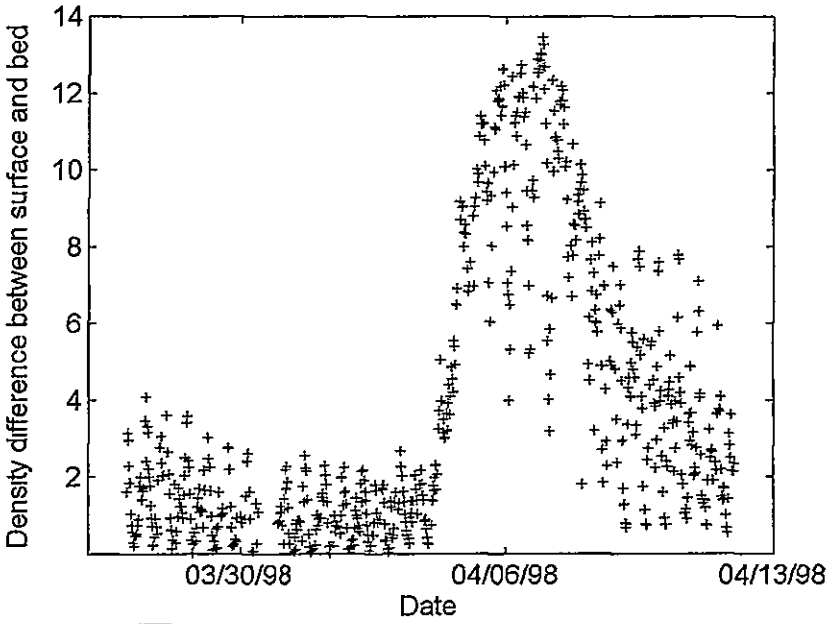

Fig 2 Difference between near bed and surface density (kg m^{-3}) over a spring–neap tidal cycle in the Dart estuary The measuring station, a remotely-logging data buoy system owned and operated by Britannia Royal Naval College, was situated approximately 2 km upriver from the estuary mouth There is little difference between surface and bed density during spring tides (03/30/98), indicating a homogeneous water column During neap tides (04/06/98), however, the large difference between surface and bed density indicates a stratified estuary

The narrow, relatively shallow estuary mouth, between Castle Point on the western bank and Kettle Point on the eastern bank thus forms a constrictive section

The estuary drains a catchment area of almost 250 km^2, with the highest flow levels generally occurring during the winter months, when the freshwater inflow can reach peak levels of $>200\ m^3\ s^{-1}$ for short periods following heavy rains During the summer months, however, freshwater inflow has been recorded as low as $2\ m^3\ s^{-1}$ During the collection of the field measurements, over the course of a week in March, more typical values of 15–20 $m^3\ s^{-1}$ were recorded The Dart is macrotidal, with a spring range of up to 5 2 m, and a range of 1 8 m at neap tides The tidal regime is asymmetrical, with the flooding spring tide typically having a duration of 6 h 30 m, and the ebb tide a duration of 5 h 40 m Tidal flows thus display a marked ebb-dominance Characteristic flow velocities on the flood tide are 0 6 m s^{-1} during spring tides at the mouth, and 0 3 m s^{-1} during neap tides The upper tidal limit of the estuary occurs at Totnes, where there is a weir, approximately 17 km from the mouth at Dartmouth.

There have been very few previous studies in the Dart estuary apart from the long-term deployment of an in situ remote data logging system located approximately 2 km landward of the mouth (50° 20 52′N, 3° 34 53′W). Analysis of the data from this system (Priestley, 1998) found that the Dart is a partially mixed estuary which experiences a complete stratification/destratification cycle with the spring–neap transition (Fig 2) This is similar to that found in the Columbia River by Jay and Smith (1990), and in Chesapeake Bay by Haas (1977) Salinity variations were found to dominate the density distribution in the Dart estuary, with temperature variations making a negligible contribution (Priestley, 1998) A V-shaped tidal intrusion front has been observed to form at the mouth at low water during spring tides (Fig 1), and remain in the same position for up to 3 h before disappearing abruptly

2. Methods

The mouth of the estuary was surveyed for several hours around low water, collecting high-density flow and CTD (conductivity, temperature and depth) data Field measurements were conducted on 13 March 2002 during a spring tide (3.9 m range), and on 22 March 2002 during a period of neap tides (2 0 m range) There was little change in weather and freshwater runoff conditions between the two surveys

An RD Instruments 600 kHz Acoustic Doppler Current Profiler (ADCP) was mounted on a non-ferrous frame over the bow of a 14 m motor launch The frame projected approximately 1 m ahead of the bow of the vessel at the waterline, to minimise errors which can effect over-the-side ADCP mountings (e g increase in

flow due to Bernoulli effects). The ADCP head was mounted as close to the waterline as possible. However, common to all such systems, no data are gathered in the near-field zone in the first 0.5 m below the transducer face. The ADCP vertical bin resolution was set to 0.5 m, and the ensemble averaging interval was 20 s, with the system operating in bottom track mode throughout. Initial measurements were verified using an Inter Ocean S4 electromagnetic current meter deployed 5 m above the seabed in the survey area.

An internally logging CTD (Valeport 604) was deployed using a frame to project the equipment 1 m from the side of the vessel. A pulley system mounted on the frame enabled rapid profiling as soon as the vessel had come to a halt. CTD measurements were taken at depth increments of 0.2 m. Position data were provided by DGPS (Differential Global Positioning System), the ADCP and CTD systems were synchronised to GPS time.

Starting approximately 300 m to seaward of the mouth of the estuary (Fig. 1) opposite Checkstone Buoy, survey lines were commenced in a landward direction keeping to the centre of the channel where possible. Heading and speed changes were kept to a minimum, thus ensuring that the ADCP data collected were as free from any vessel induced influences as possible. On reaching a location abeam of the lower ferry route, approximately 1 km landward of the mouth of the estuary, a new survey line was immediately commenced in the opposite direction, this time taking rapid CTD casts at 150 m intervals. The high quality ADCP data from the initial run were combined with the CTD data from the second run downstream to form a quasi-synoptic snapshot of the flow and density conditions in the estuary for that hour of the tidal cycle. Each pair of ADCP and CTD survey lines was conducted hourly, from 1 h before low water (LW − 1) to 3 h after low water (LW + 3). The maximum time offset for each pair of survey lines between the first ADCP reading and the last CTD dip was typically around 30 min.

3. Results

Vertical profiles of density have been divided into two discrete layers, the interface between them being defined by N^2, the Brunt Väisälä frequency. Values of density and flow speed have then been averaged within each layer to facilitate the calculation of the various frontal descriptors. Contours of density at spring and neap tides throughout the longitudinal transects are presented in Figs. 3 and 4, respectively. Interpolation and smoothing has been kept to a minimum in order to preserve the original data as much as possible, and the flow data from the ADCP have been superimposed on the contour plots. As is common when using ADCPs in a rapid flow environment, the vertical flow velocity was found to be unreliable. Significant contamination is often present in this component of the measurements, as the magnitude of the vertical flow is significantly less than that of the horizontal flow. The vertical velocity has, therefore, been neglected in Figs. 3 and 4. Thus, the flow velocity vectors represent the horizontal velocity vector component along the axis of the channel. Positive vectors represent a flooding, landward flow, whilst negative vectors represent an ebbing, seaward flow. The constricted mouth (narrowest point) is approximately 150 m from zero distance, with the seabed depression occurring between 350 m and 550 m.

3.1. Spring tide

Fig. 3a depicts the flow and density structure in the estuary 1 h before low water (LW − 1). The water column appears relatively homogeneous, with the flow being predominantly seaward. The beginnings of the appearance of an intrusion of higher density seawater can be seen at depth just outside the mouth of the estuary (at distance −100 m), with the outflow weakening in this area. $F_0^2 = 3.5$ at the constriction (150 m from the zero point), and therefore no denser water intrudes at this time.

At low water (LW) the density contours and flow vectors (Fig. 3b), indicate the presence of an outflow in the surface layer, a basal inflow current, with net inflow at the mouth at this stage of the tidal cycle. $F_0^2 = 0.2$ at the constriction, therefore the outflow is not blocked, and two-way exchange flow (between estuarine and coastal water) is possible. Maximal horizontal exchange flows can only occur if the upper layer thickness is 0.625 of the water depth at the shallowest section over a sill, or 0.5 of the water depth through a contraction (Chao and Paluszkiewicz, 1991; Farmer and Armi, 1986). Here, the upper layer thickness is 0.33 of the water depth, hence sub-maximal two-way flow is occurring, i.e. the seaward flow in the upper layer is partially arrested at this stage of the tidal cycle. With regard to the vertical stability at this stage of the tidal cycle, F_A^2 is 0.5 at the constriction, with supercritical values (implying mixing) outside the mouth, and subcritical values (stratification) inside the mouth.

By 1 h after low water (LW + 1) there is a well-mixed layer upstream of the mouth, and a two layer regime downstream (Fig. 3c). A marked horizontal density gradient has appeared at the surface just inside the mouth, corresponding to the location of the visual manifestation of the front (Fig. 1). There was a clearly apparent line of foam on the surface and a distinct colour change on either side of the front noted when taking the field measurements. The ADCP data indicate that the flow in the surface layer is almost still upstream

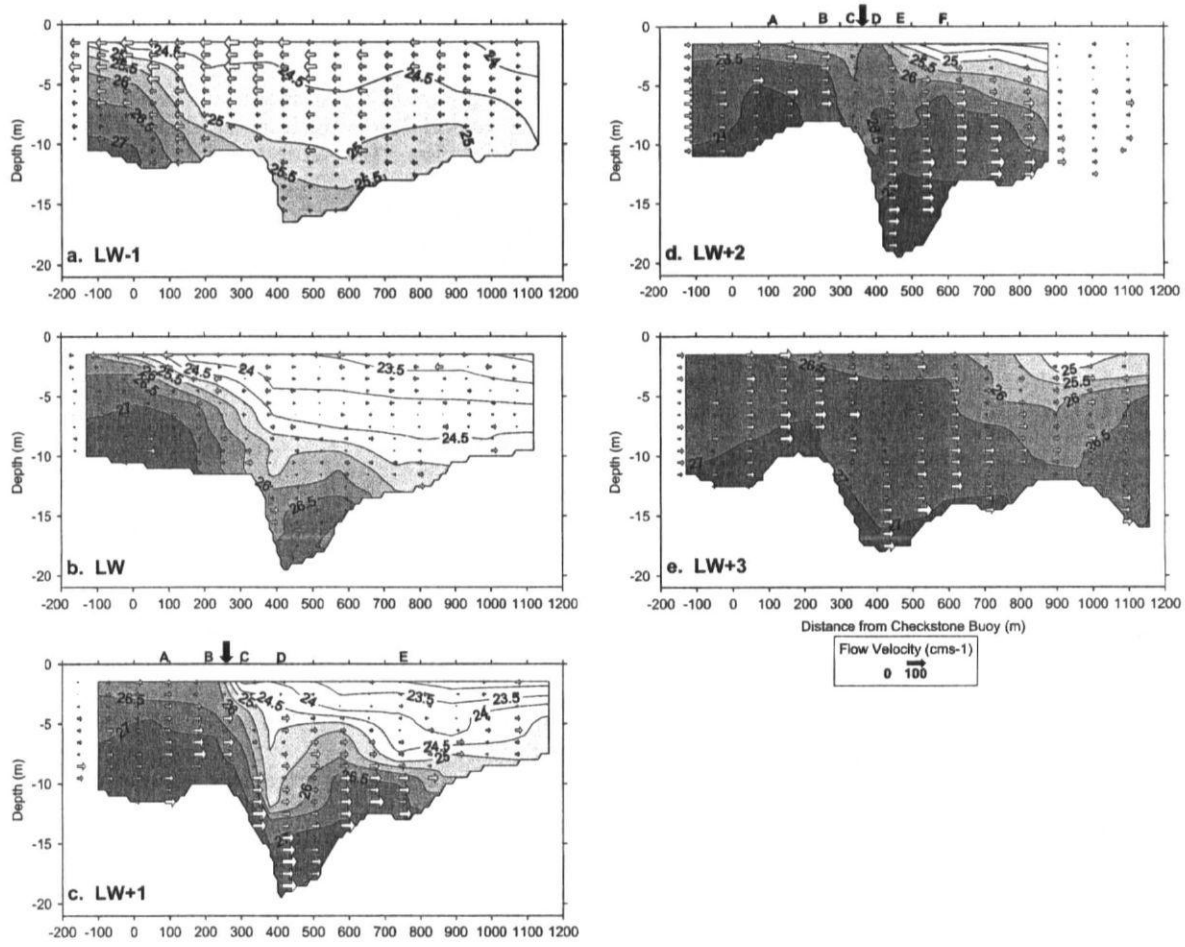

Fig. 3. Hourly contours of density anomaly at spring tides from 1 h before low water (a) to 3 h after low water (e). From Checkstone Buoy (distance = 0 m) to the lower ferry (1200 m). Flow vectors overlayed. The constricted section of the mouth starts approximately 150 m from Checkstone Buoy, represented by letter B in (c) and (d). At LW + 1, the visual manifestation of the front was between B and C. At LW + 2, it was observed between C and D (see vertical arrows).

of the front, forming a 'pool' of brackish, eddying water at the surface. G^2 becomes supercritical at the constriction (Table 1a, column b), driven largely by the higher flow speeds in the lower layer increasing the value of F_2^2. $F_0^2 = 2.4$ (strong inflow) at the constriction at this time, so that, as critical conditions can no longer be satisfied at the most constrictive section, a virtual control and plunge point must occur downstream, and the apex of the front is therefore found downstream of the mouth. At the seaward end of the seabed depression (Table 1a, column c), G^2 reduces abruptly to a critical value of 1.0, with the upper layer being blocked ($F_1^2 = 0$) and the lower layer (F_2^2) therefore also having a critical value of 1.0. The flow plunges at this point, with the abrupt decrease in the value of G^2 implying the presence of a hydraulic jump. The blocking of the upper layer increases its thickness, which correspondingly reduces the thickness of the lower layer. The velocity of the plunging inflow therefore increases as it is compressed between the upper layer and the seabed, in a similar manner to that described by Chen et al. (1994). It is possible that this is exacerbated by the transfer of kinetic energy from the arrested upper layer to the lower layer at the plunge point, further increasing the speed of the lower layer, and making it supercritical downstream of the constricted area. The plunging flow is therefore controlled mainly by the transition of the lower layer to a critical flow state at this location, with the upper layer being inactive ($F_1^2 = 0$) at this stage of the tidal cycle.

A value of $F_\Delta^2 = 2.4$ at the constriction (Table 1a, column b) indicates significant mixing is occurring in this location, just prior to the inflow plunging. Immediately downstream of the frontal interface, however, $F_\Delta^2 < 1$ implying stability in this area. This stability is controlled

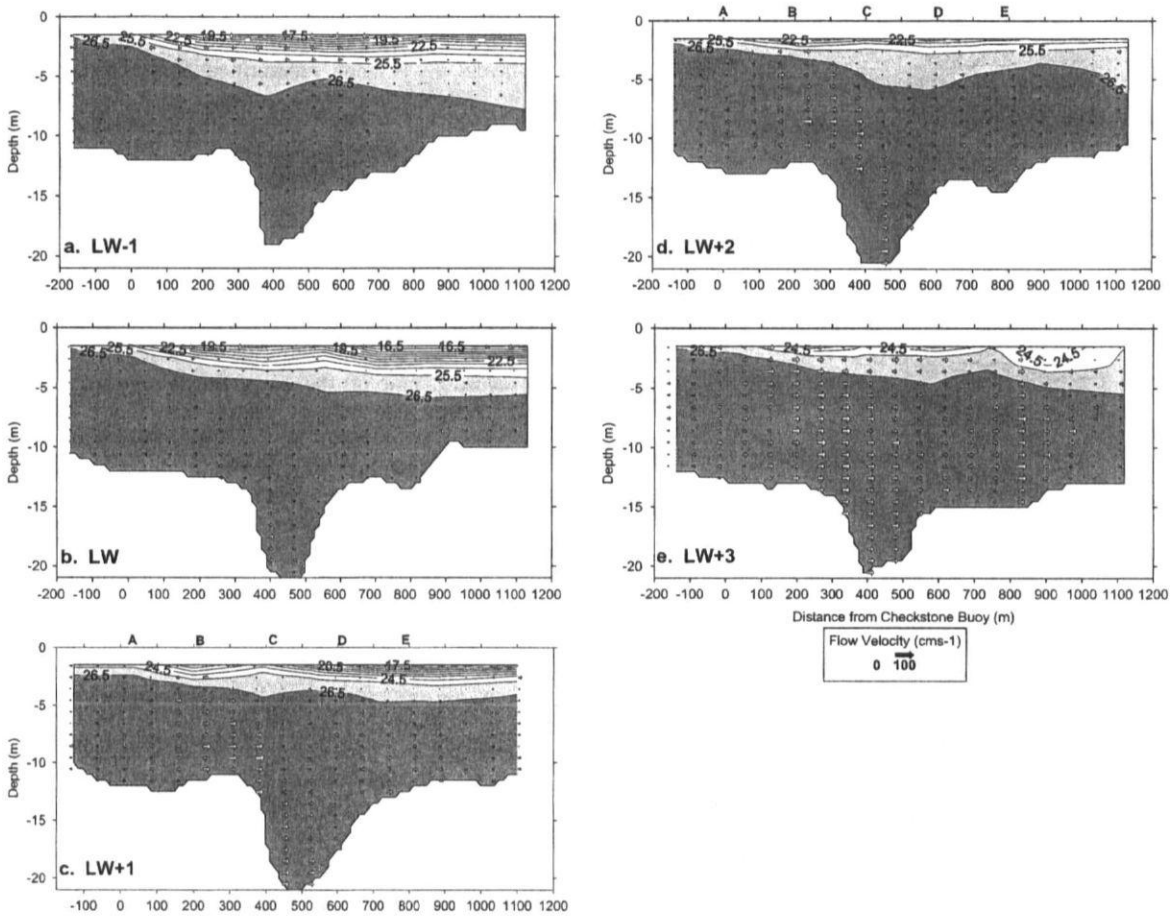

Fig. 4. Hourly contours of density anomaly at neap tides from 1 h before low water (a) to 3 h after low water (e). From Checkstone Buoy (distance = 0 m) to the lower ferry (1200 m). Flow vectors overlayed. The constricted section of the mouth starts approximately 150 m from Checkstone Buoy, represented by letter B in (c) and (d).

Table 1
Values of key frontal descriptors at LW + 1 calculated at spring tides (a) and at neap tides (b)

	A	B	C	D	E
(a) Spring tide					
F_1^2	<1	2.7	0	0	0
$F_{2,3}^2$	<1	29.3	1.0	>1	>1
G^2	1.4	32.0	1.0	>1	>1
F_0^2	–	2.4	–	–	–
F_4^2	<1	2.4	0.6	<1	<1
(b) Neap tide					
F_1^2	<1	<1	<1	<1	<1
$F_{2,3}^2$	<1	<1	<1	0	0
G^2	<1	<1	<1	<1	<1
F_0^2	–	0.1	–	–	–
F_4^2	0	<1	<1	<1	<1

Letters A–E correspond with those in Figs. 3c and 4c. The channel constriction corresponds to column B. The front was located between B and C during the spring tide.

largely by the strong density difference between the upper and lower layers at, and downstream of the front. Therefore stratification is persistent in these areas, and the front is spatially stable. The gradient Richardson number (Ri) is defined here as:

$$Ri = -\frac{g}{\rho}\frac{\partial \rho}{\partial z}\Big/\left(\frac{\partial u}{\partial z}\right)^2 \tag{6}$$

Estimates of Ri of $>\frac{1}{4}$ across the frontal zone (Fig. 5a) confirm the relative stability of the front in the near-surface region (Geyer and Smith, 1987), with the instabilities and mixing occurring across the frontal interface (where $Ri < \frac{1}{4}$) at mid-depth, and again near the bed. The implied hydraulic jump at the plunge point is unlikely to result in strong mixing ($G^2 = 32$ at the constriction, and 1.0 at the plunge point) as G^2 does not quite become subcritical (Lewis, 1997). It is therefore likely that the front should persist in this location for

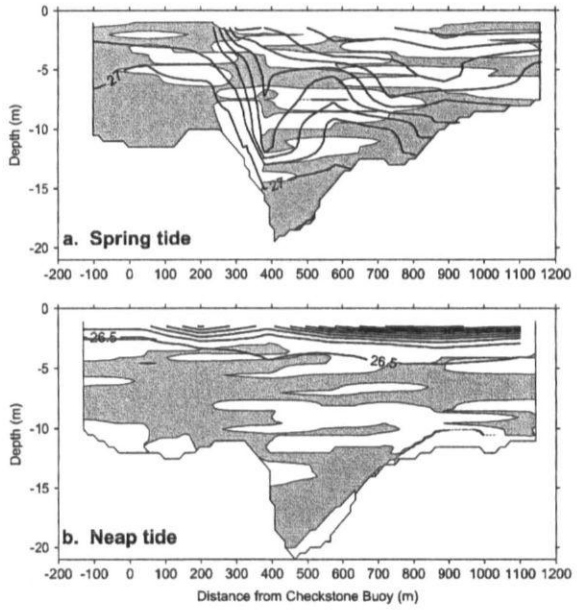

Fig. 5. Contours of Gradient Richardson number (Ri) 1 h after low water at spring tides (a) and at neap tides (b). The grey shading represents areas where $Ri < 0.25$, implying instability and mixing. Conversely, the white areas are where $Ri > 0.25$, implying stability. Density anomaly contours (heavy black lines) are overlayed in intervals of 1 kg m^3 in each case. At spring tides (a), stratification exists downstream of the front (increasing distance values), with localised areas of mixing across the frontal zone. At neap tides (b), there is significant stability across the density interface at the surface, with much of the water column appearing broadly well mixed below the surface.

a time before being weakened and dispersed by mixing. The Ri values indicate, however, that some erosion of the pycnocline by Kelvin–Helmholtz instabilities should be occurring downstream of the plunge point, which should eventually lead to the breakdown of stratification across the frontal zone (Dyer, 1988; Griffin and LeBlond, 1990).

At LW + 2 (Fig. 3d) the apex of the front has migrated slightly downstream (although it was noted that the 'arms' of the front were still anchored to the shore at the narrowest part of the estuary) forming a more pronounced V-shape. The plunge point appeared visually to be further landward, towards the middle of the seabed depression (Fig. 1). $F_0^2 = 2.1$ at the constriction, still in the strong inflow regime, implying that a virtual control and plunging will continue to occur downstream of the constriction. G^2 is now supercritical in all locations upstream of the plunge point, driven mainly by the high flow speeds in the lower layer. Across the frontal zone, G^2 reduces abruptly from supercritical ($G^2 > 80$) to zero, implying a strong hydraulic jump. There is evidence of erosion of the pycnocline having occurred by this stage of the tidal cycle, as the layer interface is much closer to the surface downstream of the front, with a much weaker density gradient between the layers. F_Δ^2 is again supercritical (4.4) just upstream of the plunge point, and subcritical throughout the remainder of the transect. This implies continuing strong mixing and instability just upstream of the plunge point, with the stratification persisting elsewhere, resulting in a spatially stable front.

By LW + 3 (Fig. 3e) the visual manifestation of the front had all but disappeared, with only slight swirls and eddies of discoloured estuarine water being apparent at the surface, and two broken lines of foam apparent, one at the seaward end of the seabed depression, and one at the seaward end of the 15 m depth contour further downstream. The current vectors are fairly uniform throughout the transect at this time, with the density contours indicating a homogeneous water column. A slight dip in the contours around 900 m from the start of the line may be indicative of the remainder of the front, and this corresponds to the area where patches of foam and discoloured water were noted. $F_0^2 = 3.6$ at the constriction, implying that the plunge point should be well downstream. G^2 is supercritical throughout the length of the transect (due to the higher flow rates at this stage of the tide) indicating that the control point has become flooded and has disappeared (Denton, 1987). The estuary has therefore become well mixed at this time, with subcritical values of F_Δ^2 throughout implying no further mixing taking place.

A solution for the depth of plunging in the strong regime, when dealing with topographic controls can be expressed by (Farmer and Armi, 1986):

$$h_p = \left(\frac{Q^2}{g' b^2}\right)^{\frac{1}{3}} \tag{7}$$

This yields a plunge depth of 12.3 m at LW + 1, corresponding favourably to the measured depth at the plunge point at this stage of the tidal cycle (Fig. 3c). Applying their solution for the width of the estuary at plunging:

$$b_p = \frac{Q}{(g' h^3)^{\frac{1}{2}}} \tag{8}$$

a solution of 343 m at LW + 1 is obtained. The nearest point to the mouth where this width can be satisfied corresponds exactly with the seaward end of the 20 m contour of the depth increase at the seabed depression, 300 m from Checkstone buoy (Fig. 1).

At LW + 2 the plunge depth was calculated to be 12.6 m. This corresponds to the approximate depth where the front was visually noted at this stage of the tidal cycle (Fig. 3d), i.e. the front has migrated approximately 30 m further landward over the increasing depth of the seabed depression. At LW + 3, the

plunge depth is 16.0 m, which is consistent with the measured depths where the patches of foam were noted.

3.2. Neap tide

At LW − 1 (Fig. 4a), an extremely well developed vertical density gradient is apparent, with a shallow layer of buoyant estuarine water at the surface overlying a homogeneous lower layer. There is a pronounced density difference between the upper and lower layer (of up to 9.1 kg m^{-3}) and the strongest ebbing flows (about 0.4 m s^{-1}) are near the surface. Near bed velocities are of the order of 0.1 m s^{-1}. F_Δ^2 values of 0–0.1 inside the estuary, increasing to 0.5 just outside the mouth indicate a high degree of stratification together with little shear or mixing between the layers. F_2^2 is zero throughout the transect at this stage of the tidal cycle, implying that the lower layer is inactive (i.e. does not interact with the bathymetry to control the flow).

At LW (Fig. 4b), there is a very weak outflow at the surface down to about 3 m, corresponding to the calculated position of the density interface. There is a basal inflow below this interface. Values of F_2^2 are still zero at this time, therefore the lower layer remains inactive, and the flow does not interact with the bottom topography to provide a control point. This situation continues for several hours, consistent with the findings of Priestley (1998) that net outflow continues at the surface further up the estuary throughout the flooding neap tide.

At LW + 1 (Fig. 4c) the flow in the surface layer has weakened, and there is an indication in the lower layer flow vectors of a sub-surface front forming over the seabed depression, although this did not manifest itself at the surface. $F_2^2 = 0.2$ at the constricted mouth (Table 1b, column b), although G^2 values were subcritical throughout the transect, and $F_0^2 = 0.1$, implying no topographic control present at this time. Estimates of Ri at this stage of the tidal cycle (Fig. 5b) indicate a highly stratified water column, $Ri > \frac{1}{4}$ at the surface along the whole length of the transect. Below a depth of approximately 4 m, $Ri < \frac{1}{4}$, and the water column appears broadly homogeneous, with some evidence of increased stratification at mid-depth above the seabed depression.

Eventually, at LW + 2 (Fig. 4d), the entire flow is landward, with F_0^2 values remaining subcritical throughout the transect at this time. G^2 is now supercritical outside the estuary mouth, and subcritical inside, with an implied hydraulic jump between these two areas. This transition is driven solely by the upper layer, with $F_1^2 = 1.5$ just seaward of the mouth, and $F_1^2 = 0$ just landward of the mouth. Therefore, as F_2^2 remains sub critical throughout the transect during this time, only the upper layer is active, and no seabed topographic control exists.

At LW + 3 (Fig. 4e), G^2 remains supercritical outside the estuary mouth, and subcritical inside. There is a slight dip in the layer interface at this point, coinciding with the depression, although again no surface manifestation of the front was present. $F_\Delta^2 < 0.3$ throughout the transect, indicating a low degree of shear-induced mixing taking place, and the density contours show some evidence that thinning of the surface layer has occurred by this stage of the tidal cycle. Stratification is often maintained on the ebb, and diminished during the flood; this is the process of tidal straining discussed by Nepf and Geyer (1996) and Uncles (2002).

Plunge depths are of the order of 4.5 m at LW + 1, to 5.6 m at LW + 2, further indicating that the flow is not topographically controlled by the seabed at any point during the neap tidal cycle, as the water depth is well in excess of these figures throughout the transect at all stages of the flooding tide. Therefore, as the lower layer remains subcritical throughout the flooding neap tide and only the upper layer becomes active at the mouth from LW + 1 to LW + 3, this buoyant surface layer at neap tides does not interact with the bottom topography to provide a control point. It is likely that the lower magnitude of the barotropic flows during neap tides maintains a high degree of stratification, this being sufficient to 'damp out' any turbulent interfacial mixing (Lewis, 1997).

4. Discussion

This study has detailed the formation and decay of a tidal intrusion front at the mouth of a narrow, partially mixed estuary during spring tides. Detailed ADCP and CTD measurements have provided insights into the hydraulic controls responsible for the arrest of the front at the mouth, and the mixing processes involved in frontal decay. Insights have also been gained as to why the front does not appear at neap tides, and the key frontal discriminators have been evaluated.

During spring tides, there is a visual manifestation of the front for approximately 2 h, starting 1 h after low water. At LW, two-way exchange flow is present, although the thickness of the upper layer indicates that the buoyant outflow at the surface is partially arrested (but not blocked) at this time, and therefore submaximal exchange flow is occurring. The front forms at LW + 1 as two-layer flow interacts with a constriction at the estuary mouth, then with a depression in the seabed, producing a hydraulic control point (Fig. 6). As the flow enters the estuary, it speeds up and becomes supercritical as it passes through the constricted mouth. When it reaches the depression in the seabed, the inflow undergoes a hydraulic jump due to the change in estuary cross sectional area, becoming abruptly critical or subcritical. At this point it no longer has sufficient velocity to push back the buoyant estuary outflow, which is arrested. The denser inflowing water plunges, gaining velocity as it is compressed between the static

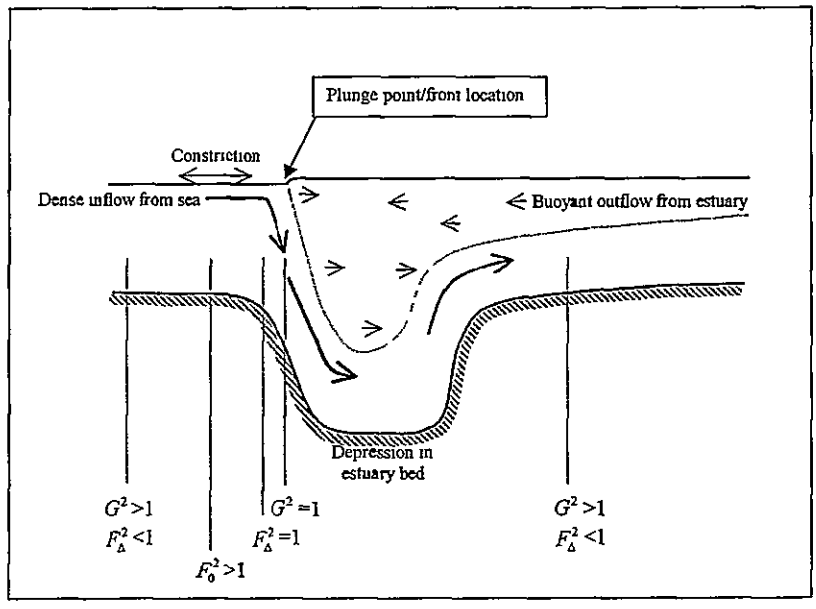

Fig 6 Schematic diagram showing the observed patterns in Froude numbers relative to a tidal intrusion front located over a seabed depression At the constriction, the inflow Froude number (F_0^2) >1, implying hydraulic control was located further downstream, towards the depression The shear Froude number (F_Δ^2) became critical just upstream of the front, where the flow was on the brink of instability The composite Froude number (G^2) was critical at the plunge point, driven solely by the flow transition of the lower layer

surface layer and seabed Density stratification is persistent just downstream of the frontal zone, and resistant to shear-induced mixing at this stage of the tide, resulting in a spatially stable front The front remains bathymetrically arrested from LW + 1 to LW + 2, consistent with the findings of field studies (Huzzey, 1982) and theoretical investigations (Akiyama and Stefan, 1984) As barotropic forcing increases, the plunge depth increases, and the front migrates downstream, over the increasing depth of the seabed depression As the tidal velocity increases further, interfacial shear dominates, and eventually overcomes the stratification, resulting in the rapid decay of the front

It thus appears that during spring tides, the flow at the mouth is behaving as if flowing over a sill The constriction at the mouth, followed by the abrupt increase in depth (and cross sectional area) at the seabed depression creates a similar topographical situation to two-layer flow over the lee side of a sill at the mouth of a fjord, or bar-built estuary (Fig 6) The contraction at the narrow mouth is unlikely to greatly influence the inflow as the flow in the upper layer is weak on the flooding tide, and therefore the control exercised by the contraction is weak (Farmer and Armi, 1986) The seabed depression (the 'sill') will have the greater effect at this time, as the lower layer interacts directly with the changes in bathymetry which protrude into this active lower layer (Armi, 1986)

During neap tides, there is no visual manifestation of the front Tidal straining exacerbates the stratification on the ebb, and lower flow velocities are not high enough to arrest the buoyant outflow from the estuary, or overcome the pronounced stratification between layers on the flood The lower layer remains subcritical throughout the flooding tide, and therefore no topographic control is exercised by the seabed in this case The low flow velocities do not allow the formation of a hydraulic control point, and the front does not appear

The composite Froude number (G^2) derived from the densimetric Froude numbers for each layer in a two-layer flow situation, has proved to be a good frontal discriminator in this case During spring tides at LW + 1, when the front first visually appeared, a critical value of unity was recorded at the plunge point, exactly as predicted by hydraulics theory The case was not quite as clear at a later stage of the tidal cycle (LW + 2), although the front occurred between values of $83 > G^2 > 0$, and therefore presumably passed through the critical value somewhere between them An abrupt change in the value of G^2 was found to be a good indicator of the presence of a front, although as G^2 was often supercritical over much of the transect, frontal location derived solely from this parameter could be open to interpretation in some cases. The inflow Froude number (F_0^2) has proved to be invaluable in ascertaining the existence of a hydraulic control point, and quantifying whether the control occurred at the constriction, or upstream or downstream of it This parameter may have even more use in such an estuary when one considers that measurements need only be taken at one

point (i.e. at the most constrictive section of the mouth) to ascertain whether, and approximately where a front will form. F_0^2 also provided a measure of the efficiency of any exchange flow present between estuarine and coastal waters, which may have use in wider estuarine applications. The shear Froude number (F_Δ^2) was found to be supercritical just upstream of the front, and subcritical just downstream in every realisation of frontal formation. The supercritical values of F_Δ^2 indicate flow on the brink of instability and mixing prior to plunging. These are a result of the small density difference between two flowing layers in the rapid, relatively homogeneous flows through the constriction. Increasing water depth by a factor of two over the seabed depression is sufficient to make F_Δ^2 abruptly subcritical. At neap tides the large density difference between the layers in the presence of lower flow velocities ensures that F_Δ^2 remains subcritical despite the spatial changes in the total water depth. As this parameter was subcritical in every case, apart from when and where a front was present, it has proved to be the best and most accurate discriminator of frontal location in addition to quantifying the magnitude of interfacial mixing. The gradient Richardson number has not proved to be an accurate frontal discriminator. Whilst providing some insights into areas of mixing and stratification across the frontal zone, it did not indicate reliably the location of the front, nor its formation and decay.

The parameters developed by Farmer and Armi (1986) and Largier (1992) for use with two-layer flow over a sill have been found to have use in such a partially mixed estuary. Although not having a sill in the strictest sense, the Dart estuary, a ria, behaves rather like a fjord, or bar-built estuary due to dramatic changes in depth and width just inside the estuary mouth. Thus, two-layer flow in this region behaves rather like that over the lee side of a sill. This frontal system is likely to vary in intensity at different stages of the spring–neap and seasonal cycle. For the front to form, a balance must exist (for a time, at least) between the tidal forcing and relative buoyancy of the estuary water. Anecdotal evidence suggests that during equinoctial spring tides, when barotropic forcing is high, the front decays extremely quickly, or may not form at all. During periods of prolonged drought, the estuary is unlikely to be sufficiently stratified to promote the creation of a front. Further studies are required to improve our understanding of the variations in intensity of such fronts that are possible on a tidal and seasonal scale.

5. Conclusions

The formation of a transient tidal intrusion front at the mouth of a narrow, partially mixed estuary has been shown to result from two-layer flow interacting with topographical changes. A hydraulic control point is created by a constriction at the estuary mouth, causing supercritical flows in this area at some stages of the flooding spring tide. These flows are sufficient to oppose the buoyant outflow from the estuary. A major depth increase over an elongated depression in the seabed just inside the mouth causes an internal hydraulic jump, and the inflow becomes abruptly critical or subcritical. At this point the inflow plunges beneath the buoyant estuarine outflow, forming a static tidal intrusion front. The lower flowing layer controls the flow in this location as it interacts directly with the seabed at this point. Thus, depth changes in the estuary are critical in frontal formation and dynamics, and are more important than width changes. Such topographical changes have also been shown to influence horizontal exchange flows at the mouth, and therefore may affect mixing throughout the estuary. During neap tides, strong vertical stratification dominates, which together with low barotropic flow, prevents the formation of a hydraulic control point. The tidal intrusion front does not, therefore, form at this time.

The use of hydraulics theory to quantify two-layer flow over topographical changes in bar-built estuaries has been employed with much success (e.g. Largier and Taljaard, 1991). This paper has demonstrated that such an approach is also valid in a partially mixed estuarine environment, where tidal intrusion fronts may be common. A Froude number analysis of the formation and dynamics of such a front has been proved to predict accurately the location of the plunge point and quantify the mixing occurring across the frontal zone. An inflow Froude number has been found to provide a good indication of whether, and approximately where a tidal intrusion front will form relative to a constriction at the estuary mouth. A composite Froude number, comprising the sum of the densimetric Froude numbers for each layer in a two-layer flow regime, has specified which layer was most important in exercising hydraulic control over the flow. Most usefully, a spatial change in the shear Froude number from supercritical to subcritical indicated reliably the location of the inflow plunge point when the front was present. This parameter reflected accurately the required balance of flow and density differences across two layers, and the critical role that changes in the total water depth have been found to play in frontal formation. It was also possible to parameterise the mixing in the frontal zone using this descriptor, providing an indication of frontal stability. Such a dimensionless analysis of the flow, together with the incorporation of detailed topographical information at the mouth, will be a valuable addition to estuarine circulation models.

Acknowledgements

This research has been financially supported by Britannia Royal Naval College. The assistance of Peter

Ganderton in setting up the fieldwork equipment, and Neil Millington in preparing the charts is gratefully acknowledged Both Travis Mason and Keith Dyer were very generous with their time in discussing and reading an early version of this paper The expert seamanship of Paul Rampling and crew was fundamental to the success of the field data collection

References

Akiyama, J, Stefan, H G, 1984 Plunging flow into a reservoir theory Journal of Hydraulic Engineering 110, 484–499

Armi, L, 1986 The hydraulics of two flowing layers with different densities Journal of Fluid Mechanics 163, 27–58

Armi, L, Farmer, D M, 1986 Maximal two-layer exchange through a contraction with barotropic net flow Journal of Fluid Mechanics 164, 27–52

Brubaker, J M, Simpson, J H, 1999 Flow convergence and stability at a tidal estuarine front. Acoustic Doppler current observations Journal of Geophysical Research 104 (C8), 18257–18268

Chao, S-Y, Paluszkiewicz, T, 1991 The hydraulics of density currents over estuarine sills Journal of Geophysical Research 96 (C4), 7065–7076

Chen, P, Grant Ingram, R, Gan, J, 1994 A numerical study of hydraulic jump and mixing in a stratified channel with a sill In Spaulding, M L, Bedford, K, Blumberg, A, Cheng, R, Swanson, C (Eds), Estuarine and Coastal Modelling III American Society of Civil Engineers, New York, pp 119–133

Denton, R A, 1987 Locating and identifying hydraulic controls for layered flow through an obstruction Journal of Hydraulic Research 25, 281–299

Dyer, K R, 1997 Estuaries A Physical Introduction John Wiley, Chichester, 195 pp

Dyer, K R, 1988 Tidally generated estuarine mixing processes In Kjerfve, B (Ed), Estuarine Physics Hydrodynamics of Estuaries, vol 1 CRC Press, Boca Raton, Florida, pp 41–57

Farmer, D M, Armi, L, 1986 Maximal two-layer exchange over a sill and through the combination of a sill and contraction with net barotropic flow Journal of Fluid Mechanics 164, 53–76

Geyer, W R, Smith, J D, 1987 Shear instability in a highly stratified estuary Journal of Physical Oceanography 17, 1668–1679

Griffin, D A, LeBlond, P H, 1990 Estuary/ocean exchange controlled by spring/neap tidal mixing Estuarine, Coastal and Shelf Science 30, 275–297

Haas, L W, 1977 The effect of the spring–neap tidal cycle on the vertical salinity structure of the James, York, and Rappahannock Rivers, Virginia, USA Estuarine and Coastal Marine Science 5, 485–496

Huppert, H E, 1980 Topographic effects in stratified fluids In Freeland, H J, Farmer, D M, Levings, C D (Eds), Fjord Oceanography Plenum Press, New York, pp 117–140

Huzzey, L M, 1982 The dynamics of a bathymetrically arrested estuarine front Estuarine, Coastal and Shelf Science 15, 537–552

Jay, D A, Smith, J D, 1990 Circulation, density structure and neap–spring transitions in the Columbia river estuary Progress in Oceanography 25, 81–112

Kuo, A Y, Byrne, R J, Hyer, P V, Ruzecki, E P, Brubaker, J M, 1990 Practical application of theory for tidal intrusion fronts Journal of Waterway, Port, Coastal and Ocean Engineering 116, 341–361

Largier, J L, 1992 Tidal intrusion fronts Estuaries 15, 26–39

Largier, J L, Taljaard, S, 1991 The dynamics of tidal intrusion, retention, and removal of sea water in a bar-built estuary Estuarine, Coastal and Shelf Science 33, 325–338

Lavelle, J W, Cokelet, E D, Cannon, G A, 1991 A model study of density intrusions into and circulation within a deep, silled estuary Puget Sound Journal of Geophysical Research 96 (C9), 16779–16800

Lewis, R, 1997 Dispersion in Estuaries and Coastal Waters John Wiley, Chichester, 312 pp

Marmorino, G O, Trump, C L, 1996 High-resolution measurements made across a tidal intrusion front Journal of Geophysical Research 101 (C11), 25661–25674

Nepf, H M, Geyer, W R, 1996 Intratidal variations in stratification and mixing in the Hudson estuary Journal of Geophysical Research 101 (C5), 12079–12086

O'Donnell, J, 1993 Surface fronts in estuaries a review Estuaries 16, 12–39

Pelegri, J L, 1988 Tidal fronts in estuaries Estuarine, Coastal and Shelf Science 27, 45–60

Priestley, A D, 1998 The Dart Observatory an estuarine monitoring system International Ocean System Design 2, 5–9

Priestley, A D, Tham, R H, 2003 Water column variability at an estuarine mouth implications for multibeam sonar surveys Proceedings of the Third International Conference on High Resolution Surveys in Shallow Water Sydney, Australia, 17–21 November 2003

Simpson, J H, Nunes, R A, 1981 The tidal intrusion front. an estuarine convergence zone Estuarine, Coastal and Shelf Science 3, 257–266

Sturley, D R., Dyer, K R, 1992 A topographically induced internal wave and mixing in the Tamar estuary In Prandle, D (Ed), Dynamics and Exchanges in Estuaries and the Coastal Zone Coastal and Estuarine Studies 40, AGU Washington, D C, pp 57–74

Tham, R H, Priestley, A D, 2002 The importance of tidal intrusion fronts for sonar Operations Proceedings of the XIIIth International Scientific Conference, Naval University of Gdynia, Poland, 14–15 November 2002

Uncles, R J, 2002 Estuarine physical processes research some recent studies and progress Estuarine, Coastal and Shelf Science 55, 829–856

Water Column Variability at an Estuarine Mouth: Implications for Multibeam Sonar Surveys

A. D. Priestley, R. H. Thain.

Third International Conference on High Resolution Surveys in Shallow Water, Sydney, Australia, 17-21 November 2003.

Introduction

The requirement for surveyors to possess greater understanding of the variability of coastal waters in order to minimise error resulting from the use of wide swath multibeam sonars is now well established (Hughes-Clarke, 2001). This study addresses the temporal and spatial scales of water column variability in the Dart estuary in Devon, England. The estuary varies from partially to well mixed, depending on tidal mixing and river discharge. Studies within the estuary conducted via the long-term deployment of a meteorological and oceanographic observatory (Priestley, 1998), have demonstrated that significant variations in estuarine stratification occur over a variety of time scales: seasonally, fortnightly and intratidally. Seasonally, the highest stratification levels occur during autumnal neap tide phases. On a fortnightly scale, a stratification/destratification cycle is evident in the estuary: stratification occurs during neap tides, rather than during spring tides when strong tidal currents mix the estuary. Within a tidal cycle, stratification peaks at low water during both spring and neap tides.

Particularly problematic from an acoustic perspective are estuarine mouths, where relatively fresh water meets seawater. Fronts of various types develop at the interface between these water masses. Major types of estuarine front include plume fronts, tidal mixing (stratification) fronts, tidal intrusion fronts and shear fronts (Lewis, 1997). Each frontal type is characterised according to its structure and flow dynamics, and is characterised acoustically by variability over periods of hours (Field *et al.*, 1998). At the mouth of the Dart estuary a characteristic tidal intrusion front develops close to low water during periods of spring tides; it is a dynamic feature, which exists only for a period of 2-3 hours, being particularly evident at the start of the flood tide. At the surface, a characteristic 'V' shaped foam and debris line is evident, and a marked halocline develops below the surface manifestation of the front.

Data Collection

A survey to provide a detailed picture of the flow, temperature, salinity, density and sound speed structure at the entrance to the Dart estuary was undertaken in March 2002 during a spring tidal cycle. CTD casts were taken to demonstrate the variations in the water mass properties and water column structure, whilst Acoustic Doppler Current Profiler (ADCP) surveys detailed the flow dynamics in the frontal zone. Longitudinal survey lines were run through the frontal zone – a distance of approximately 1200 metres. Each series of ADCP and CTD lines was repeated at hourly intervals for 6 hours to ascertain the behaviour of the estuary from 1 hour before low-water to five hours after low water. Each hourly data set, comprising data from the ADCP and CTD, represents a quasi-synoptic snapshot of the temperature, salinity, sound speed structure and flow behaviour.

Data Analysis

Contours of sound speed were produced from discrete profiles using a triangular event network (TIN), thereby ensuring that the original data were honoured and that the contouring was unambiguous. The sound speed contours show very strong correlation with the local isohalines. The ADCP data are presented here as overlays on the sound speed data. One hour prior to low water (LW-1) sound speed varies little at the surface over the length of the transect (figure 1). Vertically, however, sound speed shows a strong positive gradient at the estuary mouth of approximately 0.65 s^{-1} (averaged over the whole water column). This is due to the earliest manifestation of the flooding tide intruding into the estuary in the form of a salt wedge. Further into the estuary the vertical sound speed gradient reduces to approximately 0.3 s^{-1} at the furthest landward extent of the transect. Whilst the flood is just commencing, the ADCP data indicate that the flow direction across virtually the whole water column is still seaward, with the strongest flows occurring near the surface. Two hours later, however, at LW+1 (figure 2) sound speed shows substantial horizontal gradients just below the surface, decreasing by 7 ms^{-1} in an upstream direction across the frontal zone, a distance of less than 100 metres. A different vertical regime exists on either side of the front: vertical sound speed gradients are now relatively weak on the seaward side of the front (less than 0.4 s^{-1}), yet on the landward side of the front there are very strong sound speed gradients of up to 1.0 s^{-1}. Notably, within the frontal zone itself the sound speed

contours are steeply inclined, which is highly significant in terms of sonar beam refraction The flow data from the ADCP indicate that the flow has reversed, with the strongest (landward) flows existing near the bed in the deepest part of the transect just to the landward side of the front On the landward side of the frontal interface, there is evidence of a two-layer regime the upper layer is almost stationary and highly variable in direction, but the lower layer of the water column (below 7m in depth) is flooding strongly. At this stage the front is clearly evident on the surface of the estuary, foam and debris outlining its characteristic 'V' shape Three hours after low water (figure 3) sees further significant change in the water column structure The ADCP data indicate a flooding tide throughout the transect, with the highest magnitude flows still occurring in the frontal zone, even though the front is no longer visible at the surface The sound speed structure across the transect is more uniform, although vertical gradients are still strong (exceeding 0 3 s^{-1}) throughout the area A gradual increase in the gradient in a landward direction is evident, with a maximum gradient of 0 75 s^{-1} occurring in the estuary

Summary and Application of the work to Multibeam Sonar Surveys

Just prior to low water the flooding tide enters the estuary close to the bed and substantially modifies the structure of the water column After low water, for a period of 1-2 hours, a tidal intrusion front forms as the fresher, buoyant water at the surface is pushed back into the estuary by the incoming flood tide. The seawater plunges beneath the less dense estuarine water, resulting in the development of a very strong halocline with steeply inclined sound velocity contours and marked positive gradients in sound speed At the surface, significant lateral changes in sound speed develop Convergent currents at the surface lead to the accumulation of high concentrations of suspended particulate matter (SPM), foam and debris in the frontal zone Such high SPM concentrations present in the frontal zone are likely to lead to marked attenuation of high frequency sonar by absorption processes (Heathershaw *et al*, 1996), and are evident in high acoustic backscatter data recorded by the ADCP in this area Three hours after low water, it is likely that the shear induced mixing processes resulting from the flooding tide gaining momentum overcome the local stratification (Largier, 1992) and the water column becomes more uniform Vertical gradients in sound speed decrease and lateral variations become much less significant The data presented from this survey reinforce the highly dynamic nature of estuarine mouths Significant water column changes are evident over periods less than one hour, and laterally major changes in the vertical structure occur over distances of less than 50m. Key points of relevance for surveys conducted in such areas are.

1. It is essential to consider water column variability in survey planning
2. Periods of low stratification minimise refraction errors and allow swath width to be increased In the Dart (or other partially mixed estuaries) this would occur at high water or at spring tides when strong mixing enhances homogeneity of the water column within the estuary In other estuaries with very high seasonal discharge, the water column may become homogeneous (for example during major meltwater discharges), or in well-mixed estuaries such as the Humber, UK, which have high width to depth ratios, and/or strong tidal mixing, high stratification may simply not occur
3. Problems when surveying in areas with high stratification as refraction errors increase and the swath width needs to be reduced In the Dart and other partially mixed estuaries this is the case at low water during neap tides Other examples of high stratification include stratified/fjord systems and, in some estuaries, following high river discharge events Vertical and horizontal sound speed gradients may be particularly severe in the marked haloclines associated with frontal zones – for example in tidal intrusion fronts and at the interface between a freshwater plume and an underlying homogenous water mass
4. Sampling frequency must take account of water column spatial and temporal variability.
5. Only continuous vertical profiling can represent variability seen in the Dart or other partially mixed estuaries Consequently, taking sound velocity measurements solely at the transducer face is likely to be insufficient
6. The frequency of sampling must exceed that of water column variability In the Dart estuary during the three hours either side of low water at spring tides, every 15 minutes is the recommended minimum sampling frequency to account for the variability of the water column.
7. Spatially, only measurements taken at a minimum of every 50m would fully reflect water column variability, and it would be necessary to interpolate between the casts to give a full picture of water column Sampling must be in an appropriate location – i.e not just at the end or beginning of a survey line

8. The steeply inclined nature of the sound velocity contours in frontal zones means that refraction of even the nadir beams would occur. This should be accounted for in order to minimize refraction artefacts.

9. A suggested approach would be to avoid surveying at the times of high stratification, such as those described for the Dart in this study. Periods of near-homogeneity do occur even in partially mixed estuaries – if these were successfully identified they would minimise survey problems resulting from sonar refraction.

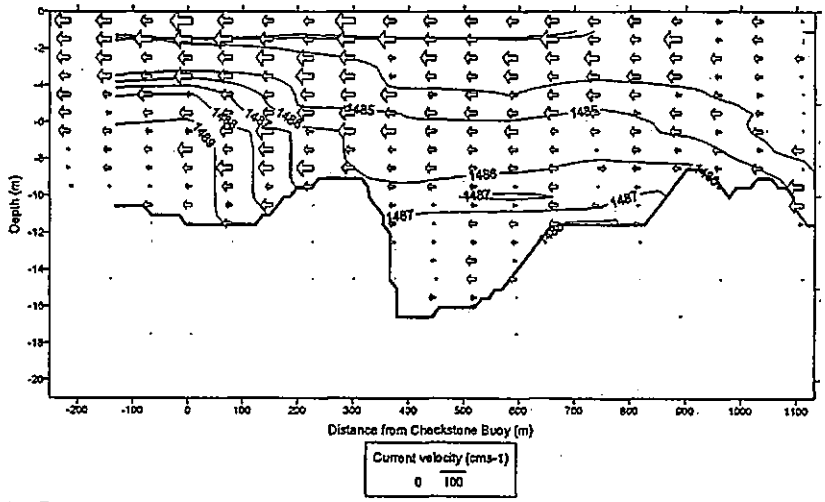

Figure 1. Sound Speed Contours and Flow Speeds one hour prior to low water (LW-1)

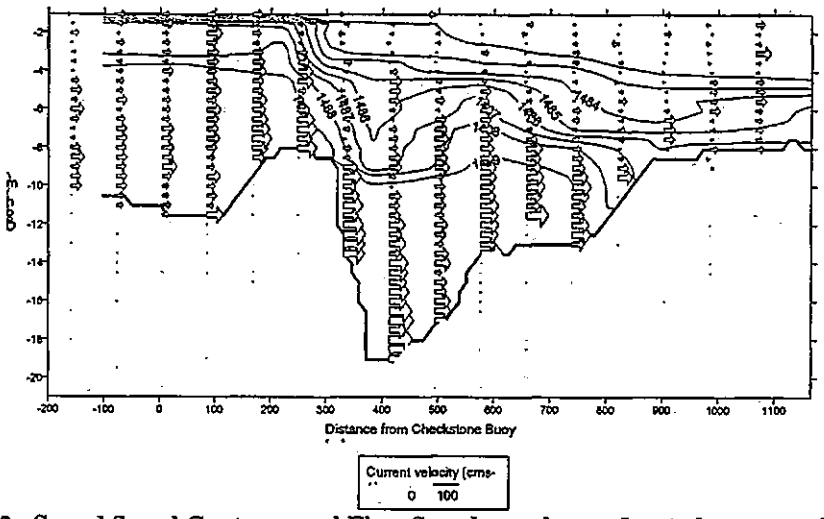

Figure 2. Sound Speed Contours and Flow Speeds one hour after to low water (LW+1)

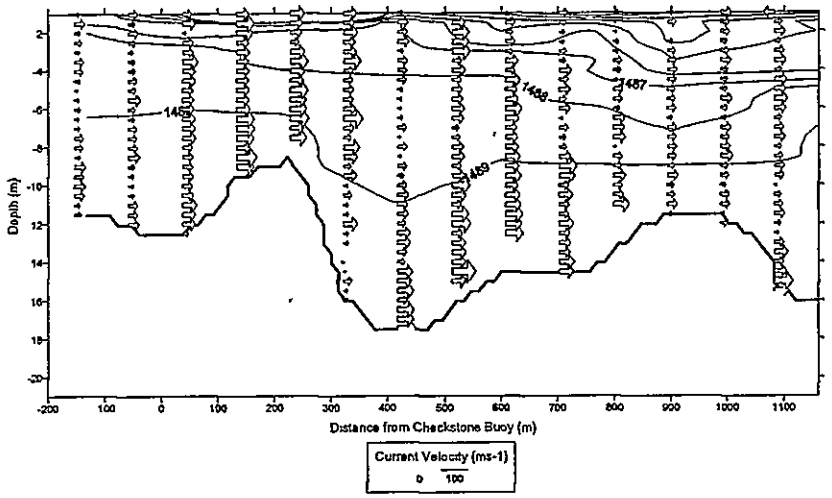

Figure 3. Sound Speed Contours and Flow Speeds three hours after to low water (LW+3)

Bibliography

Field, R L , Broadhead, M K. and Peggion, G. (1998) The effects of a dynamic shallow water front on acoustic propagation Conference: Oceans '98, Nice (France), 28 Sep-1 Oct 1998

Heathershaw, A D , Richards, S D and Thorne, P. D. (1996) Acoustic absorption and scattering by suspended sediments in turbid coastal waters Journal of Defence Science. Vol 1, no 2.

Hughes-Clarke, J E. and Parrot, R 2001. Integration of dense, time-varying water column information with high resolution swath bathymetric data United States Hydrographic Conference Proceedings, CD Rom, 9pp

Largier, J L 1992 Tidal Intrusion Fronts Estuaries, 15, p 26-39

Lewis, R E. (1997). Dispersion in Estuaries and Coastal Waters. John Wiley & Sons Ltd , Chichester, U K 312 pp

Priestley, A. D., (1998) The Dart Observatory an Estuarine Monitoring System. 1998. International Ocean Systems Design Vol 2, no 1. p.5-9

Affiliations

Priestley, A D. Senior Lecturer, Britannia Royal Naval College, Dartmouth, Devon, UK TQ6 0HJ

Thain, R H T Senior Lecturer, Britannia Royal Naval College, Dartmouth, Devon, UK TQ6 0HJ

SOUND SPEED VARIABILITY ACROSS AN ESTUARINE FRONT

Proceedings of the Undersea Defence Technology conference, La Spezia, Italy, 2002

R. H. Thain and A. D. Priestley.

Department of Marine Science, Britannia Royal Naval College, Dartmouth, Devon. TQ6 0HJ.

This paper describes the variability in sound speed across a V-shaped tidal intrusion front at the mouth of the Dart estuary in Devon, England. The well developed front forms on a flooding spring tide, approximately two hours after low water, and persists for around two hours. It is shown to significantly modify the oceanographic conditions at the estuary mouth during this period. Data have been collected using an ADCP (Acoustic Doppler Current Profiler) which indicate that convergent, downwelling currents are present in the frontal zone, whilst a CTD (Conductivity Temperature Depth) profiler was used to calculate sound speed values and develop detailed contoured sections of sound speed through the front. The variability of the sound speed structure is shown to affect sonar propagation patterns, whilst the convergent currents have implications for acoustic absorption and backscatter.

INTRODUCTION

Estuarine mouths are temporally and spatially highly variable environments where relatively fresh estuarine water meets seawater. Fronts of various types develop at the interface between these water masses. Major types of estuarine front include plume fronts, tidal mixing (stratification fronts), tidal intrusion fronts and shear fronts (Lewis [1]). Each frontal type is characterised according to its structure and flow dynamics. These fronts result in diffuse or sharp boundaries across which sound speed varies markedly.

As has been suggested by previous authors (e.g. Field *et al.* [2]), shallow water frontal zones are characterised acoustically by variability over periods of hours, and hence there exists a need to consider the dynamics of fronts when trying to draw conclusions about their effects on sound propagation.

In addition, convergence in frontal zones can result in high concentrations of suspended particulate matter, which has been demonstrated by

Heathershaw *et al.* [3] to degrade MW/MCM sonar performance and reduce detection ranges by up to 50%.

In the Dart estuary in Devon, UK, at least three of the fronts identified above form under different tidal and river discharge conditions Tidal mixing fronts form at neap tides when the estuary is stratified and the waters of the English Channel are well mixed. Plume fronts form at the estuary mouth when very high discharge events occur (especially at neap tides). A tidal intrusion front develops close to low water during periods of spring tides, when the flood tide enters the estuary and plunges beneath the estuarine water. At the surface, a characteristic 'V'-shaped foam and debris line is evident, and a marked halocline develops below the surface manifestation of the front.

This study examines the temperature, salinity and sound speed structure of the Dart tidal intrusion front with a view to providing sound speed data for the prediction of sonar propagation patterns across such fronts. The front is a dynamic feature, which exists only for a period of 2-3 hours, being particularly evident just after low water, and moves in a landward direction as it develops. It eventually decays when the increasing velocity of the flood current destroys the stratification. CTD surveys conducted close to low water demonstrate the evolution and structure of the front, whilst Acoustic Doppler Current Profiler (ADCP) surveys detail the flow dynamics in the frontal zone

METHODS

A survey to provide a detailed picture of the flow, temperature, salinity, density and sound speed structure of the entrance to the Dart estuary was undertaken in March 2002, during a spring tidal cycle. A 13.7 metre GRP twin screw motor launch provided an ideal survey platform.

A Valeport 604 CTD was deployed from the vessel, internally logging temperature, conductivity and depth (and calculated salinity, density and sound speed) at depth intervals of 0.2 metre. Data from the down-column casts only were used, previous studies having highlighted the unreliability of up-column casts with this instrument.

An RDI Instruments 'Workhorse' 600KHz broadband ADCP (Acoustic Doppler Current Profiler) was mounted on a custom-made steel pole, designed specifically to fit vertically over the bow of the survey vessel. The pole extended approximately two metres below the waterline, allowing some flexibility in the mounting depth of the instrument. Mounted and calibrated using the suggestions of other workers wherever possible (e.g. Murphy *et al.* [4]; Brubaker & Simpson [5]), the transducer head was affixed to the pole, at a depth of approximately 0.5 metre to

minimise flow disturbance around the head. The depth of the transducer, combined with the 'blanking depth' of 0.5 metre below the transducers common to all ADCP's, resulted in an area of 'no data' in the first 1 metre of the water column. The ADCP was set to bottom track mode, with a bin size of 0.5m, and an ensemble length of 5 seconds. Although a longer averaging period would have been beneficial for data quality, earlier studies indicated that much of the longitudinal resolution across the front would have been lost. Likewise, a slower vessel speed would have been desirable. However, safe vessel handling became an issue at slower speeds, especially in the strong current shears apparent around the frontal interface.

An InterOcean S4 buoy, an electro-magnetic current meter, was deployed in the estuary prior to commencing the main survey, in order to verify the accuracy of the ADCP measurements. The vessel was sailed as closely as possible to the S4, both in an upstream and downstream direction, and the current magnitudes of the two instruments were found to agree to within 5cm s^{-1}.

A Trimble 4000SE Single frequency 9 Channel GPS provided the positioning for the survey, providing both reliable and stable positions throughout the survey period. Both the ADCP and the GPS were interfaced to a portable PC in the aft cabin, and all the instruments were powered by a portable petrol generator lashed to the after deck

Survey lines were run from Checkstone Buoy to the Lower Ferry – a distance of approximately 1200 metres (figure 1). ADCP data were collected on the first leg, heading to landward, with the helmsman attempting to maintain a course as near to the centre of the channel as possible at a steady speed of around 4 knots. It typically took around 10-12 minutes to complete the ADCP survey line. At the Lower Ferry, a survey line was immediately commenced in the opposite direction (to seaward), taking a CTD cast every 100-200 metres. The CTD survey line typically took about 30 minutes to complete, a combined data set of ADCP data and CTD data taking around 40 minutes to record.

Each series of ADCP and CTD lines was then repeated at hourly intervals, to ascertain the behaviour of the estuary over a 6 hour cycle, from 1 hour before low water to five hours after low water, the results from low water –1 hour and low water +1 hour being presented in this paper.

The two data sets (the ADCP data and the CTD data) have been combined to represent a quasi-synoptic snapshot of the flow behaviour, and the temperature, salinity and sound speed structure of the estuary at that stage

of the tide, the small time-lags between the data sets being deemed to be insignificant.

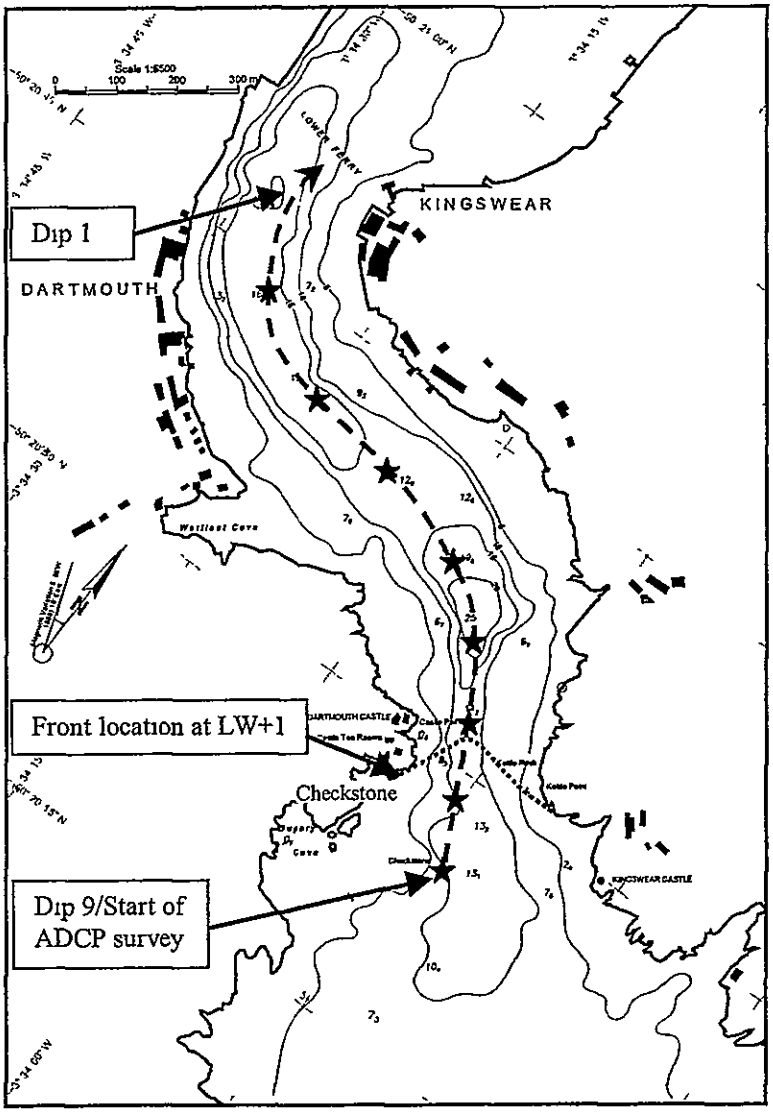

Figure 1. The mouth of the Dart estuary, Devon. The stars denote CTD dip locations, the heavy dashed line, the track of the vessel during the ADCP surveys

RESULTS

Figure 2 and figure 3 illustrate the salinity contours (from the CTD casts) along the length of the survey transect at one hour before low water (LW-

1) and one hour after low water (LW+1) respectively. The depth of the bed has been measured using the ADCP, and is slightly different for each transect. This is due to the survey vessel following a different track along the estuary (figure 1) each time, and in figure 2, the significant depth increase near the estuary mouth has been added for clarity. Zero distance (figures 2 and 3) represents the start point of each survey line, located approximately abeam of Checkstone buoy.

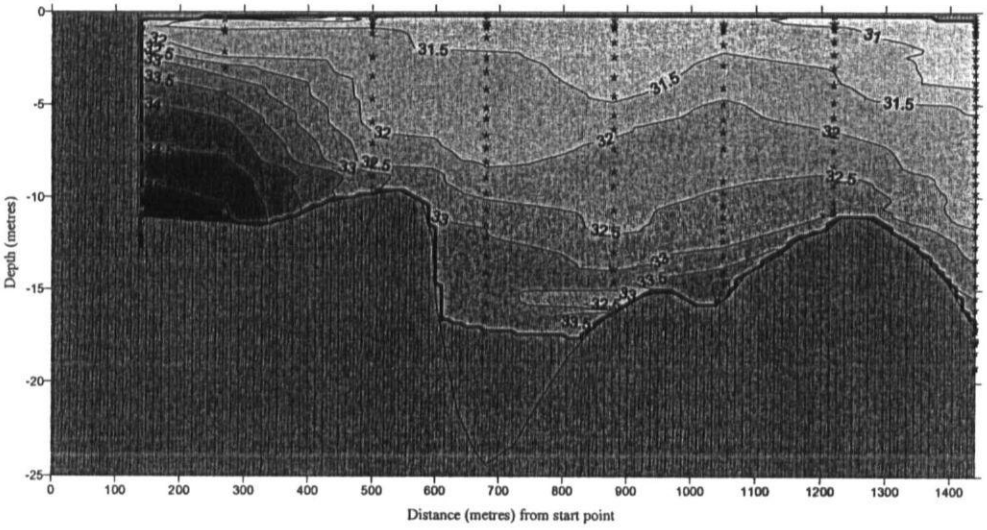

Figure 2. Salinity contours along the Dart estuary at LW-1

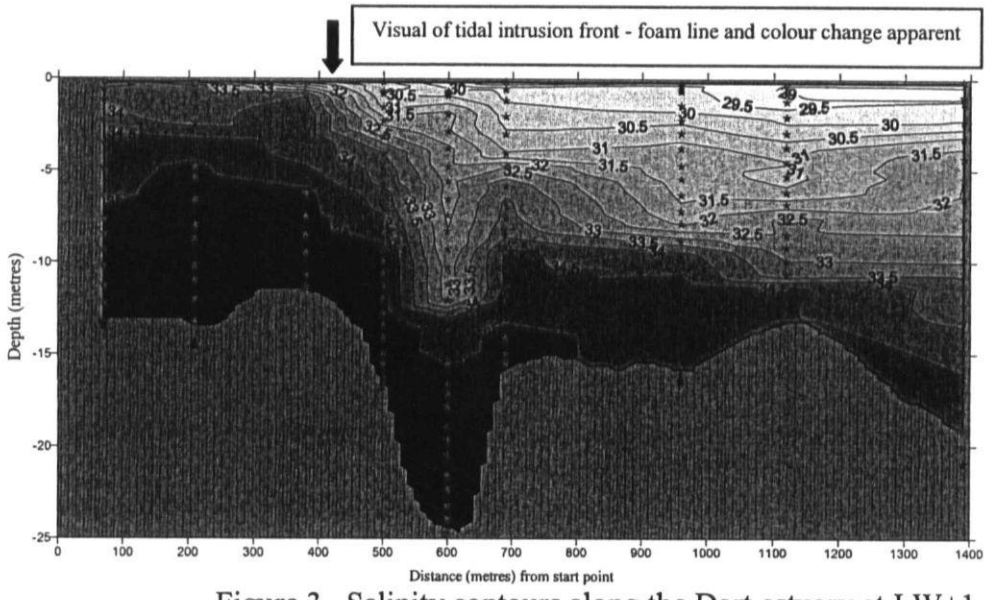

Figure 3. Salinity contours along the Dart estuary at LW+1

At LW–1 (figure 2) the water column appears uniformly weakly stratified, with a vertical salinity value of 31 at the surface, and 35 at the bed. There is no significant horizontal salinity gradient evident over the length of the transect. During this period of the survey, no foam line, colour change or surface convergence was visible to the naked eye, and the ADCP data indicated a slight ebbing flow.

However, at LW+1 (figure 3) there was a clear line of foam visible at the entrance to the estuary (figure 1), with at slight colour change also apparent on either side of the front. The salinity contours (figure 3) indicate a clear horizontal gradient, between dips six and seven, values ranging from 30.5 to 33.5 over a distance of less than 100 metres. This was the location where the foam line and colour change was visually noted. There is also a clear difference in vertical structure evident on either side of the front. On the seaward side of the front (from 0 metres to 400 metres), a well-mixed regime is apparent, with a salinity difference of only 2 between surface and bed. However, on the landward side of the front (from 400 metres to 1400 metres), the water column has become stratified, with a salinity difference of 5 between surface and bed. A downward dip in the bathymetry between 500 metres and 700 metres is reflected in the the salinity contours.

The temperature data showed little variation horizontally or vertically, as at this time of year, the seawater and estuarine water have similar temperatures.

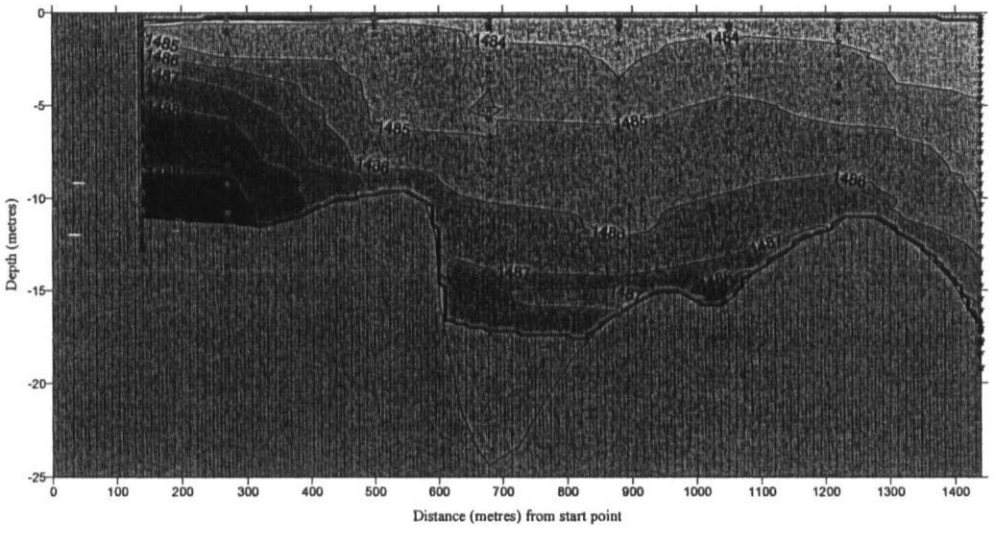

Figure 4. Sound speed contours along the Dart estuary at LW-1

Contours of sound speed at LW-1 and LW+1 (figure 4 and figure 5 respectively) show broadly similar gradients to those of salinity. At LW-1, there is little horizontal variation over the length of the transect, and a vertical gradient of 4 ms^{-1} from the surface to the bed of the estuary. However, at LW+1 (figure 5) there is a horizontal gradient of over 7 ms^{-1} across the frontal zone, a distance of less than 100 metres. As observed for the salinity contours, there is a different vertical regime on either side of the front. Little vertical variation is present on the seaward side of the front (from 0 metres to 400 metres). On the landward side of the front however (from 400 metres to 1400 metres), there is a significant vertical variation in sound speed of over 10 ms^{-1} from the surface to the bed.

A two-dimensional analysis of the flow velocity (figure 6) at LW+1 indicates an abrupt decrease in velocity in the frontal area. The vertical velocity component of the flow should be regarded as unreliable due to significant amounts of pitch and roll by the survey vessel over the large swell. The flow on the seaward side of the front is relatively constant in magnitude and direction, flowing up-river (flooding) in this area. However, on the landward side of the frontal interface, there is evidence of a two-layer regime. The upper layer is highly variable in direction and magnitude, with the lower layer of the water column being much more constant in direction, flooding strongly from a depth of around seven metres down to the bed.

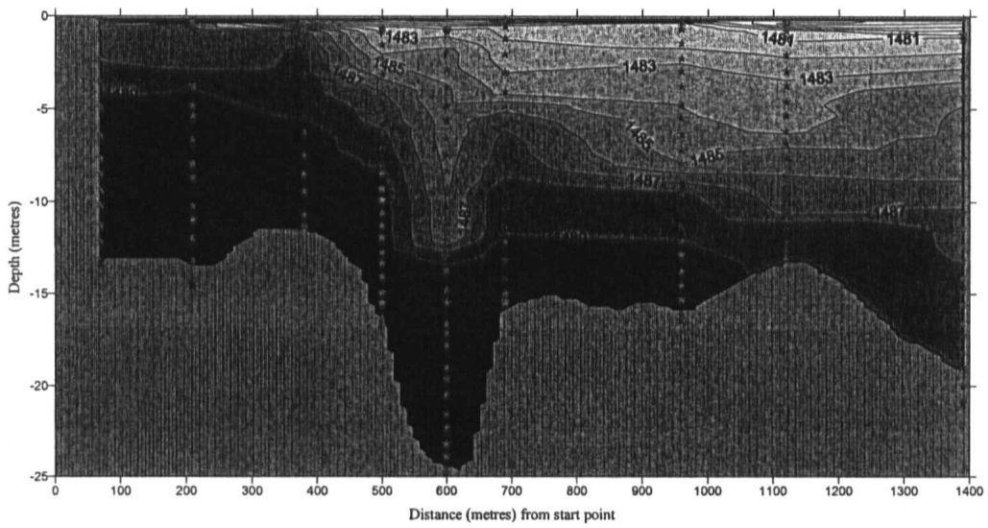

Figure 5. Sound speed contours along the Dart estuary at LW+1

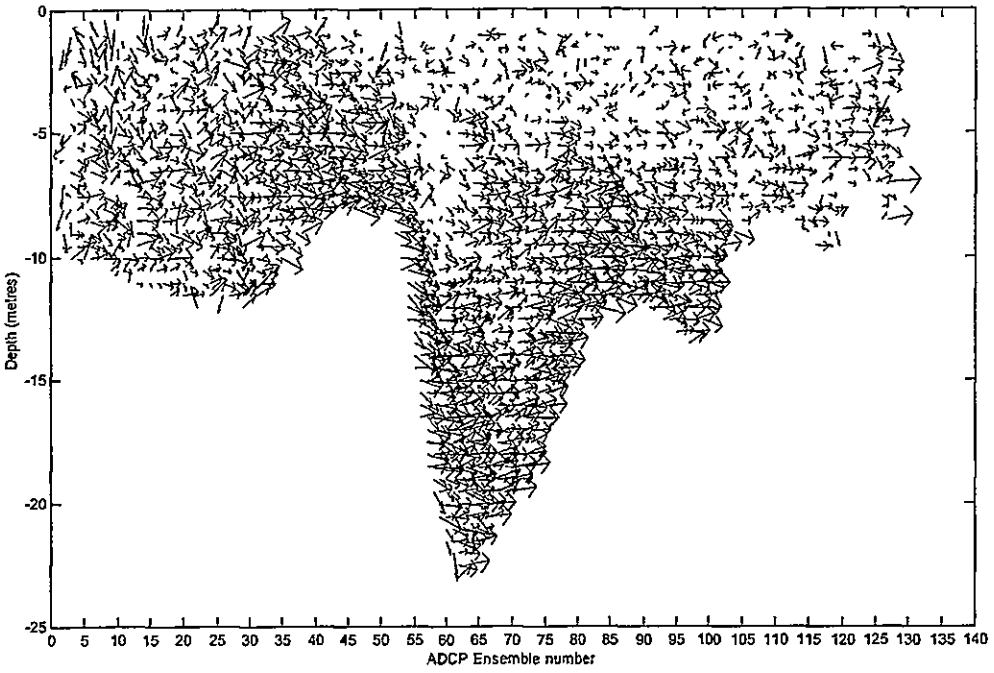

Figure 6. Relative flow velocity and direction at LW+1 hour

CONCLUSIONS

The data gathered in this survey serve to illustrate the dynamic nature of estuarine mouths and outline the variability of the key oceanographic parameters that influence sound speed in these strategically important environments

Prior to low water (at LW-1 hour) the flood tide is starting to enter the estuary close to the bed, and simultaneously, the tide is ebbing at the surface. Relatively weak salinity gradients and low levels of stratification exist and, consequently, the sound speed gradients are weakly positive.

After low water, for a period of 1-2 hours, the tidal intrusion front forms as the fresher water is pushed back into the estuary by the flood tide. The seawater plunges beneath the estuarine water, resulting in the development near vertical isohalines (and isovels), a very strong positive halocline and very marked positive gradients in sound speed. At the surface, there are significant lateral changes in salinity and sound speed.

Data from the Acoustic Doppler Current Profiler (ADCP) gathered at LW+1 hour closely mirror the CTD data and clearly show the higher

current velocities in the lower part of the water column (figure 6). Variable current directions and low current speeds are present landward of the front where the estuarine water flowing seawards is arrested by the flooding tide. Additionally, convergent currents at the surface lead to the accumulation of high concentrations of suspended particulate matter (SPM) and foam in the frontal zone.

The severe sound speed gradients that exist in the vicinity of this tidal intrusion front can be expected to create major problems for high frequency acoustic systems (minehunting sonars or multibeam echsounders, for example) operating in such a zone. Additionally, the high SPM concentrations present in the frontal zone are likely to lead to marked attenuation of high frequency sonar by absorption processes (Heathershaw *et al.* [3]).

At all stages of the tide, salinity is shown to be the dominant influence on sound speed, emphasising the requirement to consider (and measure) this parameter in shallow water environments when developing acoustic propagation models and predicting sonar ranges.

Dependence on the tidal current velocity is evident from the variability of the data gathered over a period of only 2-3 hours. However, tidal range and associated current speeds are also important, as at neap tides the tidal intrusion front is not evident at the estuary mouth. At neap tides the Dart estuary stratifies (Priestley [6]) and it is likely that a tidal mixing front develops in the estuary between the stratified waters of the estuary and the well-mixed waters of the English Channel. As a result, sound speed profiles would vary markedly over the tidal cycle at the estuary mouth.

Other factors that influence the nature of the front include river discharge. The tidal intrusion front in the Dart estuary forms when there is sufficient buoyancy of the estuarine waters, which may be the result of fresh water inflow or surface heating. However, when very high levels of river discharge occur, plume fronts form at estuarine mouths, which would tend to result in thin low salinity surface waters overlying a very marked halocline.

In summary, the tidal intrusion front, which forms close to low water at the mouth of the Dart estuary at spring tides, creates very short scale temporal and spatial variations in sound propagation conditions. Such dynamic features should be given careful consideration when utilising acoustic sensors in the littoral environment.

ACKNOWLEDGEMENTS

The authors wish to thank,Dr Paul Rampling for acting as coxwain for the duration of the data collection, Mr Peter Ganderton for his assistance and patience with setting up and calibrating the equipment, and Mr Gregory Borne for his help during the fieldwork. The charts produced by Mr Neil Millington have been invaluable, and the co-operation of the River Staff at BRNC, and Enseignes de Vaisseau Faure and Pelatan of the Ecole Navale, France is also gratefully acknowledged.

REFERENCES

[1] Lewis, R.E., 1997. *Dispersion in Estuaries and Coastal Waters* John Wiley & Sons Ltd., Chichester, U.K. 312 pages.

[2] Field, R L ; Broadhead, M.K ; Peggion, G 1998. The effects of a dynamic shallow water front on acoustic propagation. *Conference: Oceans '98*, Nice (France), 28 Sep-1 Oct 1998.

[3] Heathershaw, A. D , Richards, S. D. & Thorne, P. D. 1996. Acoustic absorption and scattering by suspended sediments in turbid coastal waters. *Journal of Defence Science* Vol1, no2.

[4] Murphy, D. J., D. C. Biggs and M. L Cooke (1992) Mounting and Calibrating an Acoustic Doppler Current Profiler, MTS Journal, 26, 34-38.

[5] Brubaker, J. M. and J. H. Simpson. 1999. Flow convergence and stability at a tidal estuarine front: Doppler current observations. *Journal of Geophysical Research.*, 104, 18, 257-18, 268.

[6] Priestley, A D. 1998. The Dart Observatory: an estuarine monitoring system. *International Ocean Systems Design* Vol 2, no 1. pp 5-9

Appendix three. Matlab code

All the Matlab m.files may be found on the compact disc attached to the back cover of this thesis.

I shall not be satisfied unless I produce something that shall for a few days supersede the last fashionable novel on the tables of young ladies.

Lord Thomas B. Macaulay


900656079
Richard H. C. Thain
The Dynamics of a Tidal Intrusion Front in a Natural Estuary: Effects on Multibeam Sonar Accuracy
Matlab files